Results of the LOCA bundle test QUENCH-L2 with M5® claddings (SR-7677)

J. Stuckert, M. Große, C. Rössger, M. Steinbrück, M. Walter

KIT

Karlsruher Institut für Technologie

Karlsruher Institut für Technologie

in der Helmholtz-Gemeinschaft

Wissenschaftliche Berichte

QUENCH – LOCA – REPORTS Nr.3

Results of the LOCA bundle test QUENCH-L2

with M5® claddings (SR-7677)

J. Stuckert*, M. Große*, C. Rössger*, M. Steinbrück*, M. Walter**

Institut für Angewandte Materialien:

* Angewandte Werkstoffphysik (IAM-AWP)

** Werkstoff- und Biomechanik (IAM-WBM)

Programm Nukleare Entsorgung und Sicherheit

Karlsruher Institut für Technologie

Mai 2018

Zusammenfassung

Ergebnisse des unter Bedingungen eines LOCA-Störfalls ausgeführten Versuches QUENCH-LOCA-2 mit M5®-Hüllrohren

Der QUENCH-L2-Bündelversuch wurde im Rahmen der QUENCH-LOCA-Testserie durchgeführt. Die M5®-Rohre im Lieferzustand mit Außendurchmesser von 10,75 mm wurden als Hüllrohre von 21 elektrisch beheizten Stäbe verwendet. Wie schon im früheren QUENCH-L1-Test, wurden die Brennstabsimulatoren separat mit Krypton bis zu einem Innendruck von 55 bar beaufschlagt. Bündelkonfiguration und Testprotokoll waren ähnlich denen des Referenztests QUENCH-L1 mit Zry-4-Hüllrohren. Eine Änderung zu dem vorhergehenden Versuch war die Verwendung von Wolfram für die Heizelemente mit 4,6 mm Durchmesser statt der Tantalheizer mit 6,0 mm Durchmesser. Diese Maßnahme erlaubte, den störenden Einfluss der hohen Duktilität des Tantals bei hohen Temperaturen zu vermeiden. Das spezifische Ziel des QUENCH-L2-Tests war es, Informationen über das Verhalten der M5®-Legierung unter Bedingungen eines LOCA-Störfalls mit komplettem Bruch eines Rohres des Kühlkreislaufes (LB-LOCA) bereitzustellen, besonders mit Fokus auf die so genannte sekundäre Hydrierung des Hüllrohrmaterials.

Der Versuch wurde am 30. Juli 2013 am Karlsruher Institut für Technologie erfolgreich durchgeführt. Das Temperatur-Zeit-Szenario entsprach dem eines typischen LB-LOCA-Störfalls in einem deutschen DWR. Die Vortestberechnungen wurden am Paul Scherrer Institut mit dem SCDAP/RELAP5-Code durchgeführt.

Vor dem Experiment wurden die Stäbe mit Krypton bis zu einem Druck von 20 bar gefüllt. Der Versuch startete mit der Stabilisierung des Bündels bei einer elektrischen Leistung von 3,6 kW. Dabei wurden 6 g/s Argon und 2 g/s überhitzter Dampf in das Bündel injiziert, sodass die maximale Bündeltemperatur der Stabilisierungsphase von ca. 860 K erreicht wurde. Während dieser Phase wurde der Stabinnendruck auf 55 bar erhöht. Das Bündel wurde bei 860 K und 55 bar für 1000 s gehalten. Die Transiente wurde durch schnelles Erhöhen (3,8 s) der elektrischen Leistung auf 42 kW gestartet, gefolgt von einem Anstieg auf 60 kW innerhalb der nächsten 42 s. In diesem Zustand wurde das Bündel für den Rest der transienten Phase (bis 77 s) gehalten. Während dieses Zeitraums stieg die Temperatur wie geplant auf ein maximales Niveau von etwas oberhalb 1350 K (maximal gemessen wurden 1398 K). Die durchschnittliche Aufheizgeschwindigkeit in der transienten Phase betrug 7,6 K/s.

Die erhöhte Duktilität der Hüllrohre führte zu einer fortschreitenden Rohrdehnung und schließlich zum Bersten von allen Hüllrohren. Das erste Bersten erfolgte 48 s nach Start der Transiente beim inneren Stab # 08 bei etwa 1113 K. Alle Stäbe versagten innerhalb der nächsten 20 s. Die Bersttemperaturen lagen zwischen 1050 K und 1195 K (ähnlich denen beim QUENCH-L1-Versuch). Der azimutale Temperaturunterschied erreichte 70 K für einige Stäbe zum Zeitpunkt des Berstens. Die durchschnittliche Dauer des Druckabbaus in den Stäben auf Systemdruck betrug etwa 38 s (ähnlich den Versuchen QUENCH-L0 und -L1).

Der Versuch wurde fortgesetzt mit einer Leistungsrücknahme auf 3,5 kW (Simulation der Nachzerfallswärme) bei 78 s und der Injektion von 20 g/s Dampf. In dieser Phase fand eine kontinuierliche Abkühlung auf ca. 1030 K statt. Der Kühlphase folgte nach 208 s das Abschrecken mit 100 g/s Wasser. Die ersten 40 s waren nötig, um das kleine Volumen am Bündelfuß zu füllen; während dieser Zeit erhöhte sich die Temperatur etwas aufgrund der Abschaltung der Dampfeinspeisung. Das erste Abschrecken wurde nach 238 s in den unteren Ebenen des Bündels registriert. Die Abschreckfront bewegte sich allmählich nach oben, und das erste Abschrecken im Ballooning-Bereich fand nach 265 s statt. Die komplette Bündelkühlung wurde nach 300 s erreicht.

Zusammenfassung

Die Nachuntersuchung mit Videoskop zeigte typische Ballooning-Bilder in den Ebenen zwischen 800 und 1000 mm. Einige Stäbe wiesen zwischen den Gitterabstandshaltern bei 550 und 1050 mm Höhe Krümmungen auf. Fragmentierungen der Hüllrohre wurde nicht beobachtet (Restduktilität ist ausreichend). Es wurde umfangreiches Datenmaterial aus den Laserscanner-Messungen herangezogen, um das Ausmaß der Bündel-Blockade für jede Ebene zu ermitteln. Die maximale Blockade des Kühlkanals (15% bei 960 mm) war niedriger im Vergleich zu QUENCH-L0 und -L1 (ca. 23%). Aufgrund moderater Blockade wurde eine gute Kühlbarkeit für alle drei Bündel QUENCH-L0, -L1 und -L2 beobachtet. Wirbelstrommessungen an den Außenoberflächen jedes Hüllrohres zeigten im Vergleich zu den QUENCH-L0 und L1-Tests einen niedrigeren Oxidationsgrad.

Eine detaillierte Bestimmung der Konzentration und Verteilung des absorbierten Wasserstoffs wurde mittels Neutronenradio- und Tomographie durchgeführt. Ausgeprägte Wasserstoffbänder wurden nur bei fünf Innenstäben beobachtet, und nur in zwei Fällen lag die Wasserstoffkonzentration über 1000 Gew.-ppm (ca. 1100 Gew.-ppm). Alle anderen zwölf geprüften Hüllrohre zeigten Konzentrationen zwischen 60 und 670 Gew.-ppm.

Alle 21 Hüllrohre wurden in Zugversuchen getestet. Ähnlich den QUENCH-L0-Stäben mit Wasserstoffkonzentrationen unter 1500 Gew.-ppm versagten neun QUENCH-L2-Hüllrohre an der Berststelle aufgrund von Spannungskonzentration. Alle anderen Hüllrohre versagten nach Einschnürung außerhalb des Ballooning-Bereiches.

Abstract

The QUENCH-L2 bundle experiment was performed in the framework of the QUENCH-LOCA test series[*]. As-received M5® tubes with an outside diameter of 10.75 mm were used as claddings of 21 electrical heated rods. Similar to the previous QUENCH-L1 test, the fuel rod simulators were separately internally pressurized with krypton to 55 bar. Bundle configuration and test protocol were similar to the reference test QUENCH-L1 with Zry-4 cladding. A change related to the previous experiment was the use of tungsten for the heater elements with 4.6 mm diameter instead of tantalum heaters with 6.0 mm diameter. This measure avoids a disturbing influence of too high ductility of tantalum at high temperatures. Specific objectives of QUENCH-L2 were to provide information about the behaviour of the M5® alloy on the response to a best-estimate large break LOCA sequence, as regards the impact of burst parameters on secondary hydriding of the cladding.

The experiment was successfully conducted at the Karlsruhe Institute of Technology on July 30, 2013 according to a temperature/time-scenario typical for a LB LOCA in a German PWR. Pre-test calculations were performed at Paul Scherrer Institute by using the SCDAP/RELAP5 code system.

Before the experiment, the rods were filled with krypton to 20 bar. The experiment started by stabilizing the bundle conditions with an application of electrical bundle power of 3.6 kW in 6 g/s argon plus 2 g/s superheated steam, resulting in maximum bundle temperatures of about 860 K. During this stabilization phase the rods were pressurized with krypton to 55 bar. The bundle was kept at peak cladding temperature (PCT) of 860 K and internal rod pressure 55 bar for 1000 s before the transient started. The transient was initiated by rapidly increasing the electrical power to 42 kW, reached after 3.8 s, followed by a steady increase to 60 kW within the next 42 s and maintained at that level for the rest of the transient (until 77 s). During this period, the temperatures increased from their initial values to a maximum in excess of 1350 K, as planned. The average heatup rate at the maximum temperature location was 7.6 K/s.

The increased ductility of the heated cladding resulted in a progressive ballooning and consequent burst of all claddings. The first burst occurred 48 s after transient initiation at the inner rod #08 at about 1113 K. All rods failed within the next 20 s. The burst temperatures were between 1050 K and 1195 K (similar to QUENCH-L1). The azimuthal temperature gradient for several rods reached 70 K on the burst time. The average depressurization duration of rods to the system pressure was about 38 s (similar to tests QUENCH-L0 and -L1).

The experiment continued with a power decrease to 3.5 kW at 78 s to simulate decay heat and injection of steam at nominal 20 g/s. After short period of peak cladding temperature increase to 1398 K, the bundle cooling was established. In this test stage mostly steady cooling to about 1030 K occurred. The cooling phase was followed by the injection of up to 100 g/s water from 208 s. The first 40 s were needed to fill the lower volume; during this time the temperatures increased somewhat in the absence of significant steam flow. The first quenching occurred at the bottom of the bundle at 238 s. Quenching progressed readily toward the top, and the first quench in the region of ballooning occurred at 265 s. Complete quenching was achieved at 300 s.

The post-test videoscope inspection showed typical ballooning pictures at elevations between about 800 and 1000 mm. Some rods seem to be bent between the grid spacers located at 550 and 1050 mm. No fragmentation of claddings was observed (residual ductility is sufficient). The data from the laser scanner measurements allow defining the degree of the bundle blockage for each elevation. The maximum blockage ratio of the cooling channel (15% at 960 mm) was lower in comparison to QUENCH-L0 and -L1 (about 23%).

Abstract

Due to moderate blockage a good bundle coolability was kept for all three bundles QUENCH-L0, -L1 and -L2. Eddy-current measurements at the outer surface of each cladding revealed lower degree of oxidation in comparison to QUENCH-L0 and -L1 tests.

A detailed determination of concentration and distribution of the absorbed hydrogen was realized by means of neutron radio- and tomography. Pronounced hydrogen bands in the claddings were observed only for five inner rods and only in two cases the hydrogen concentration exceeds 1000 wppm (about 1100 wppm). All other twelve investigated claddings showed concentrations between 60 and 670 wppm.

All 21 claddings were subjected to tensile tests. Nine claddings failed during tensile tests due to stress concentration at the burst position – similar to rods of the QUENCH-L0 bundle with hydrogen concentration less of 1500 wppm. All other claddings failed due to fracture after necking at elevations outside of ballooning region.

Contents

List of Tables

List of Figures

Introduction

Under the licensing procedures for pressurized water reactors (PWR) evidence must be given that the impacts of all pipe ruptures hypothetically occurring in the primary loop implying a loss of coolant can be controlled. The double-ended break of the main coolant line between the main coolant pump and the reactor pressure vessel is considered to constitute the design basis for the emergency core cooling system (ECCS) in a loss-of-coolant accident (LOCA). The break of a coolant line leads to the loss of coolant in the primary circuit of a PWR and the decrease in system pressure from 15.5 MPa to eventually around 0.32 MPa (boiling point, corresponding to 135°C). Consequently, the remaining coolant in the core as well as the emergency cooling water fed into the reactor core evaporate, the temperature of the fuel elements rises and the fuel rods start to balloon since they contain pressurized filling gas and fission gas products. At temperatures above 700°C, the load within the metallic cladding wall reaches a critical value and the most ballooned tube section finally bursts.

Upon rupture of the reactor coolant line the reactor is shut down. However, as the production of decay heat will be continued, reliable sustainment of the reactor core rod geometry and long-term emergency cooling of the core are required. To retain the core rod geometry the cladding embrittlement increasing during oxidation in steam has to be limited to an acceptable value. The current LOCA criteria and their safety goals are applied worldwide with minor modifications since the NRC release in 1973 [1, 2]. The criteria are given as limits on peak cladding temperature ($T_{PCT} \leq 1200°C$) and on oxidation level ECR (equivalent cladding reacted) calculated as a percentage of cladding oxidized (ECR $\leq$ 17% using the Baker-Just oxidation correlation). These two items constitute the criterion of cladding embrittlement due to oxygen uptake and, according to the RSK (Reactor Safety Commission) Guidelines, are included in the current German LOCA criteria, too [3].

The results elaborated worldwide in the 1980's on the Zircaloy-4 (Zry-4) cladding tubes behavior (oxidation, deformation and bundle coolability) under LOCA conditions constitute a reliable data base and an important input for the safety assessment of LWRs. With respect to the LOCA conditions for German LWRs, different out-off-pile [4, 5, 6], the FR2 in-pile [7] single rod as well as the REBEKA bundle tests [8, 9] were performed. It was concluded that the ECC-criteria established by licensing authorities are conservative and that the coolability of an LWR and the public safety can be maintained in a LOCA [10]. In-pile test data (with burn-up up to 35 MWd/kgU) were consistent with the out-of-pile data and did not indicate an influence of the nuclear environment on cladding deformation.

Due to major advantages in fuel-cycle costs, optimised reactor operation, and waste management, the current trend in the nuclear industry is to increase fuel burn-up. At high burn-up, fuel rods fabricated from conventional Zry-4 often exhibit significant oxidation, hydriding, and oxide spallation. Thus, fuel vendors have developed and proposed the use of new cladding alloys, such as Duplex DX-D4, M5®, ZIRLO™ and other. Therefore, it is important to verify the safety margins for high burn-up fuel and fuel claddings with advanced alloys. In recognition of this, LOCA-related behaviour of new types of cladding is being actively investigated in several countries [11, 12]. Due to long cladding hydriding period for the high fuel burn-up, post-quench ductility is not only influenced by oxidation, it is also significantly depending on the hydrogen concentration. Consequently, the 17% ECR limit is inadequate to ensure post-quench ductility at hydrogen concentrations higher than ≈500 wppm [13]. Due to so-called secondary hydriding (during oxidation of inner cladding surface after burst), which was firstly observed by JAERI [14], the hydrogen content can reach 4000 wppm in Zircaloy cladding regions around the burst [15].

Particularly to investigate the influence of the secondary hydriding phenomena on the applicability of the embrittlement criteria for the German nuclear reactors, it was decided to perform the QUENCH-LOCA bundle test series in the QUENCH facility of KIT, supported by the association of the German utilities (VGB). Additionally, the QUENCH-LOCA bundle tests could support experiments performed in-pile and in-cell, respectively, e.g. single-rod tests as those planned in the OECD SCIP-2 project [16]. Compared to single-rod experiments, bundle tests have the advantage to study the mutual interference of rod ballooning among fuel rod simulators as well as to take into account the local coolant channel blockages in this more realistic arrangement.

The first test QUENCH-L0 was performed with Zry-4 cladding tubes not pre-oxidised on 22.07.2010 as commissioning test and terminated with reflood immediately after the transient phase [17, 18]. The QUENCH-L1 test was performed on 02.02.2012 as reference test, using a similar bundle compared to the QUENCH-L0 test but including a cool-down phase between transient and reflood [19].

1   Description of the Test Facility

The QUENCH facility was constructed 1997 at KIT for investigation of the hydrogen source term during reflood, i.e. of the measurement of hydrogen release during the reflood of an overheated reactor core. Since then 17 bundle tests were successfully performed under severe accident conditions (Table 1). The main components of the QUENCH test facility are presented in Fig. 1. The test section is enclosed by a safety containment with a wall thickness of 5.6 mm and an inner diameter of 801.8 mm. The facility can be operated in two modes: a forced-convection mode depicted in the flow diagram of Fig. 2 and a boil-off mode. In the forced-convection mode (relevant for QUENCH-L2) superheated steam from the steam generator and superheater together with argon as a carrier gas enter the test bundle at the bottom (Figs. 3 and 4). The system pressure in the test section for the QUENCH-LOCA test is about 0.3 MPa. The argon, steam and hydrogen produced in the zirconium-steam reaction flow upward inside the bundle and from the outlet at the top through a water-cooled off-gas pipe to the condenser where the remaining steam is separated from the non-condensable gases argon and hydrogen. The water cooling circuits for bundle head and off-gas pipe are temperature-controlled to guarantee that the steam/gas temperature is high enough so that condensation at the test section outlet and inside the off-gas pipe can be avoided. The temperature at the bundle head is kept at 348 K, and the flow rate of the cooling water is ~250 g/s.

The off-gas pipe consists of a water-cooled inner pipe with a countercurrent flow and a flow rate of ~370 g/s. The water inlet temperature is controlled at 393 K. Between the off-gas pipe and inner cooling jacket there is stagnant off-gas. The main dimensions of the tubes that make up the off-gas pipe are:

- Inner pipe: outer diameter 139.7 mm, wall thickness 4.5 mm; total length 3256 mm, material: stainless steel;
- Inner cooling jacket: outer diameter 154 mm, wall thickness 2 mm, material: stainless steel;
- Outer cooling jacket: outer diameter 168.3 mm, wall thickness 5 mm, material: stainless steel.

The quenching water is injected into the bundle through a separate line marked "bottom quenching" in Fig. 4. The design characteristics of the test bundle are given in Table 2. The test bundle is made up of 21 fuel rod simulators, each with a length of approximately 2.5 m, and of four corner rods (see cross section in Fig. 5). The bundle is surrounded by a Zr shroud, which has two functions: 1) The shroud acts as steam and gas guide tube; 2) It simulates an adiabatic surrounding of the reactor core. The consideration of heated rod claddings, corner rods and shroud, manufactured from similar zirconium alloys, results in the surface of 30.6 effective rod simulators.

The fuel rod simulators (Fig. 6) are held in their positions by five grid spacers, four made of Zry-4, and one of Inconel 718 in the lower bundle zone. This bundle design is applied with a pitch of 14.3 mm. All test rods are heated electrically over a length of 1900 mm (thereof 1024 mm in the middle with W heater and residual length with Mo heaters at rod ends). The M5® cladding of the fuel rod simulator has an outside diameter of 10.75 mm and a wall thickness of 0.725 mm (see also Table 2). The cladding properties are listed in Table 3.

Tungsten (chemically clean tungsten) heating elements of 4.6 mm diameter are installed in the center of rods. W heaters with this small diameter were used for the first time in the QUENCH-L2 experiment. Their higher electrical resistance in comparison to tungsten heaters of 6 mm diameter (used for commissioning test QUENCH-L0) results in higher maximum heating rates, especially during the first transient phase and hence to a more prototypical test conduct. The tungsten heater with diameter of 4.6 mm produce similar heat amount as the tantalum heaters with diameter of 6 mm (used for the QUENCH-L1 test) but they are more rigid at high

temperatures. These heaters are surrounded by annular yttria-stabilized ZrO_2 pellets. The physical properties of the ZrO_2 pellets are described in Table 4.

The tungsten heaters are connected to molybdenum heater (chemically clean molybdenum) and copper electrode (material 2.1293 with Cr 0.8, Zr 0.08 and balance Cu) at each end of the W heater. The molybdenum and copper parts are joined by high-frequency/high-temperature brazing under vacuum ($2x10^{-3}$ mbar) using an AuNi 18 powder (particle size <105 μm). For electrical insulation the surfaces of both Mo and Cu parts are plasma-coated with 0.2 mm ZrO_2. To protect the copper electrodes and the O-ring-sealed wall penetrations against excessive heat they are water-cooled (lower and upper cooling chambers filled with demineralized water).

The copper electrodes are connected to the DC electric power supply by means of special sliding contacts at the top and bottom. The total heating power is limited by a maximal current of 7200 A and voltage of 9 V. Two DC-generators were used for two groups of rods connected in parallel: 1) 10 internal rods: #1 - #9 and rod #15; 2) 11 external rods: #10 - #14 and #16 - #21. The electrical resistance of the internal rod heating system, combined of W and Mo heaters as well as Cu alloy electrodes, was measured before (at the end of bundle assembling) and after the test (Table 5). The measured electric resistance of a single heater (W+Mo+Cu sections) is about 4.7 mΩ at room temperature. This value increases significantly with temperature. The additional resistance of the external electric circuit between the axial end of the single heater and the connection to the generator (sliding contacts, cables, and bolts) is 3.75 mΩ for the inner rod group and 4.05 mΩ for the outer rod group. These values can be taken as constant because the external electric circuit remains at ambient temperature throughout the experiment.

The lower boundary for the lower cooling chamber is a sealing plate made of stainless steel with plastic inlays for electrical insulation, sealed toward the system by O-shaped rings. The upper boundary of the lower cooling chamber is a sealing plate of stainless steel. An insulation plate made of plastic (PEEK) forms the top of the upper cooling chamber, and a sealing plate of Al_2O_3, functioning as a heat-protection shield, is the lower boundary of the upper cooling chamber (see Fig. 6).

In the region below the upper Al_2O_3 plate the copper electrode is connected firmly to the cladding. This is done by rotary swaging the cladding onto the electrode. In the swaging region a sleeve of boron nitride is put between electrode and cladding for electrical insulation. The axial position of the fuel rod simulator in the test bundle is fixed by a groove and a locking ring in the top Cu electrodes. Referred to the test bundle the fixing point of the fuel rod simulators is located directly above the upper edge of the upper insulation plate. So, during operation the fuel rod simulators are allowed to expand downwards. Clearance for expansion of the test rods is provided in the region of the lower sealing plate. Also in this region, relative movement between cladding and internal heater/electrode can take place.

The test bundle is surrounded by a 3.17 mm thick shroud (79.66 mm ID) made of Zr 702 with a 36 mm thick ZrO_2 fiber insulation (physical properties are given in Table 6) and an annular cooling jacket made of Inconel 600 (inner tube) and stainless steel (outer tube; see Fig. 5). The annulus between shroud and cooling jacket was filled (after several cycles of degasing) with stagnant argon of about 0.3 MPa (Fig. 18) and was connected to a flow-controlled argon feeding system in order to prevent steam access to the annulus after possible shroud failure. The 6.7 mm annulus of the cooling jacket is cooled by an argon flow. Above the W heater, i.e. above the 1024 mm elevation there is no ZrO_2 fiber insulation to allow for higher radial heat losses. This region of the cooling jacket is cooled by a water flow (Figs. 3 and 4). Both, the lack of ZrO_2 insulation above the W heaters and the water cooling, force the axial temperature maximum downward.

Insertion of four corner rods avoids an atypically large flow cross section at the outer positions and hence helps to obtain a rather uniform radial temperature profile.

According to LOCA scenarios the fuel rod simulators were separately pressurized. The gas supply system (Fig. 7) for individual pressurization of rods consists of pressure controller, 21 valves, 21 pressure transducers, and 21 justified compensation volumes for setting of original volume value of 31.5 cm³ (the compensation is needed because of the absence of empty plenums inside the rod simulators). The gas supply is connected with capillary tubes (with inner diameter 1 mm, length ca. 1.2 m) to each rod at its lower end with drilled copper electrode (Fig. 8). The gas gap between the cladding and the Cu/Mo parts and the W-heater/ZrO$_2$-pellets is 0.15 mm and 0.075 mm, respectively. Before gas filling the rods and the gas supply system were evacuated.

At the beginning of experiment, the fuel rod simulators were backfilled with Kr gas to 20 bar. Then, before the transient, they were separately pressurized to the target pressure of 55 bar as shown in Fig. 9

2 Test Bundle Instrumentation

A list of all instruments for the experiment QUENCH-L2, which were installed in the test section and at the test loop is given in Table 7. The distribution of the thermocouples along the bundle is shown in Table 8. No failed thermocouples were detected during the test.

2.1 Thermocouples

The test bundle was instrumented with sheathed thermocouples (TC) attached to the rod claddings (Fig. 10) at 17 different elevations between -250 mm and 1350 mm and at different orientations according to Figs. 11 and 12. The NiCr/Ni thermocouples (1 mm diameter, stainless steel sheath 1.4541 (X6CrNiTi18-10), MgO insulation) are used for temperature measurement at rod cladding and shroud outer surfaces. The TC tip is held in place by a Zr ferrule welded to the surface. The cables of the rod-thermocouples from the -250 mm to the 850 mm level leave the test section at the bottom whereas those of the TCs above 850 mm are routed out on the top of the test section to prevent TC cables passing the hot zone. On the same account the cables of the shroud-thermocouples in this region are routed outside the isolation. The thermocouples are designated as following:

- "TFS" for the thermocouples attached to the outer surface of the rod claddings;

- "TSH" for the shroud thermocouples mounted at the outer surface between -250 mm
and 1250 mm;

- "TIT" for the thermocouples installed inside the Zry-4 instrumentation rods at the three corner positions of the bundle (positions A, C and D) (see Fig. 13);

- "TCI" for the thermocouples at the cooling jacket are installed inside the wall of the inner
cooling tube (from -250 mm to 1150 mm, designation);

- "TCO" for the thermocouples at the outer surface of the outer cooling tube
(from -250 mm to 950 mm).

2.2   Gas Measurement System

The flow rates of noble gases (Ar, Kr) are regulated with the BRONKHORST flow controllers. Steam and water flows are controlled with the SIEMENS flow controllers. Numerous pressure transmitters from WIKA measure absolute and differential pressures along the gas supply system, at inlet and outlet of the test section.

The outlet steam and released hydrogen are analyzed by a Balzers mass spectrometer (MS) "GAM 300" (Fig. 14). Due to its location at the off-gas pipe in the facility the mass spectrometer responds almost immediately (less than 10 s). The "BALZERS GAM 300" is a completely computer-controlled quadrupole MS with an 8 mm rod system which allows reliable quantitative measurement of gas concentrations down to about 10 ppm. For the MS measurement a sampling tube is inserted in the off-gas pipe located approx. 2.7 m downstream from the test section outlet (see Fig. 2 and 4). It has several holes at different elevations to guarantee that the sampling of the gas to be analyzed is representative (see Fig. 15). To avoid steam condensation in the gas pipes between the sampling position and the MS the temperature of the gas at the MS inlet is controlled by heating tapes to about 150 °C (the upper operating temperature of the MS inlet valves). This allows the MS to analyze the steam production rate. Besides, the concentrations of the following species were continuously measured by the mass spectrometer during all test phases: argon, hydrogen, steam, nitrogen, oxygen, and krypton. The fuel rod simulators are filled with krypton which can be used as an indicator for cladding failure. Additionally, the MS is used to control the atmosphere in the facility, e.g., to monitor the gas composition at the beginning of the test.

The temperature and pressure of the analyzed gas are measured near to the inlet valve of the MS. The MS is calibrated for hydrogen with well-defined argon/gas mixtures and for steam with mixtures of argon and steam supplied by a BRONKHORST controlled evaporator mixing (CEM) device. The MS off-gas is released into the atmosphere because the amount of sampling gas taken out of the system is negligible. A heated measuring gas pump was used to ensure a continuous flow of the steam-gas mixture from the off-gas pipe to the mass spectrometer.

For the MS the mass flow rate of each gas specious is calculated by referring the measured gas concentration to the known argon mass flow rate according to equation (1):

$$\dot{m}_G = \frac{M_G}{M_{Ar}} \cdot \frac{C_G}{C_{Ar}} \cdot \dot{m}_{Ar} \tag{1}$$

with M representing the molecular masses, C the concentrations in vol% and $\dot{m}$ the mass flow rates of the corresponding gases.

3   Data Acquisition and Process Control

A LabView-based control and data acquisition system is used in the QUENCH facility. Data acquisition, data storage, online visualization as well as process control, control engineering and system protection are accomplished by three computer systems that are linked in a network.

The data acquisition system allows recording of about 200 measurement channels at a maximum frequency of 25 Hz per channel. The experimental data and the date and time of the data acquisition are stored as raw data in binary format. After the experiment the raw data are converted into SI units and stored as ASCII data.

For process control, a system flow chart with the most important actual measurement values is displayed on the computer screen. Furthermore, the operating mode of the active components (pumps, steam generator, superheater, DC power system, valves) is indicated. Blocking systems and limit switches ensure safe plant operation. Operating test phases, e.g. heating or quenching phases, are pre-programmed and can be started on demand during the experiment. The parameter settings of the control circuits and devices can be modified online.

Online visualization allows to observe and to document the current values of selected measurement positions in the form of tables or line graphs. Eight diagrams with six curves each can be displayed as graphs. This means that altogether 48 measurement channels can be selected and displayed online during the course of the experiment.

The data of the main data acquisition system and of the mass spectrometers are stored on different computers. Both computers are synchronized. The data of the main acquisition system are stored at a frequency of 5 Hz. The mass spectrometer data are recorded at a frequency of approx. 1 Hz during the entire test.

4   Test Performance and Results of Online Measurements

The test procedure was based on pre-test calculations for the QUENCH-LOCA series performed by the Paul Scherrer Institute (PSI, Villigen). According to the planned LOCA scenario, the transient phase should be performed with 8 K/s followed by slow cool-down phase and quenching.

The sequence of the test events is represented in Table 9. As a start the experiment began by stabilizing the bundle conditions with an application of electrical bundle power of 3.5 kW (corresponding to a linear heat rate of ≈1 W/cm) in argon - superheated steam mixture (with rates of 6 g/s argon and 2 g/s steam, or specific rates 0.2 g/s/(effective rod) and 0.07 g/s/(effective rod) correspondingly) resulting in a peak bundle temperatures of 850 K (Fig. 16).

Oscillation of the gas pressures during the test are presented in Figs. 17, 18. Fig. 19 shows the water flow characteristics. Mass spectrometer data on steam registration (during steam supply and evaporation phases), hydrogen production (due to oxidation of bundle and shroud) and krypton release (due to failure of claddings) are presented in Fig. 20. The development of integral hydrogen production is illustrated in Fig. 46. The dependence of evaporation rate of the quench water on the position of collapsed water front is depicted in Fig. 47.

The transient was initiated by rapidly increasing the electrical power to 42 kW (linear heat rate ≈9 W/cm) followed by steady increase to 60 kW (linear heat rate ≈13 W/cm) within 42 s and stayed at that level for the rest of the transient (until 78 s). During this period the temperatures increased from their initial values to a maximum in excess of 1300 K, as planned. Due to limitation of the maximal electrical current of the DC generators the average heating rate of about 6 K/s was realised. The readings of thermocouples at each bundle elevation are shown in Figs. 21 - 37. The temperatures of cooling jacket were practically not changed during the whole test (Fig. 38). The bundle inlet and outlet gas mixture temperatures were registered at -410 mm (T511) and +1350 mm (T512) correspondingly (Fig. 39). Two additional (in comparison to the reference test QUENCH-L1) thermocouples TFS 7/12i and TFS 7/13i installed at cladding surface of rod #7 at the

azimuthal position adjacent to the central rod #1 (i.e. opposite to thermocouples TFS 7/12 and TFS 7/13) allowed the registration of radial temperature gradients at the hottest elevations (Fig. 40).

The axial temperature profile in the bundle has a pronounced maximum between 850 and 1050 mm (Figs. 41 - 44). There is also a radial temperature gradient due to two reasons: 1) radial heat flux to the shroud, 2) electrical power supplied to the internal rod group was higher than the power for the external group because both DC generators reached current limit (~3600 A) but the electrical resistance of 11 external rods connected in parallel is lower than for 10 internal rods.

The experiment continued with power decrease to 3.5 kW at 78 s to simulate decay heat and injection of steam at a nominal value of 20 g/s. There was an initial minor temporary increase in temperatures at some locations, but this phase was mostly steady cooling to about 900 K.

This cooling phase was followed by 100 g/s water injection at 216 s. There was a period of about 40 s while the lower volume was being filled during which time the temperatures increased somewhat in the absence of significant flow. The first quench occurred at the bottom of the bundle at 238 s. Quenching progressed readily toward the top (indicated by wetting of thermocouples at different elevations, Figs. 48, Table 12), and the first quench in the ballooned region occurred at 264 s. Complete quench was achieved at 302 s.

The decreased yield strength and increased ductility of the claddings during the transient phase resulted in a progressive ballooning and consequent burst of all pressurized rods (Table 10). The first burst occurred 48 s after initiation of the transient phase at about 1113 K at rod #8. All 21 pressurized rods failed within 20 s (Fig. 45). The individual rod failures were indicated by internal pressure readings and correlated with krypton peaks measured in the off-gas pipe by the mass spectrometer. The Kr release indicates failure of inner and outer rod groups (Fig. 46). The first failed rod was the internal rod #8, the last one was the peripherical rod #12 (Table 10). The temperature range for bursts is estimated from thermocouple readings to be between 1050 and 1195 K.

5 Posttest Examination

5.1 Optical Observation of Outer Cladding Surfaces

First observations of burst positions were performed immediately after the test by means of the OLYMPUS videoscope. The camera of the videoscope (diameter 6 mm, total cable length 9 m) was introduced through the bundle bottom at positions of withdrawn corner rods (Figs. 49 - 53). For the peripheral rods no contacts between adjacent claddings due to ballooning or rod bending were observed. All observed thermocouples remained intact after the test.

The bundle was withdrawn from the shroud for further investigations. No noticeable changed bundle geometry was indicated (Fig. 54). Grid spacers were removed for the separation of the single rods. Moderate rod bending was observed for the inner rods (Fig. 55) with values between 6 and 12 mm deviation from original rod axis and some of the outer rods (Fig. 56) with values between 3 and 11 mm.

The shape and geometry of burst openings of all inner rods are very similar among each other (Fig. 57). The lengths of these openings varied between 10 and 14 mm, and the opening areas determined by image analyses are 12 - 29 mm² (Table 10). The scattering of the geometrical parameters for openings of the outer rods is larger: the length varies between 10 and 24 mm, and the areas bandwidth is 12 - 94 mm². The tangential burst positions of all rods, except the central one, correspond to the hottest rod region and are

directed mostly to the bundle centre (Fig. 58). All bursts are axially located between 770 and 970 mm (Fig. 59). No global blockage was formed due to the variation of the ballooning positions.

Observations of the cladding surface were performed with a Keyence digital microscope equipped with a macroscopic objective. The shapes of burst openings are shown in Figs. 60 - 63. Fig. 64 illustrates the structure of oxidized cladding surfaces near to the opening of rod #1. It can be seen that the cladding surface is covered with a network of crossed longitudinal cracks developed during the ballooning process. A large-scale crack cells network is located near to the burst opening, whereas small-scale cells are typical for the cladding side opposite to burst. The cell sizes change not only circumferentially, but also longitudinally: they decrease with increasing distance to the burst location. The surface cracks disappear at distances between 50 and 60 mm from the burst position – according to the strong strain decrease shown in the upper diagrams of Fig. 66. The cell size strongly depends on strain: the higher the strain the larger are the cells.

5.2 Profilometry of Claddings with Laser Scanner

5.2.1 Linear Laser Scanning

The profilometry of the rods was performed with a Linear Laser Scanner (Fig. 65) made by ANT Antriebstechnik GmbH for quantifying the deformations produced on the rods as a result of the QUENCH LOCA experiments. The ballooned parts of the bundle rods exposed to LOCA scenarios acquire a variety of shapes and sizes due to different temperature conditions. Therefore a precise method to detect the local variations in diameter along the rods was required.

5.2.2 Main Characteristics of the Measuring Device and Procedures

The measuring mechanism is based upon photocells which compare the amount of laser light blocked by the rod in relation to the portion of light that reaches the sensors. The equipment is mounted vertically and supported on a wall of the experimental hall in order to minimize the effects of shocks and vibrations propagated by the floor. The rod to be measured is placed vertically and linked to a step motor which is responsible for the precise turning of the rod according to a given number of measurements that should be made during a rotation of 360°. A resolution of 0.25° is provided. The laser scanner itself moves a predetermined length up or down the driving rails in order to cover a specific section of the examined rod. The smallest vertical step is 100 µm and the maximum length which the scanner can handle is 2000 mm.

Automatic settings allow the scanner to work for many hours without the need of supervision. For safety reasons and because of mechanical limitations, the data gathering is quite slow. A total of approximately 5700 points are measured each hour. This means that a scanning of a 1500 mm rod section takes roughly 4 days considering a measurement every 1 mm and 1°.

All data generated can be processed in various ways in order to determine different information. For instance, it allows the exact location and orientation of each burst, determination of circumferential cladding strain, calculation of increase of the cladding cross-section area and thus blockage. Also, a digital 3D rendered image is generated as a record and for further analysis, since every rod is sooner or later damaged by mechanical testing or cut for metallographic examination.

5.2.3 Results of the Scans

The evaluation of the scans can be divided into azimuthal and longitudinal analysis.

The azimuthal plots (Figs. 66 - 86, bottom) clearly show the orientation of the bursts and also give an idea of the shape. It was revealed that the bursts were oriented mainly to the center of the bundle, because of the radial thermal gradient which was established in the test section. The maximal cladding diameter was observed in the burst plane, the minimal diameter – in the perpendicular plane. It is interesting to mention, that immediately below and above the burst opening the maximal diameter was measured in the plane perpendicular to the burst plane. All azimuthal plots illustrate this fact: the neighboring elevations lower the burst evident the maximal diameter in the plane perpendicular to the burst. I.e. during ballooning, the cladding extends here more in the directions perpendicular to the burst plane.

The shape of the bursts vary widely, neither size nor symmetry have any apparent correlation to burst temperature.

Also based on these scans, the circumferential strains can be calculated (Table 13), which are depicted on Figs. 66 - 86, top. Inside the burst axial region, the strain includes here the burst opening width at each measured elevation. To obtain the maximum strain before burst, the opening width in its middle should be subtracted from the measured cladding perimeter at this elevation.

There is a clear correlation of the burst mean location and the temperature distribution on the longitudinal axis. Maximum strain of 29.3% was observed on the outer rod #10, minimum strain of 11.6% was observed on the outer rod #21.

For all rods the deformation starts at elevations about 250 mm and ends at 1250 mm. The axial extension of each rod with more than 5% strain is usually shorter than 185 mm. It is worth to notice that besides the main strain maximum most of the rods (#1 - #6, #12 - #15, #17 - #21) have a second (or sometimes even third) strain maximum located ≈100 mm (or ≈200 mm) below or above main maximum too. I.e. the ballooning was initiated at many axial locations inside the hot zone.

The blockage is the quotient of total increase of the rod cross-sections divided by initial empty area inside the inner surface of the shroud. Since the burst locations are scattered between elevations 784 and 963 mm, the blockage wasn´t too significant. As shown in Fig. 87, the maximum blockage occurs at about 960 mm and reaches 15% of area reduction. If, hypothetically, all burst were located at the same level, the blockage would be 28%.

5.3 Nondestructive Eddy Current and Ultrasound Measurements

Before cutting the cladding tubes for further investigations, the oxidation degree of each cladding was measured by means of the eddy current measurement device ISOSCOPE FMP30 from Helmut Fischer GmbH. The device was calibrated with two plastic foils of 24.3 and 99.3 µm thicknesses, which were disposed at the surface of as-received M5® tube. At least 20 circumferential measurements at each axial position were used to achieve the averaged result. The axial step width was 20 mm. The device shows the distance between the gauge and the internal metallic layer; i.e. the measured values correspond to the sum of the thicknesses of ZrO_2 and α-Zr(O) layers. The comparison of eddy current results with metallographic results confirms this assumption.

Fig. 88 and Fig. 89 show results of eddy current measurements for the inner and the outer groups of rods respectively. The most oxidized region is between 750 and 950 mm, what corresponds to the axial temperature profile. The comparison of measurement results for one rod with the same position (rod #3) in

three bundles (QL-0, -1, and -2) shows that the QL2 bundle has the smaller oxidation degree than the commissioning and reference bundles (Fig. 90).

Fig. 91 illustrates clearly the existence of a radial temperature gradient. This radial temperature gradient causes an azimuthal difference in the oxidation of each rod: the side of the cladding oriented to the central (hottest) rod is more oxidized than the cladding side oriented to shroud. Irregular thickness changes were observed inside the axial zone with the pronounced ballooning due to variations of the cladding thickness from this parameter for the original calibration sample. The thinning of the cladding wall along the line of the burst opening in the ballooning region was proved by ultrasound measurements (Fig. 92). The wall thickness increases from 500 μm in vicinity of the opening tip to the regular thickness of 725 μm at a distance of about 40 mm.

5.4   Metallographic Examination

The metallographic investigation of the longitudinal section of the claddings at the burst elevation evidences oxide layer growth at the outer cladding surface as well as oxidation of the inner surface (Fig. 93). The thickness of the inner oxide layer decreases axially: at the elevation 30 mm above and below the burst opening edge only very thin oxide layers were observed.

The detailed optical mapping of the inner surface (Fig. 94) shows a transition from oxidised inner surface in the ballooning region to a metallic surface outside the ballooning region. A part of inner surface outside the ballooning was not oxidised due to a close contact between pellets and cladding. The axial locations of contacts between adjacent pellets have become visible due to strips of deposited tungsten transported through the gas phase from the tungsten electrical heater to the Zry cladding. The presence of tungsten in these strips was proved by an EDX analysis of the inner cladding surface (Fig. 95). Deposition of tungsten was also observed at the pellet surfaces (Fig. 96).

The internal cladding oxidation is caused by steam penetration through the burst opening after release of filling and fission gases (Fig. 97). The hydrogen, produced during the oxidation of the inner cladding surface, propagated in the gap between cladding and pellet up to boundary of the inner oxidised region. Outside of this region there are no more barriers for the absorption of hydrogen by the metal, and this internally oxidised region should be surrounded by hydrided zones. This assumption was confirmed by neutron radiography.

5.5   Results of Neutron Radiography and Tomography: Analysis of Absorbed Hydrogen.

5.5.1   Basic Principles

Neutron radiography is a powerful tool for the determination of hydrogen concentration and distribution in zirconium alloys [20-24]. Hydrogen can be quantitatively and non-destructively determined with a spatial resolution of up to 25 μm. The method was applied for the post-test hydrogen analysis of selected QUENCH-L2 cladding tubes.

Firstly, a short introduction into neutron radiography will be given. The sample is positioned into a parallel neutron beam. The intensity distribution behind the sample is measured for each pixel. From the intensity the transmission T can be calculated:

$$T(x, y) = \frac{I(x, y) - I_B(x, y)}{I_0(x, y) - I_B(x, y)} \tag{2}$$

where x and y are the coordinates of the pixel position. I, I_0 and I_B are the intensities behind and before the sample and the background intensity, respectively. From the neutron transmission the total macroscopic neutron cross section Σ_{total} can be calculated:

$$\Sigma_{total}(x, y) = \frac{-\ln(T(x, y))}{s(x, y)} \tag{3}$$

where s is the neutron path length through the material. The total macroscopic neutron cross section is the sum of the total microscopic cross section σ of the isotopes i multiplied with their number density N:

$$\Sigma_{total}(x, y) = \sum_i \sigma_i \cdot N_i = \underbrace{N_{Zry}(x, y) \overline{\sigma_{Zry}}}_{\Sigma_{sample\ as\ reseived}} + N_O(x, y)\, \sigma_O + N_H(x, y)\, \sigma_H \tag{4}$$

In the case of steam oxidation of cladding materials it can be assumed that only the amount of oxygen and hydrogen is changed whereas the amount of zirconium and the alloying elements is not influenced significantly.

In order to reconstruct the specimen three-dimensionally, radiography projections have to be taken from different orientations. According to the sampling theorem, the number n of projections is connected with the spatial resolution (pixel size) d and the radius R of the object circle that fully encompasses the object formed by the rotating of the sample:

$$n = \sqrt{2\pi}\, \frac{R}{d} \tag{5}$$

5.5.2   Technique

The neutron radiography measurements were performed at the ICON facility at the Swiss neutron source SINQ at Paul Scherrer Institute Villigen. The investigations were performed applying the so called micro-tomography setup providing the highest resolution (pixel distance 13 µm). The field of view is 28 mm x 28 mm. The samples were scanned through the field of view with a step width of 25 mm. Exposure times of 300 s were applied. The specimens were measured horizontally.

The neutron tomography experiments were performed at the ANTARES facility at the FRM2 research reactor in Garching. 401 projections were measured with a pixel size of 75 µm and an illumination time of 30 s. A field of view of 77 mm (axial direction) x 77 mm (radial direction) was applied.

5.5.3   Results of Radiography

The investigations comprise measurements of all rods of the QUENCH-L2 test. At first, the calibration of the correlation between number density ratio of hydrogen to zirconium atoms and total macroscopic neutron cross section was performed for the experimental setup applied. Calibration specimens were produced by annealing cladding tube segments in argon/hydrogen atmosphere with different hydrogen partial pressures at various temperatures. The hydrogen uptake of calibration samples was determined by measurement of the weight gain. From the slope of the curve the calibration was determined:

$$\frac{H}{Zr} = \frac{\Sigma_{total} - 0.22\ cm^{-1}}{2.1573\ cm^{-1}} \qquad (6)$$

Fig. 98 shows the radiographs taken from internal rods, whereas Fig. 99 reveals depicted results for outer rods. For the inner rods, not only the bended hydrogen enriched bands known from the QUENCH-L0 test were found but also tungsten stripes corresponding to contacts of adjacent pellets. The tungsten was transported from heaters when their temperatures exceeded 1200°C.

5.5.4 Hydrogen Content: Results of Tomography

All 21 rods were investigated. For the experimental setup applied the following correlation was determined:

$$\Sigma_{total} = 0.1954\ cm^{-1} + 2.6838\ cm^{-1}\ \frac{H}{Zr} \qquad (7)$$

The reasons for the difference between equations (6) and (7) are different neutron spectra of the SINQ and the Garching research reactor and different wavelength efficiencies of the two detector systems applied (Gadox transmitter at PSI, LiF$_6$ at FRM2).

This procedure was applied for the reconstructions of QUENCH-L2 rods. Seven inner rods and eight outer rods were investigated before the tensile tests. Fig. 100 and Fig. 101 illustrate the tomography results for inner and outer rods correspondingly. The concentration of absorbed hydrogen for relatively cold outer rods was noticeably low (if any) in comparison to inner rods.

The statistical analysis of the tomography data allows determining the axial distribution of hydrogen concentration in the vicinity of burst openings. The resolution of this distribution is very high due to small pixel size (75 µm). Figs. 102 - 112 depict distribution of mean and maximal concentrations calculated for each cross section (width of cross section is 75 µm). Mean value corresponds to arithmetic average for all pixels of cross section. Maximal value was determined by scanning of each cross section with window x*y*z=3*3*1 pixels. It can be seen that the mean hydrogen concentration within the burst opening region is between 10 and 50 wppm. Inner rods show a significant increase of hydrogen content above (hydrogen band) and below (hydrogen longitudinal spot) the burst opening, whereas for outer rods only increased background hydrogen signal was measured. Additionally, tungsten rings at the inner cladding surface were detected. A comparison between inner and peripheral rods indicates that zones with noticeable hydrogen enrichments are formed if the temperature exceeds 1273 K. The axial profiles of maximal concentrations are similar to profiles of mean values and shifted by several hundred wppm in comparison to mean curves. The maxima of both curves for each measured rod are represented in Table 11.

5.5.5 Cladding Cross Sections Reconstructed by Tomography

Tomographic reconstructions allow rebuilding very precisely the shape of cladding tubes at each axial elevation. Fig. 113 compares the initial tube form (given in cyan) with the post-test tomography images of burst claddings at the axial position of the maximal burst opening. This comparison shows that claddings were practically not deformed at positions opposite to burst openings. The wall thinning occurred essentially in vicinity of the burst openings.

5.6   Mechanical Tests

To determine the residual strength and ductility of QUENCH-LOCA tested claddings, particularly to identify the embrittlement in dependence of the different quench test conditions, tensile tests on relevant cladding sections were performed at room temperature. Previously, the mechanical properties of the axially homogeneous hydrogenated Zircaloy-4 claddings were investigated in 2010 during the single rod test series [25].

5.6.1   Tensile Test Set-up

The tensile tests were carried out using a universal testing machine from INSTRON (type 4505, 50 kN load cell), equipped with specially developed grip holders. The experiments were performed displacement-controlled with a displacement rate of 2 mm/min at room temperature (RT). To clamp the tubes without deforming their end sections, exact fitting end plugs were mounted. Since a cladding tested in a QUENCH experiment usually shows an inhomogeneous ZrO_2/α-Zr(O) layer thickness along the main tube axis, the specimens were optically subdivided with paint markers to determine both the global and the local axial elongation during a test by using a CCD-camera measurement system. To increase the resolution of the optical measurement device, three cameras were used for the tests. Generally, the initial gauge length l_0 of a specimen was 750 mm and a sample was prepared in that way, that the ballooning section was positioned in the axial center. However, since some of the specimens (#3, 5, 8, 9, 14 and 15) showed a strongly warped shape after the QUENCH test, they had to be cut that the ballooning section revealed a distance of 50 mm related to the center, in order to avoid strong bending moments in the claddings at the edge of the grips. After the tests, the strain was calculated from the captured pictures by using the Digital Image Correlation and Tracing program provided by MATLAB [26] and the stress was calculated by using average values of the measured initial inner and outer diameters from the ends of a tube.

5.6.2   Results of the Tensile Tests

During the tensile tests, two different failure modes were observed (Fig. 113) – typical fracture after necking with fracture surfaces perpendicular to the load direction, as well as fracture from (pre)crack tip to (pre)crack tip at which the final crack propagates around a sample (compare Fig. 115). The second mode doesn't occur abruptly. In fact one can observe that the onset of failure is driven by strong local deformations, starting at the (pre)crack tips. It is interesting to note, that almost only claddings from the outer area of the bundle failed in this mode (#8, 10, 15 – 21), in parts with remarkable elongations at fracture up to more than 11 %.

In general, the elongation at fracture varies between 2.7 and 16.5 %, and the strength at fracture of the QUENCH tested cladding varies between ca 300 and ca 500 MPa. An overview of all determined mechanical properties is given in Table 14. Fig. 116 and Fig. 117 depict the stress-strain curves of all inner and outer specimens respectively. Since every tube showed a more or less pronounced individual warped shape, the claddings were differently straightened at the beginning of a test. However, even if the single samples reveal greater differences in elongation with respect to the onset of deformation and afterwards also with respect to both fracture behaviour and fracture specific values, the general deformation behaviour is definitely very similar. When comparing Zircaloy-4 (QUENCH-L0, QUENCH-L1) with M5® (QUENCH-L2) one can see that the general deformation behaviour of individual Zircaloy-4 claddings is more heterogeneous within a bundle. Additionally it is found, that the embrittlement of M5® claddings during a QUENCH-LOCA test is on average significantly lower, even in the ballooning section.

6 Summary and Conclusions

Test QUENCH-LOCA-2 was performed according to a temperature/time-scenario typical for a LBLOCA in a German PWR with a maximal heat-up rate of 8 K/s, a cooling phase lasting 120 s and the terminated with 3.3 g/s/rod water flooding.

The maximum temperature of 1400 K was reached at the end of the heat-up phase at elevation 850 mm. The tangential temperature difference across a rod was up to 70 K on the burst onset.

Due to the low ballooning degree the maximum blockage ratio of the cooling channel (15% at 960 mm) was lower in comparison to QUENCH-L0 and -L1 (about 23%). Due to moderate blockage good bundle coolability was kept for all three bundles.

The cladding burst occurred at temperatures between 1050 and 1195 K (similar to QUENCH L1). The inner rod pressure relieved to the system pressure during about 35 s (similar to QUENCH-L0 and -L1).

During quenching, following the high-temperature phase, no cladding fragmentation was observed, stands for sufficiently residual ductility.

Eddy current measurements showed a quite low degree of oxidation of the outer surface of the cladding with less than 25 μm for both layers ZrO_2 and α-Zr(O). The inner cladding surface was oxidized in vicinity of the burst to about 10 μm ZrO_2 and 15 μm α-Zr(O). The thickness of inner oxide layer was reduced to less than 5 μm at distance 30 mm from the edges of burst openings.

The three experiments performed so far (QUENCH-L0, -L1 and -L2) show that the formation of hydrogen-containing bands is expected above 930°C. The pronounced hydrogen bands inside QUENCH-L2 claddings were observed only for five inner claddings and only in two cases (rods #1 and #8) the hydrogen concentration was higher than 1000 wppm (about 1100 wppm). All other twelve claddings investigated showed concentrations between 60 and 670 wppm.

Nine claddings (one from inner rods and eight from outer rods) failed during tensile tests due to stress concentration at the burst position – similar to rods of the QUENCH-L0 bundle with hydrogen concentration < 1500 wppm. All other claddings failed due to fracture after necking at elevations outside of the ballooning region

7 Acknowledgments

8   References

[1]   Atomic Energy Commission Rule-Making Hearing, Opinion of the Commission, Docket RM-50-1, 28 December, 1973.

[2]   G. Hache and H. M. Chung, "The History of LOCA Embrittlement Criteria," NUREG/CP-0172, May 2001, pp. 205-237.

[3]   RSK-Leitlinien für Druckwasserreaktoren. Ursprungsfassung (3. Ausgabe vom 14. Oktober 1981) mit Änderungen vom 15.11.1996.
  http://www.rskonline.de/downloads/8110dwr.pdf

[4]   P. Hofmann, S. Raff. Verformungsverhalten von Zircaloy-4-Hüllrohren unter Schutzgas im Temperaturbereich zwischen 600 und 1200°C. Wissenschaftliche Berichte, KFK-3973, Karlsruhe, 1981.
  http://bibliothek.fzk.de/zb/kfk-berichte/KFK3168.pdf

[5]   L. Schmidt, H. Lehning, D. Piel. Berstversuche an Zircaloy-Huellrohren unter kombinierter mechanisch-chemischer Beanspruchung (FABIOLA). In: Projekt Nukleare Sicherheit. Jahresbericht 1982. KfK-3350 (Juli 83) S.4200/69-4200/70.

[6]   M. E. Markiewicz, F. J. Erbacher. Experiments on Ballooning in Pressurized and Transiently Heated Zircaloy-4 Tubes. Wissenschaftliche Berichte, KFK-4343, Karlsruhe, 1988.
  http://bibliothek.fzk.de/zb/kfk-berichte/KFK4343.pdf

[7]   E. H. Karb, M. Prüßmann, L. Sepold, P. Hofmann, G. Schanz. LWR Fuel Rod Behavior in the FR2 ln-pile Tests Simulating the Heatup Phase of a LOCA. Final Report. Wissenschaftliche Berichte, KFK-3346, Karlsruhe, 1983.
  http://bibliothek.fzk.de/zb/kfk-berichte/KFK3346.pdf

[8]   K. Wiehr. REBEKA-Bündelversuche Untersuchungen zur Wechselwirkung zwischen aufblähenden Zircaloyhüllen und einsetzender Kernnotkühlung. Abschlußbericht. Wissenschaftliche Berichte, KFK-4407, Karlsruhe, 1988.
  http://bibliothek.fzk.de/zb/kfk-berichte/KFK4407.pdf

[9]   F. J. Erbacher, H. J. Neitzel, K. Wiehr. Cladding Deformation and Emergency Core Cooling of a Pressurized Water Reactor in a LOCA. Summary Description of the REBEKA Program. Wissenschaftliche Berichte, KFK-4781, Karlsruhe, 1990.
  http://bibliothek.fzk.de/zb/kfk-berichte/KFK4781.pdf

[10]   F. J. Erbacher, S. Leistikow. A Review of Zircaloy Fuel Cladding Behavior in a Loss-of-Coolant Accident. Wissenschaftliche Berichte, KFK-3973, Karlsruhe, 1985.
  http://bibliothek.fzk.de/zb/kfk-berichte/KFK3973.pdf

[11]   J.-C. Brachet, V. Vandenberghe-Maillot, L. Portier, D. Gilbon, A. Lesbros, N. Waeckel, and J.-P. Mardon, Hydrogen Content, Preoxidation, and Cooling Scenario Effects on Post-Quench Microstructure and Mechanical Properties of Zircaloy-4 and M5® Alloys in LOCA Conditions. J. ASTM Intl., Vol. 5, No. 5 (2008). Available online as JAI101116 at www.astm.org.

[12]   T. Chuto, F Nagase and T. Fuketa. High Temperature Oxidation of Nb-containing Zr Alloy Cladding in LOCA Conditions. Nuclear Engineering and Technology, Vol.41, No.2, March 2009.

[13]   Hee M. Chung. Fuel Behavior under Loss-of-Coolant Accident Situations. Nuclear Engineering and Technology, Vol.37 No.4, August 2005.

[14]   H. Uetsuka, T. Furuta and S. Kawasaki. Zircaloy-4 Cladding Embrittlement due to Inner Surface Oxidation under Simulated Loss-of-Coolant Condition. Journal of Nuclear Science and Technology, 18[9], pp. 705~717 (September 1981).

References

[15] M. Billone, Y. Yan, T. Burtseva, R. Daum. Cladding Embrittlement During Postulated Loss-of-Coolant Accidents, NUREG/CR-6967, July 2008.

[16] OECD SCIP-2 Project: http://www.oecd-nea.org/jointproj/scip-2.html

[17] J. Stuckert, M. Große, C. Rössger, M. Steinbrück, M. Walter. Results of the commissioning bundle test QUENCH-L0 performed under LOCA conditions. KIT Scientific Reports, KIT-SR 7571 (March 2013).

[18] J. Stuckert, M. Große, C. Rössger, M. Klimenkov, M. Steinbrück, M. Walter. QUENCH-LOCA program at KIT on secondary hydriding and results of the commissioning bundle test QUENCH-L0. Nuclear Engineering and Design, 255(2013), pp. 185-201. DOI:10.1016/j.nucengdes.2012.10.024.

[19] J. Stuckert, M. Große, C. Rössger, M. Steinbrück, M. Walter. Results of the LOCA reference bundle test QUENCH-L1 with Zircaloy-4 claddings. KIT Scientific Reports, KIT-SR 7651 (2013).

[20] M. Grosse, E. Lehmann, P. Vontobel, M. Steinbrueck: "Quantitative determination of absorbed hydrogen in oxidised zircaloy by means of neutron radiography", Nucl. Instr. & Methods in Phys. Res. A 566 (2006), 739.

[21] M. Große, G. Kühne, M. Steinbrück, E. Lehmann, P. Vontobel, J. Stuckert. Determination of the hydrogen uptake of steam-oxidised zirconium alloys by means of quantitative analysis of neutron radiographs. J. Phys.: Condens. Matter 20 (2008), 104263.

[22] M. Grosse, E. Lehmann, M. Steinbrueck, G. Kühne, J. Stuckert. Influence of oxide layer morphology on hydrogen concentration in tin and niobium containing zirconium alloys after high temperature steam oxidation. J. Nucl. Mater. 385 (2009), 339.

[23] J. Stuckert, J. Birchley, M. Grosse, B. Jaeckel, M. Steinbrück. Experimental and calculation results of the integral reflood test QUENCH-14 with M5 cladding tubes. Annals of Nuclear Energy, 37(2010) S.1036-47, DOI:10.1016/j.anucene.2010.04.015.

[24] M. Grosse, M. Van den Berg, C. Goulet E. Lehmann, B. Schillinger. In-situ neutron radiography investigations of hydrogen diffusion and absorption in zirconium alloys. Nuclear Instruments and Methods in Physics Research Section A: Accelerators, Spectrometers, Detectors and Associated Equipment, Volume 651, Issue 1, 21 September 2011, Pages 253–257.

[25] J. Stuckert, M. Große, M. Walter. Mechanical properties of pre-hydrogenated (600 – 5000 wppm) cladding segments. 16th International QUENCH-Workshop, Karlsruhe, November 2010, ISBN 978-3-923704-74-3.

[26] C. Eberl, D.S. Gianola, K. J. Hemker. Mechanical Characterization of Coatings Using Microbeam Bending and Digital Image Correlation Techniques. Experimental Mechanics, January 2010, Volume 50, Issue 1, pp 85-97.

Tables and Figures

Table 1:   QUENCH Test Matrix 1997 – 2013

Test	Quench medium and injection rate	Temp. at onset of flooding[1]	Max. ZrO$_2$ before transient[2]	Max. ZrO$_2$ (X s) before flooding[2]	Posttest average ZrO$_2$ thickness[3]	H$_2$ production before / during cooldown, g	Remarks, objectives
QUENCH-00 Oct. 9 - 16, 97	Water 80 g/s	≈ 1800 K			completely oxidized		Commissioning tests.
QUENCH-01 Febr 26, 98	Water 52 g/s	≈ 1830 K	312 μm		500 μm at 913 mm	36 / 3	COBE Project; partial fragmentation of pre-oxidized cladding.
QUENCH-02 July 7, 98	Water 47 g/s	≈ 2400 K			completely oxidized	20 / 140	COBE Project; no additional pre-oxidation; quenching from high temperatures.
QUENCH-03 January 20, 99	Water 40 g/s	≈ 2350 K			completely oxidized	18 / 120	No additional pre-oxidation, quenching from high temperatures.
QUENCH-04 June 30, 99	Steam 50 g/s	≈ 2160 K	82 μm		280 μm	10 / 2	Cool-down behavior of slightly pre-oxidized cladding by cold steam injection.
QUENCH-05 March 29, 2000	Steam 48 g/s	≈ 2020 K	160 μm		420 μm	25 / 2	Cool-down behavior of pre-oxidized cladding by cold steam injection.
QUENCH-06 Dec 13 2000	Water 42 g/s	≈ 2060 K	207 μm[5]	300 μm, (60 s), SVECHA modeling	670 μm[4] (60% metal converted to outer ZrO$_2$)	32 / 4	OECD-ISP 45; prediction of H$_2$ source term by different code systems.
QUENCH-07 July 25, 2001	Steam 15 g/s	≈ 2100 K	230 μm		completely oxidized	66 / 120	COLOSS Project; impact of B$_4$C absorber rod failure on H$_2$, CO, CO$_2$, and CH$_4$ generation.
QUENCH-09 July 3, 2002	Steam 49 g/s	≈ 2100 K			completely oxidized	60 / 400	As QUENCH-07, steam-starved conditions prior to cooldown.
QUENCH-08 July 24, 2003	Steam 15 g/s	≈ 2090 K	274 μm		completely oxidized	46 / 38	As QUENCH-07, no absorber rod
QUENCH-10 July 21, 2004	Water 50 g/s	≈ 2200 K	514 μm	613 μm (at 850 mm)	completely oxidized	48 / 5	LACOMERA Project; Air ingress.

Test	Quench medium and injection rate	Temp. at onset of flooding[1]	Max. ZrO_2 before transient[2]	Max. ZrO_2 (X s) before flooding[2]	Posttest average ZrO_2 thickness[3]	H_2 production before / during cooldown, g	Remarks, objectives
QUENCH-11 Dec 08, 2005	Water 18 g/s	≈ 2040 K		170 μm	completely oxidized	9 / 132	LACOMERA Project; Boil-off.
QUENCH-12 Sept 27, 2006	Water 48 g/s	≈ 2100 K	160 μm, breakaway	300 μm, (110 s), breakaway	completely oxidized	34 / 24	ISTC Project No. 1648.2; VVER bundle with E110 claddings
QUENCH-13 Nov 7, 2007	Water 52 g/s	≈ 1820 K		400 μm, after AgInCd rod failure	750 μm	42 / 1	SARNET; impact of AgInCd absorber rod failure on aerosol generation.
QUENCH-14 July 2, 2008	Water 41 g/s	≈ 2100 K	170 μm[6]	470 μm[6], (30 s)	840 μm[4] (74% metal converted to outer ZrO_2)	34 / 6	ACM series: M5® cladding
QUENCH-15 May 27, 2009	Water 48 g/s	≈ 2100 K	145 μm[6]	380 μm[6], (30 s)	630 μm[4] (70% metal converted to outer ZrO_2)	41 / 7	ACM series: ZIRLO™ cladding
QUENCH-L0 *July 22, 2010*	*Water, 100 g/s*	*1330 K*	*1 μm*	*≈18 μm*	*≈20 μm (central rod)*	*0.748/0.3*	*VGB Project; Commissioning test*
QUENCH-16 July 27, 2011	Water 53 g/s	≈ 1870 K	135 μm	130 μm at 450-950 mm, breakaway	1075 μm at 550-650 mm	16 / 128	LACOMECO Project; Air ingress.
QUENCH-L1 *Feb. 02, 2012*	*Water, 100 g/s*	*1373 K*	*1 μm*	*≈19 μm*	*≈22 μm (central rod)*	*0.718/0.01*	*VGB Project; Reference test*
QUENCH-17 Jan 31, 2013	Water 10 g/s	≈ 1800 K	-	completely oxidized	completely oxidized	110 / 1	SARNET-2; Debris formation and coolability.
QUENCH-L2 *July 30, 2013*	*Water, 100 g/s*	*1373 K*	*1 μm*	*n.a.*	*≈20 μm (central rod)*	*0.4 total*	*VGB Project; M5® test*

[1] Maximum measured bundle temperature at 950 mm elevation.

[2] Measured at the withdrawn corner rod at 950 mm elevation.

[3] Measured posttest at the bundle elevation of maximum temperature, i.e. 950 mm.

[4] Some claddings were completely oxidized at 950 mm elevation.

[5] Oxide thickness during transient phase.

[6] Zircaloy-4 corner rods.

Table 2: Design characteristics of the QUENCH-L2 test bundle

Bundle type		PWR
Bundle size		21 heated rods
Effective number of rods	(considering surface of heated rods, shroud and corner rods)	30.6 rods (21 + 7.4 from shroud + 2.2 from corner rods)
Pitch		14.3 mm
Coolant channel area		29.65 cm^2
Hydraulic diameter		11.5 mm
Cladding material		M5®
Cladding outside diameter		10.75 mm
Cladding thickness		0.725 mm
Cladding length	(position in the bundle)	2278 mm (between -593 and 1685 mm)
Rod length	(elevations)	2480 mm (-690 to 1790 mm)
Internal rod pressure; gas)		5.5 MPa abs.; Kr
Material of middle heater		Tungsten (W)
	surface roughness	Ra=1.6 µm
Tungsten heater length		1024 mm (between 0 and 1024 mm)
Tungsten heater diameter		4.6 mm
Annular pellet	material	ZrO_2;Y_2O_3-stabilized
	dimensions	$\varnothing$ 9.15/4.75 mm; L=11 mm
	surface roughness	Ra=0.3 µm
Pellet stack		0 mm to ~1020 mm
Corner rod (4)	material	Zircaloy-4
	instrumented (A, C, D)	tube $\varnothing$ 6x0.9 (bottom: -1140 mm)
		rod $\varnothing$ 6 mm (top: +1300 mm)
	not instrumented (B)	rod $\varnothing$ 6 mm (-1350 to +1155 mm)
Grid spacer	material	Zircaloy-4, Inconel 718
	length	Zircaloy: 42 mm, Inconel: 38 mm
	sheet thickness	0.5 mm
	elevation of lower edge	Inc: -100; Zry: 150, 550, 1050, 1410 mm
Shroud	material	Zirconium 702 (flange: Zry-4)
	wall thickness	3.17 mm
	outside diameter	86.0 mm
	length (extension)	1600 mm (-300 mm to 1300 mm)
Shroud insulation	material	ZrO_2 fiber
	insulation thickness	~ 36 mm
	elevation	-300 to ~1000 mm
Molybdenum heaters and copper electrodes	length of upper part	766 mm (576 Mo, 190 mm Cu)
	length of lower part	690 mm (300 Mo, 390 mm Cu)
	outer diameter:	
	prior to coating	8.6 mm
	after coating with ZrO_2	9.0 mm
	coat. surface roughness	Ra=6-12 µm
	borehole of Cu-electrodes	diameter 2 mm, length 96 mm
Cooling jacket	Material: inner/outer tube	Inconel 600 (2.4816) / SS (1.4571)
	inner tube	$\varnothing$ 158.3 / 168.3 mm
	outer tube	$\varnothing$ 181.7 / 193.7 mm

Table 3:   Properties of M5® cladding tubes

Chemical composition of M5® in weight-% (delivery specification)

Element	Symbol	*Measured value*
Niobium	Nb	0.99
Oxygen	O	0.14
Sulfur	S	0.0017-0.0025

Mechanical properties of M5® at RT in tension

Element	*Measured value*
0.2 Yield strength Rp 0.2	384 MPa
Ultimate tensile stress Rm	516 MPa
Elongation at fracture A_{50} mm	38%

Microstructure of M5®

Grain size: 5.6 µm	Nr. 12.0 according to ASTM E 112 (acceptable average grain size shall be < Nr. 11, i.e. < 7.9 µm)
Surface Conditions: - Roughness (inside): Ra = 0.15 µm (accepted 0.80 µm) - Roughness (outside): Ra = 0.32 µm (accepted 0.80 µm)	

Table 4: **Main characteristics of the ZrO$_2$ pellet material, yttria-stabilized (type FZY) ***

Property		Data
Density		5.5-5.8 g/cm^3
Open porosity		0
Mean grain size		50 μm
Hardness (Knoop, 100 g)		17000 N/mm^2
Yield strength under compression		2000 N/mm^2
Bending strength		350 N/mm^2
Elastic modulus		165 GPa
Specific heat at 20 °C		400 J/kg K
Thermal conductivity at 100 °C		2.5 W/m K
Linear expansion, 20-1000 °C		10.5 x 10^{-6}/K
Specific electric resistance	at 20 °C	10^{10} Ω cm
	at 500 °C	5000 Ω cm
	at 1000 °C	50 Ω cm

*According to FRIATEC, Mannheim

Table 5: QUENCH-L2; Electrical resistances of rods [mΩ] at 20°C

a) Internal circuit with 9+1 rods

rod	1	2	3	4	5	6	7	8	9	15	*Average*	*10 rods parallel*
pre-test	4.7	4.7	4.7	4.6	4.7	4.7	4.7	4.7	4.7	4.7	*4.7*	*0.47*
post-test	4.7	4.8	4.6	4.6	4.7	4.7	6.0	4.7	4.8	4.7	*4.8*	*0.48*

Note: Measured values include the resistance of slide contacts R_s=0.75 mΩ

Table B2. External circuit with 11 rods

rod	10	11	12	13	14	16	17	18	19	20	21	*Average*	*11 rods parallel*
pre-test	4.7	4.7	4.6	4.6	4.7	4.7	4.7	4.7	4.7	4.7	4.7	*4.7*	*0.42*
post-test	4.8	4.8	4.7	4.7	4.7	4.7	4.7	4.7	4.8	4.7	4.8	*4.7*	*0.43*

Note: Measured values include the resistance of slide contacts R_s=0.75 mΩ

Each circuit connected to the DC generator with 4 parallel bonded cables. The resistance of each cable is R_c=1.2 mΩ. Therefore, the external (outside) resistance

corresponding to each heated rod (indicated by SCDAP/RELAP as **fxwid**) is $R_{ie}=R_s+10*R_c/4=3.75$ mΩ for the inner rod group and $R_{oe}=R_s+11*R_c/4=4.05$ mΩ for the outer rod group.

Table 6 :   Properties of zirconia fiber insulating boards*

a) Chemical composition

Oxide	ZrO_2	Y_2O_3	HfO_2	TiO_2	SiO_2	CaO	MgO	Fe_2O_3	Al_2O_3	Na_2O
typical wt%	88	10	2	0.14	0.12	0.09	0.03	0.04	0.01	0.01

Table B2.   Physical properties

bulk density	poro-sity	shrinkage		thermal expansion coefficient @298-1453 K	melting point	max. service tempe-rature	flexural strength	Compressive strength @10% compression
		1 hour @1925 K	24 hours @1925 K					
g/cm³	%	%		1/K	K	K	MPa	MPa
0.48	92	1.2	2.8	$10.7*10^{-6}$	2866	2500	0.59	0.29

*According to specifications of manufacturer ZIRCAR PRODUCTS on the ZYFB3 material

Thermal conductivity

temperature, K	673	1073	1373	1673	1923
conductivity, W/(m*K)	0.08	0.11	0.14	0.19	0.24

Specific heat capacity

temperature, K	366	2644
specific heat capacity, J/(kg*K)	544	754

Table 7:   List of instrumentation for the QUENCH-L2 test

Chan	Designation	Instrument, location	Unit
0	P rod 13	Internal pressure of rod #13	bar
1	P rod 14	Internal pressure of rod #14	bar
2	P rod 15	Internal pressure of rod #15	bar
3	P rod 12	Internal pressure of rod #12	bar
4	P rod 03	Internal pressure of rod #03	bar
5	P rod 04	Internal pressure of rod #04	bar
6	P rod 05	Internal pressure of rod #05	bar
7	P rod 16	Internal pressure of rod #16	bar
8	P rod 11	Internal pressure of rod #11	bar
9	P rod 02	Internal pressure of rod #02	bar
10	P rod 01	Internal pressure of rod #01	bar
11	P rod 06	Internal pressure of rod #06	bar
12	P rod 17	Internal pressure of rod #17	bar
13	P rod 10	Internal pressure of rod #10	bar
14	P rod 09	Internal pressure of rod #09	bar
15	P rod 08	Internal pressure of rod #08	bar
16	P rod 07	Internal pressure of rod #07	bar
17	P rod 18	Internal pressure of rod #18	bar
18	P rod 21	Internal pressure of rod #21	bar
19	P rod 19	Internal pressure of rod #19	bar
20	P rod 20	Internal pressure of rod #20	bar
21..23		20 mA, Reserve	
24	P 511 top	Pressure at top leg of differential level sensor L 501	bar
25..31		20 mA, Reserve	
32..34		TC (W/Re), Reserve	
35	TSH 15/0	TC (NiCr/Ni), shroud outer surface, 1150 mm, 21° feed cable outside of shroud isolaton	K
36	TSH 14/270	TC (NiCr/Ni), shroud outer surface, 1050 mm, 289°, feed cable outside of shroud isolaton	K
37		TC (W/Re), Reserve	K
38	TFS 15/13	TC (NiCr/Ni), surface of fuel rod simulator 15, group 5, 950 mm	K
39	TFS 19/12	TC (NiCr/Ni), surface of fuel rod simulator 19, group 5, 850 mm	K
40..41		TC (W/Re), Reserve	

Chan	Designation	Instrument, location	Unit
42	TFS 7/12	TC (NiCr/Ni), surface of fuel rod simulator 7, group 3, 850 mm	K
43	TFS 15/12	TC (NiCr/Ni), surface of fuel rod simulator 15, group 5, 850 mm	K
44	TFS 2/12	TC (NiCr/Ni), surface of fuel rod simulator 2, group 2, 850 mm	K
45	TFS 4/12	TC (NiCr/Ni), surface of fuel rod simulator 4, group 2, 850 mm	K
46	TFS 19/13	TC (NiCr/Ni), surface of fuel rod simulator 19, group 5, 950 mm	K
47..57		TC (W/Re), Reserve	K
58	TFS 7/10	TC (NiCr/Ni), surface of fuel rod simulator 7, group 3, 650 mm	K
59..60		TC (W/Re), Reserve	K
61	TFS 11/12	TC (NiCr/Ni), surface of fuel rod simulator 11, group 4, 850 mm	K
62	P 206	Reserve	
63	F 206	Reserve	
64	T 402 b	TC (NiCr/Ni), Ar super heater	K
65..67		TC (W/Re), Reserve	K
68	T 512	TC (NiCr/Ni), gas temperature bundle outlet	K
69..70		TC (W/Re), Reserve	K
71	*Ref. T01*	*Temperature of measuring crate 1 (reference temperature)*	K
72	TFS 11/13	TC (NiCr/Ni) surface of fuel rod simulator 11, group 4, 950 mm	K
73	TFS 7/13	TC (NiCr/Ni), surface of fuel rod simulator 7, group 3, 950 mm	K
74	TFS 2/13	TC (NiCr/Ni), surface of fuel rod simulator 2, group 2, 950 mm	K
75	TFS 4/13	TC (NiCr/Ni), surface of fuel rod simulator 4, group 2, 950 mm	K
76	TFS 15/11	TC (NiCr/Ni), surface of fuel rod simulator 15, group 5, 750 mm	K
77	TFS 19/11	TC (NiCr/Ni), surface of fuel rod simulator 19, group 5, 750 mm	K
78	TFS 11/11	TC (NiCr/Ni) surface of fuel rod simulator 11, group 4, 750 mm	K
79	TFS 7/11	TC (NiCr/Ni), surface of fuel rod simulator 7, group 3, 750 mm	K
80	TFS 2/11	TC (NiCr/Ni) surface of fuel rod simulator 2 group 2, 750 mm	K
81	TSH 12/90	TC (NiCr/Ni), shroud outer surface, 850 mm, 109°	K
82	TFS 2/10	TC (NiCr/Ni); surface of fuel rod simulator 2, group 2, 650 mm	K
83	TSH 10/270	TC (NiCr/Ni), shroud outer surface, 650 mm, 289°	K
84	TSH 9/180	TC (NiCr/Ni), shroud outer surface, 550 mm, 191°	K
85	TSH 8/90	TC (NiCr/Ni), shroud outer surface, 450 mm, 109°	K
86	TSH 7/0	TC (NiCr/Ni), shroud outer surface, 350 mm, 11°	K
87	TSH 6/270	TC (NiCr/Ni) shroud outer surface, 250 mm, 281°	K
88	TSH 5/180	TC (NiCr/Ni), shroud outer surface, 150 mm, 191°	K

Chan	Designation	Instrument, location	Unit
89	TSH 4/90	TC (NiCr/Ni), shroud outer surface, 50 mm, 109°	K
90	TSH 11/0	TC (NiCr/Ni), shroud outer surface, 750 mm, 11°	K
91	TCI 9/270	TC (NiCr/Ni), cooling jacket inner tube wall, 550 mm, 270°	K
92	TCI 10/270	TC (NiCr/Ni), cooling jacket inner tube wall, 650 mm, 270°	K
93	TCI 11/270	TC (NiCr/Ni), cooling jacket inner tube wall, 750 mm, 270°	K
94	TCI 13/270	TC (NiCr/Ni), cooling jacket inner tube wall, 950 mm, 270°	K
95	TFS 4/11	TC (NiCr/Ni), surface of fuel rod simulator 4, group 2, 750 mm	K
96	TFS 15/10	TC (NiCr/Ni), surface of fuel rod simulator 15, group 5, 650 mm	K
97	TFS 19/10	TC (NiCr/Ni), surface of fuel rod simulator 19, group 5, 650 mm	K
98	TFS 11/10	TC (NiCr/Ni), surface of fuel rod simulator 11, group 4, 650 mm	K
99	TSH 13/180	TC (NiCr/Ni), shroud outer surface, 950 mm, 191°, feed cable outside of shroud isolaton	K
100	TSH 3/0	TC (NiCr/Ni), shroud outer surface, -50 mm, 11°	K
101	TFS 4/10	TC (NiCr/Ni), surface of fuel rod simulator 4, group 2, 650 mm	K
102	TFS 15/14	TC (NiCr/Ni), surface of fuel rod simulator 15, group 5, 1050 mm	K
103	TFS 19/14	TC (NiCr/Ni), surface of fuel rod simulator 19, group 5, 1050 mm	K
104	TFS 11/14	TC (NiCr/Ni), surface of fuel rod simulator 11, group 4, 1050 mm	K
105	TFS 7/14	TC (NiCr/Ni), surface of fuel rod simulator 7, group 3, 1050 mm	K
106	TFS 2/14	TC (NiCr/Ni), surface of fuel rod simulator 2, group 2, 1050 mm	K
107	TFS 4/14	TC (NiCr/Ni), surface of fuel rod simulator 4, group 2, 1050 mm	K
108	TFS 15/9	TC (NiCr/Ni), surface of fuel rod simulator 15, group 5, 550 mm	K
109	TFS 11/9	TC (NiCr/Ni), surface of fuel rod simulator 11, group 4, 550 mm	K
110	TFS 7/9	TC (NiCr/Ni), surface of fuel rod simulator 7, group 3, 550 mm	K
111	TFS 4/9	TC (NiCr/Ni), surface of fuel rod simulator 4, group 2, 550 mm	K
112	TFS 15/15	TC (NiCr/Ni), surface of fuel rod simulator 15, group 5, 1150 mm	K
113	TFS 19/15	TC (NiCr/Ni), surface of fuel rod simulator 19, group 5, 1150 mm	K
114	TFS 11/15	TC (NiCr/Ni), surface of fuel rod simulator 11, group 4, 1150 mm	K
115	TFS 7/15	TC (NiCr/Ni), surface of fuel rod simulator 7, group 3, 1150 mm	K
116	TFS 2/15	TC (NiCr/Ni), surface of fuel rod simulator 2, group 2, 1150 mm	K
117	TFS 4/15	TC (NiCr/Ni), surface of fuel rod simulator 4, group 2, 1150 mm	K
118	TFS 11/8	TC (NiCr/Ni), surface of fuel rod simulator 11, group 4, 450 mm	K
119	TFS 7/8	TC (NiCr/Ni), surface of fuel rod simulator 7, group 3, 450 mm	K
120	TFS 4/8	TC (NiCr/Ni), surface of fuel rod simulator 4 group 2, 450 mm	K
121	TFS 11/16	TC (NiCr/Ni), surface of fuel rod simulator 11, group 4, 1250 mm	K

Chan	Designation	Instrument, location	Unit
122	TFS 7/16	TC (NiCr/Ni), surface of fuel rod simulator 7, group 3, 1250 mm	K
123	T 601	Temperature off-gas, 2660 mm from test section outlet (flange)	K
124	TFS 11/7	TC (NiCr/Ni), surface of fuel rod simulator 11, group 4, 350 mm	K
125	TFS 7/12i	TC (NiCr/Ni), surface of fuel rod simulator 7, group 3, 850 mm, near to rod #1	K
126	TFS 7/7	TC (NiCr/Ni), surface of fuel rod simulator 7, group 3, 350 mm	K
127	TFS 4/7	TC (NiCr/Ni), surface of fuel rod simulator 4, group 2, 350 mm	K
128	T 104	Temperature quench water	K
129	T 201	Temperature steam generator heating pipe	K
130	TIT C/12	TC (NiCr/Ni), center line of corner rod C, 850 mm	K
131	T 205	Temperature upstream steam flow instrument location 10 g/s	K
132	T 301A	Temperature downstream superheater	K
133	T 302	Temperature superheater heating pipe	K
134	T 303	Temperature upstream total flow instrument location	K
135	T 401	Temperature upstream Ar flow instrument (orifice) location	K
136	T 403	Temperature of Ar at inlet cooling jacket	K
137	T 404	Temperature of Ar at outlet cooling jacket	K
138	T 501	Temperature in containment (near from bundle head)	K
139	TFS 7/6	TC (NiCr/Ni), surface of fuel rod simulator 7, group 3, 250 mm	K
140	TFS 4/6	TC (NiCr/Ni), surface of fuel rod simulator 4, group 2, 250 mm	K
141	TFS 7/17	TC (NiCr/Ni), surface of fuel rod simulator 7, group 3, 1350 mm	K
142	TFS 7/5	TC (NiCr/Ni), surface of fuel rod simulator 7, group 3, 150 mm	K
143	TFS 7/4	TC (NiCr/Ni), surface of fuel rod simulator 7, group 3, 50 mm	K
144	TFS 7/3	TC (NiCr/Ni), surface of fuel rod simulator 7, group 3, -50 mm	K
145	TFS 7/2	TC (NiCr/Ni), surface of fuel rod simulator 7, group 3, -150 mm	K
146	TFS 7/1	TC (NiCr/Ni), surface of fuel rod simulator 7, group 3, -250 mm	K
147	TFS 7/13i	TC (NiCr/Ni), surface of fuel rod simulator 7, group 3, 950 mm, near to rod #1	K
148	T 511	Gas temperature at bundle inlet	K
149	TIT D/11	TC (NiCr/Ni), center line of corner rod D, 750 mm	K
150	TIT A/13	TC (NiCr/Ni), center line of corner rod A, 950 mm	K
151	*Ref. T02*	*Temperature of measuring crate 2 (reference temperature)*	K
152	P 201	Pressure steam generator	bar
153	P 204	Pressure at steam flow instrument location 50 g/s	bar
154	P 205	Pressure at steam flow instrument location 10 g/s	bar

Chan	Designation	Instrument, location	Unit
155	P 303	Pressure upstream total flow instrument (orifice) location	bar
156	P 401	Pressure upstream gas flow instrument location	bar
157	P 511	Pressure at bundle inlet, L501 low leg	bar
158	P 512	Pressure at bundle outlet	bar
159	P 601	Pressure upstream off-gas flow instrument (orifice) F 601	bar
160	P 901	Pressure at bundle inlet, L501 upper leg	bar
161	L 201	Liquid level steam generator	mm
162	L 501	Liquid level quench water	mm
163	L 701	Liquid level condensation vessel	mm
164	Fm 401	Argon (carrier gas) mass flow rate (Bronkhorst device)	g/s
165	P 411	Reserve (Pressure Kr supply for heated rods)	bar
166	P 403	Pressure Ar cooling of cooling jacket	bar
167	P 406	Pressure insulation shroud/cooling jacket	bar
168	Fm 104	Flow rate quench water	g/s
169	Fm 204	Flow rate steam 50 g/s	g/s
170	Fm 205	Flow rate steam 10 g/s	g/s
171	F 303	Flow rate at bundle inlet (steam + argon), orifice	mbar
172	F 401	Argon (carrier gas) volumetric flow rate	Nm³/h
173	Fm 403	Mass flow rate of cooling gas (Ar)	g/s
174	F 601	Flow rate off-gas (orifice), 2000 mm from test section outlet (flange)	mbar
175	Fm 406	Flow rate argon into room between shroud and cooling jacket	g/s
176	E 201	Electric current steam generator	A
177	E 301	Electric current superheater	A
178	E 501	Electric current of left group of fuel rod simulators	A
179	E 502	Electric current of right group of fuel rod simulators	A
180	E 503	Electric voltage of left group of fuel rod simulators	V
181	E 504	Electric voltage of right group of fuel rod simulators	V
182	Hub_V302	Gas supply valve lift	%
183	*Ref. T03*	*Temperature of buffer amplifier (reference temperature)*	K
184…199		Binary inputs	
200..215		Analog outputs	
250	E 505	Electric power inner ring of fuel rod simulators	W

Chan	Designation	Instrument, location	Unit
251	E 506	Electric power outer ring of fuel rod simulators	W
252	EP	Gross electrical power	kW

Indications:

TFS - TC at the rod surface;

TIT - TC at inside of corner rods;

TSH - TC at outer surface of shroud;

[   ] -   gauge outside of containment.

Groups of the rods for modeling:

central groups:
group 1: rod 1;
group 2: rods 2, 4, 6, 8;
group 3: rods 3, 5, 7, 9;

peripherical groups:
group 4: rods 11, 14, 17, 20;
group 5: rods 10, 12, 13, 15, 16, 18, 19, 21.

Table 8: **QUENCH-L2; Rod thermocouple positions**

Elevation, mm	-250	-150	-50	50	150	250	350	450	550	650	750	850	950	1050	1150	1250	1350
Rod/Elevation	1	2	3	4	5	6	7	8	9	10	11	12	13	14	15	16	17
1																	
2										X	X	X	X	X	X		
3																	
4						X	X	X	X	X	X	X	X	X	X		
5																	
6																	
7	X	X	X	X	X	X	X	X	X	X	X	X, Xi	X, Xi	X	X	X	X
8																	
9																	
10																	
11							X	X	X	X	X	X	X	X	X	X	
12																	
13																	
14																	
15									X	X	X	X	X	X	X		
16																	
17																	
18																	
19										X	X	X	X	X	X		
20																	
21																	
Number per elevation	1	1	1	1	1	2	3	3	4	6	6	6+1	6+1	6	6	2	1

TFS (rod surface, shroud direction), indicated as **X** in table above	**56**
TFS (rod surface, central rod direction), indicated as **Xi** in table above	**2**
TIT (inside corner rods)	*3*
TSH (outer shroud surface)	*13*

TCs to bundle bottom   TCs to bundle top

(7 W/Re+20 NiCr/Ni)
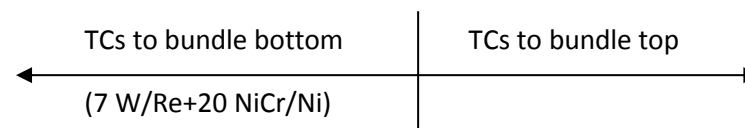
Table 9:   **QUENCH-L2; Sequence of events**

Time [s]	Event
-2283.6 (10:25:04; 30.07.2013)	Start data recording, Tmax = TFS 7/13i = 847 K, el. power at 3.56 kW. L701 = 485 mm. L 501 = -400 mm. System pressure 3 bar. Hot Ar 6 g/s (heated in superheater), superheated steam 2 g/s.
-2260… -1060	Pressurization of rods from 20 to 55 bar.
0	Start of transient with max electrical power increase rate.
3.8; 46	Electrical power 42; 60 kW.
40…52	Sequential onset of ballooning from inner rod #4 to peripheral rod #20.
48…68	Sequential onset of burst for rods from inner rod #8 to peripheral rod #12. See burst table (Table 10).
78	Switch of the electrical power from max 59.4 kW to decay heat of 3.5 kW. Initiation of rapid steam supply line (20 g/s) additionally to carrier argon (6 g/s). Switch-off of slow steam supply (2 g/s). Tmax = TFS 7/12i = 1336 K.
85.2	Cladding surface temperature maximum reached. Maximal hydrogen production rate. Tmax = TFS 7/12i = 1400 K.
85.2…210.4	*Cool-down* of bundle in steam. Decrease of TFS 7/12i reading from 1400 K to 1026 K.
160…176	Temporary decrease of Ar flow rate due to switch between two Ar suppliers
210.4…220	Increase of maximal bundle temperatures to ≈1044 K due to switch-off of the steam cooling (closing of gas inlet valve at 210.4 s).
216	Initiation of *quench* water supply. Switch of argon to bundle top supply.
237	Maximal quench rate (about 100 g/s) reached.
238…302	Wetting of cladding surface thermocouples (TFS) at elevations between -250 and 1350 mm at temperatures between 520 (TFS 7/1; -250 mm) and 856 K (TFS 7/14; 1050 mm). (Table 12).
260…295	Maximal water evaporation rate (about 25 g/s).
365	Bundle completely filled with water (L 501 = 1307 mm).
474	Electrical power switched off. Tmax = TFS 15/15 = 321 K.
662	End of data recording.

Table 10:   QUENCH-L2; Burst parameters

rod	burst time, s	interpolated burst T, K	burst azimuth. position, °	burst middle elev., mm	max burst width, mm	burst length, mm	burst area, mm²
1	50.4	1135	354	875	3.4	14	29
2	52.6	1167	186	958	2.9	11	20
3	52.7	1168	135	961	2.5	10	15
4	52.4	1167	163	963	2.9	11.5	21
5	53.1	1163	308	890	3.0	11.5	21
6	49.8	1121	312	869	2.6	11	17
7	52.9	1136	248	967	3.1	12	23
8	48.4	1113	100	875	3.3	12	24
9	52.7	1162	66	887	1.7	11	12
10	66.2	1125	97	917	6.6	22	85
11	65	1145	147	963	2.8	12	21
12	67.8	1195 (max)	141	948	2.5	11	19
13	67.4	1178	151	946	2.4	10	15
14	66.2	1167	129	959	3.1	12	23
15	57.2	1124	174	951	2.4	13	25
16	64	1143	188	951	3.4	13	27
17	62	1102	289	803	3.9	20	66
18	65	1139	274	957	3.3	12	24
19	67.4	1093	342	885	1.8	11	12
20	62.8	1110	230	814	5.5	24	94
21	65.8	1050 (min)	68	784	1.5	15	16
average		1138 ± 34		911 ± 58	3.1 ± 1.2	13.3 ± 3.9	29 ± 23

Table 11: QUENCH-L4; Content of hydrogen absorbed by secondary hydrogenation (post-tensile n^0 tomography): axial maximum averaged for cross section and axial absolute local maximum

rod #	C_H above burst opening (H-band), wppm		elevation, mm		C_H below burst opening (H-spot), wppm		elevation, mm	
	averaged	absolute	aver.	abs.	averaged	absolute	aver.	abs.
1	490±10	920±20	904	900	205±10	880±30	848	850
2	260±10	545±30	988	988	210±10	670±30	909	934
3	260±10	550±30	990	990	180±10	590±30	946	943
6	225±10	560±30	886	885	115±10	620±30	829	830
9	311±10	785±30	914	912	150±10	520±30	862	866
13*	25±10	150±30	960	960	20±10	160±30	937	937
14*	35±10	155±30	970	970	35±10	160±30	948	948
16*	55±10	175±30	965	965	45±10	165±30	945	945
18	104±10	230±30	992	992				
20*	25±10	195±30	830	830	30±10	175±30	815	810
21	160±10	410±30	810	812				

*hydrogen content around burst opening for outer rods

Table 12: QUENCH-L2; Wetting of TFS thermocouples

Bundle elevation, mm	Wetting time, s	Collapsed water front, mm
-250	238	-364
-150	240	-280
-50	246	-138
50	247	-100
150	250	-5
250	257	116
350	258..258.5	143..154
450	255.5..262	56.6..211
550	260..262	182..211
650	263..269	235..361
750	264..272	275..422
850	264..285	275..576
950	274..292	456..700
1050	265..293	300..727
1150	273..295	460..767
1250	275..302	462..917
1350	261*	194

*condensation of stagnant steam inside the bundle head due to injection of cold argon

Table 13:   QUENCH-L2; Strain parameters at the middle of burst elevation

rod group	rod #	elevation of burst *middle, mm*	max strain %	max D mm	*at azimuth* °	min D mm	*at azimuth* °
central group	1	875	22	13.99	338	12.42	77
	2	958	20	13.88	169	12.27	259
	3	961	19.5	13.84	123	12.06	207
	4	963	21	13.96	151	12.31	252
	5	890	23.7	14.42	291	12.43	212
	6	869	18.6	13.71	326	12.09	228
	7	963	22.4	14.06	238	12.42	161
	8	875	19	14.06	81	11.92	124
	9	887	15.4	13.40	67	11.89	325
peripherical group	10	917	29.3	15.65	63	12.64	170
	11	963	20.4	13.90	161	12.33	243
	12	948	18.5	13.67	131	12.03	49
	13	946	19.4	13.81	167	12.14	248
	14	959	21.3	14.19	147	12.31	231
	15	951	22.3	13.99	189	12.18	268
	16	951	20.5	17.06	209	12.12	289
	17	803	17.9	13.68	335	11.78	288
	18	957	24	14.51	291	12.40	191
	19	885	18.4	14.15	28	11.76	120
	20	814	22.1	17.09	278	12.20	352
	21	784	11.6	12.73	26	11.15	69
average		910 ± 58	20.3 ± 3.5	14.27 ± 1.07		12.14 ± 0.32	

Table 14:   QUENCH-L2; Results of tensile tests

rod l₀=800 mm	ultimate tensile strength [MPa]	fracture stress [MPa]	elongation at fracture (graded) [%]	rupture based on
01	*513*	*374*	13.3	*fracture after necking*
02	*494*	*436*	3.1	*fracture after necking*
03	*512*	*356*	11.5	*fracture after necking*
04	*514*	*367*	10.7	*fracture after necking*
05	*511*	*360*	11.3	*fracture after necking*
06	*513*	*422*	11.2	*fracture after necking*
07	*517*	*372*	11.5	*fracture after necking*
08	**450**	**448**	**2.7**	**stress concentration**
09	*509*	*365*	14.0	*fracture after necking*
10	**502**	**296**	**11.3**	**stress concentration**
11	*486*	*445*	4.3	*fracture after necking*
12	*505*	*370*	16.5	*fracture after necking*
13	*504*	*361*	16.3	*fracture after necking*
14	***506***	***389***	**14.0**	**stress concentration**
15	**499**	**495**	**6.9**	**stress concentration**
16	**512**	**493**	**9.0**	**stress concentration**
17	**502**	**483**	**6.7**	**stress concentration**
18	**498**	**488**	**10.1**	**stress concentration**
19	**500**	**483**	**6.9**	**stress concentration**
20	**494**	**484**	**4.7**	**stress concentration**
21	**497**	**476**	**5.5**	**stress concentration**
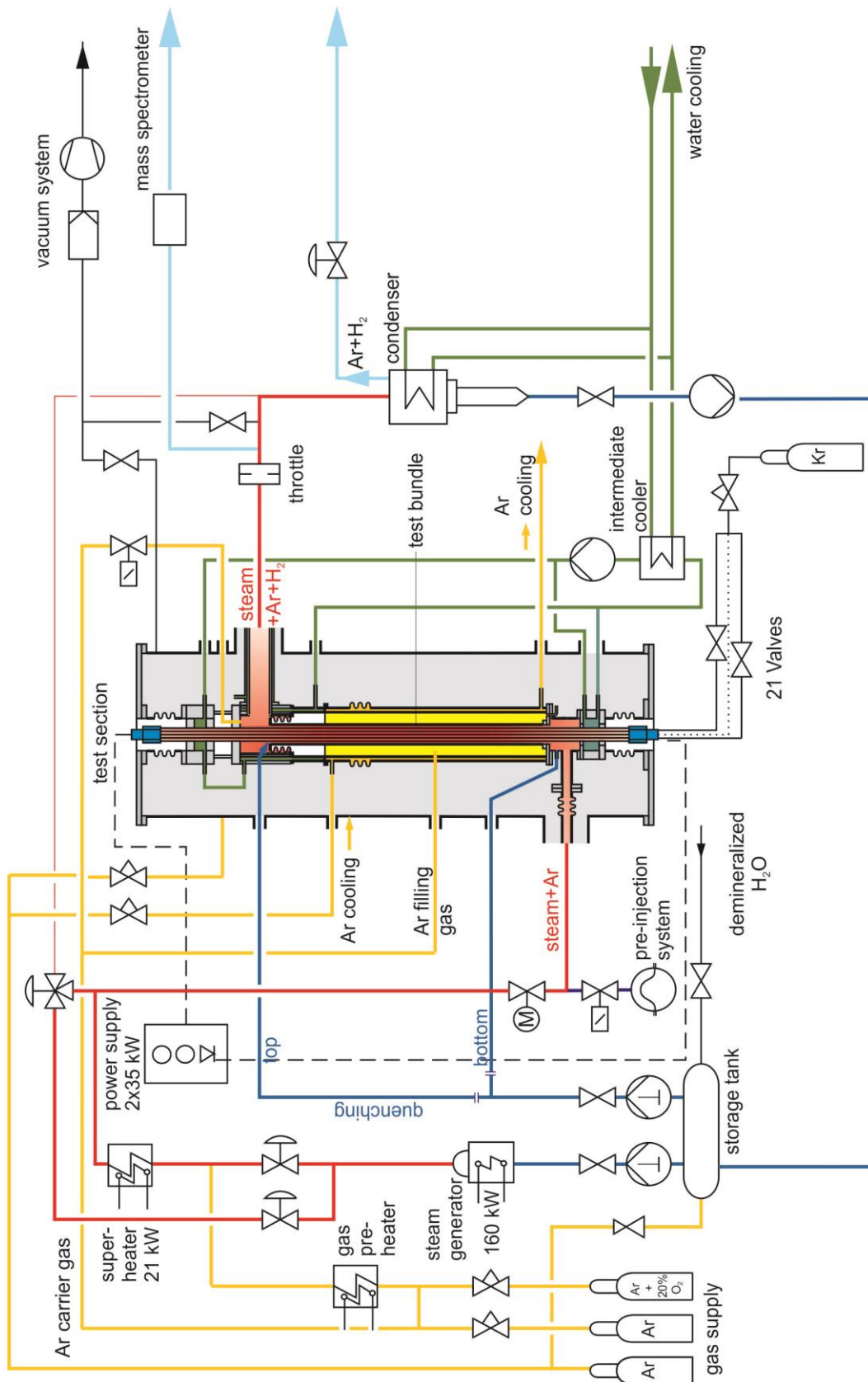
Figure 1   Flow diagram of the QUENCH test facility.
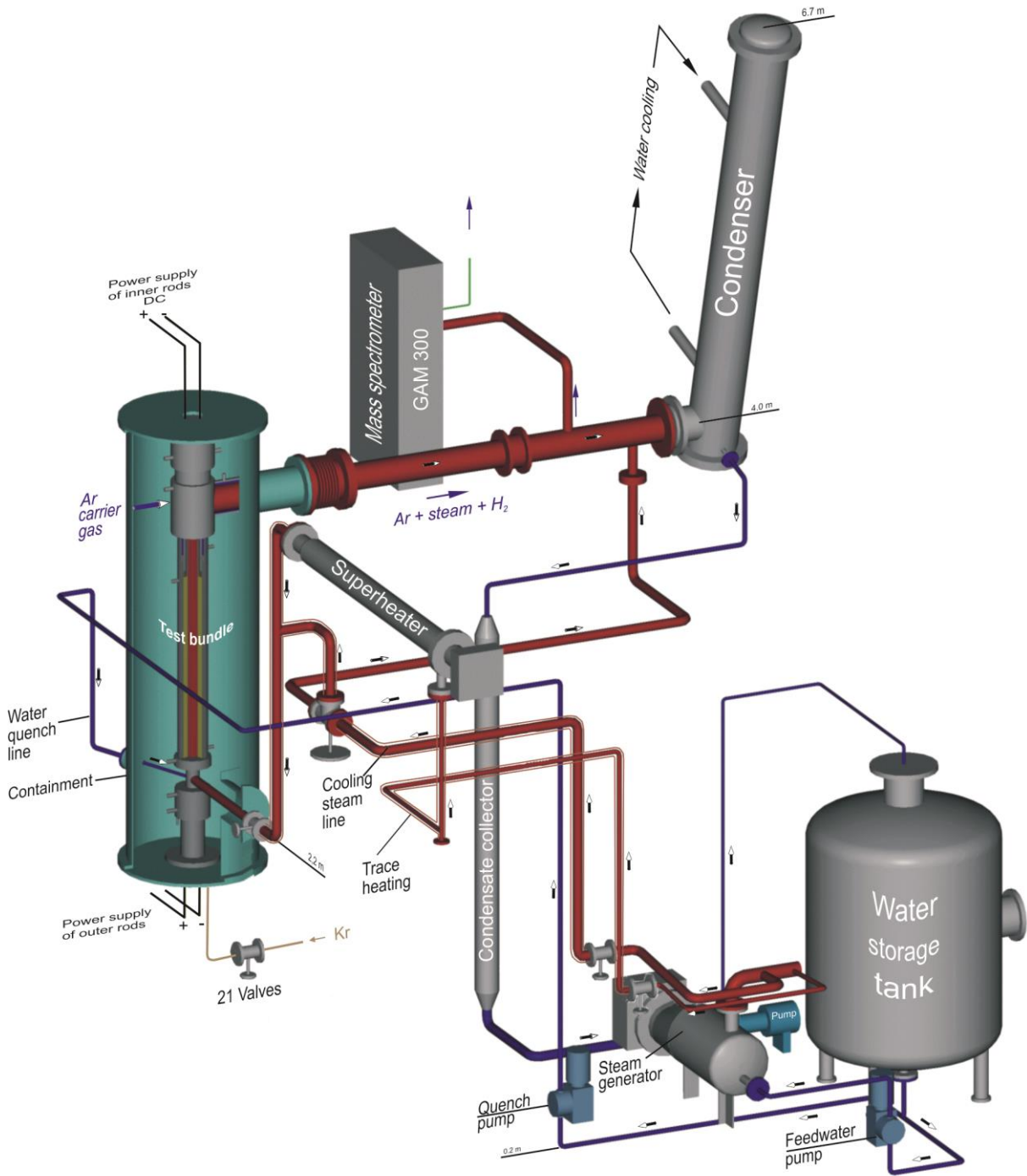
Figure 2   QUENCHFacility - Main components.
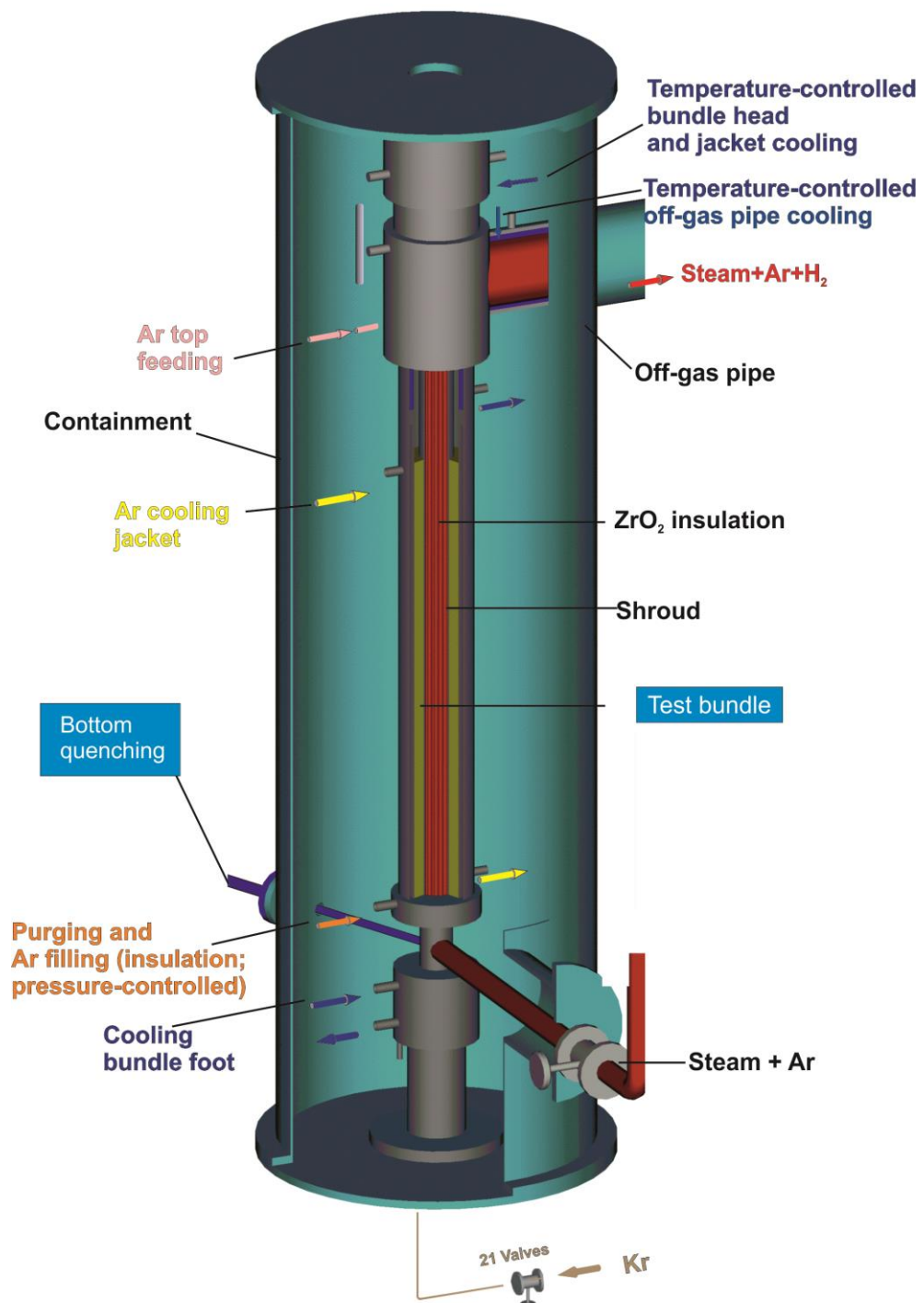
Figure 3   QUENCH Facility; Containment and test section
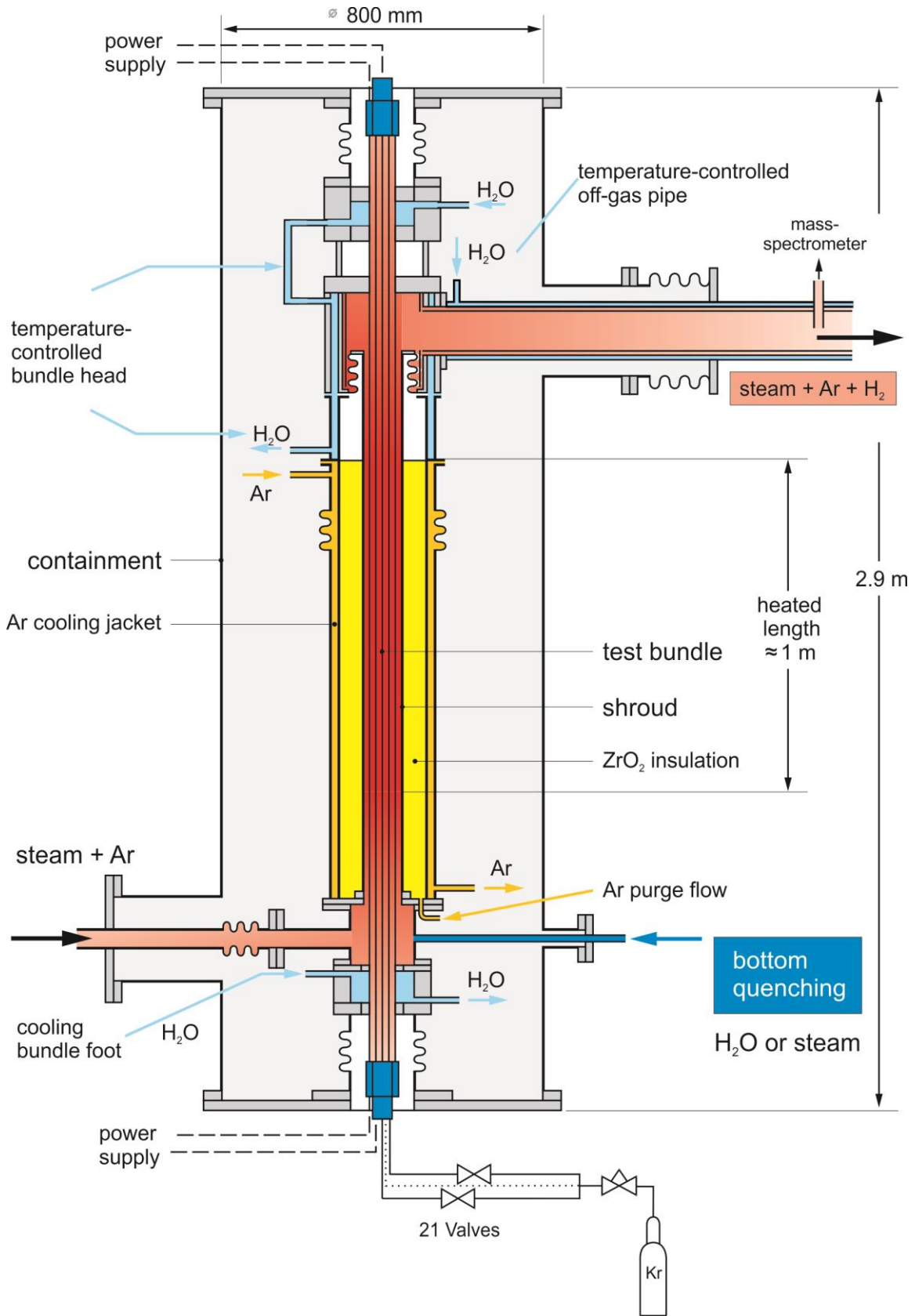
Figure 4   QUENCH-L02; Test section with flow lines.
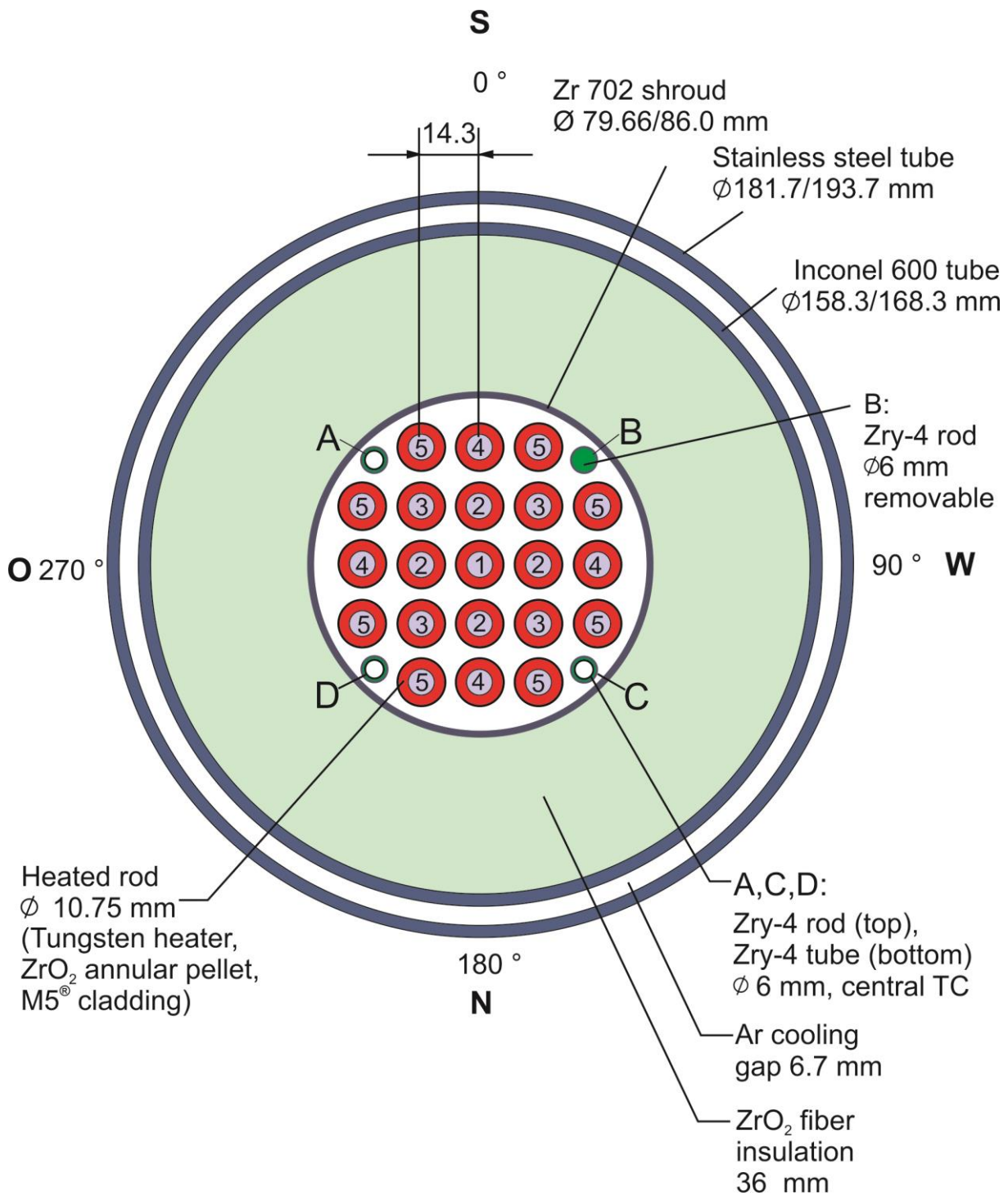
Figure 5   QUENCH-L2; Fuel rod simulator bundle (cross section, top view) including rod type indications corresponding to table "List of Instrumentation".
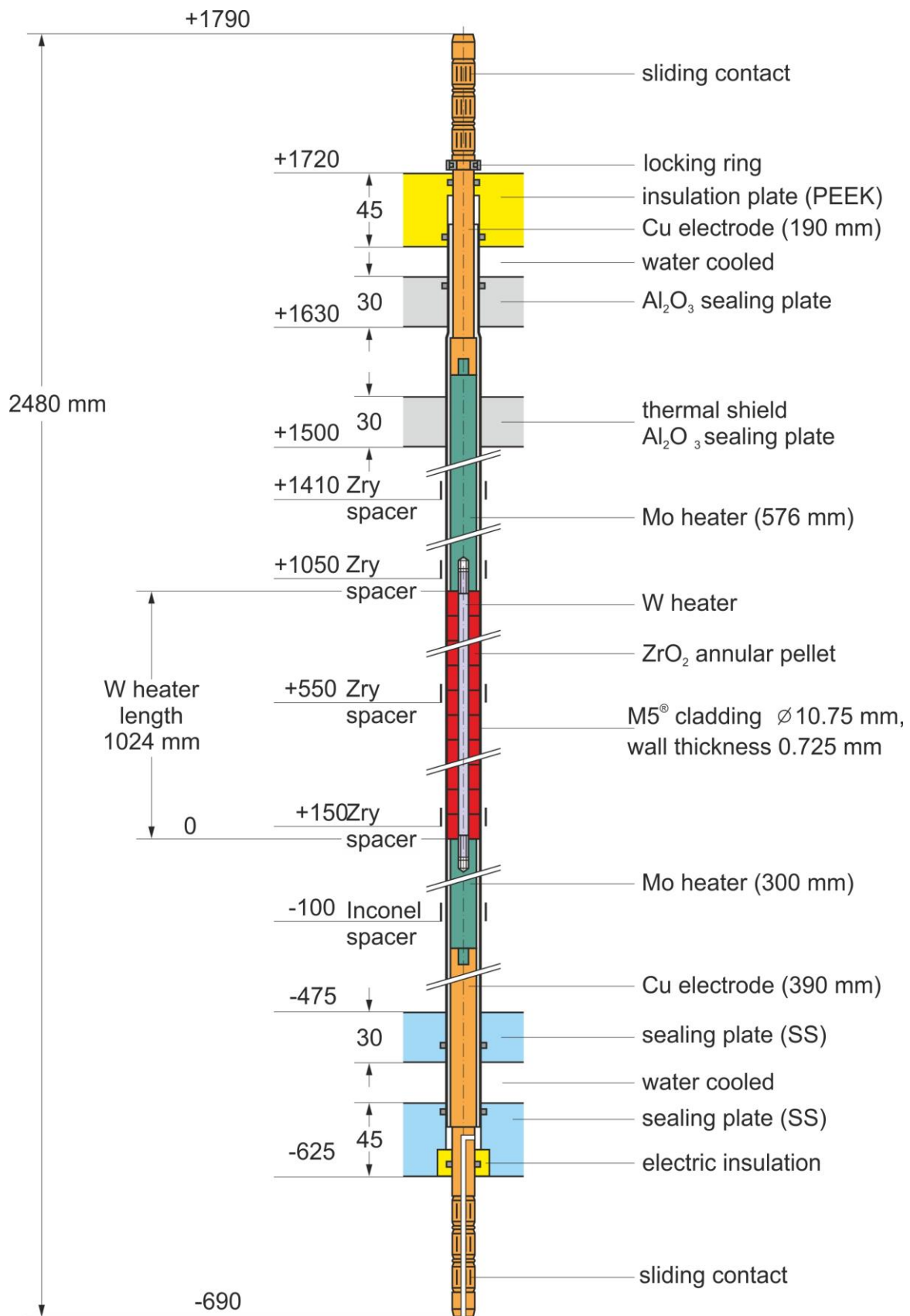
Figure 6   Heated fuel rod simulator.
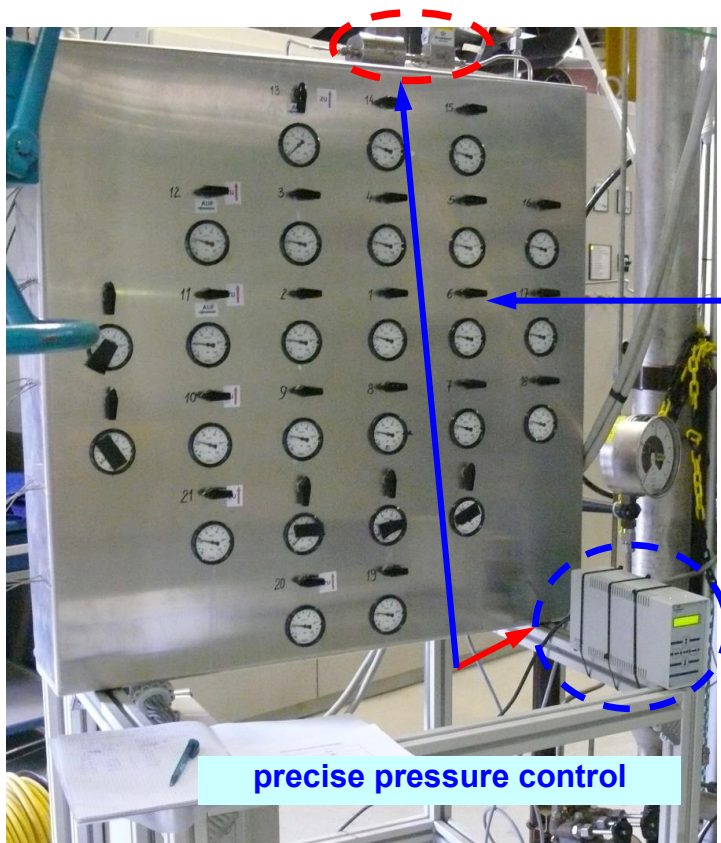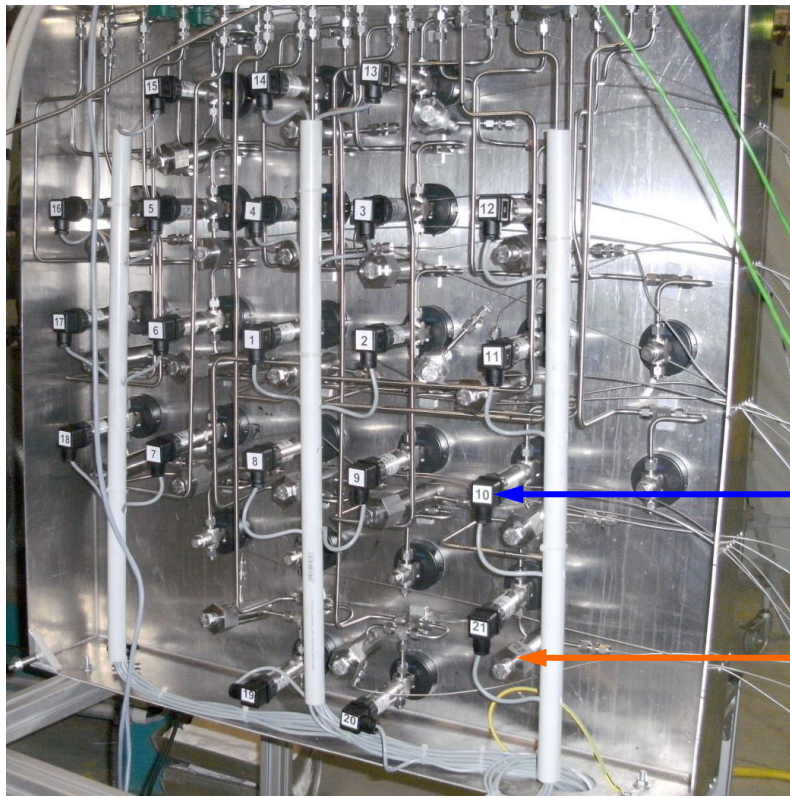
44

Figure 7   QUENCH-L2; Rod pressure control and measurement panel.
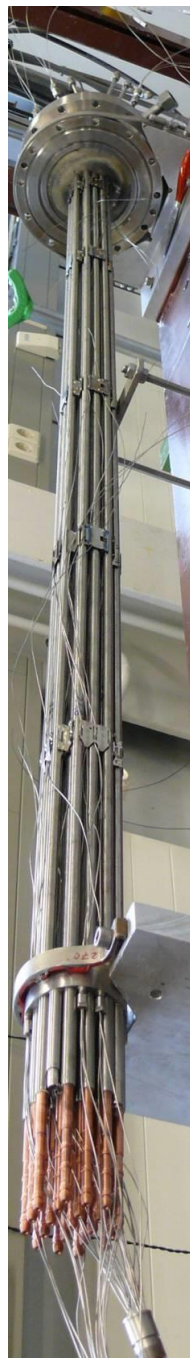
bundle top

2 m

bundle bottom

Mo heater

Rod cladding

Cu electrode

475 mm

30

O-seals

45

625 mm

Ø 2mm

Kr filling for rod
internal pressurisation
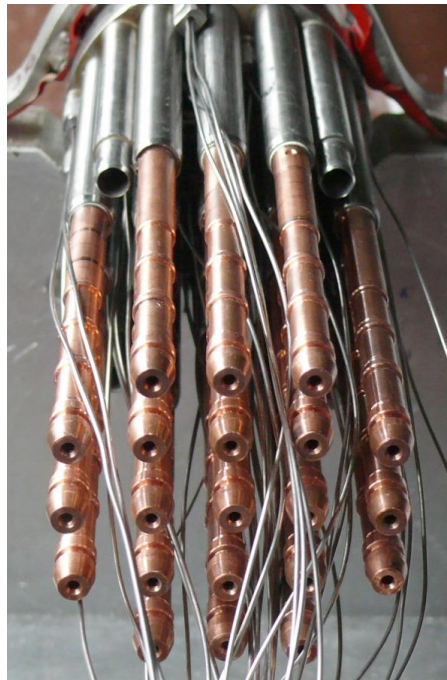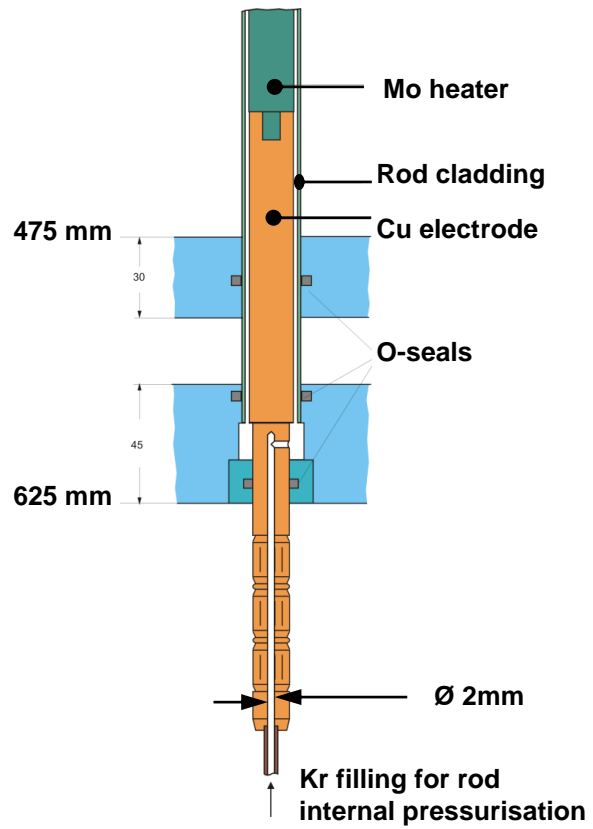
boreholes
through bottom Cu-electrodes

Figure 8   QUENCH-L2; Rod pressurization.
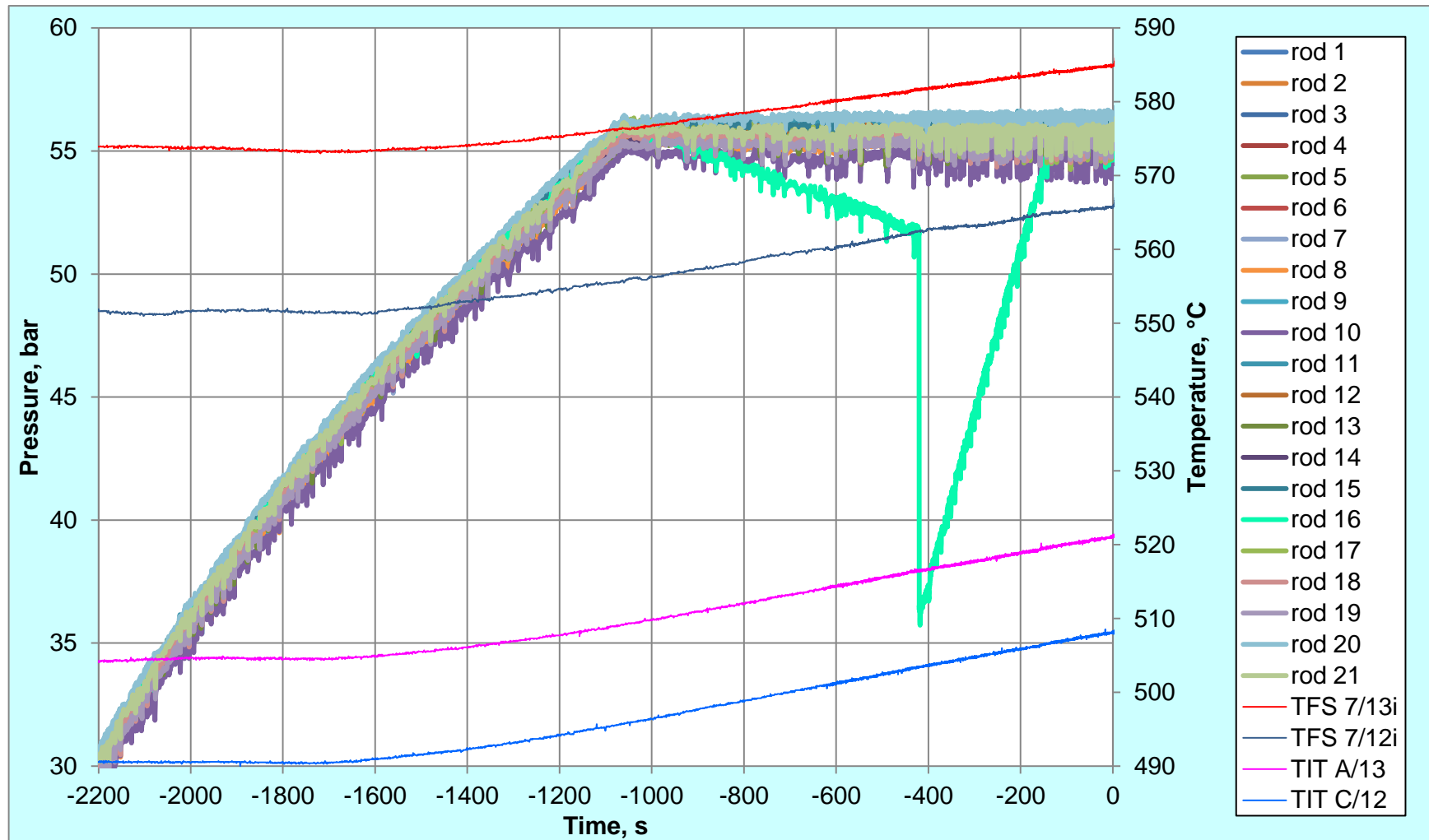
Figure 9   QUENCH-L2; Individual rod pressurization with Kr at max cladding temperature Tpct between 500°C and 585°C.
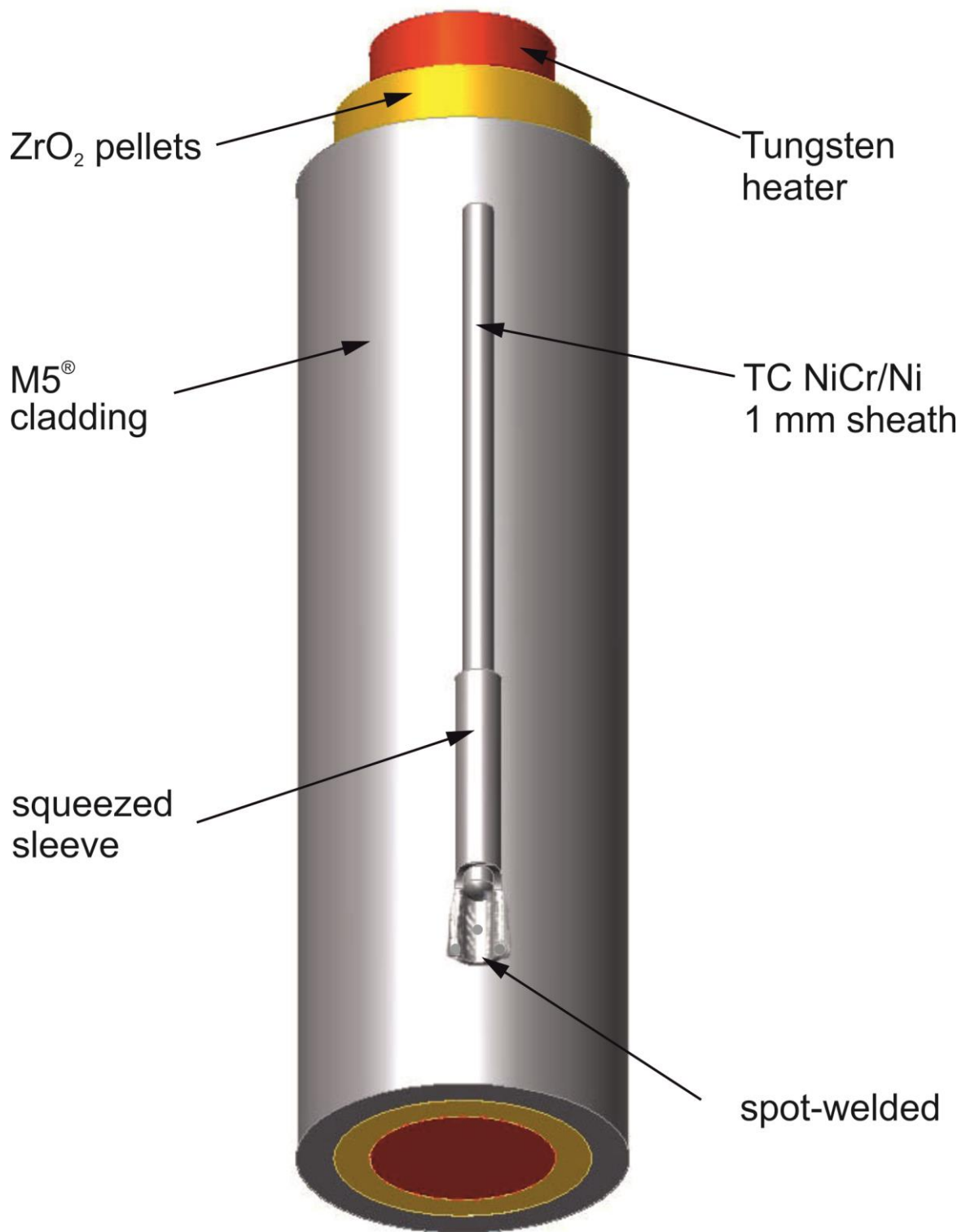
Figure 10   QUENCH-L2; Concept for TC fastening at the test rod.
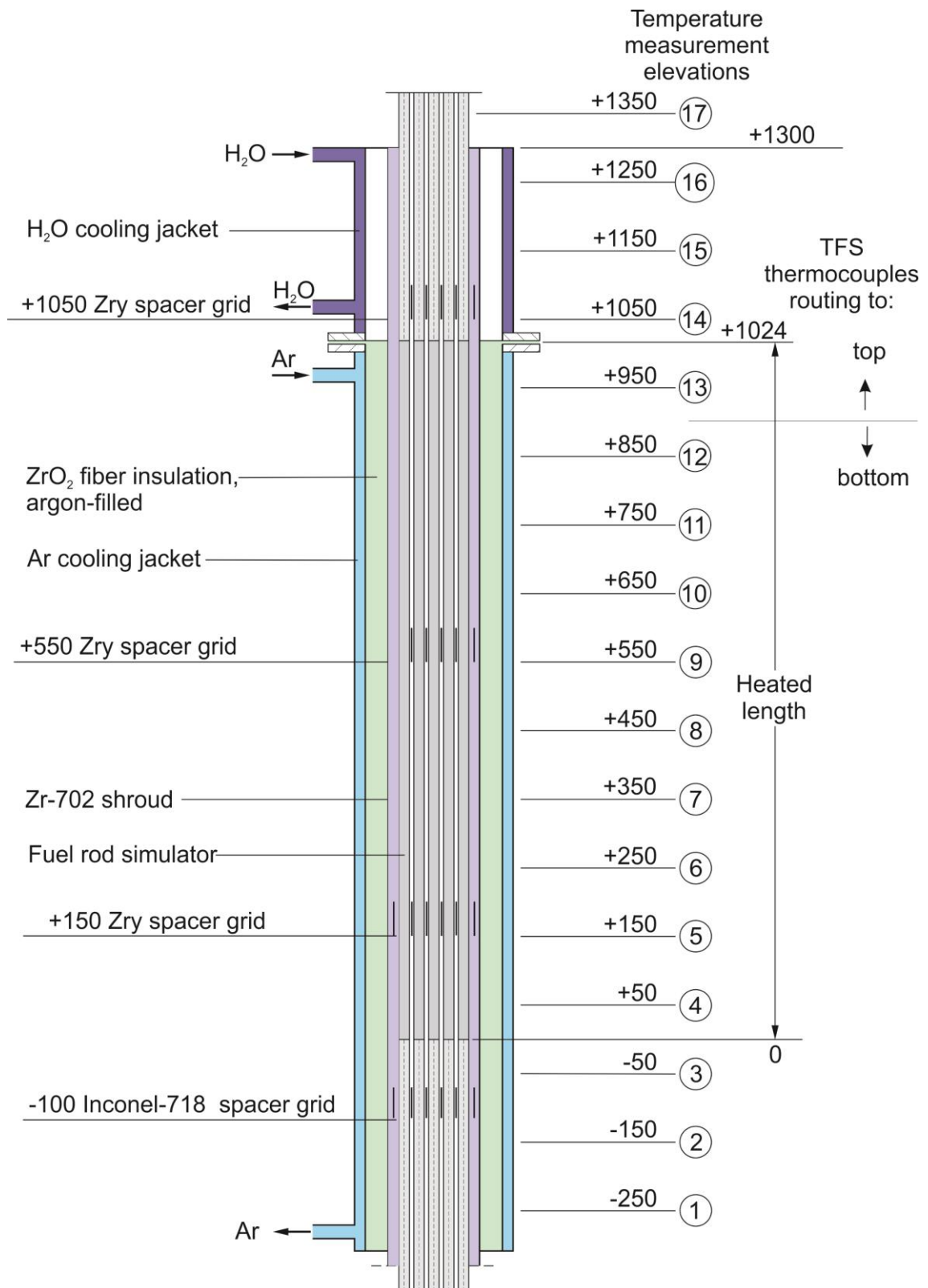
Figure 11   Axial temperature measurement locations in the QUENCH-L2 test section.
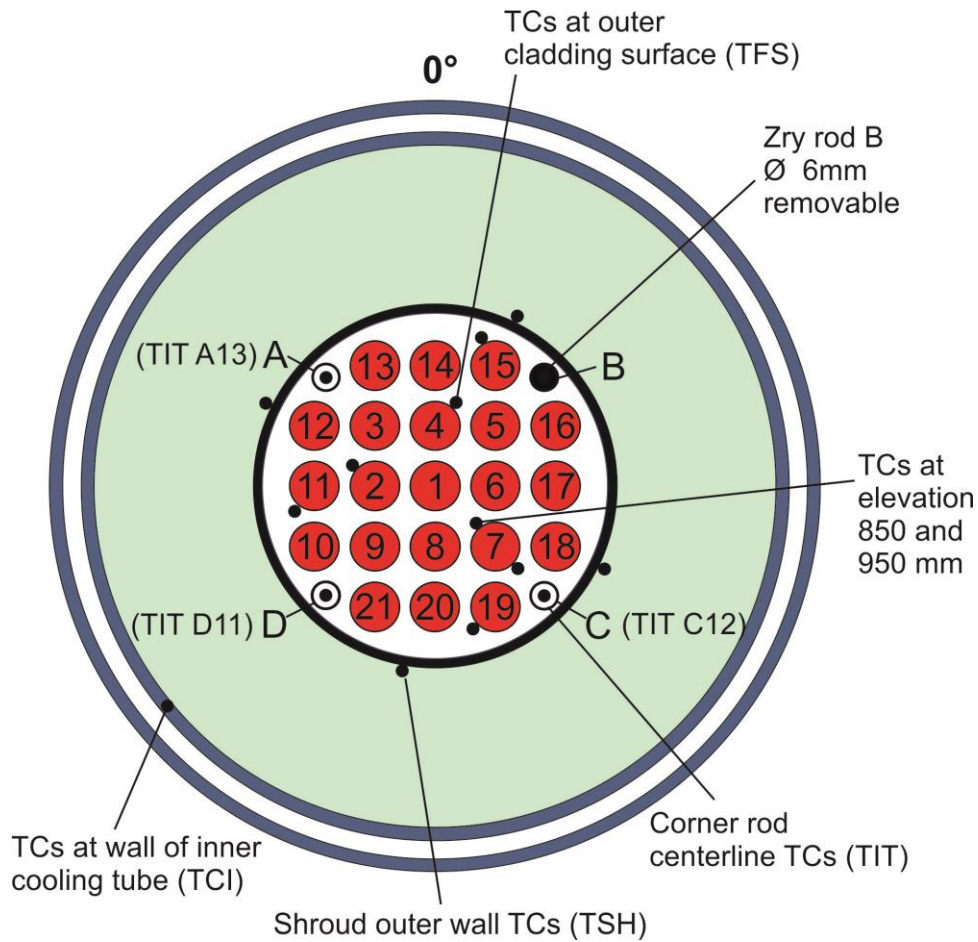
Figure 12   QUENCH-L2; Test bundle; TC instrumentation and rod designation (top view).
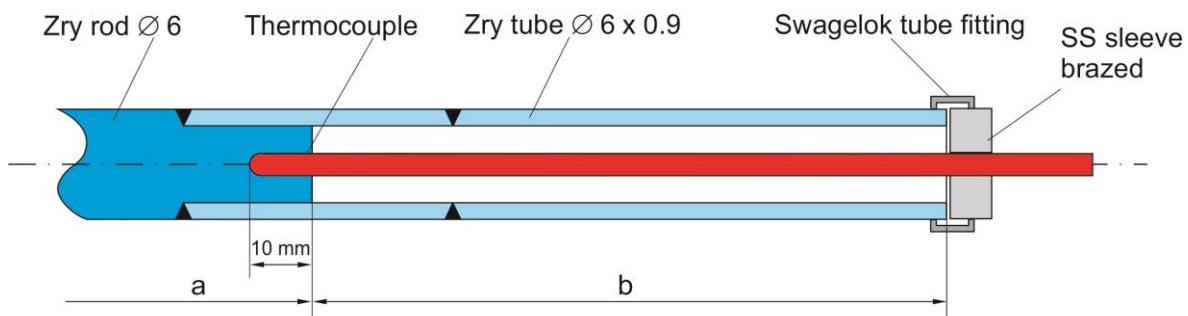
Rod A: TIT A13 (950 mm),   a = 360 mm, b = 2080 mm

Rod C: TIT C12 (850 mm),   a = 460 mm, b = 1980 mm

Rod D: TIT D11 (750 mm),   a = 560 mm, b = 1880 mm

Figure 13   QUENCH-L2; Arrangement of the thermocouples inside the corner rods.
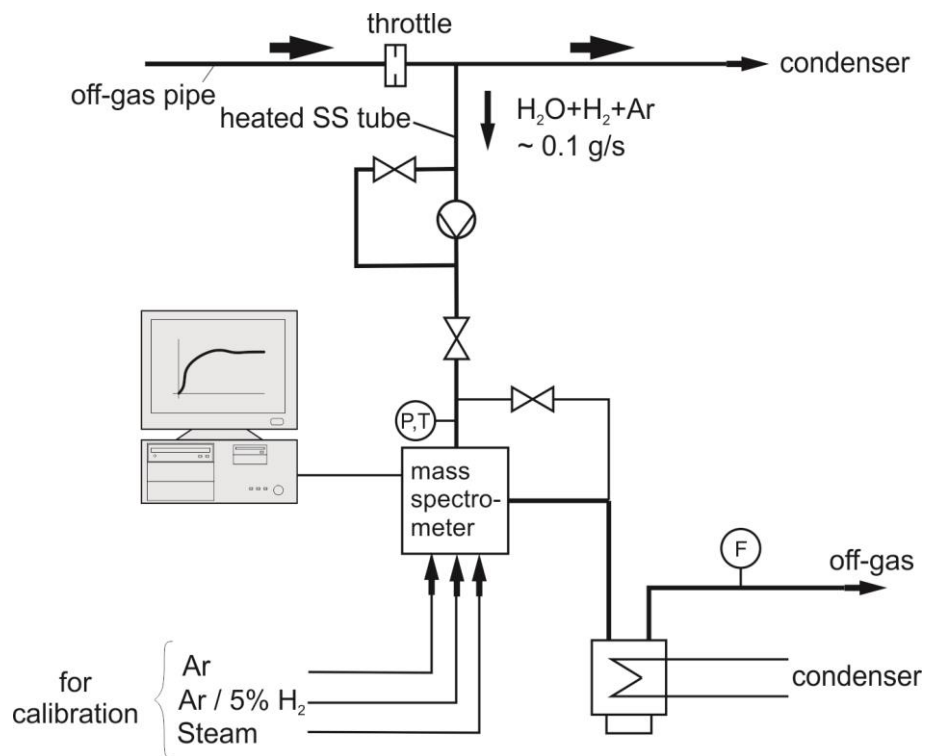
Figure 14   QUENCH Facility; H2 measurement with the GAM 300 mass spectrometer.
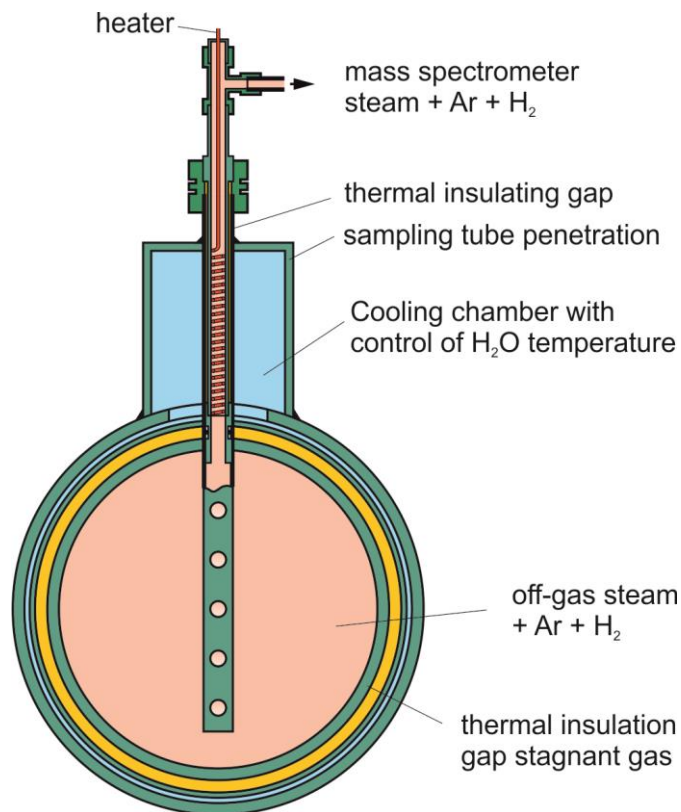
Figure 15   Mass spectrometer sampling position at the off-gas pipe of the QUENCH test facility.
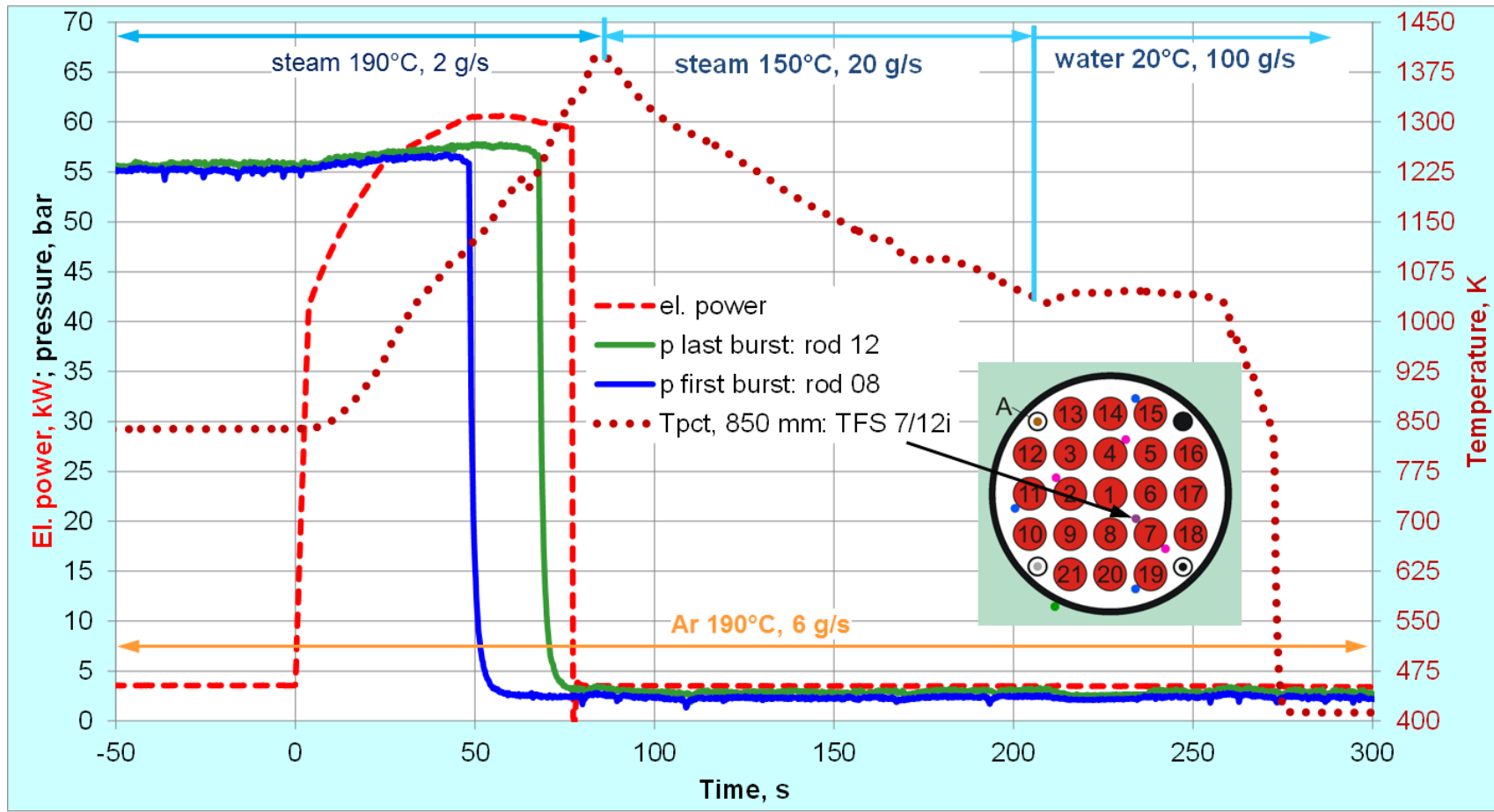
maximal reached power:
QUENCH-L1 (Ta-heaters, Ø 6 mm): 58.5 kW,
QUENCH-L2 (W-heaters; Ø 4.6 mm): 60.5 kW

Figure 16   QUENCH-L2; Test scenario.
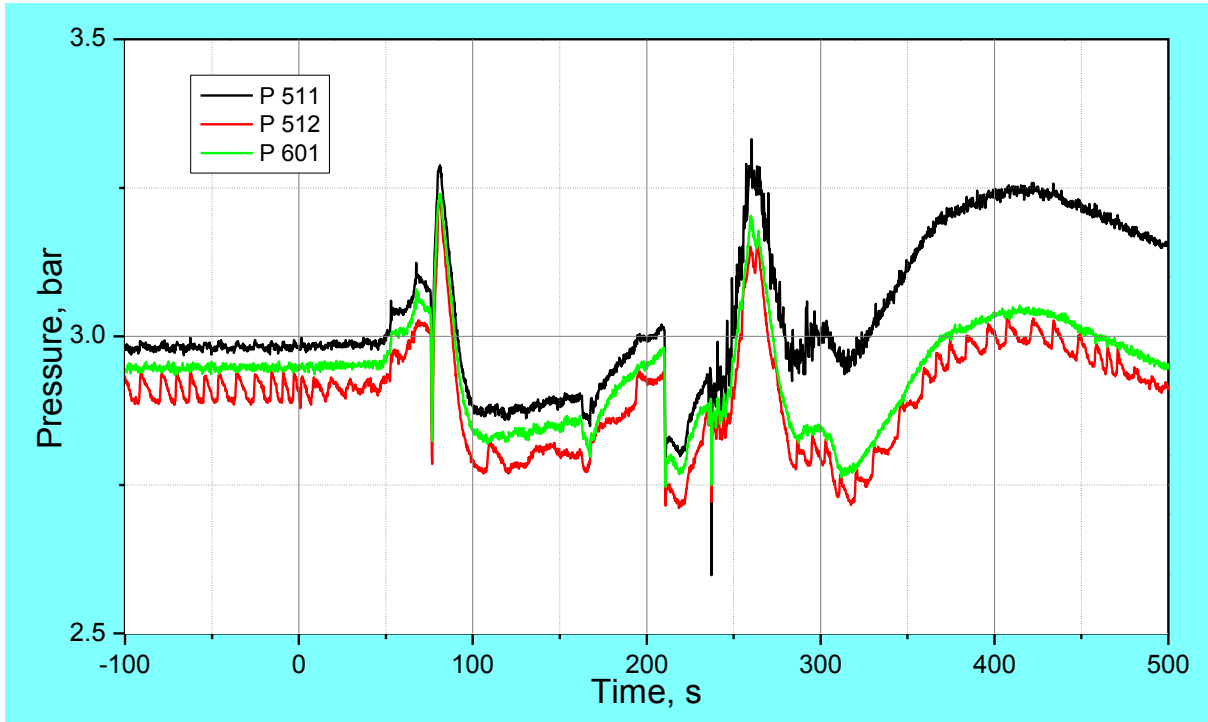
Figure 17   QUENCH-L2; System pressure measured at test section inlet P 511, at outlet P 512, and in the off-gas pipe P 601.
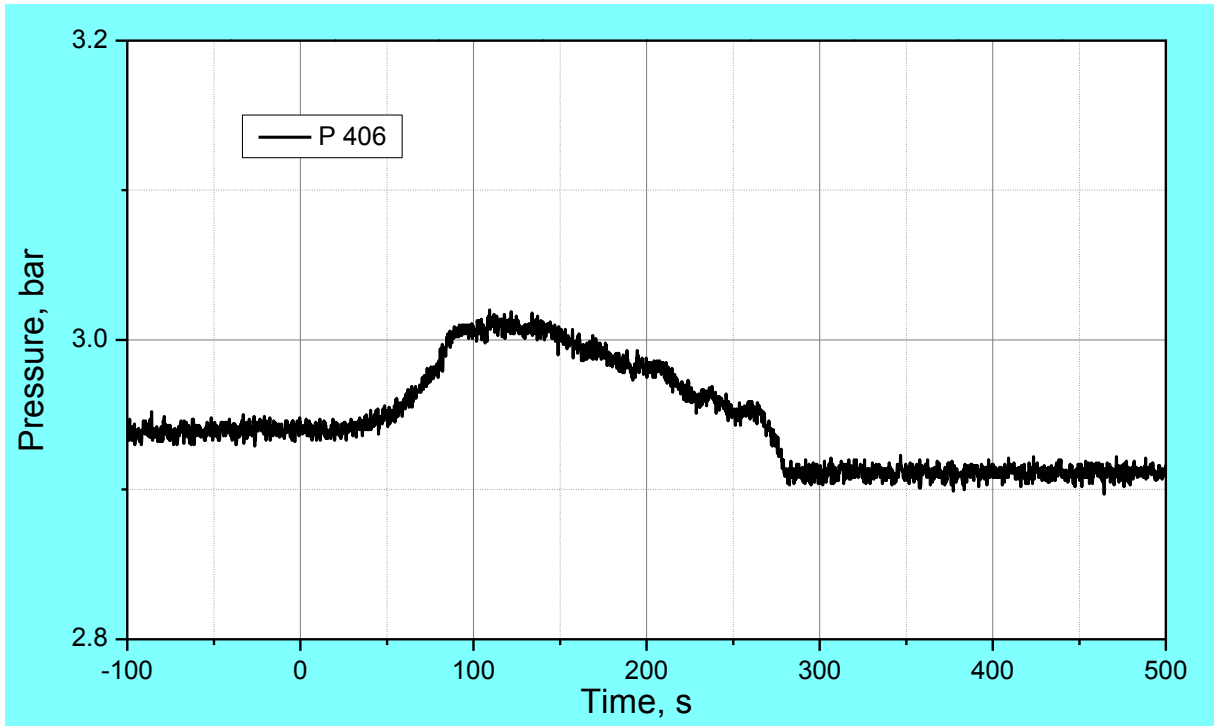
Figure 18   QUENCH-L2; Argon pressure between shroud and cooling jacket P 406 demonstrates tightness of the shroud.
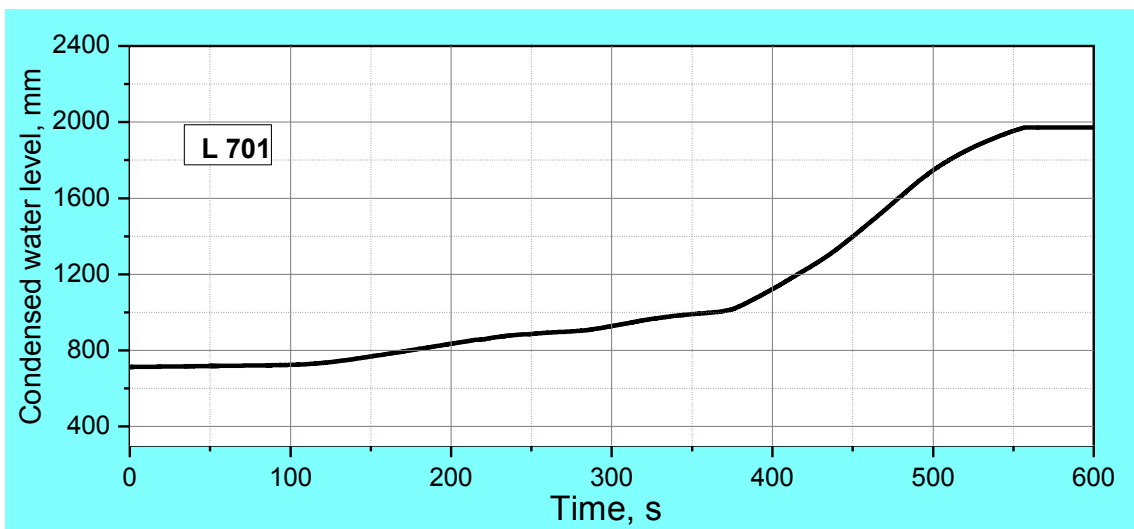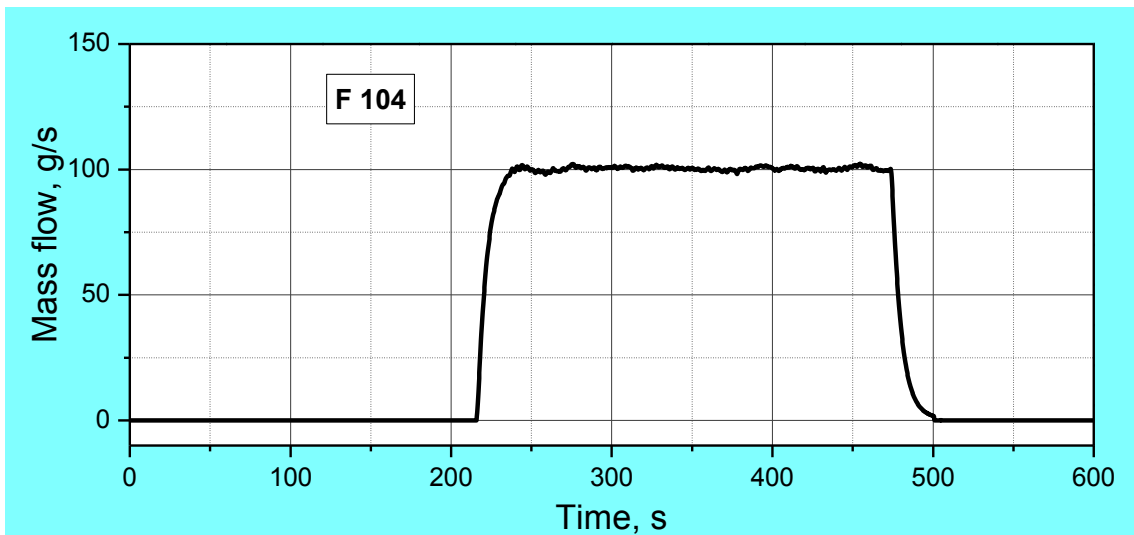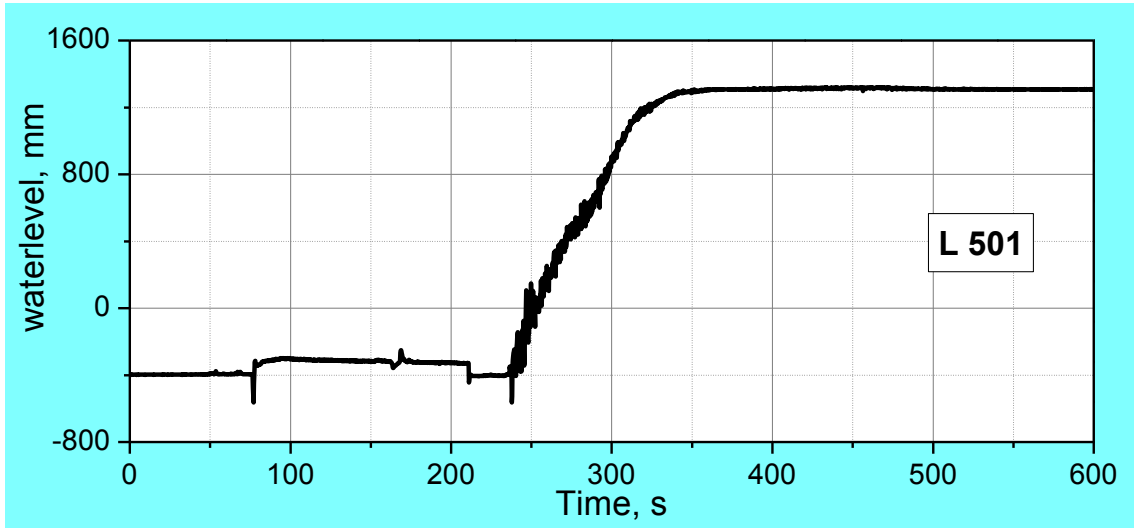
Figure 19   QUENCH-L2; Quench measurement of collapsed water level (L 501), top, water mass flow rate
(Fm 104), center, condensed water (L 701), bottom.
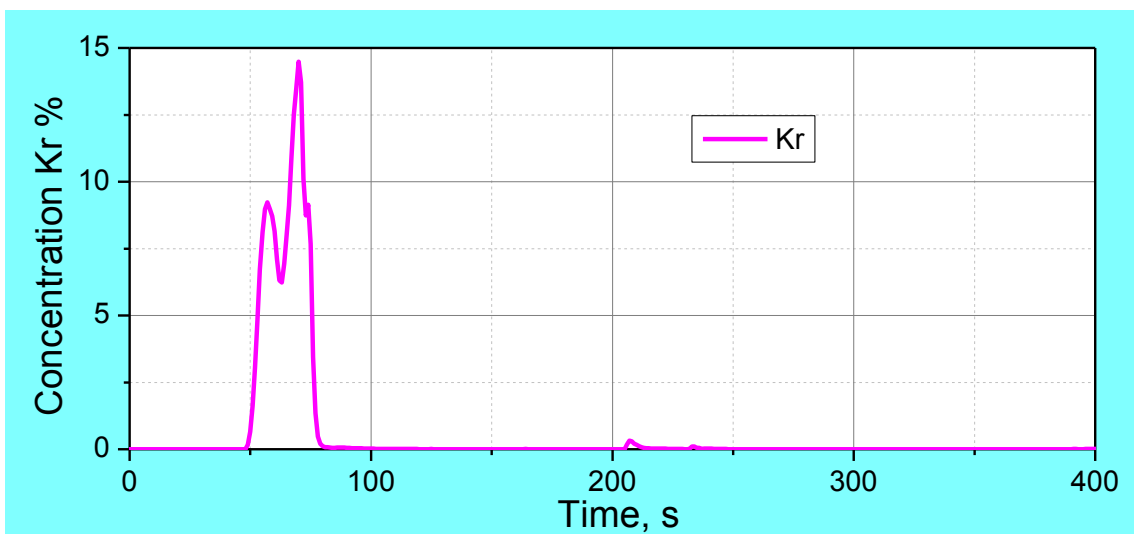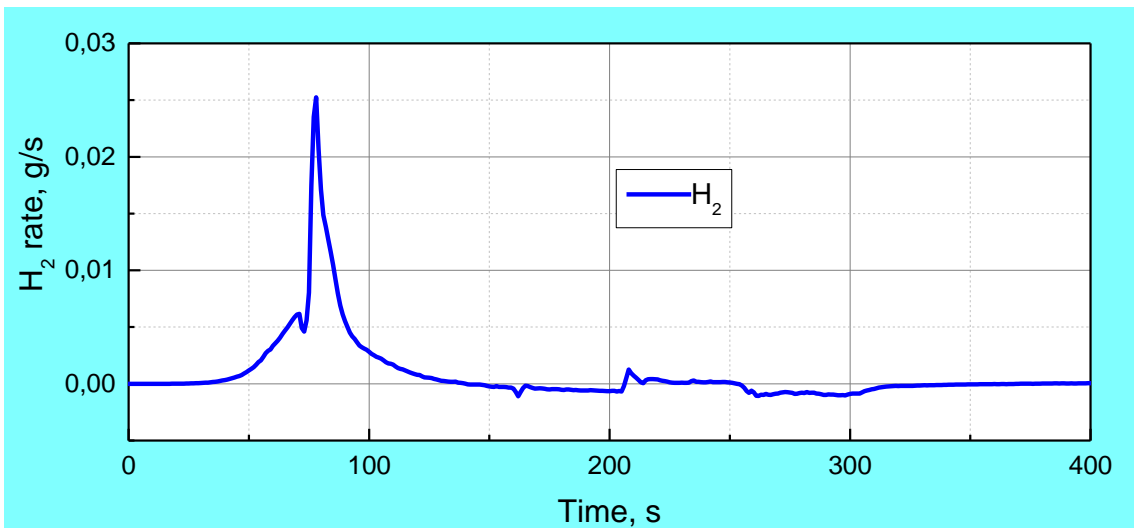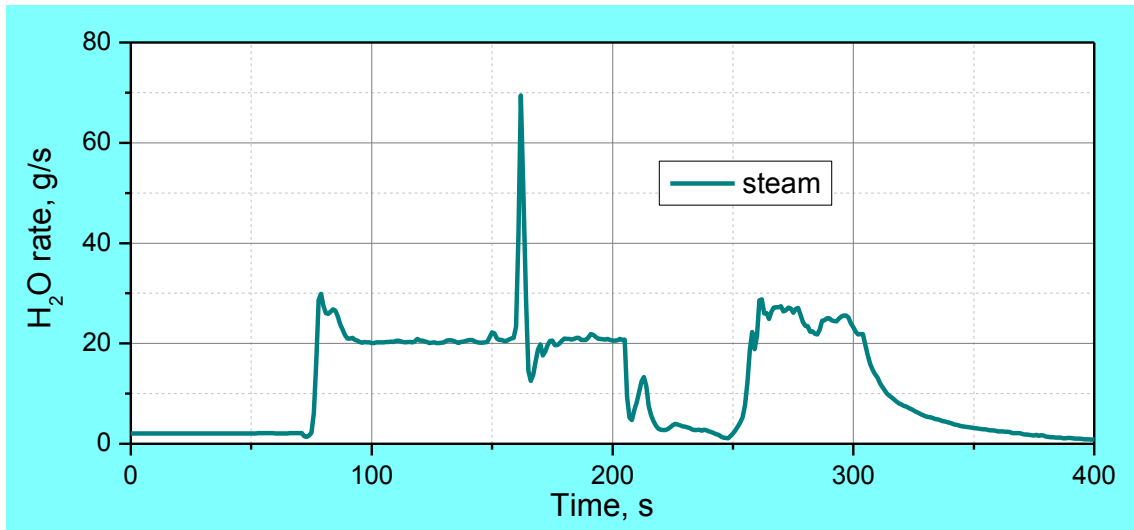
Figure 20   QUENCH-L2; Steam rate, top, Hydrogen, center, Krypton, bottom, measured by mass spectrometry (MS).
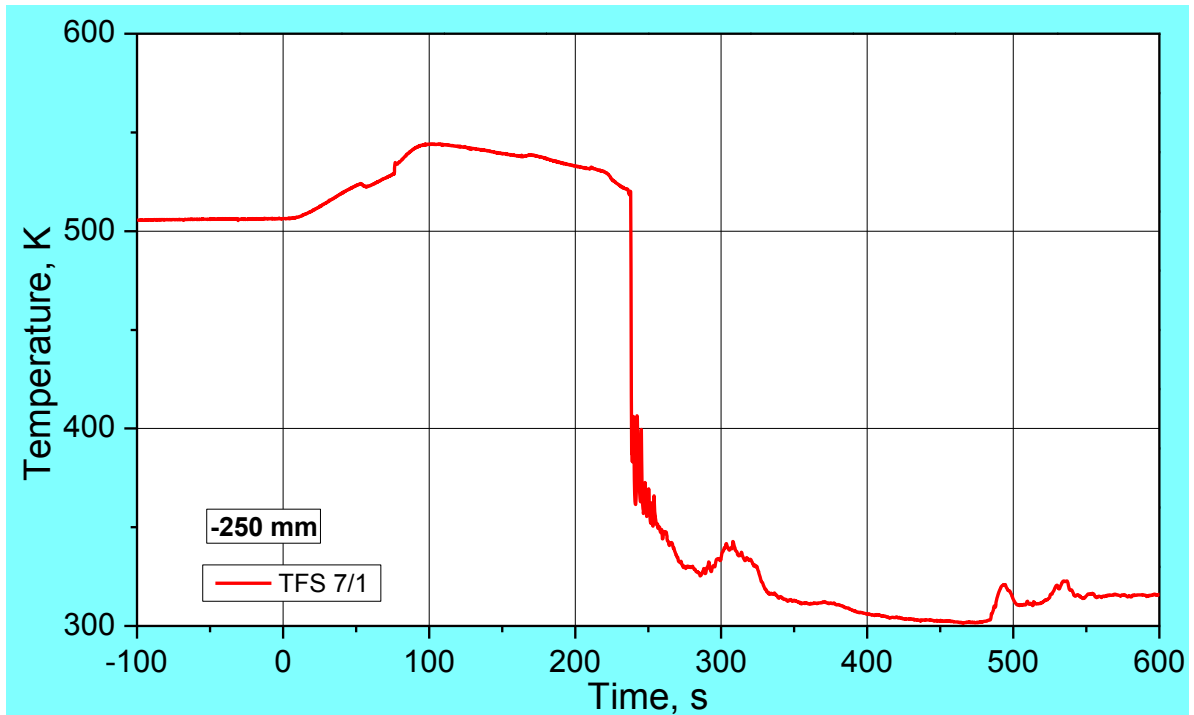
Figure 21   QUENCH-L2; Temperatures measured by rod cladding (TFS 7/1) thermocouple at -250 mm elevation.
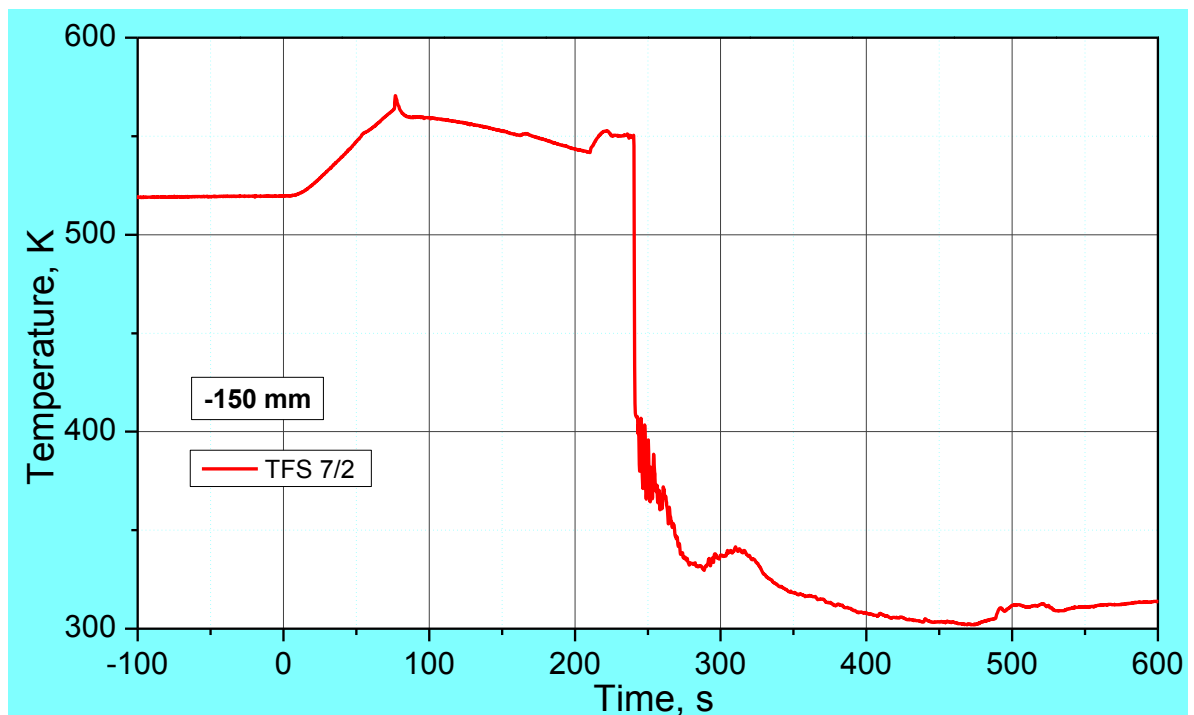
Figure 22   QUENCH-L2; Temperatures measured by rod cladding (TFS 7/2) thermocouple at -150 mm elevation.
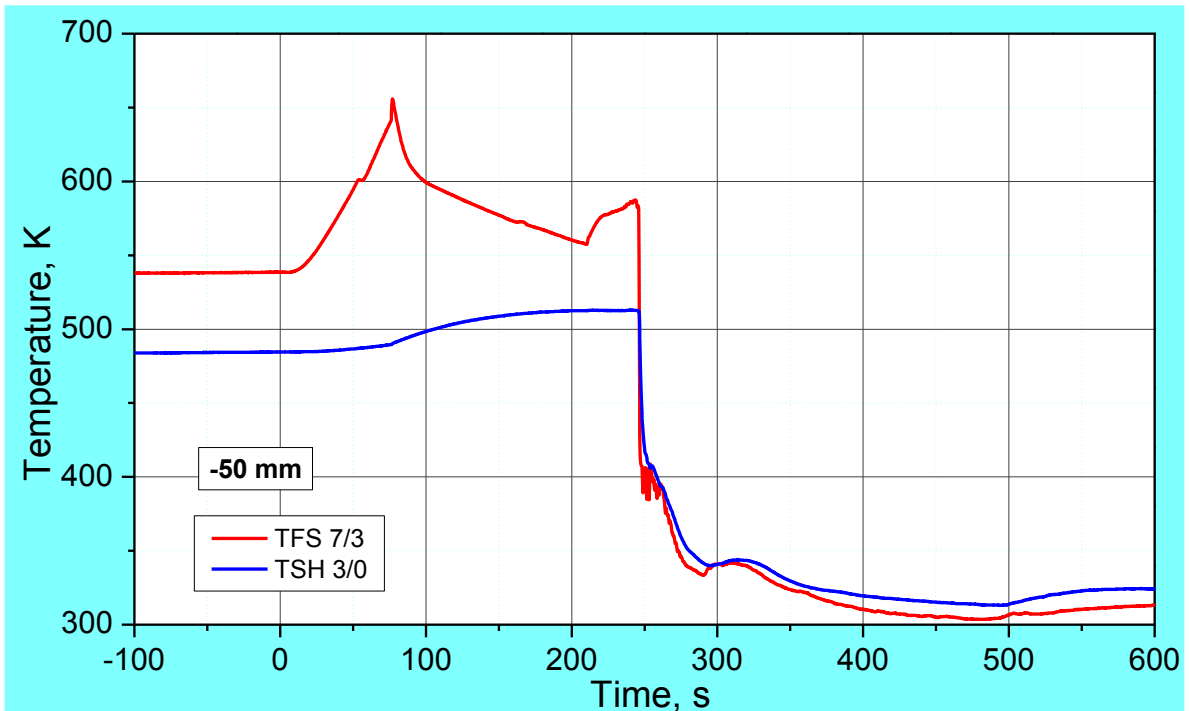
Figure 23   QUENCH-L2; Temperatures measured by rod cladding (TFS 7/3) and shroud (TSH 3/0) thermocouples at -50 mm elevation.
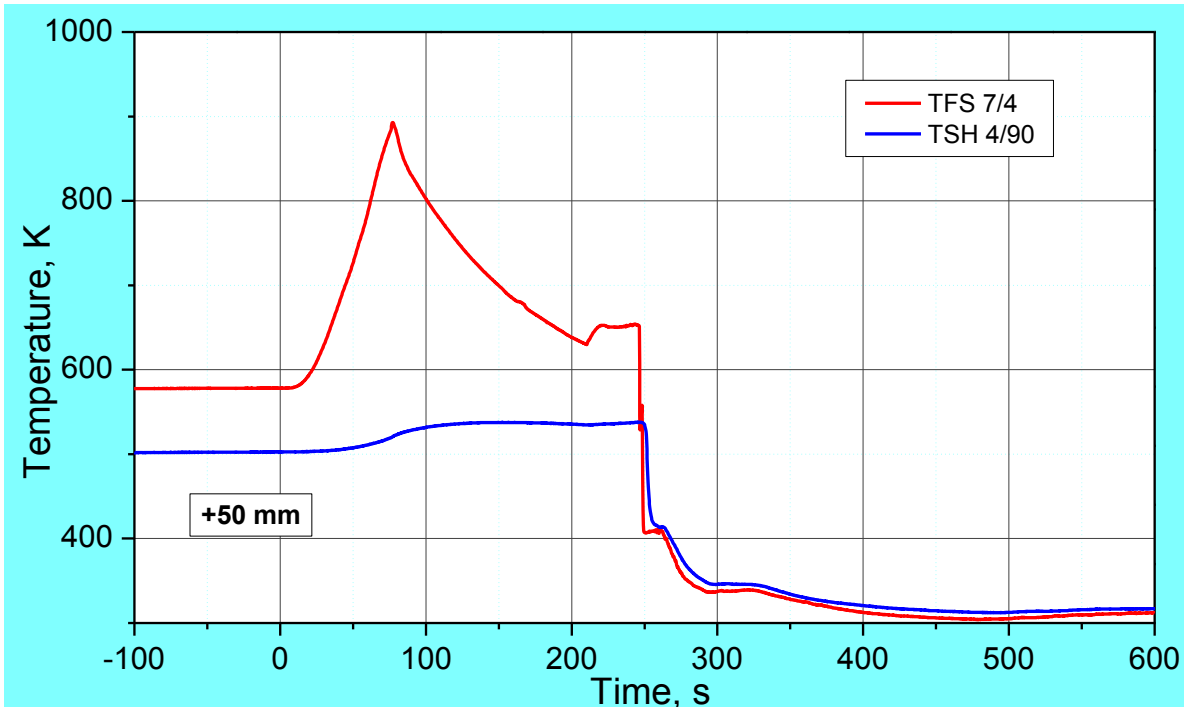
Figure 24   QUENCH-L2; Temperatures measured by rod cladding (TFS 7/4) and shroud (TSH 4/90) thermocouples at 50 mm elevation.
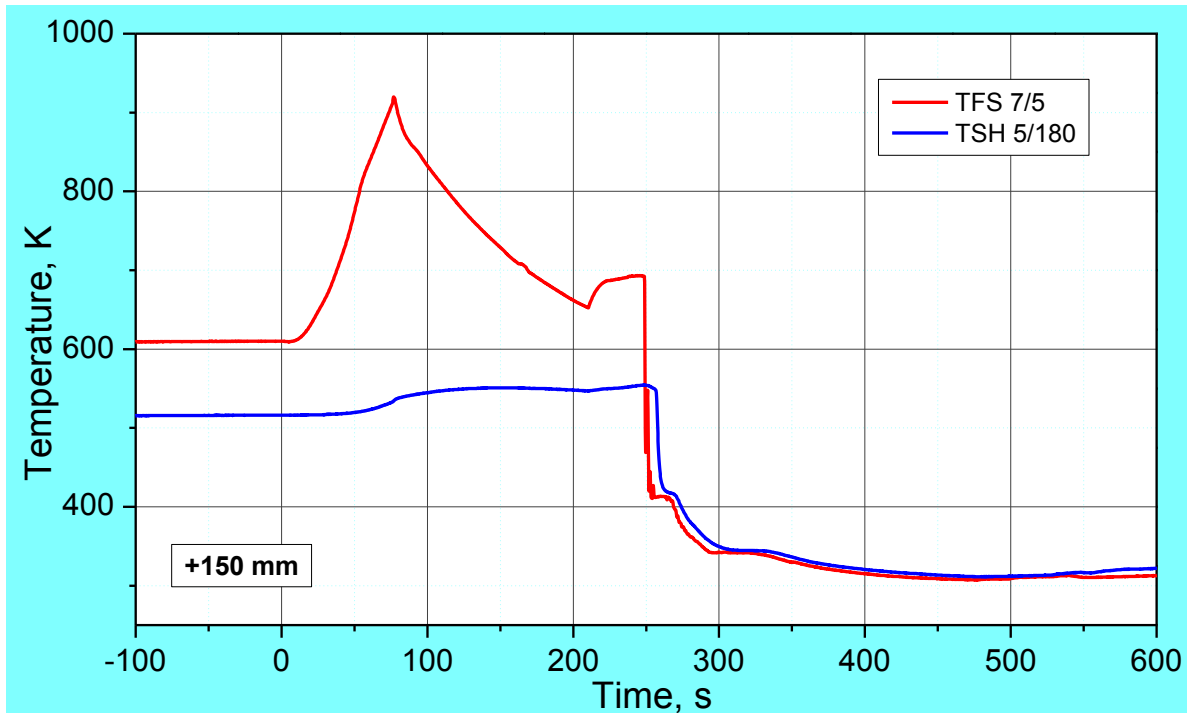
Figure 25   25: QUENCH-L2; Temperatures measured by rod cladding (TFS 7/5) and shroud (TSH 5/180) thermocouples at 150 mm elevation.
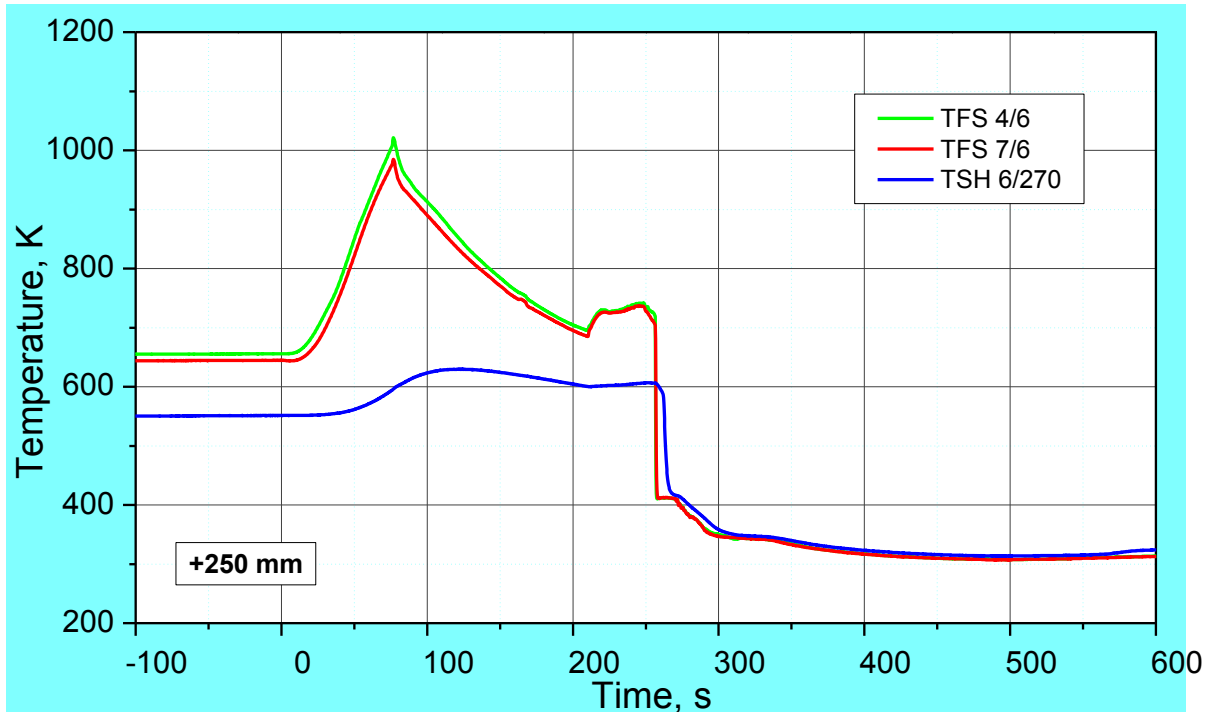
Figure 26   QUENCH-L2; Temperatures measured by rod cladding (TFS) and shroud (TSH 6/270) thermocouples at 250 mm elevation.
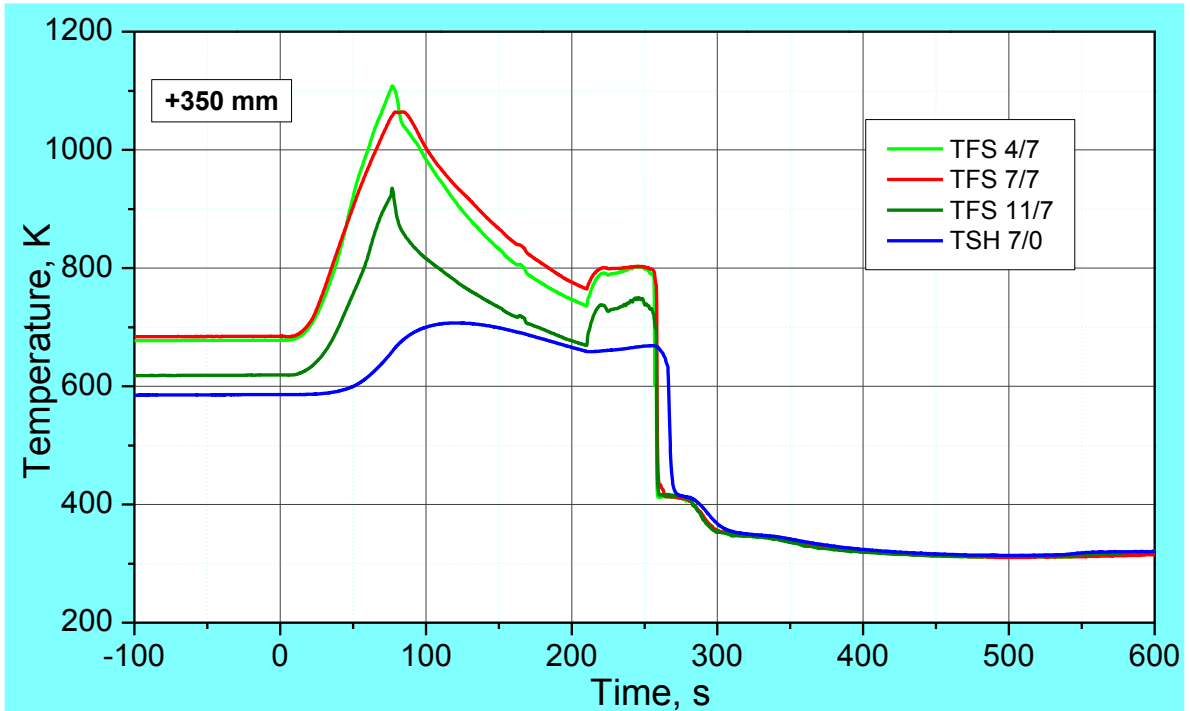
Figure 27   QUENCH-L2; Temperatures measured by rod cladding (TFS) and shroud (TSH 7/0) thermocouples at 350 mm elevation.
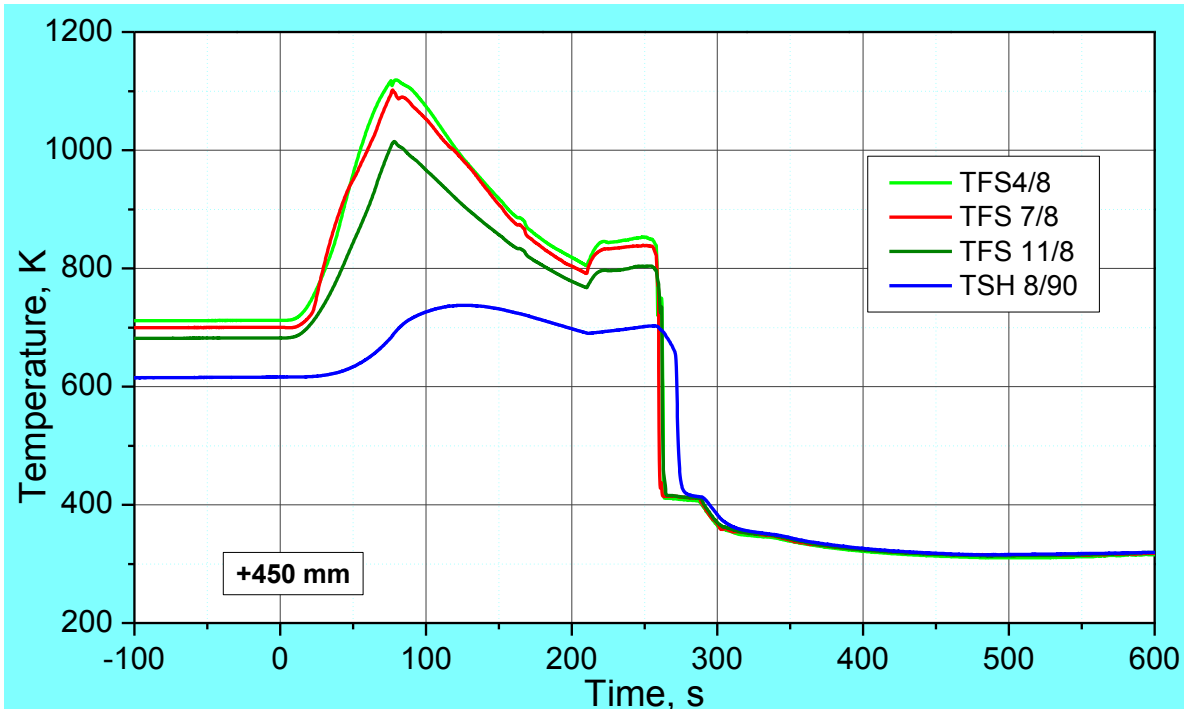
Figure 28   QUENCH-L2; Temperatures measured by rod cladding (TFS) and shroud (TSH 8/90) thermocouples at 450 mm elevation.
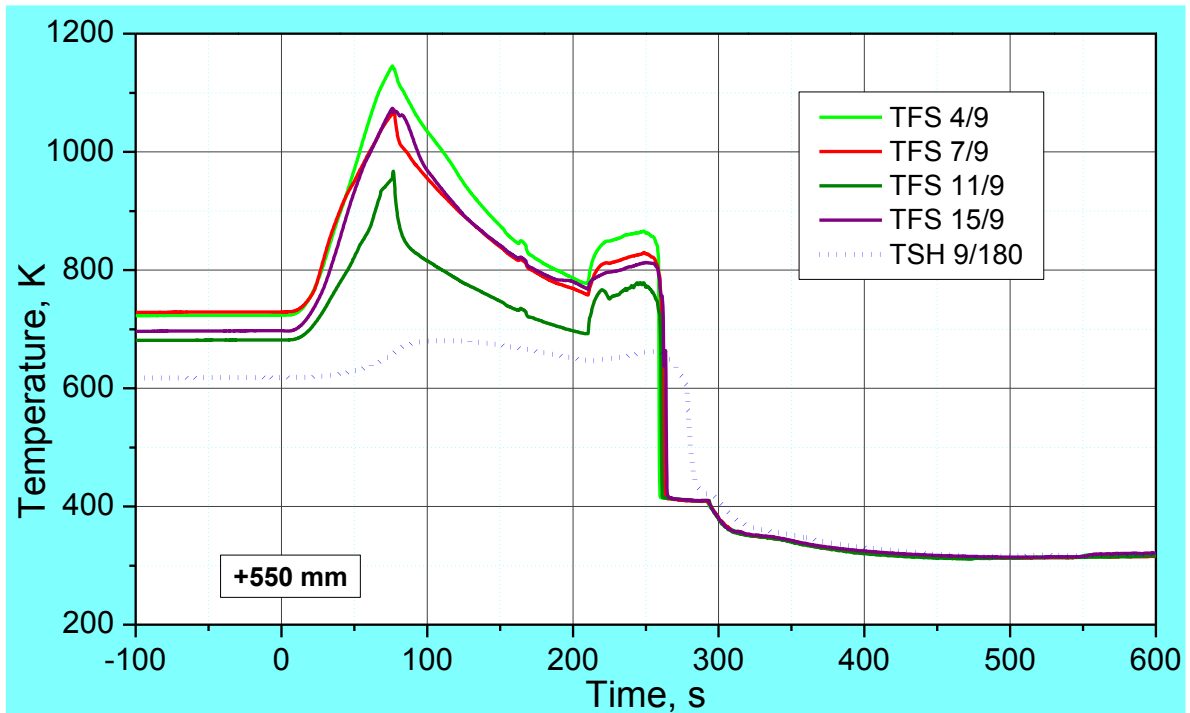
Figure 29   QUENCH-L2; Temperatures measured by rod cladding (TFS) and shroud (TSH 9/180) thermocouples at 550 mm elevation.
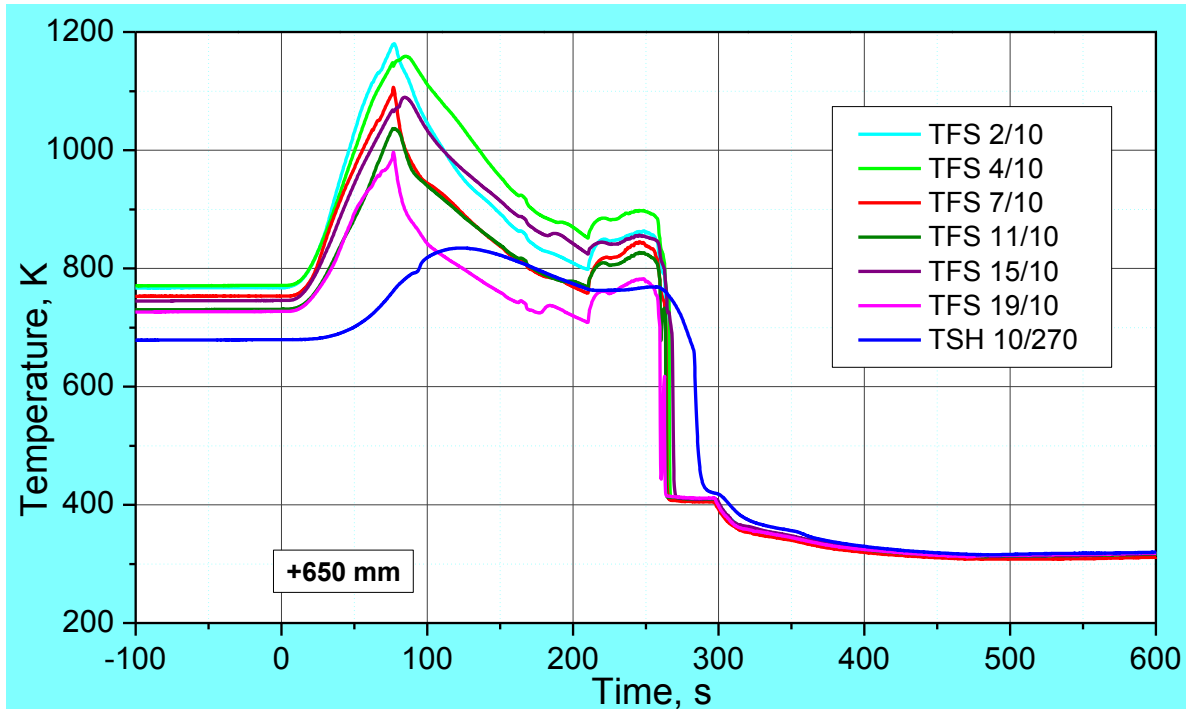
Figure 30   QUENCH-L2; Temperatures measured by rod cladding (TFS) and shroud (TSH 10/270) thermocouples at 650 mm elevation.
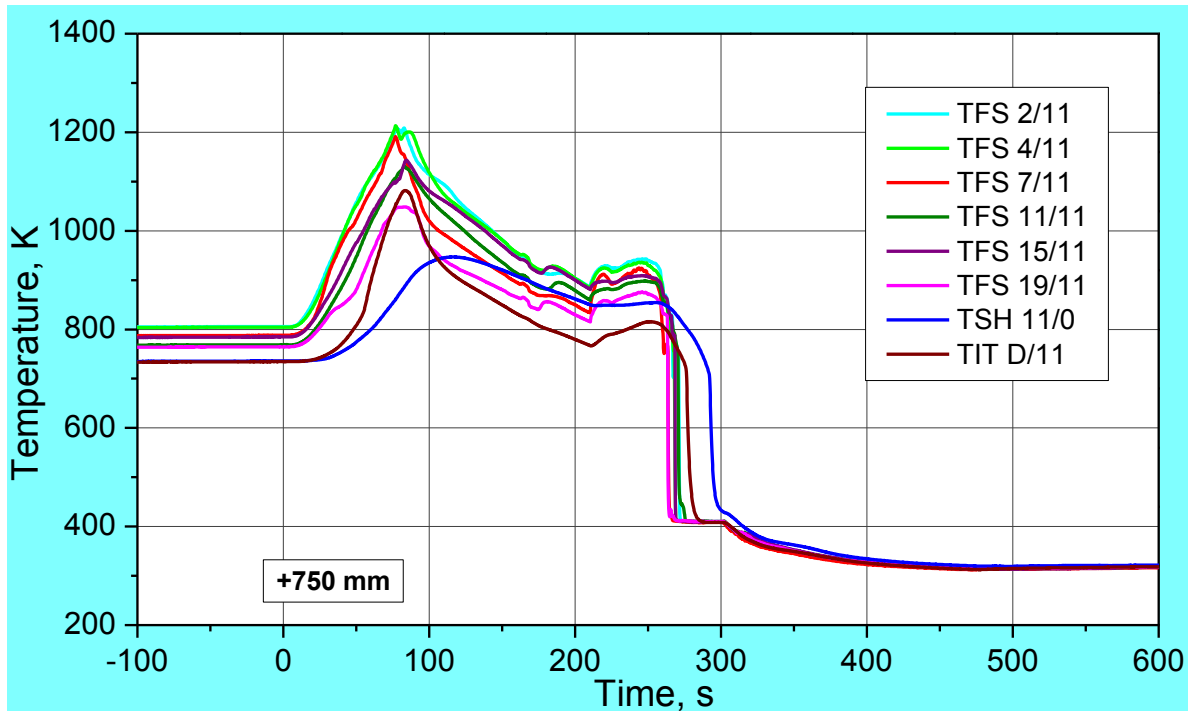
Figure 31   QUENCH-L2; Temperatures measured by rod cladding (TFS) and shroud (TSH 11/0), and corner rod internal (TIT D/11) thermocouples at 750 mm elevation.
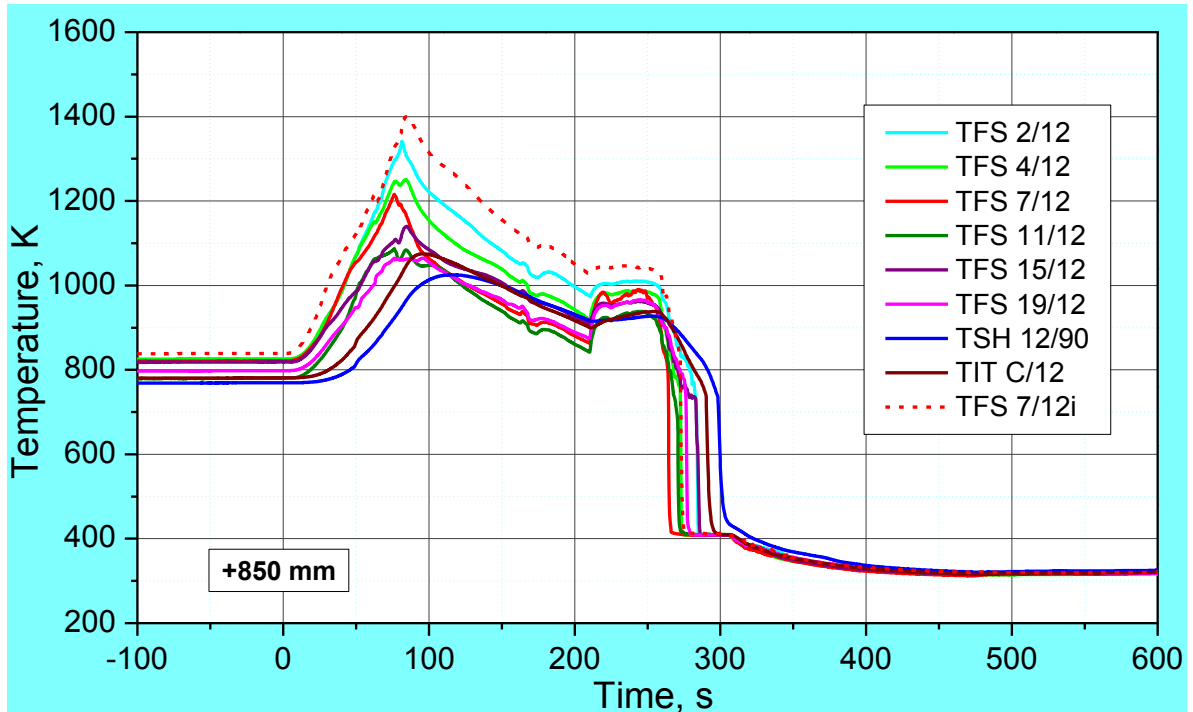
Figure 32   QUENCH-L2; Temperatures measured by rod cladding (TFS) and shroud (TSH 12/90), and corner rod internal (TIT C/12) thermocouples at 850 mm elevation.
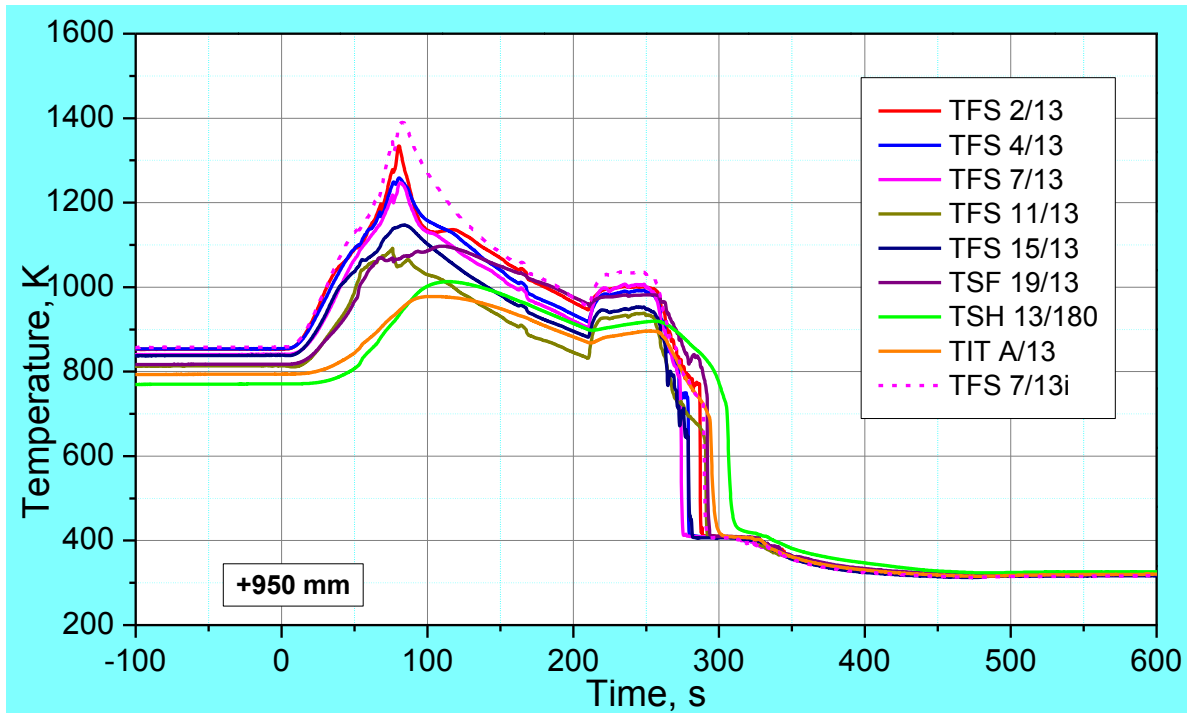
Figure 33   QUENCH-L2; Temperatures measured by rod cladding (TFS) and shroud (TSH 13/180), and corner rod internal (TIT A/13) thermocouples at 950 mm elevation.
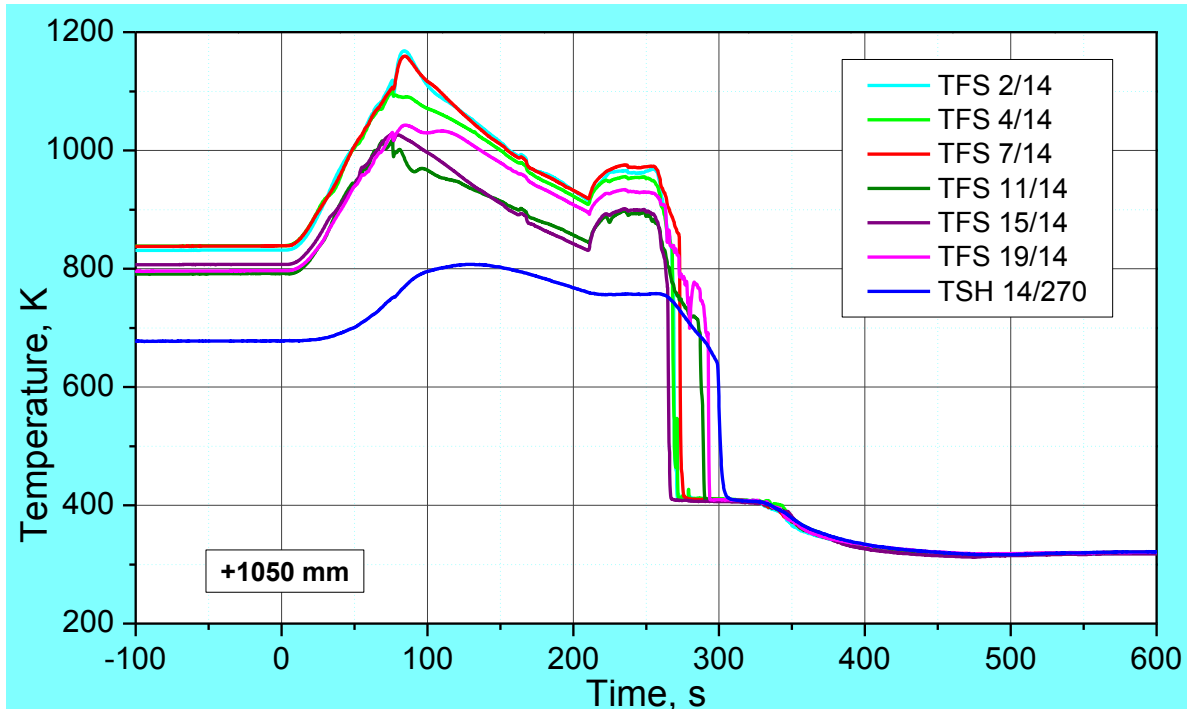
Figure 34   QUENCH-L2; Temperatures measured by rod cladding (TFS) and shroud (TSH 14/270) thermocouples at 1050 mm elevation.
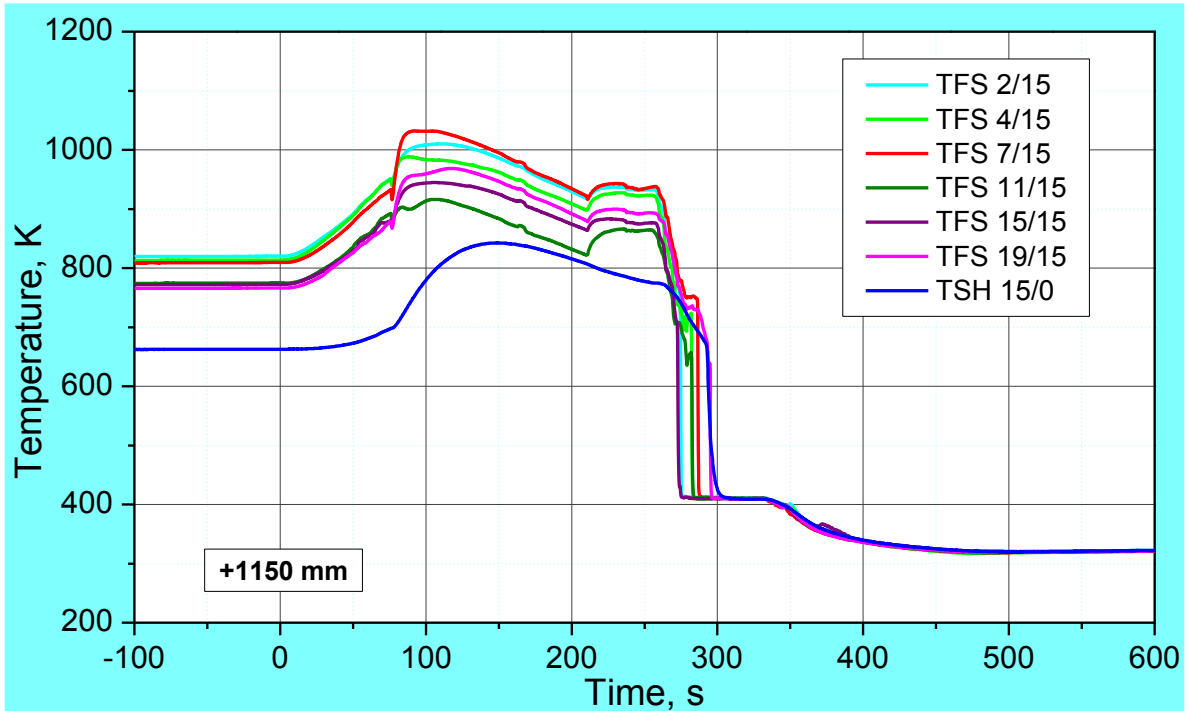
Figure 35   QUENCH-L2; Temperatures measured by rod cladding (TFS) and shroud (TSH 15/0) thermocouples at 1150 mm elevation.
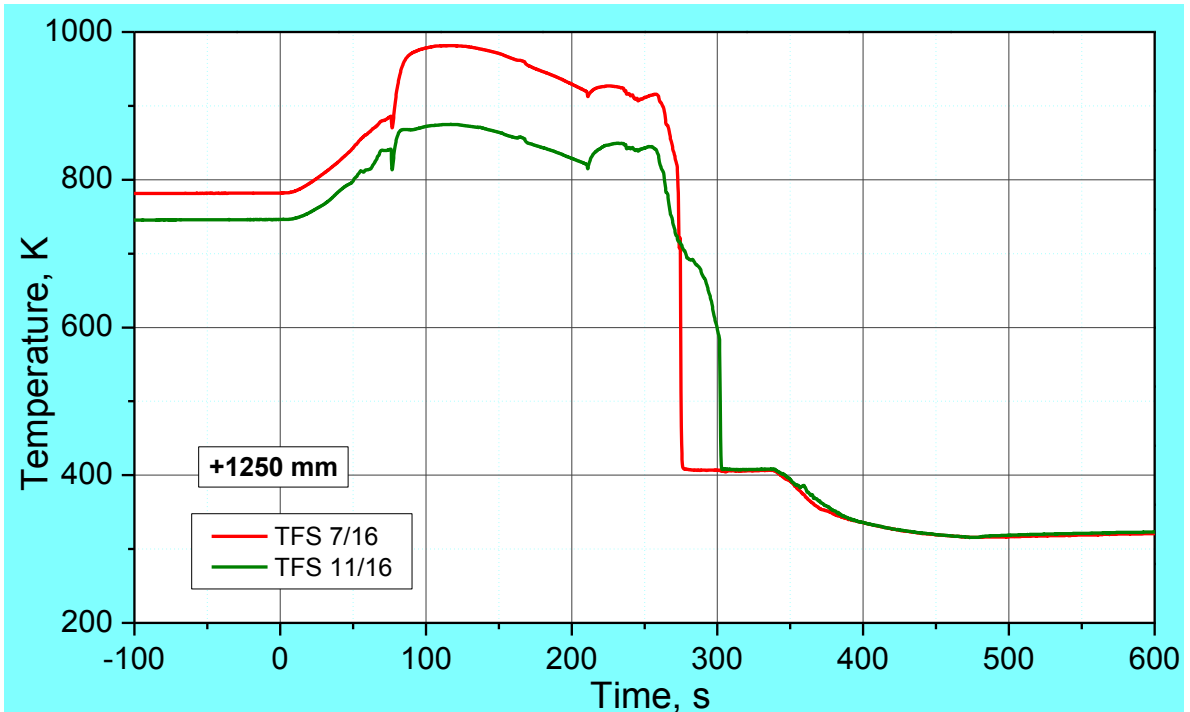
Figure 36   QUENCH-L2; Temperatures measured by rod cladding (TFS) thermocouples at 1250 mm elevation.
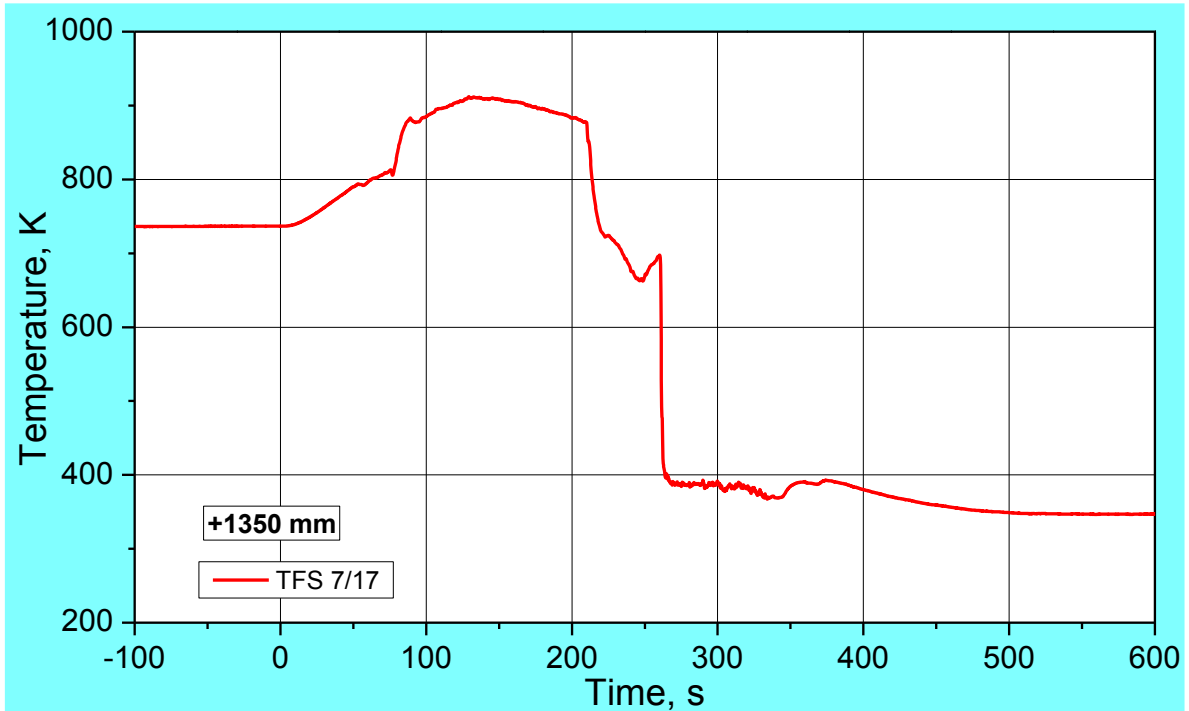
Figure 37   QUENCH-L2; Temperatures measured by rod cladding (TFS 7/17) thermocouple at 1350 mm elevation.
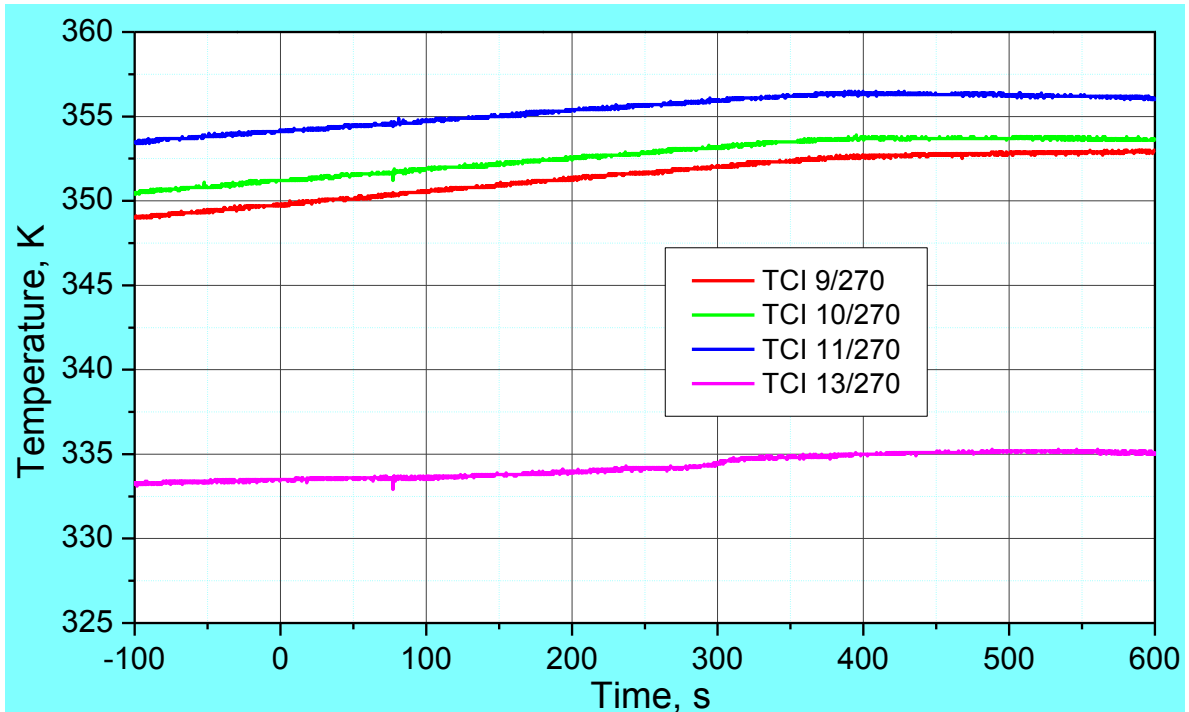
Figure 38   QUENCH-L2; Overview of the TCI (inner cooling jacket).
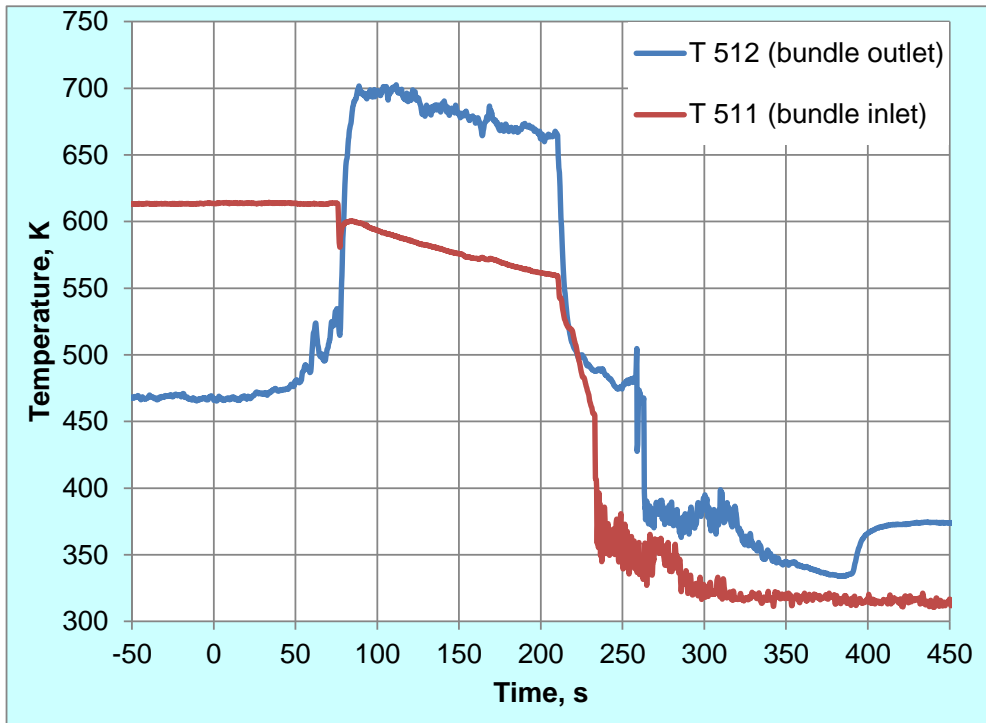
Figure 39   QUENCH-L2; Gas temperatures at inlet and outlet of the bundle.
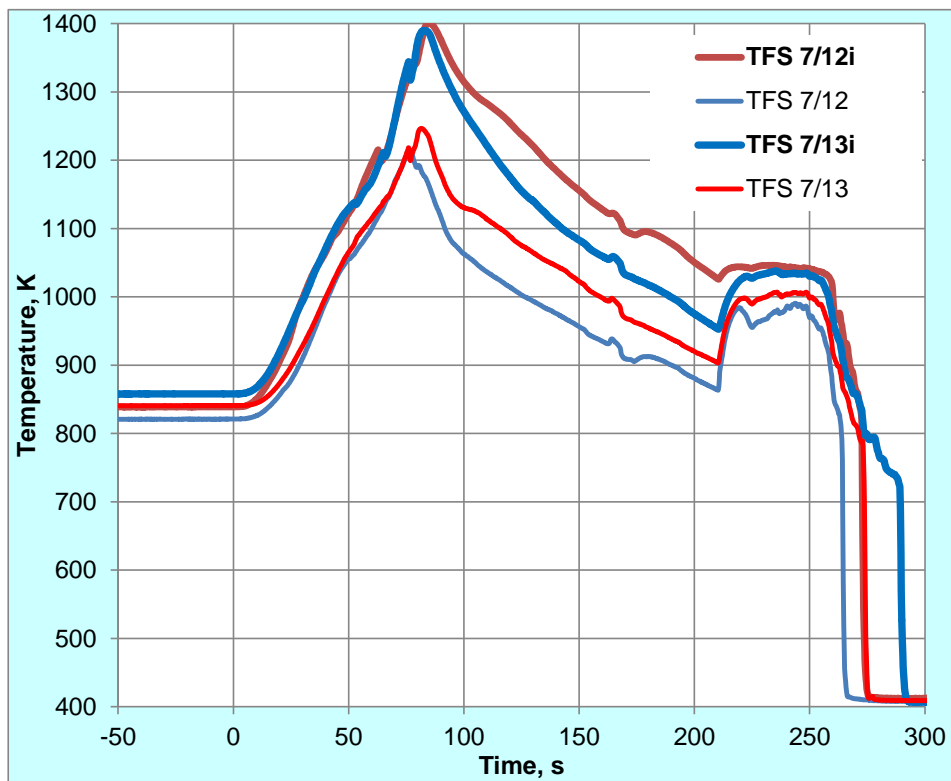
Figure 40   QUENCH-L2; Tangential temperature differences at 850 and 950 mm.
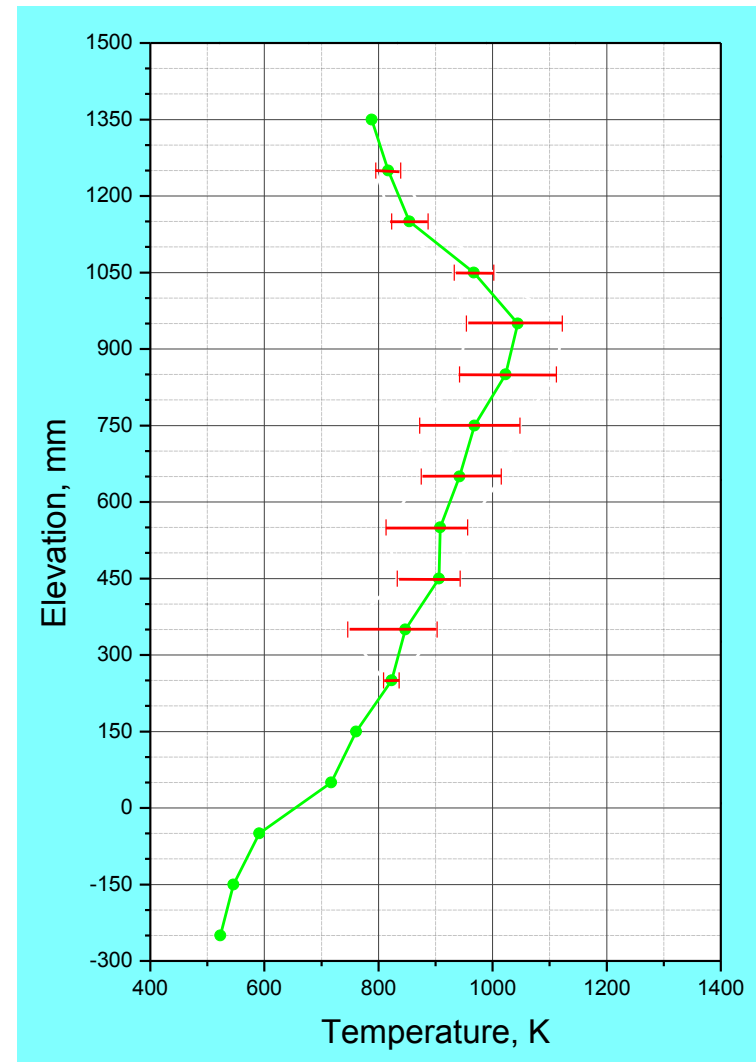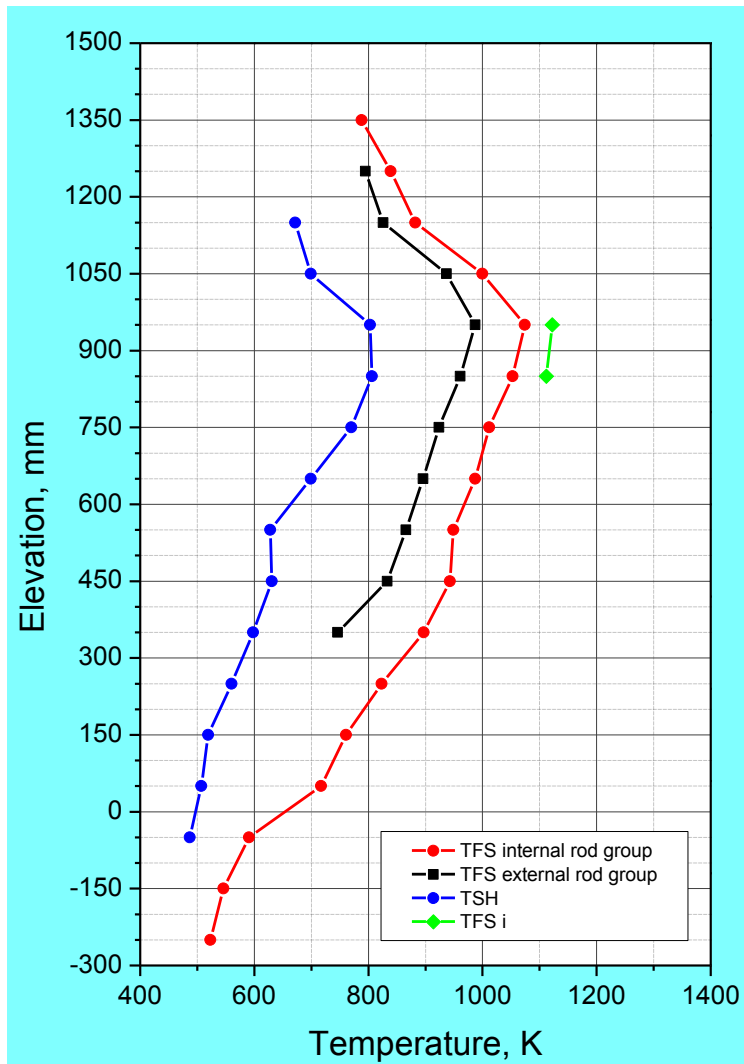
Figure 41   QUENCH-L2; Axial temperature profile TFS internal and external rod group together with TSH, left, and axial temperature profile of all TFS, right, at 48,2 s (first cladding burst).
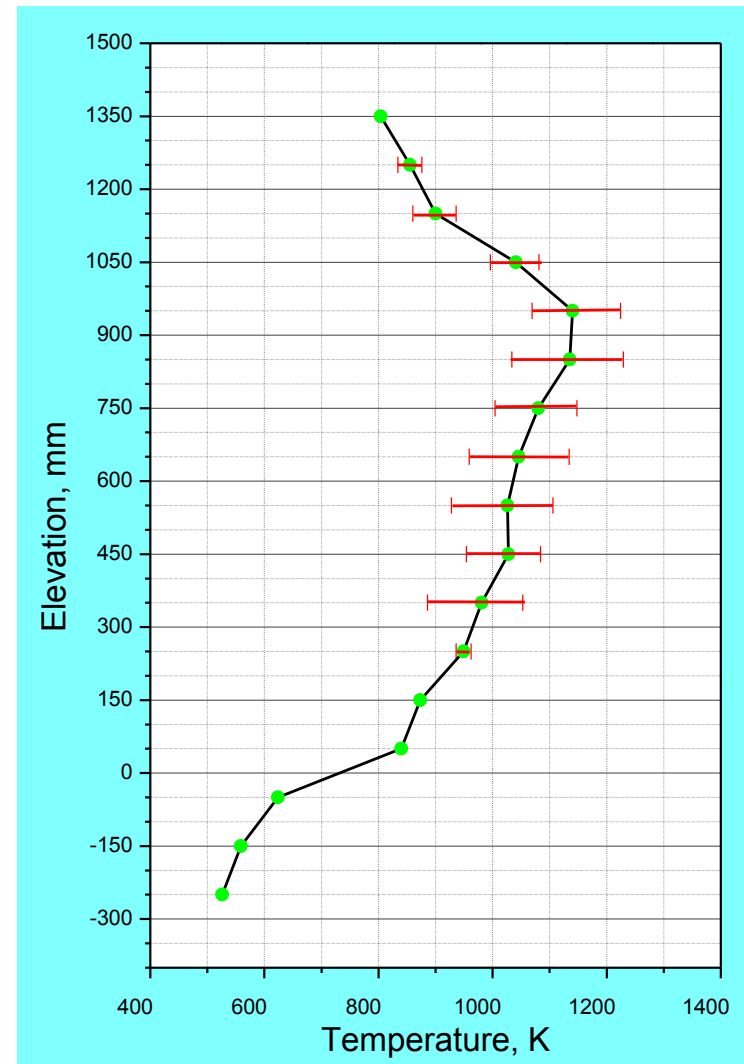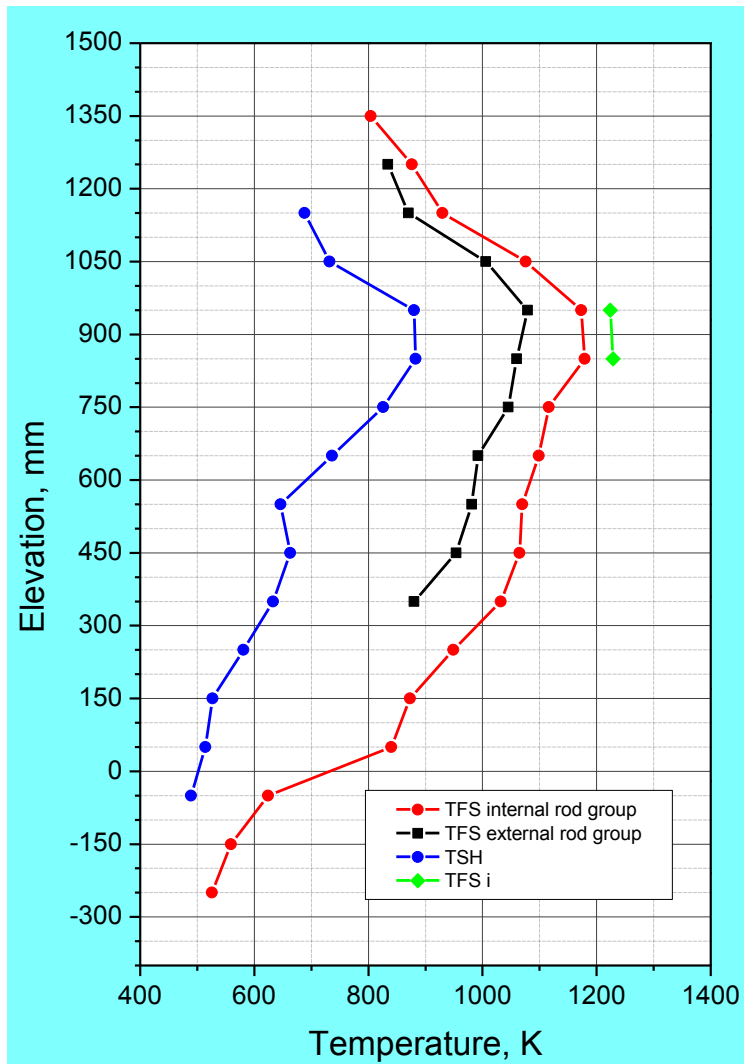
Figure 42   QUENCH-L2; Axial temperature profile TFS internal and external rod group together with TSH, left, and axial temperature profile of all TFS, right, at 48,2 s (first cladding burst).
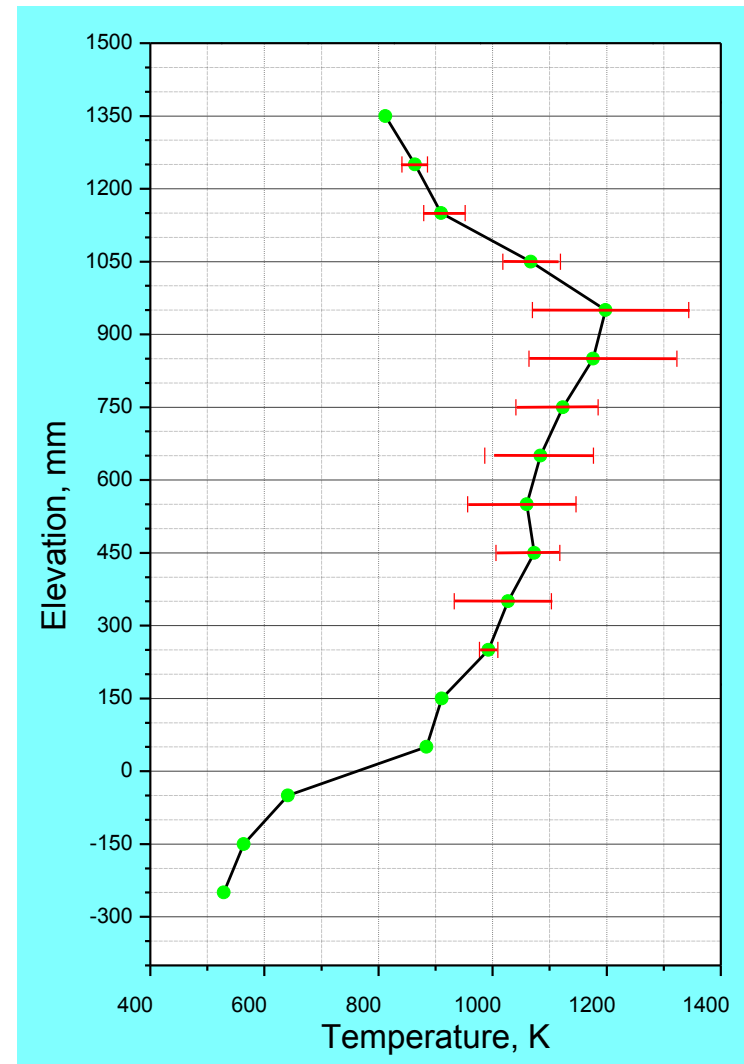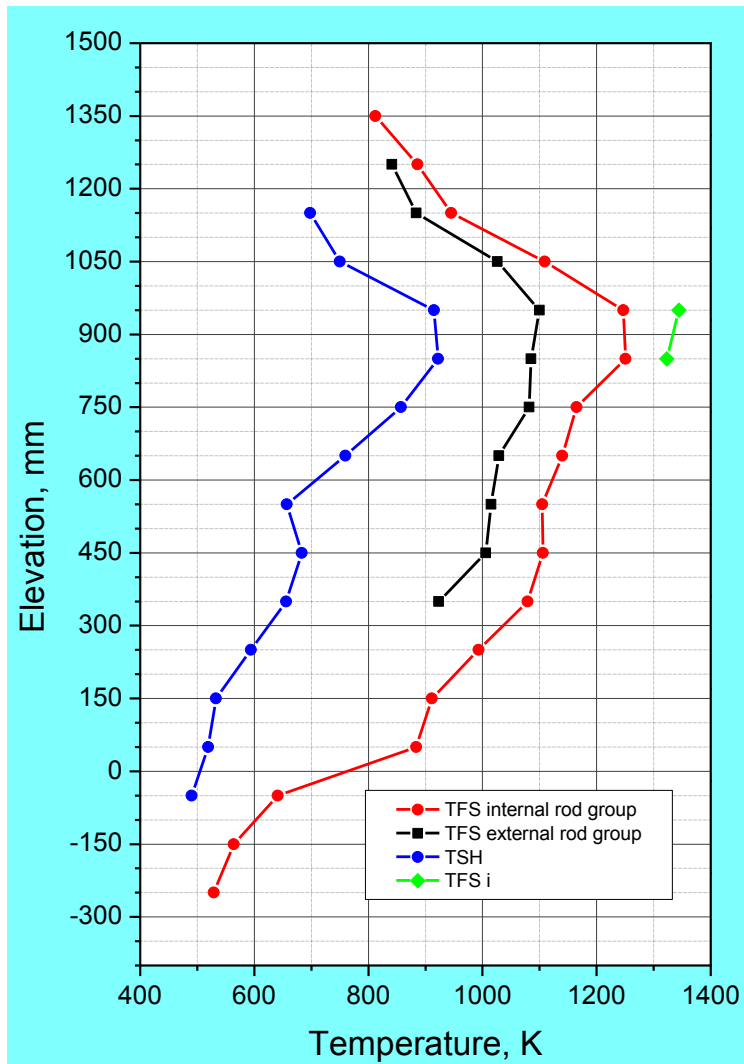
Figure 43   QUENCH-L2; Axial temperature profile TFS internal and external rod group together with TSH, left, and axial temperature profile of all TFS, right, at 76 s (before end of transient).
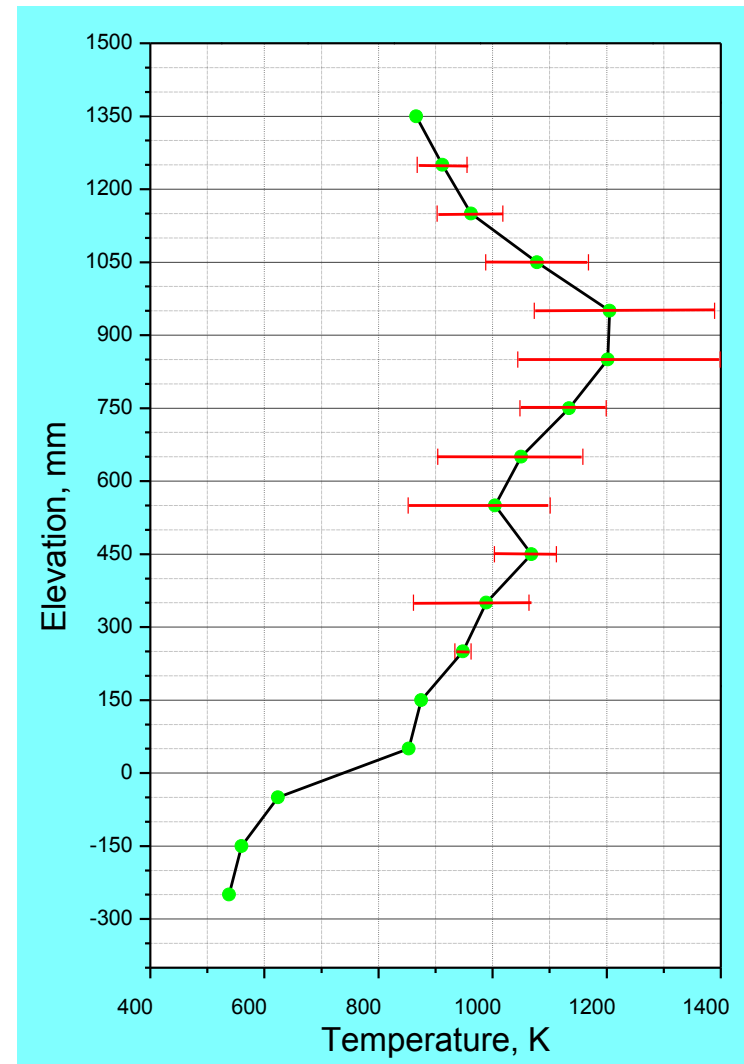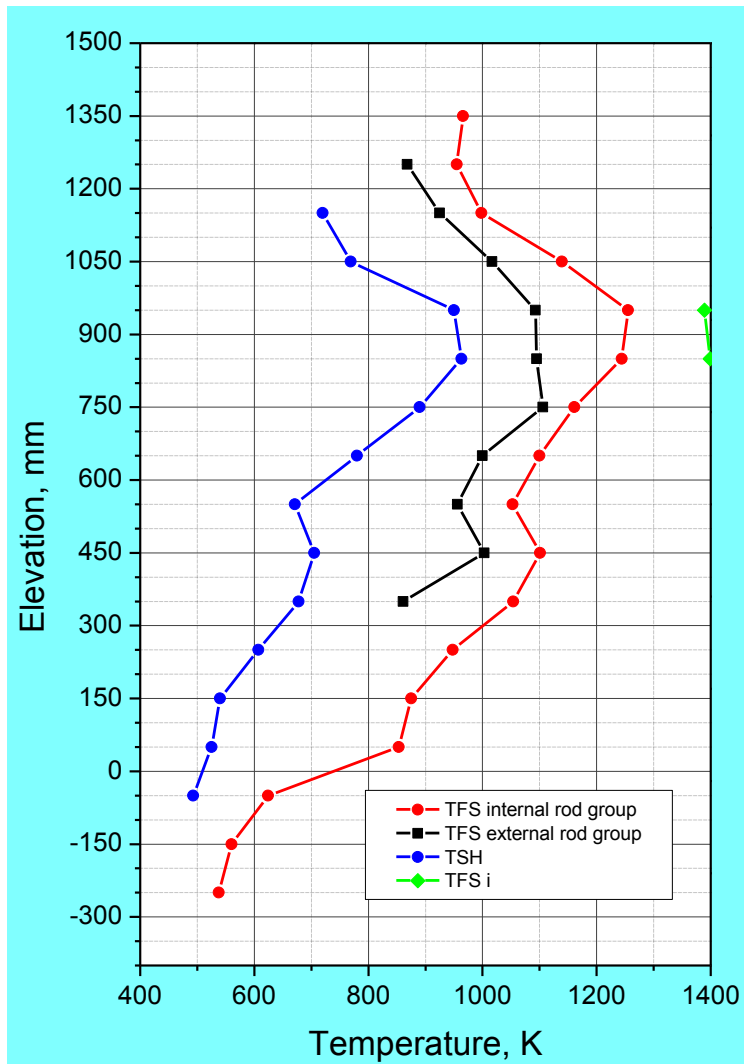
Figure 44   QUENCH-L2; Axial temperature profile TFS internal and external rod group together with TSH, left, and axial temperature profile of all TFS, right, at 84 s (max temperature at 900 mm).
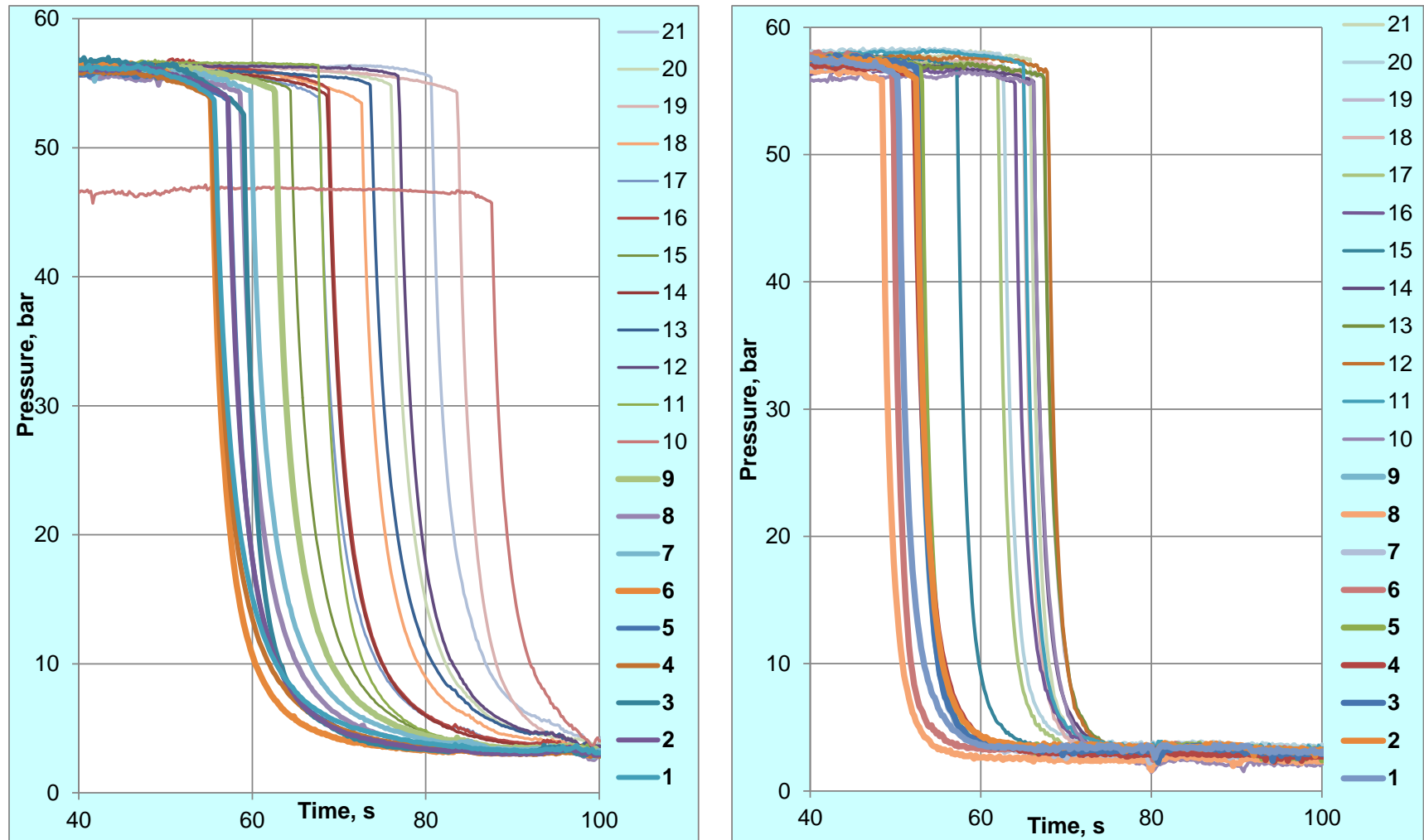
Figure 45   QUENCH-L2; Rod pressure evolution during heating phase for QUENCH-L1 and -L2.
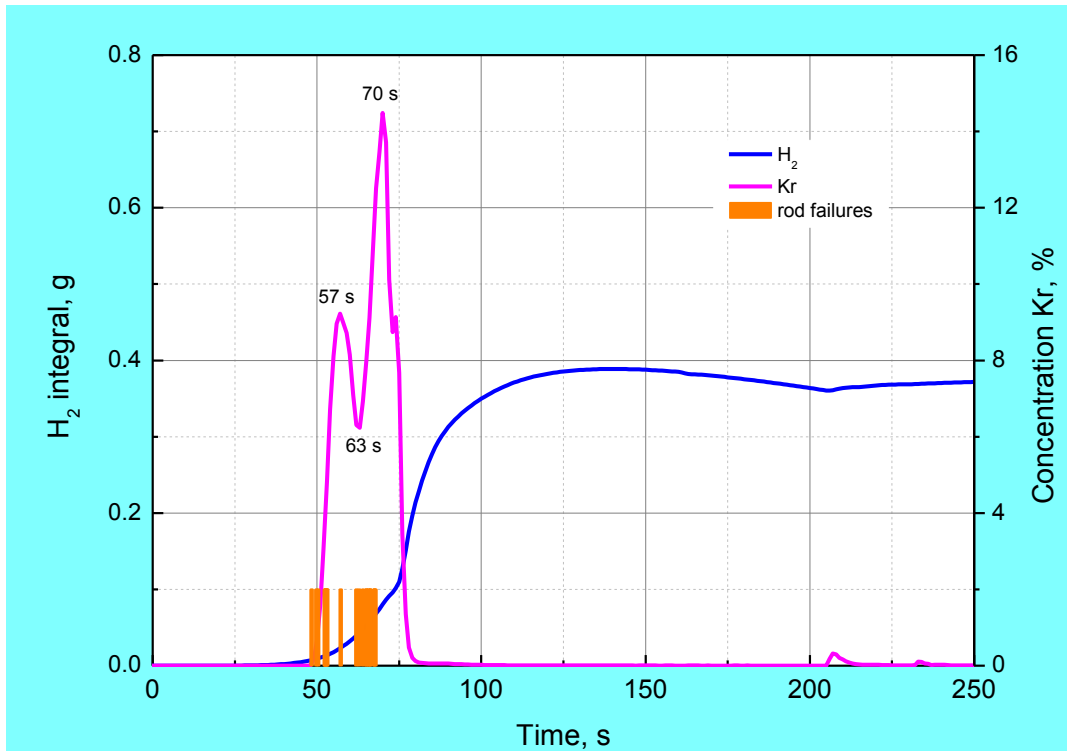
Figure 46   QUENCH-L2; Mass spectrometer measurements: integral hydrogen release and krypton as burst indicator.
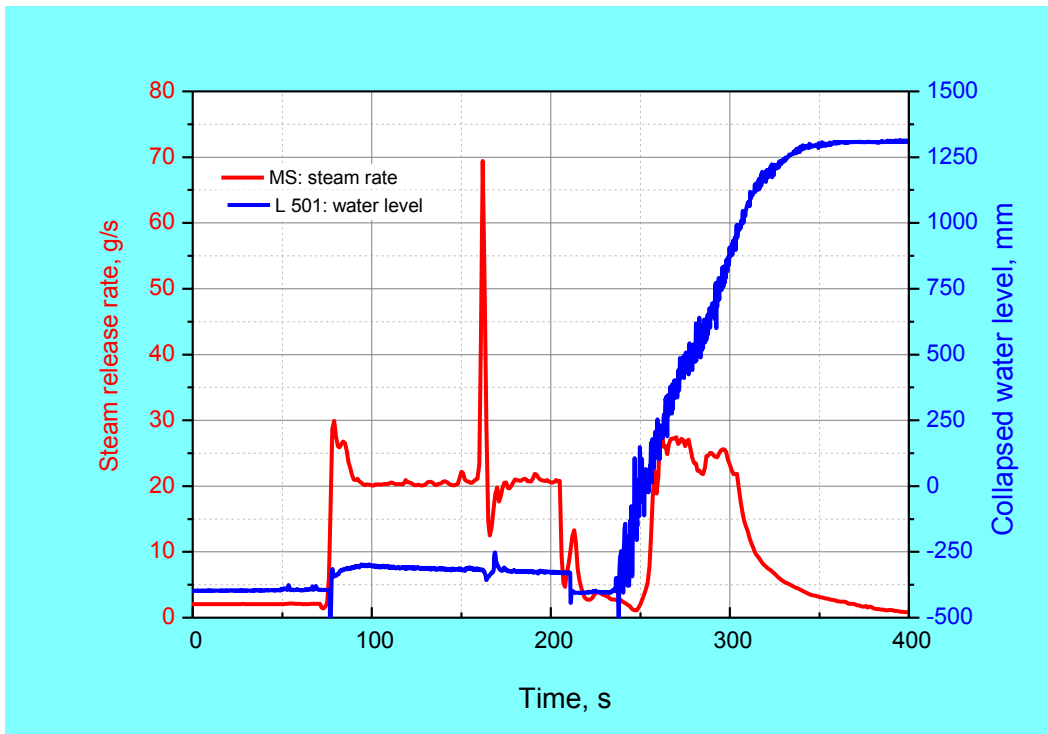
Figure 47   QUENCH-L2; Mass spectrometer measurements: steam during reflood.
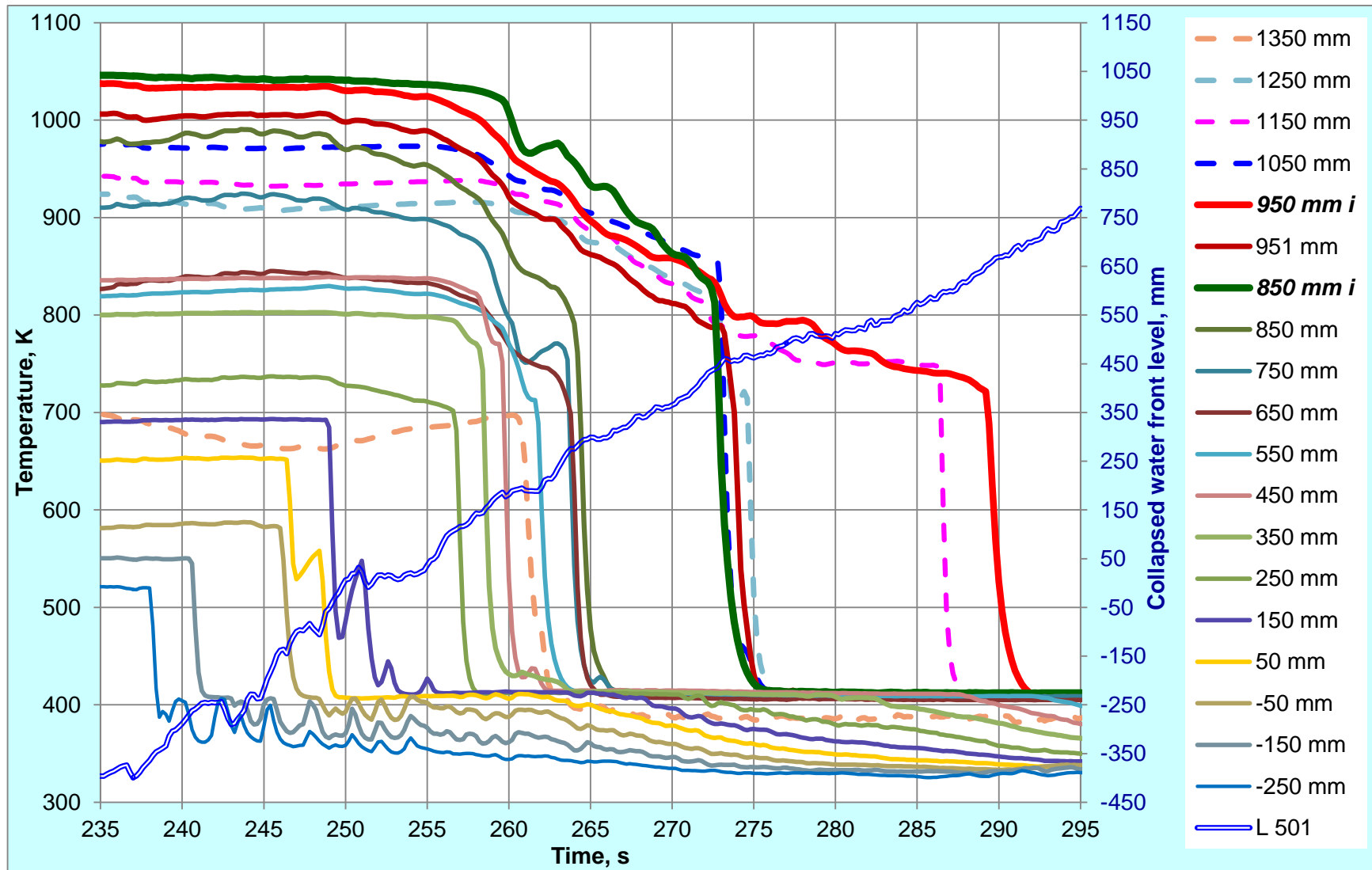
Figure 48   QUENCH-L2; Sequence of wetting of surface thermocouples for rod #7 by 2-phase fluid formed above collapsed water front (L 501).
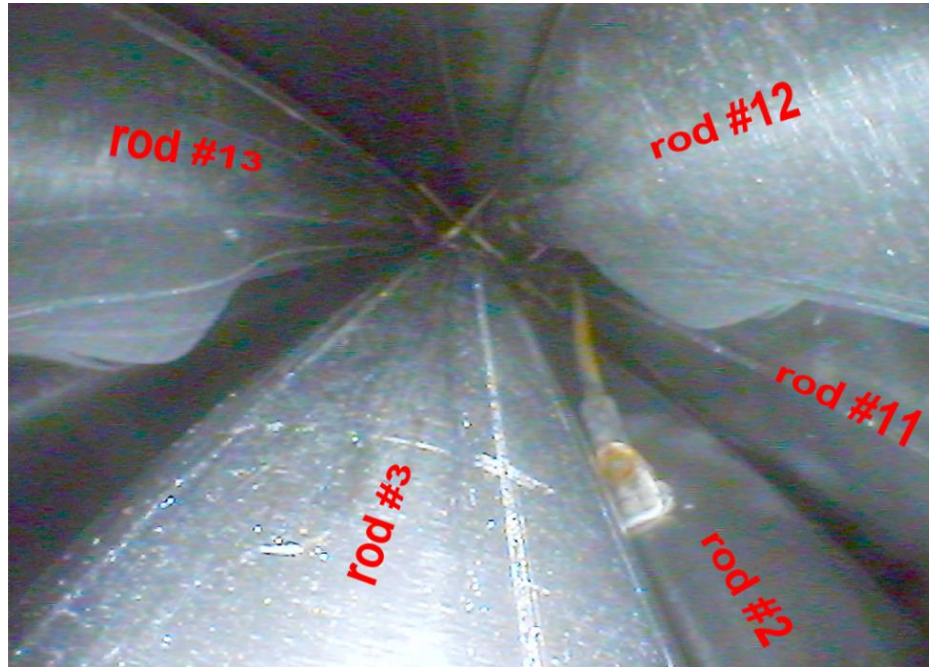
balloning and burst of cladding tubes #12 and #13

at elevation 950 mm;

intact thermocouple TFS 2/13 attached to cladding #2
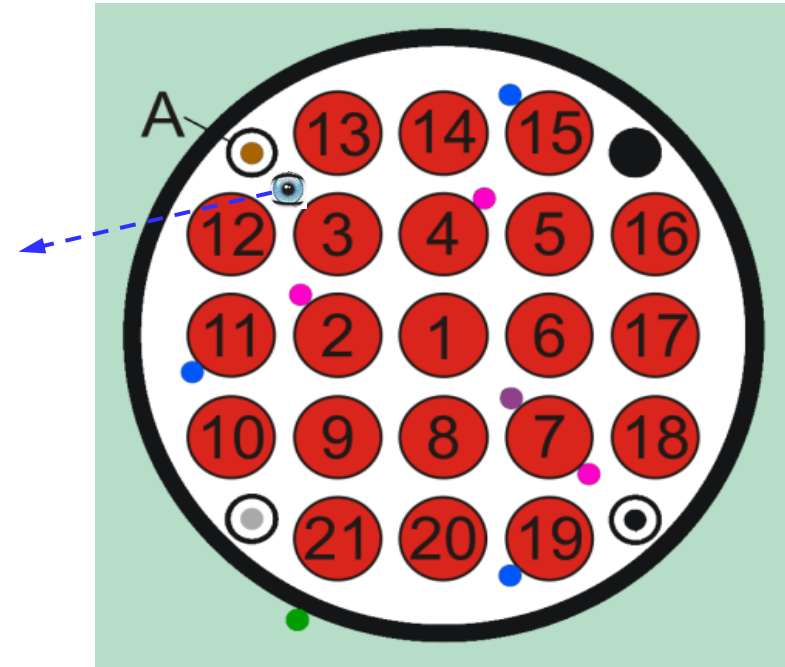
camera location in bundle at the position of

withdrawn corner rod A;

bundle top view

Figure 49   QUENCH-L2; videoscope observations with camera inserted from the bundle bottom at position of corner rod A.
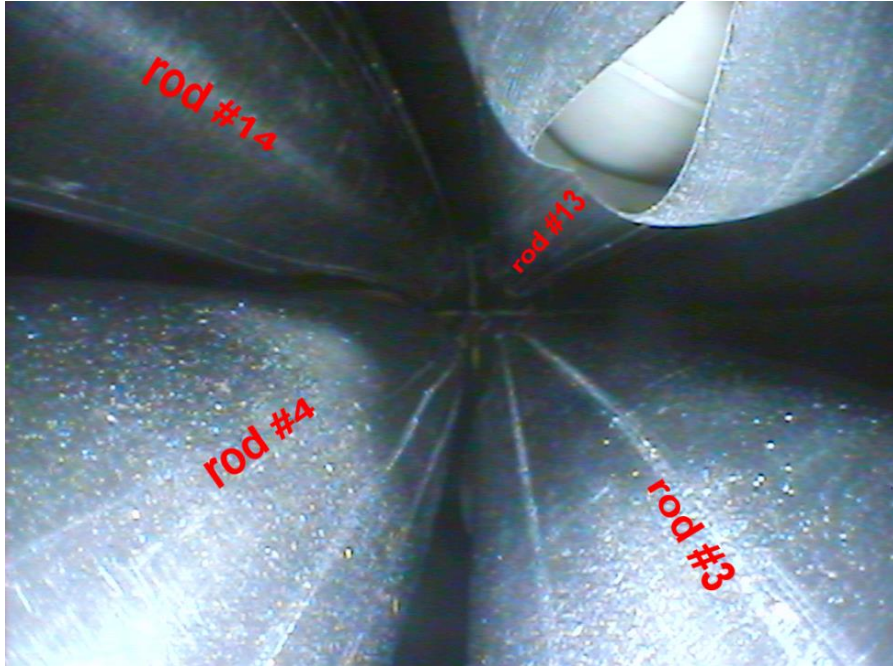
pellets under burst opening of cladding #13

at elevation 950 mm
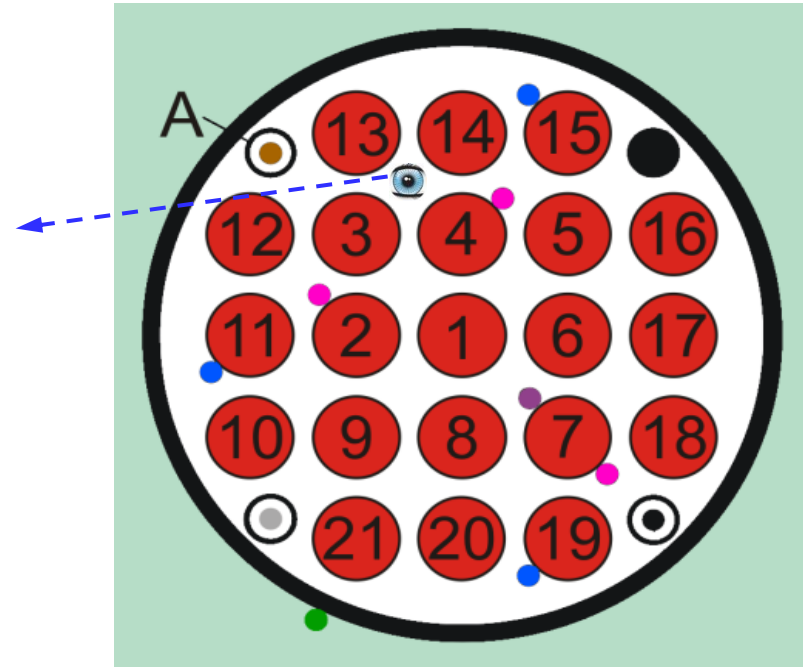
camera location in bundle;

bundle top view

Figure 50   QUENCH-L2; videoscope observations with camera inserted from the bundle bottom at position of corner rod A and threaded between rods #13 and #3.
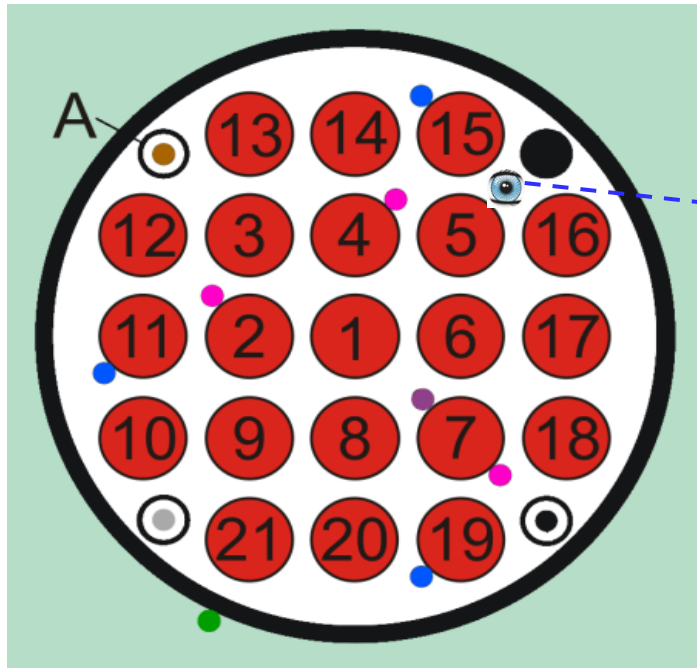
camera location in bundle;

bundle top view
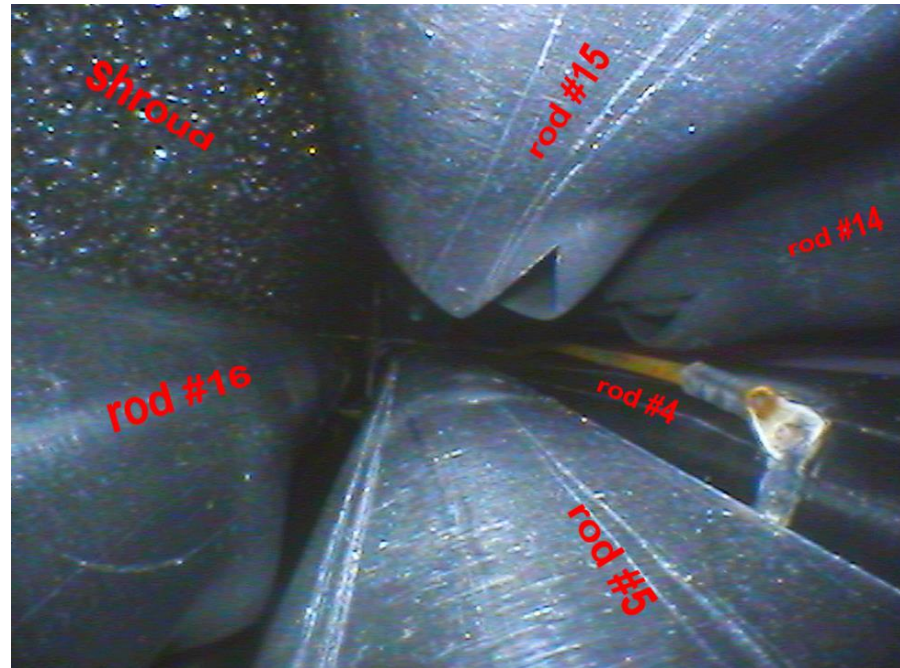
ballooning and burst of cladding tubes #14, #15 and #16 at elevation 950 mm;

intact thermocouple TFS 4/13 attached to cladding #4

Figure 51   QUENCH-L2; videoscope observations with camera inserted from the bundle bottom at position of corner rod B.

camera location in bundle; bundle top view
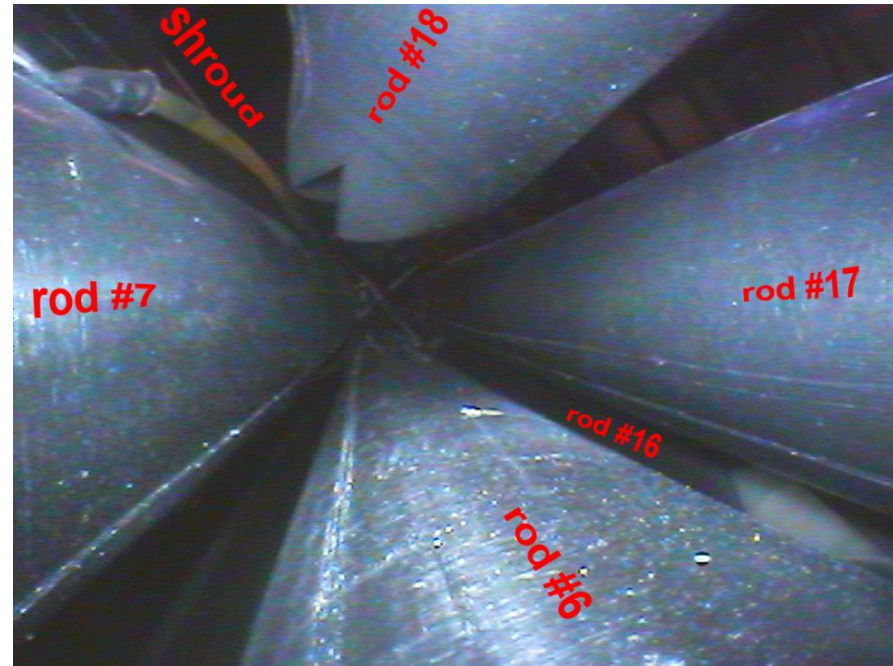
balloning and burst of cladding tubes #18 at elevation 950 mm; intact thermocouple TFS 7/13 attached to cladding #7; pellets under burst opening of cladding #16

Figure 52   QUENCH-L2; videoscope observations with camera inserted from the bundle bottom at position of corner rod C.

ballooning and burst of cladding tubes #10 (top) and #11 (down) at elevation 950 mm;intact thermocouple TFS 2/13 attached to cladding #2 (top)
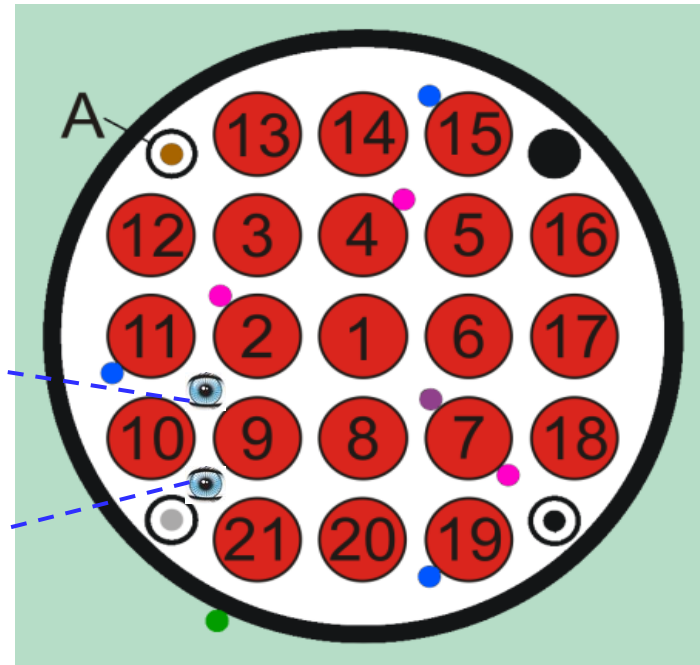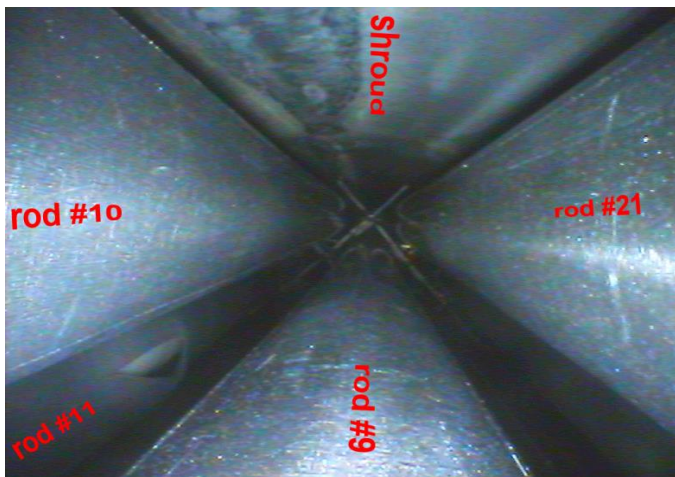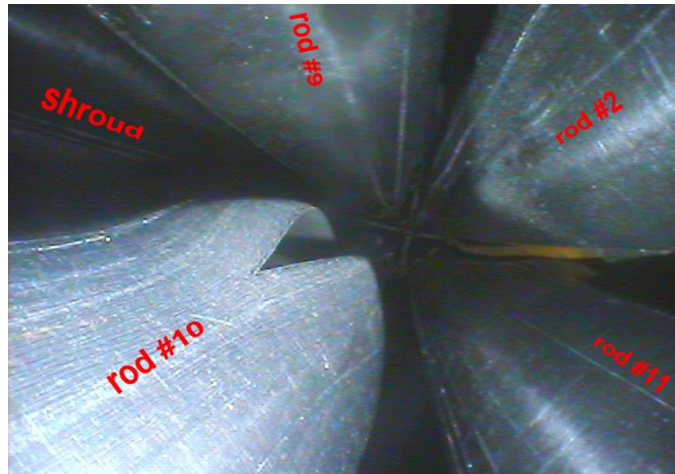
camera location in bundle at the position of withdrawn corner rod D; bundle top view

Figure 53   QUENCH-L2; videoscope observations with camera inserted from the bundle bottom at position of corner rod D.

0°   90°   180°   270°

Figure 54   QUENCH-L2; Post-test bundle view between GS3 and GS4: buckled rods.

GS4

820 mm

GS3

#1: 6 mm   #2: 8 mm   #3: 12 mm   #4: 9   #5: 10 mm   #6: 10   #7: 12   #8: 9   #9: 7 mm
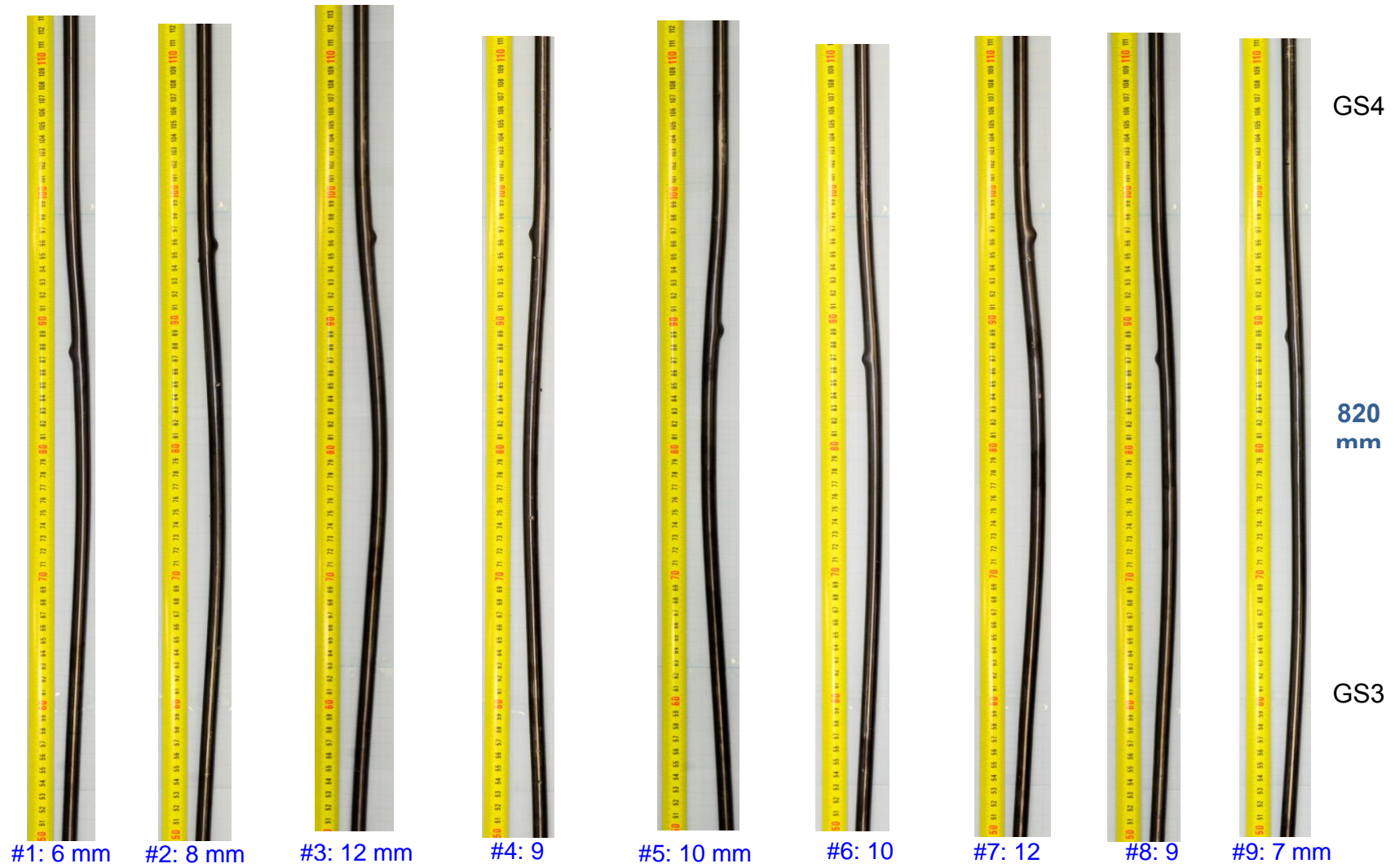
Figure 55   QUENCH-L2; Bending of internal rods with indication of maximal bending for each rod.
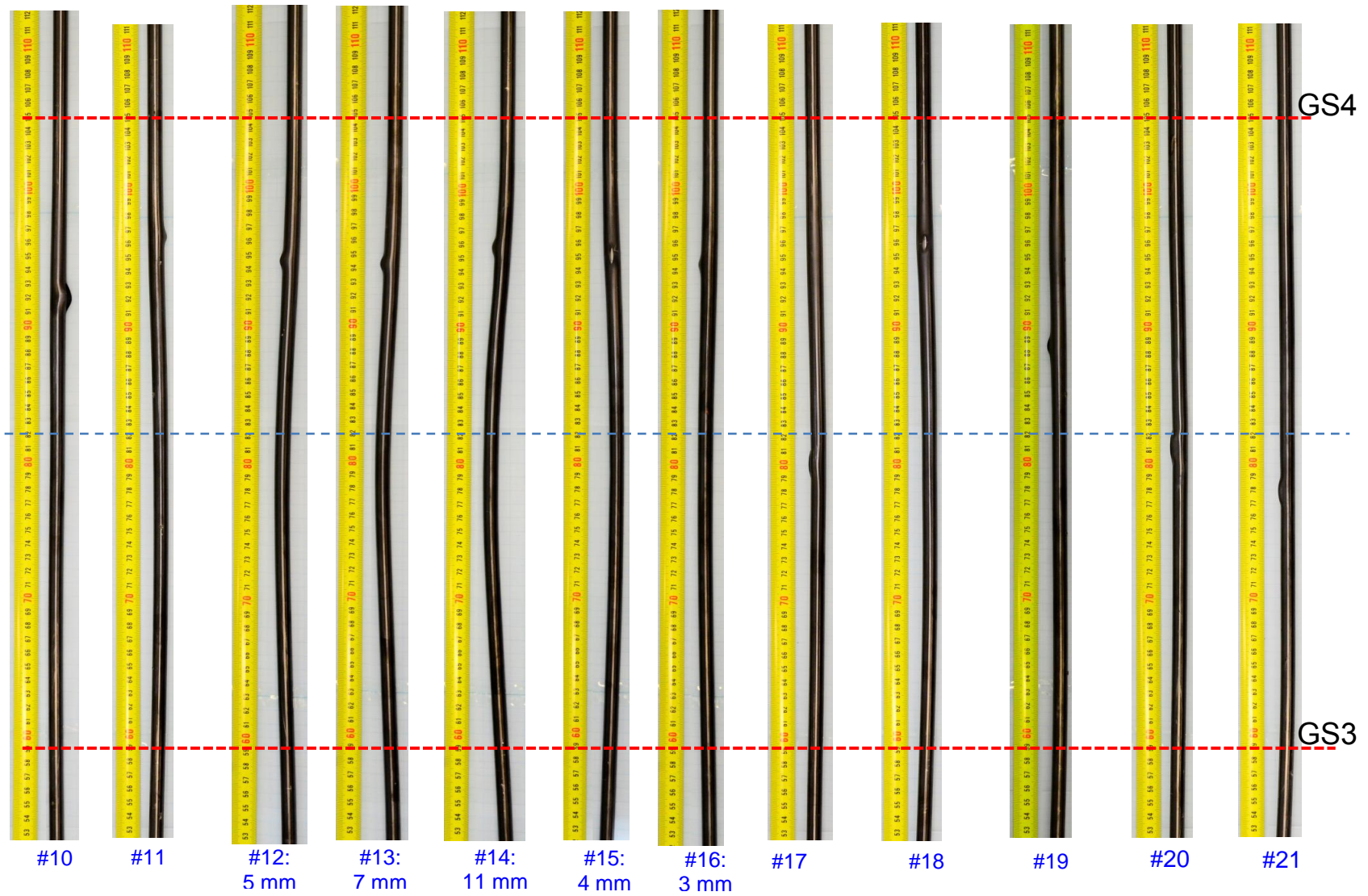
Figure 56   QUENCH-L2; Bending of periphery rods with indication of maximal bending values.
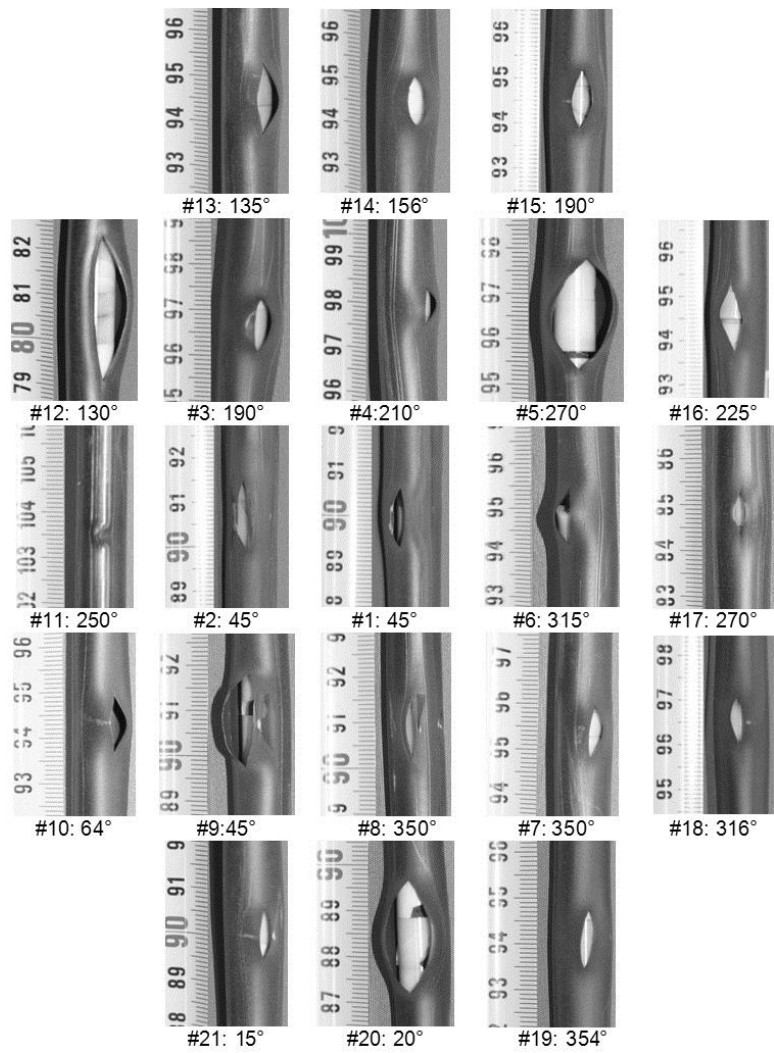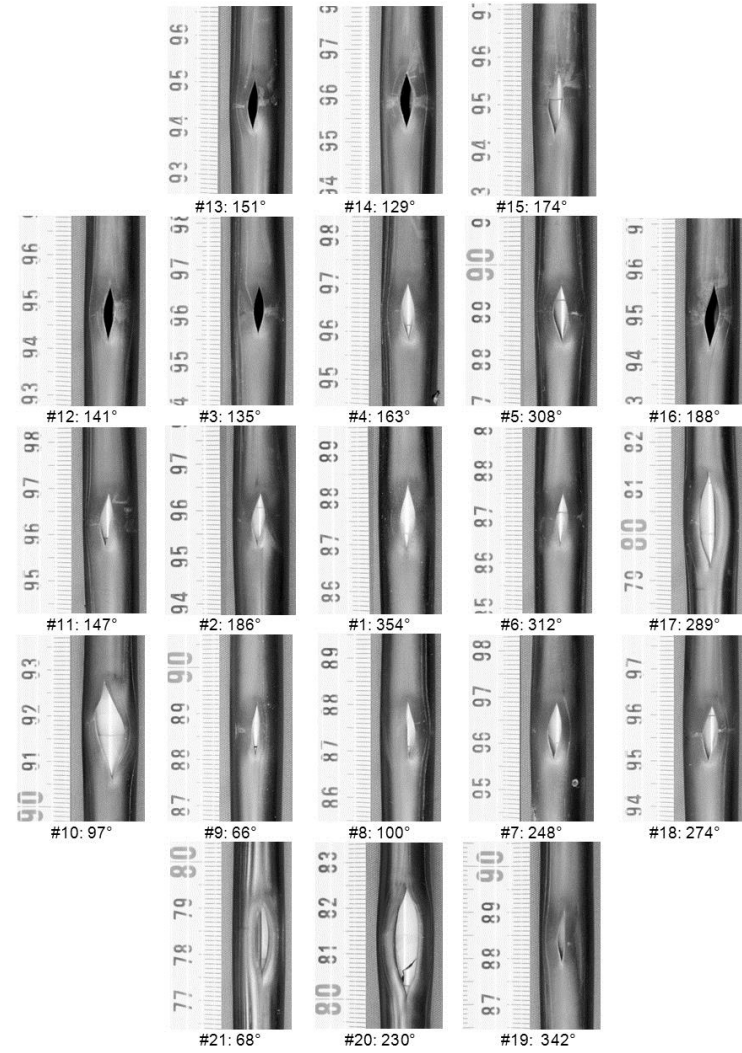
Figure 57   QUENCH-L2; Overview of burst positions.
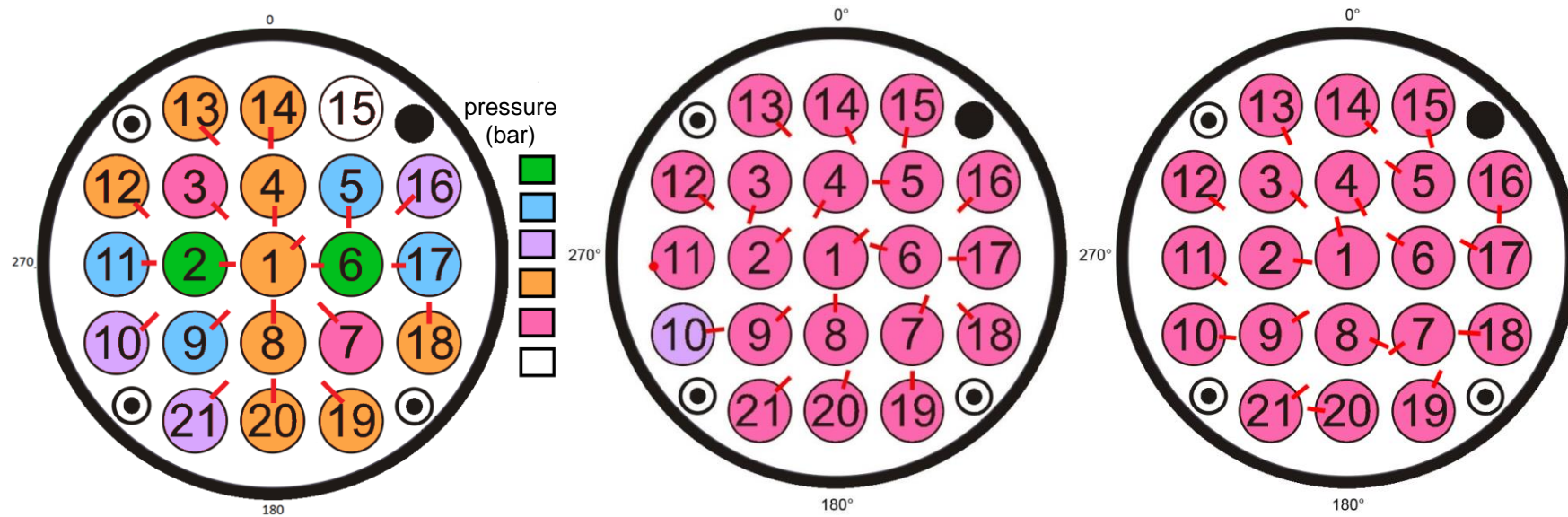
LOCA-0:

openings oriented

to bundle center

due to strong radial T gradient

LOCA-1:

no strong orientation

to bundle center

LOCA-2:

similar to LOCA-1

excluding adjacent rods

7, 8, 20

Figure 58   QUENCH-L2, -L1 and -L0; Comparison of circumferential positions of bursts.
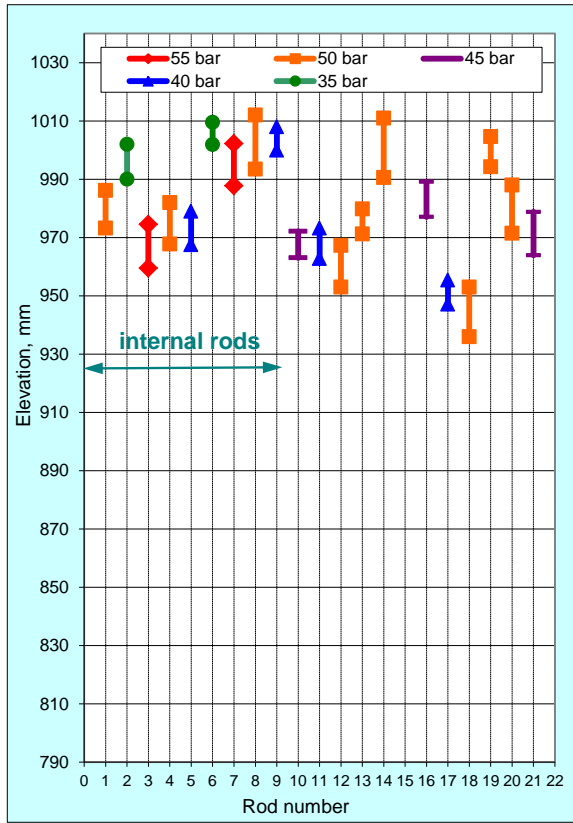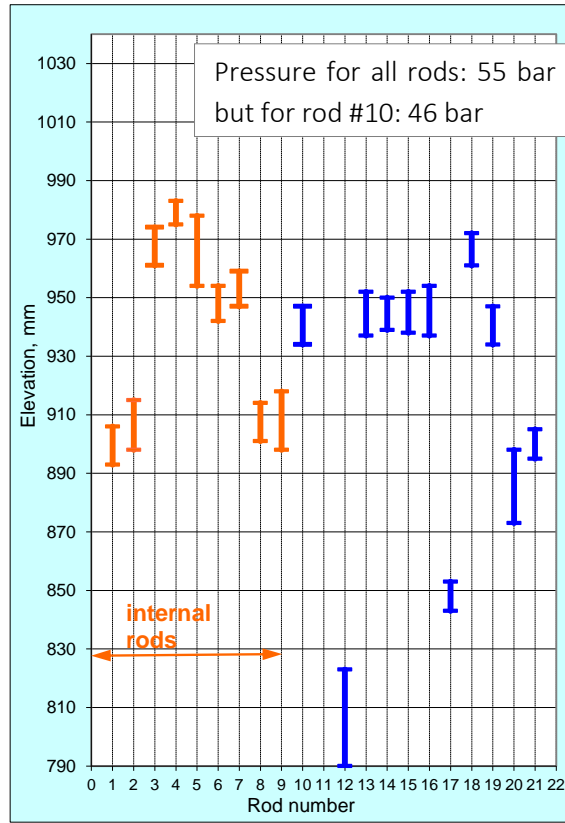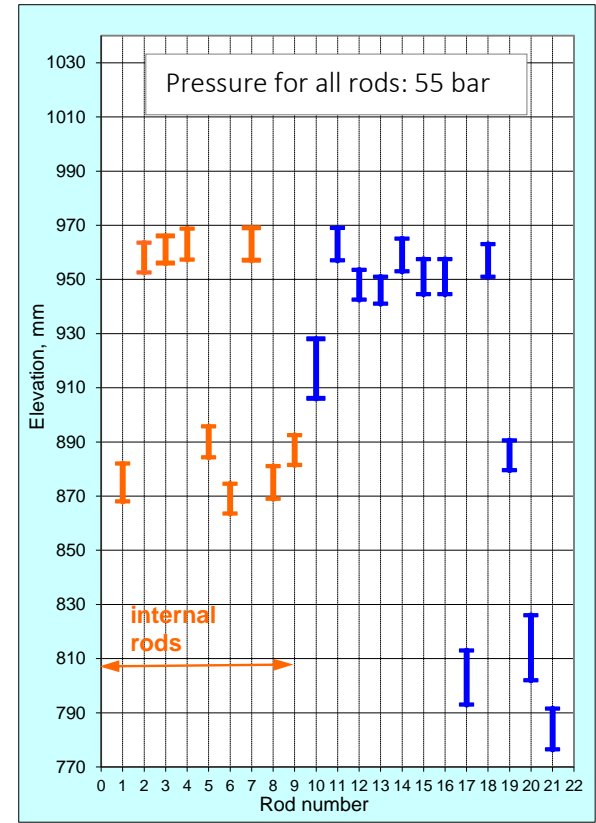
Figure 59   QUENCH-L2, L1, L0; Axial burst positions.
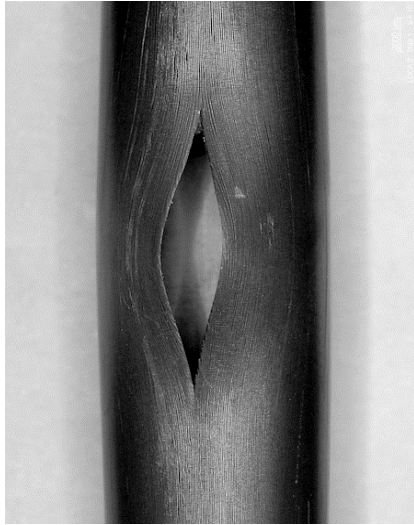
rod #1 at 354°, A_{burst}= 29 mm², w_{burst}=3.4 mm   rod #2 at 186°, A_{burst}= 20 mm², w_{burst}=2.9 mm   rod #3 at 135°, A_{burst}= 15 mm², w_{burst}=2.5 mm
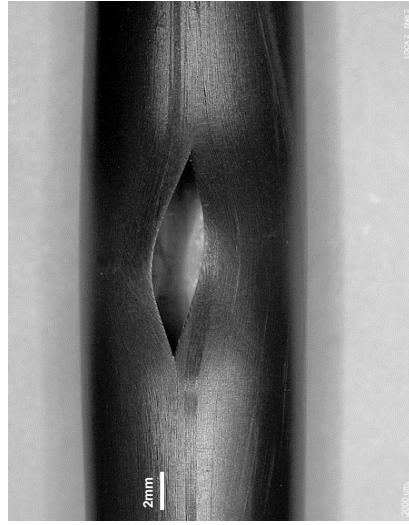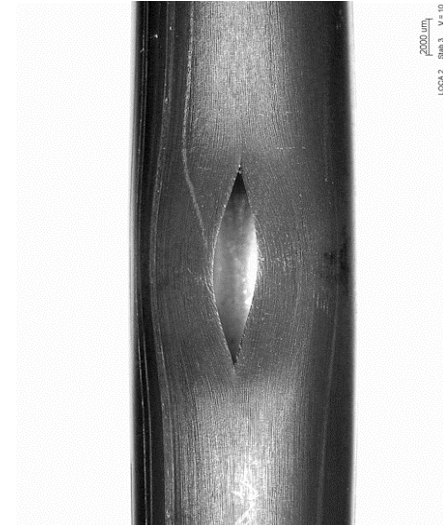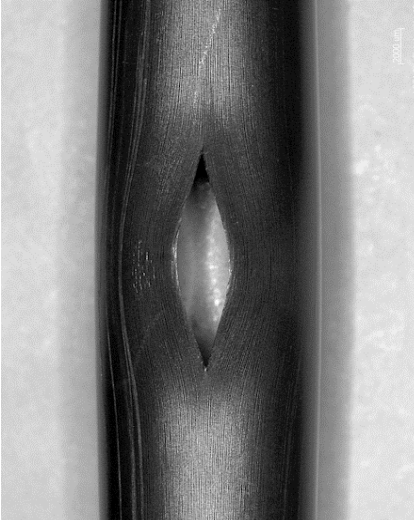
rod #4 at 163°, A_{burst}= 21 mm², w_{burst}=2.9 mm   rod #5 at 308°, A_{burst}= 21 mm², w_{burst}=3.0 mm   rod #6 at 312°, A_{burst}= 17 mm², w_{burst}=2.6 mm
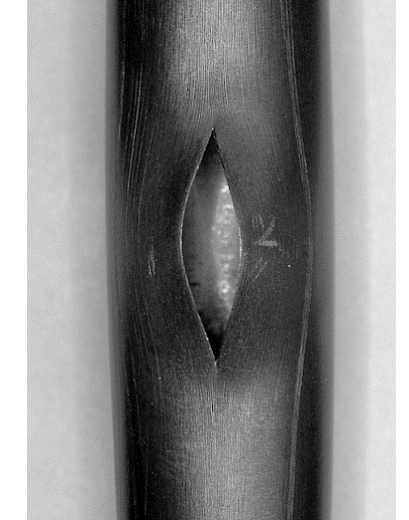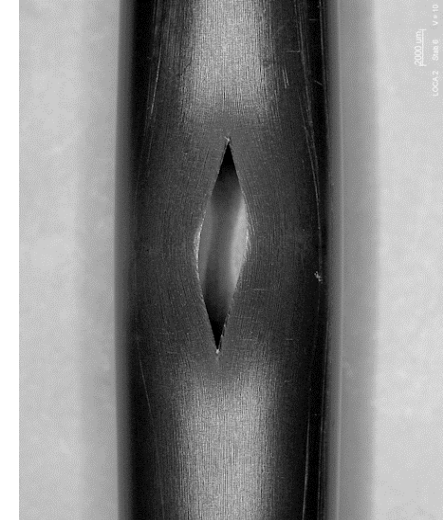
Figure 60   QUENCH-L2; Overview of burst structures of rods #1 - #6.
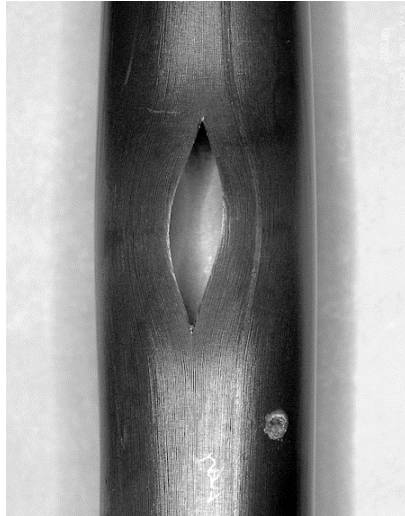
rod #7 at 248°, A_{burst}= 23 mm², w_{burst}=3.1 mm

rod #8 at 100°, A_{burst}= 24 mm², w_{burst}=3.3 mm
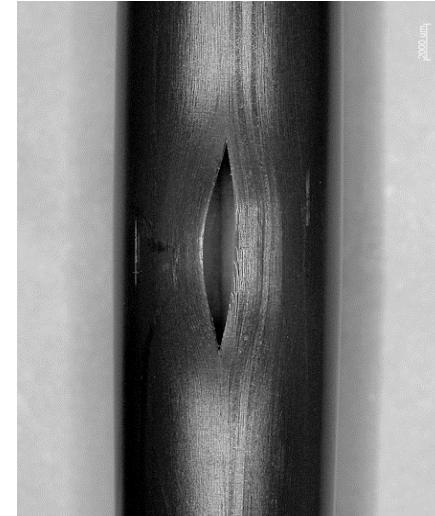
rod #9 at 66°, A_{burst}= 12 mm², w_{burst}=1.7 mm
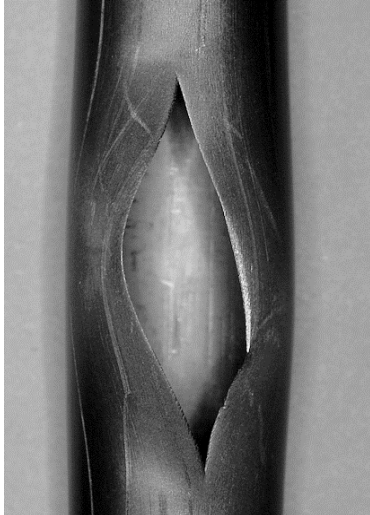
rod #10 at 97°, A_{burst}= 85 mm², w_{burst}=6.6 mm
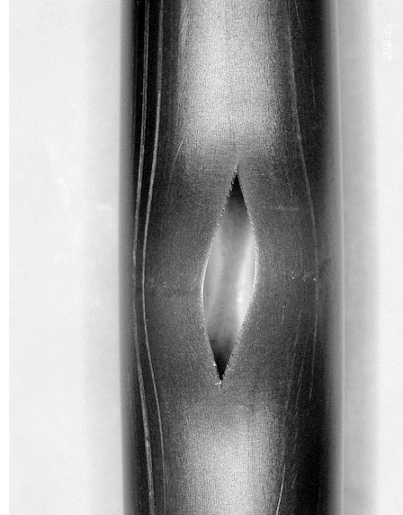
rod #11 at 147°, A_{burst}= 21 mm², w_{burst}=2.8 mm
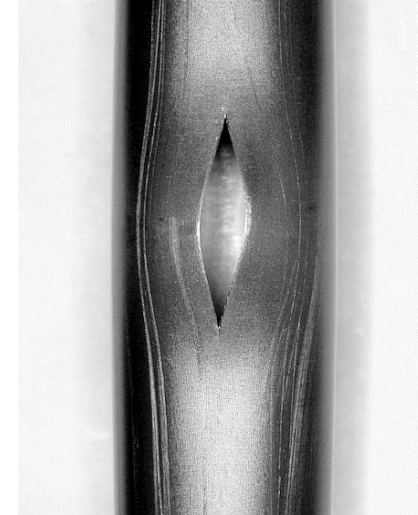
rod #12 at 141°, A_{burst}= 19 mm², w_{burst}=2.5 mm

Figure 61   QUENCH-L2; Overview of burst structures of rods #7 - #12.

rod #13 at 151°, A_{burst}= 15 mm², w_{burst}=2.4 mm rod #14 at 129°, A_{burst}= 23 mm², w_{burst}=3.1 mm rod #15 at 174°, A_{burst}= 25 mm², w_{burst}=2.4 mm
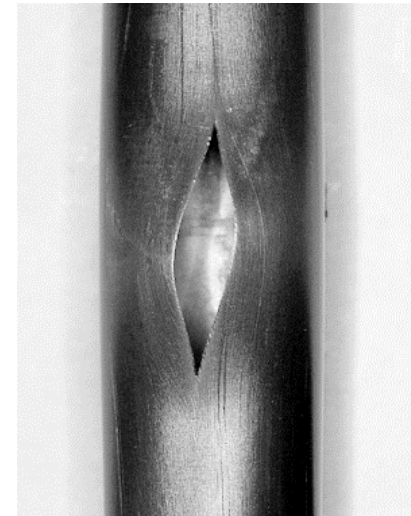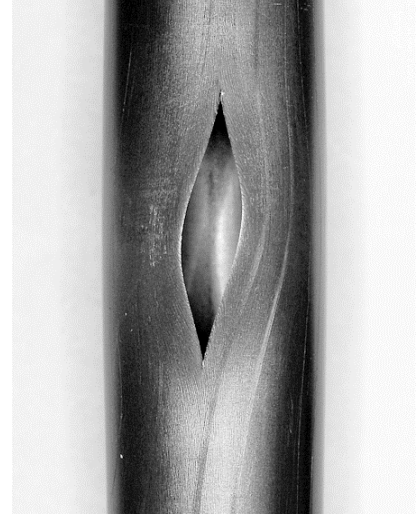
rod #16 at 188°, A_{burst}= 27 mm², w_{burst}=3.4 mm rod #17 at 289°, A_{burst}= 66 mm², w_{burst}=3.9 mm rod #18 at 274°, A_{burst}= 24 mm², w_{burst}=3.3 mm
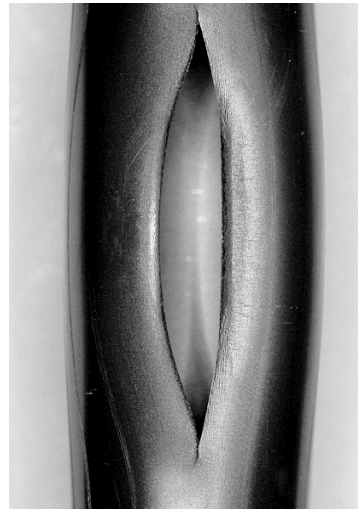
Figure 62   QUENCH-L2; Overview of burst structures of rods #13 - #18.
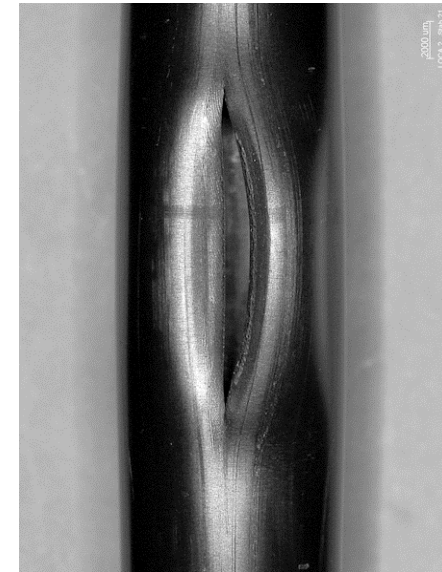
rod #19 at 342°, A_{burst}= 12 mm², w_{burst}=1.8 mm   rod #20 at 230°, A_{burst}= 94 mm², w_{burst}=5.5 mm   rod #21 at 68°, A_{burst}= 16 mm², w_{burst}=1.5 mm

Figure 63   QUENCH-L2; Overview of burst structures of rods #19 - #21.

875 mm, 309°   *875 mm, 354°*   *875 mm, 39°*

880 mm, 309°   880 mm, 354°   880 mm, 39°

875 mm, 309°   875 mm, 15° (cracks are light)   875 mm, 39°

870 mm, 309°   870 mm, 354°   870 mm, 39°
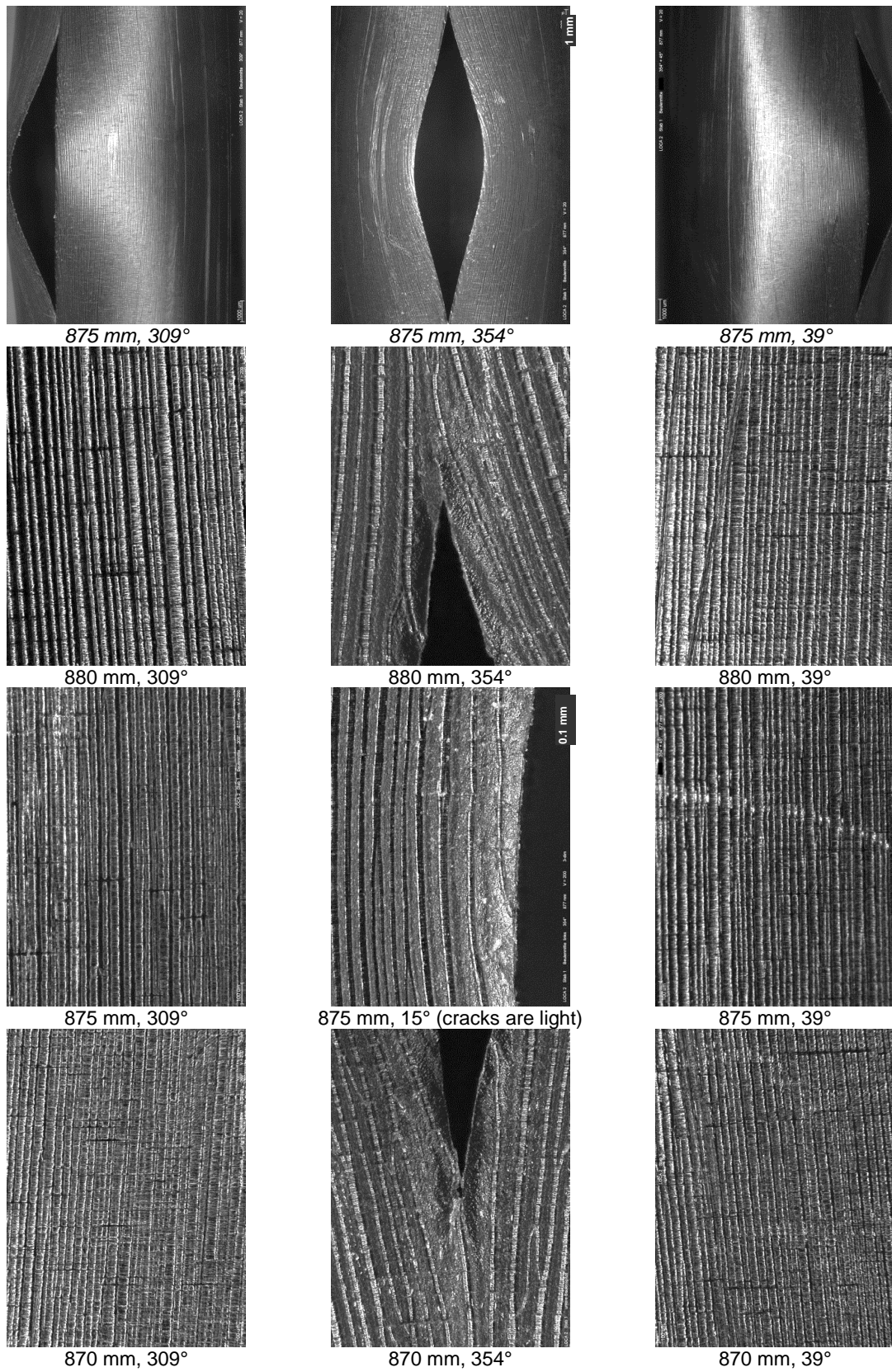
Figure 64   QUENCH-L2; surface cracks (dark stripes) inside of outer oxide layer of rod #1 at burst.

scanner facility

reconstructed sc
angle step 1°; axial step (
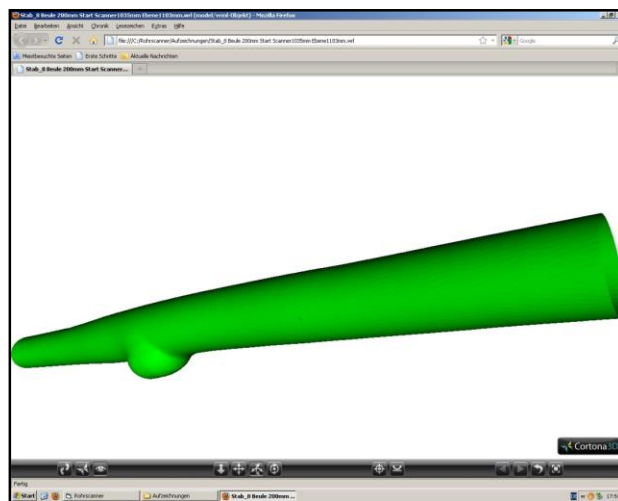
reconstructed scanned surface of rod #8:
angle step 1°; axial step 0.5 mm; scanned length 200 mm

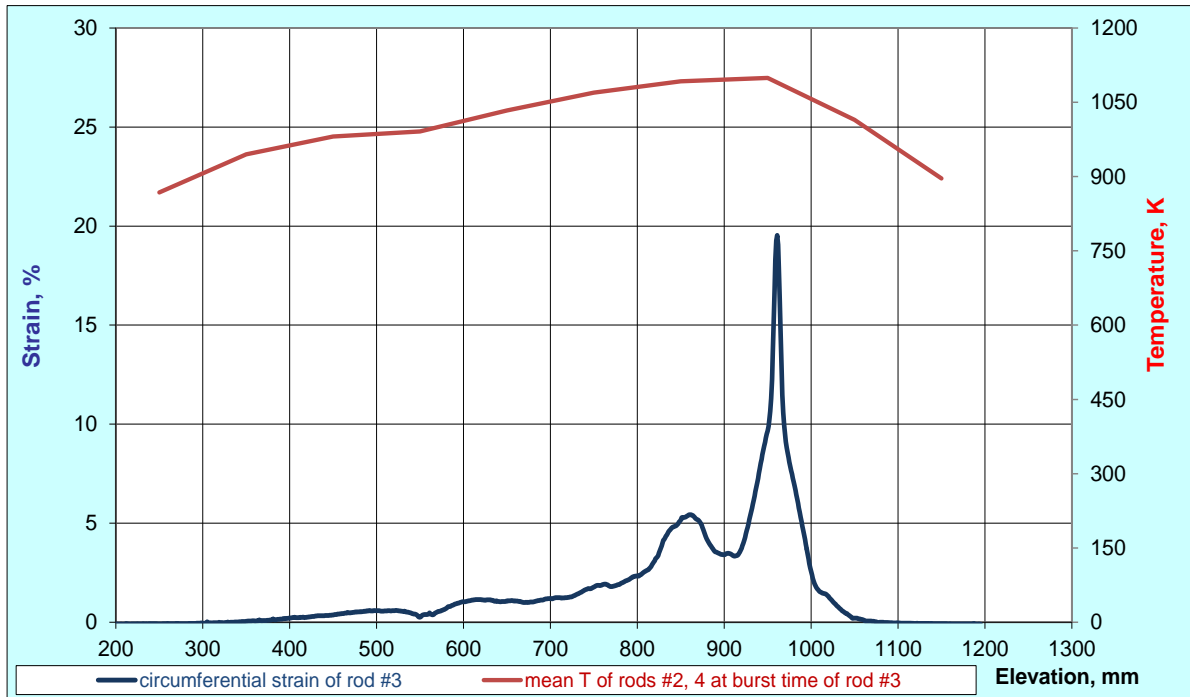Figure 65   QUENCH-L2; Tube scanner laser profilometry.
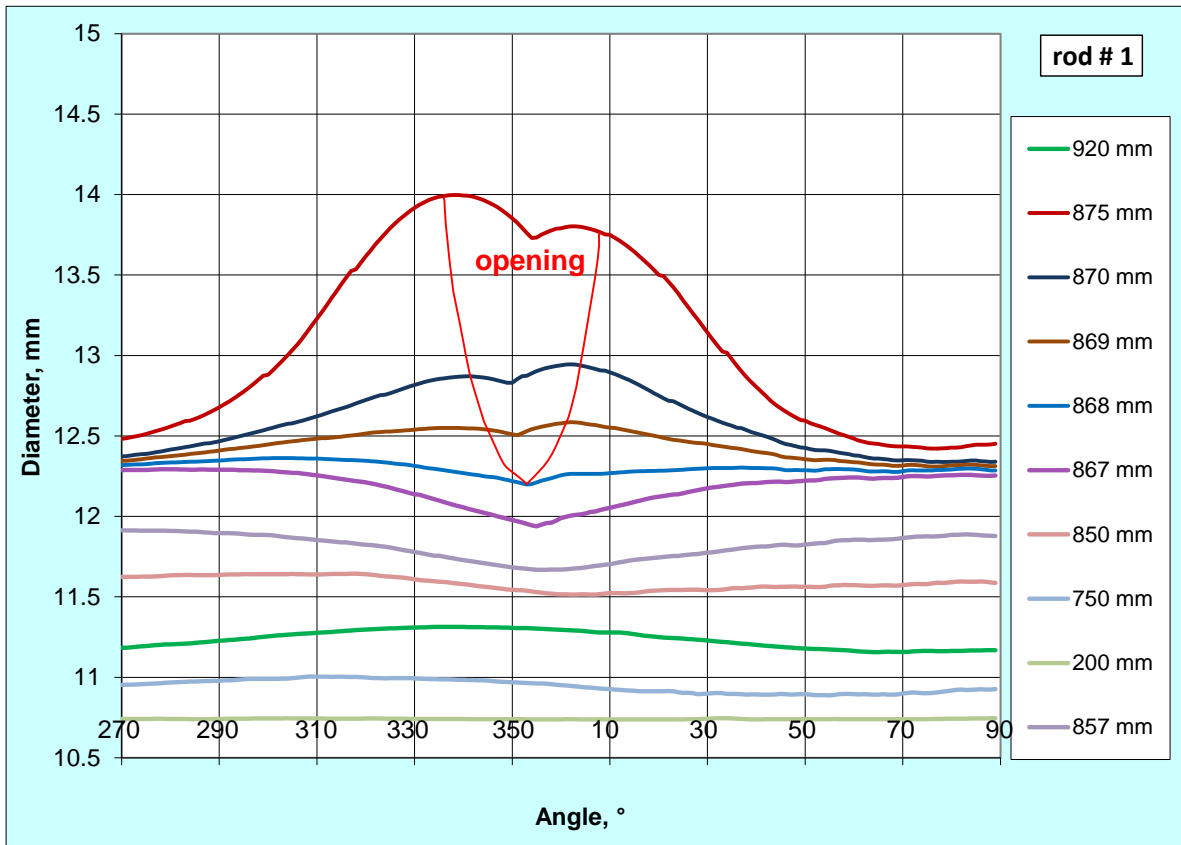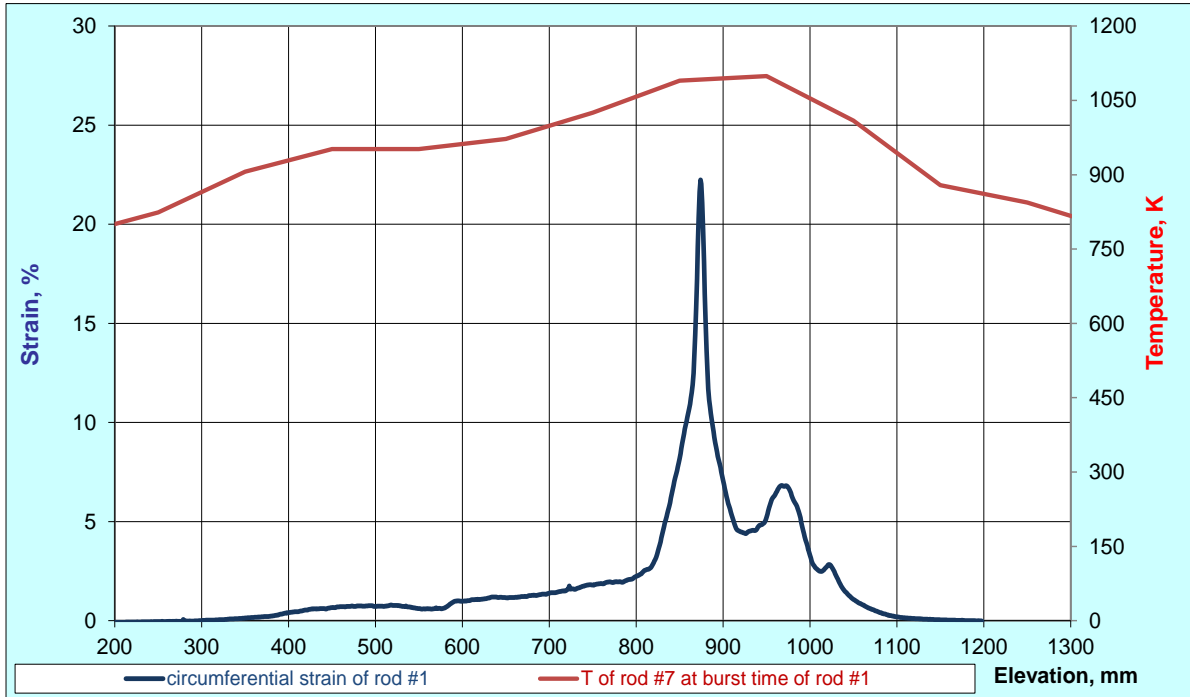
Figure 66   QUENCH-L2, Rod #1; longitudinal changing of circumferential strain (top); azimuthal diameter downwards from burst (bottom).
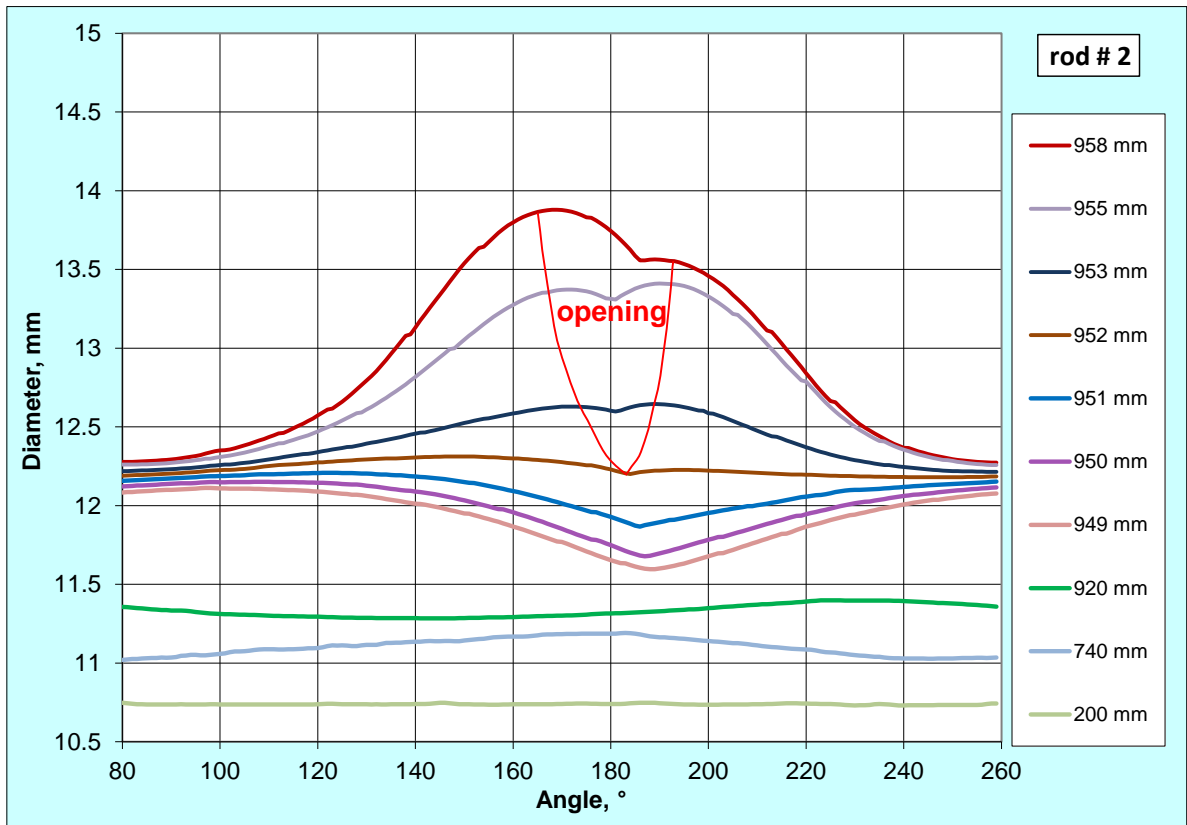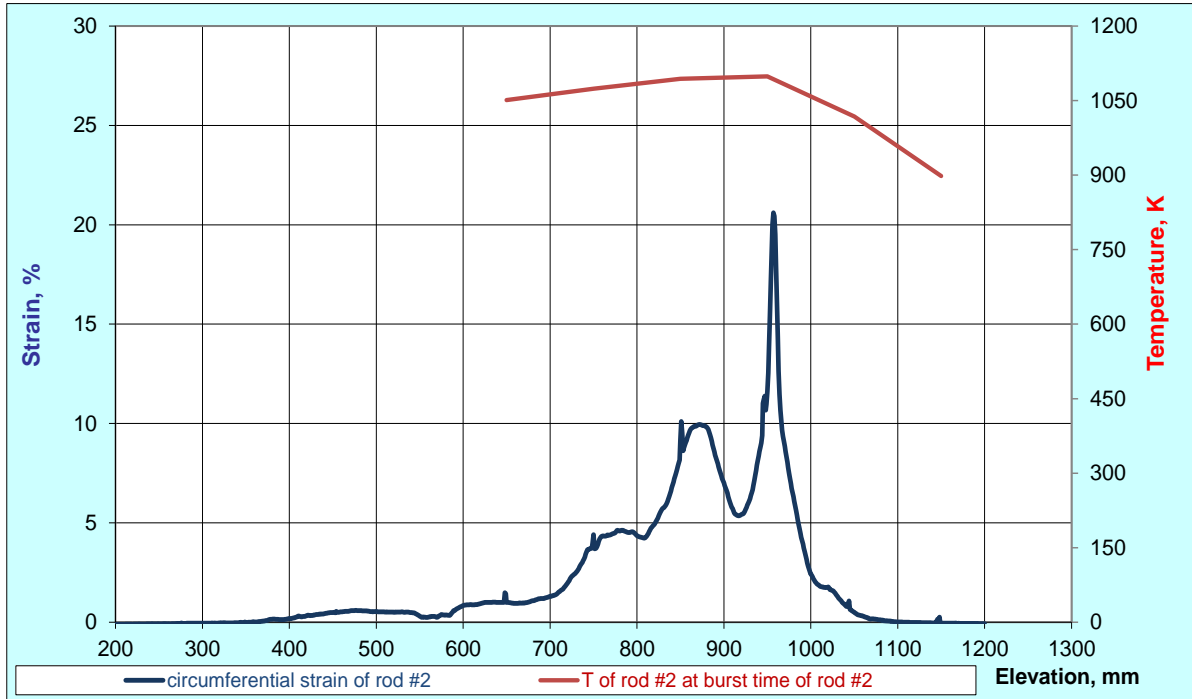
Figure 67   QUENCH-L2, Rod #2; longitudinal changing of circumferential strain (top); azimuthal diameter
downwards from burst (bottom).
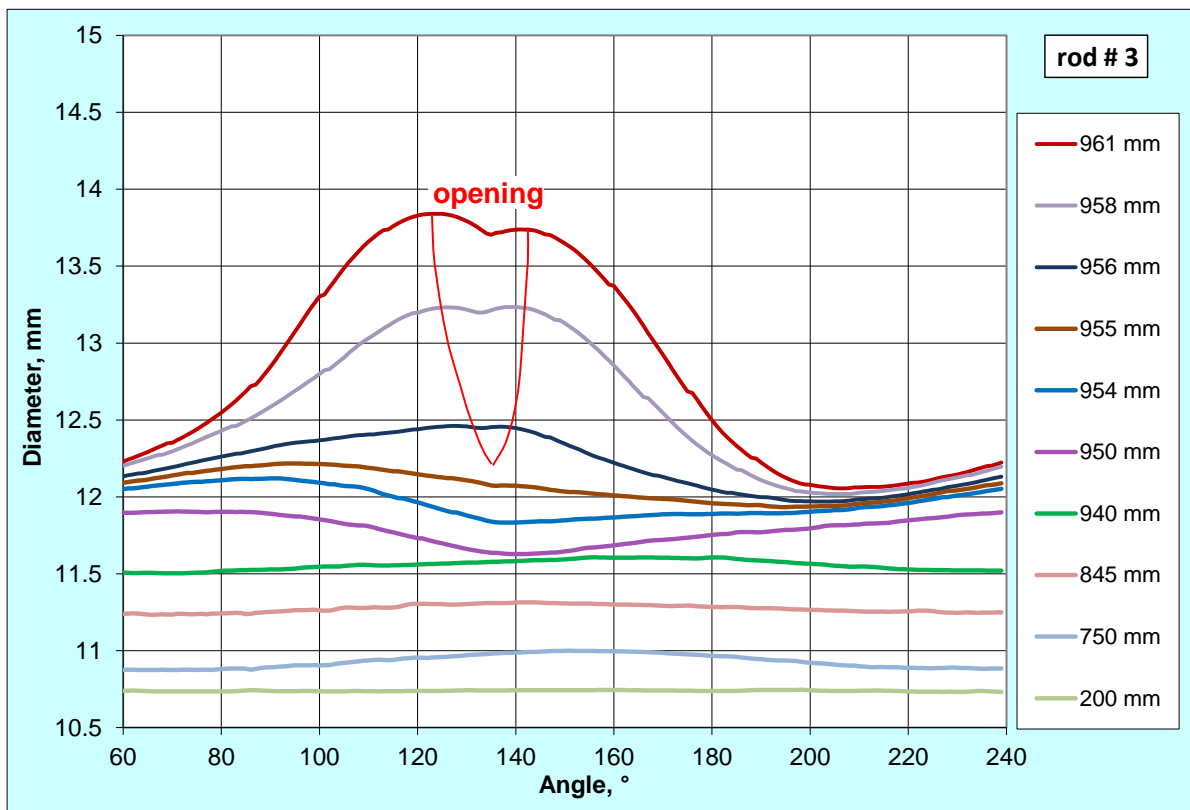
Figure 68   QUENCH-L2, Rod #3; longitudinal changing of circumferential strain (top); azimuthal diameter downwards from burst (bottom).
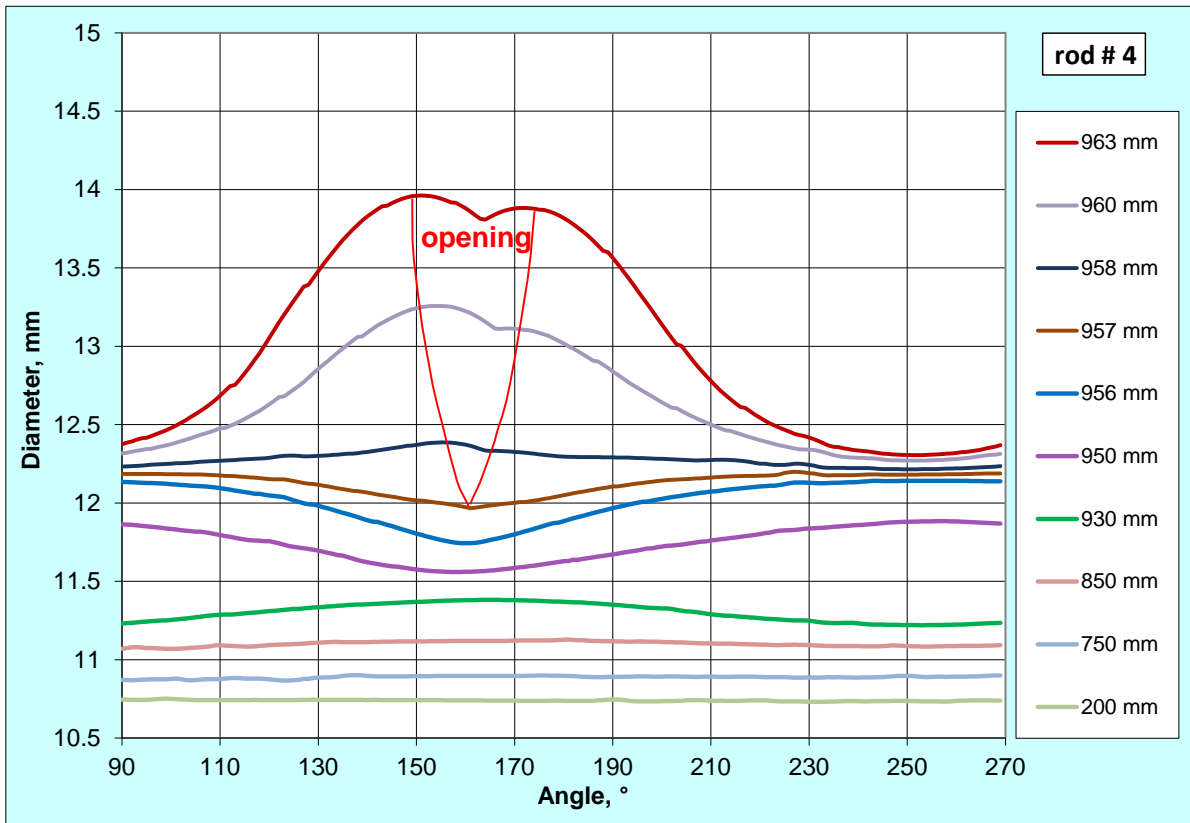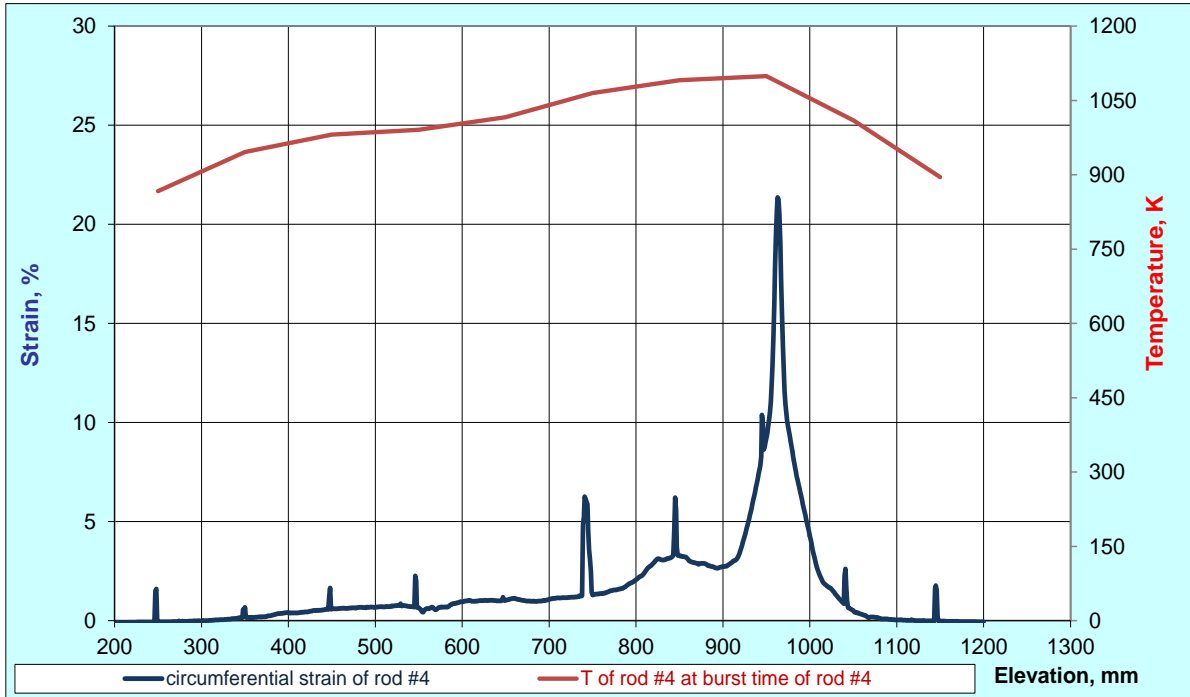
Figure 69   QUENCH-L2, Rod #4; longitudinal changing of circumferential strain (top); azimuthal diameter downwards from burst (bottom). Spikes: thermocouple.
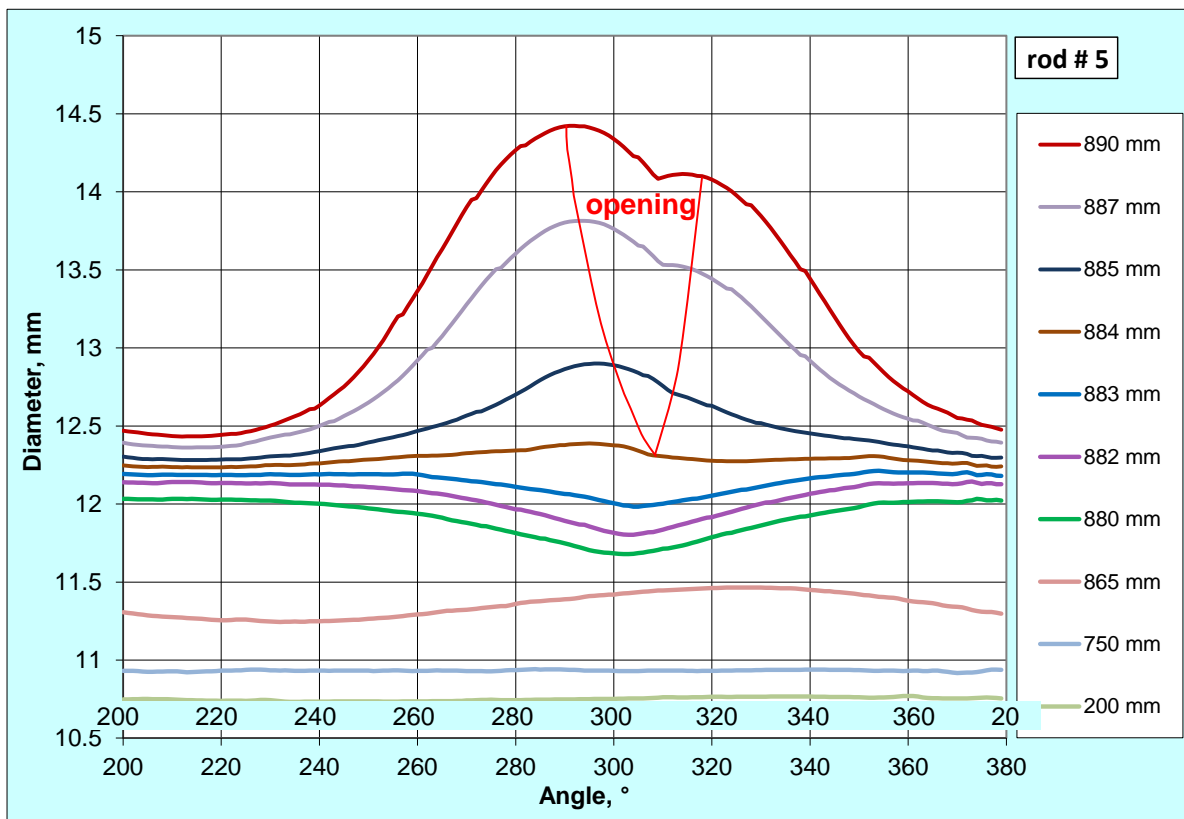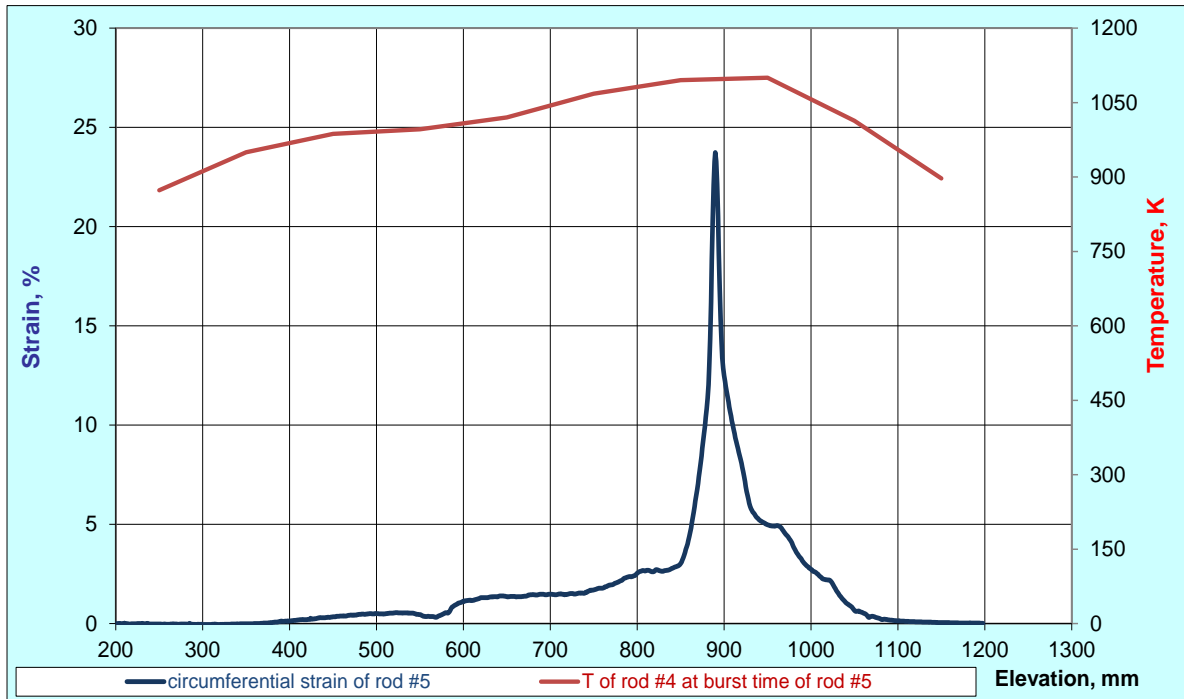
Figure 70   QUENCH-L2, , Rod #5; longitudinal changing of circumferential strain (top); azimuthal diameter downwards from burst (bottom).
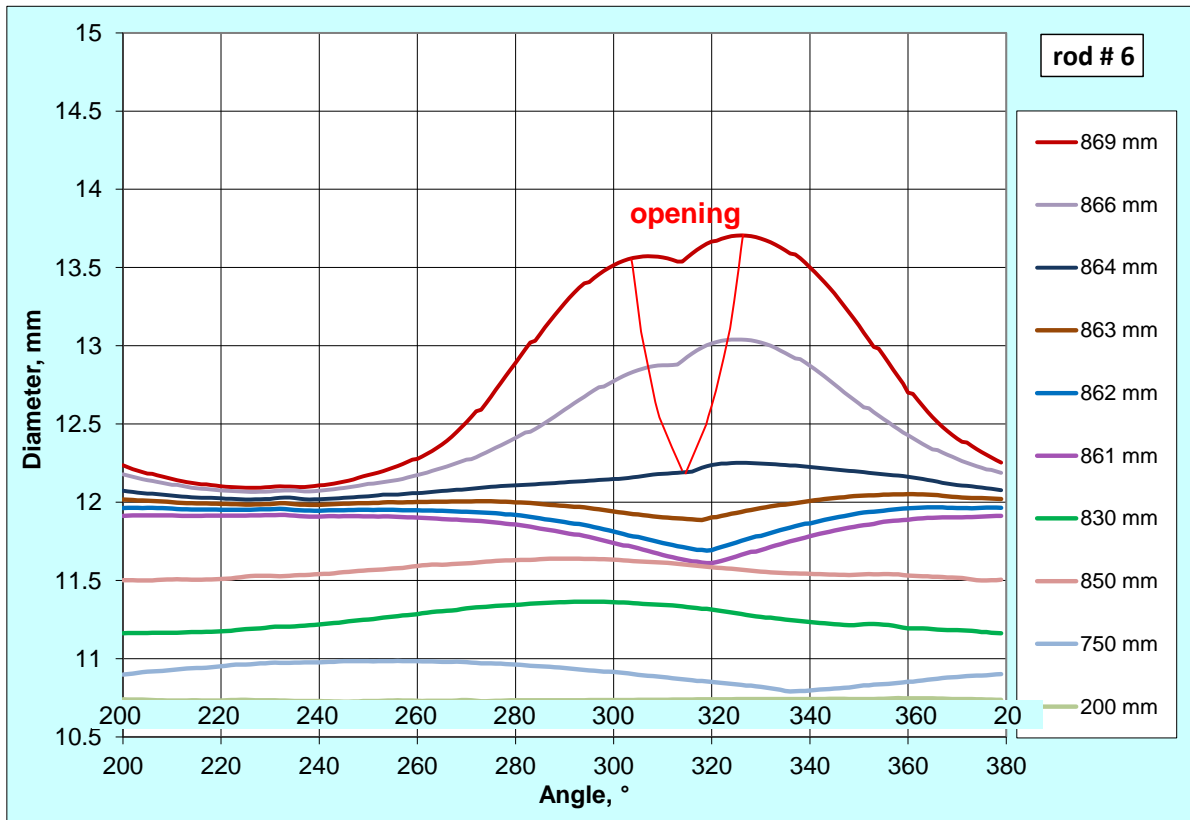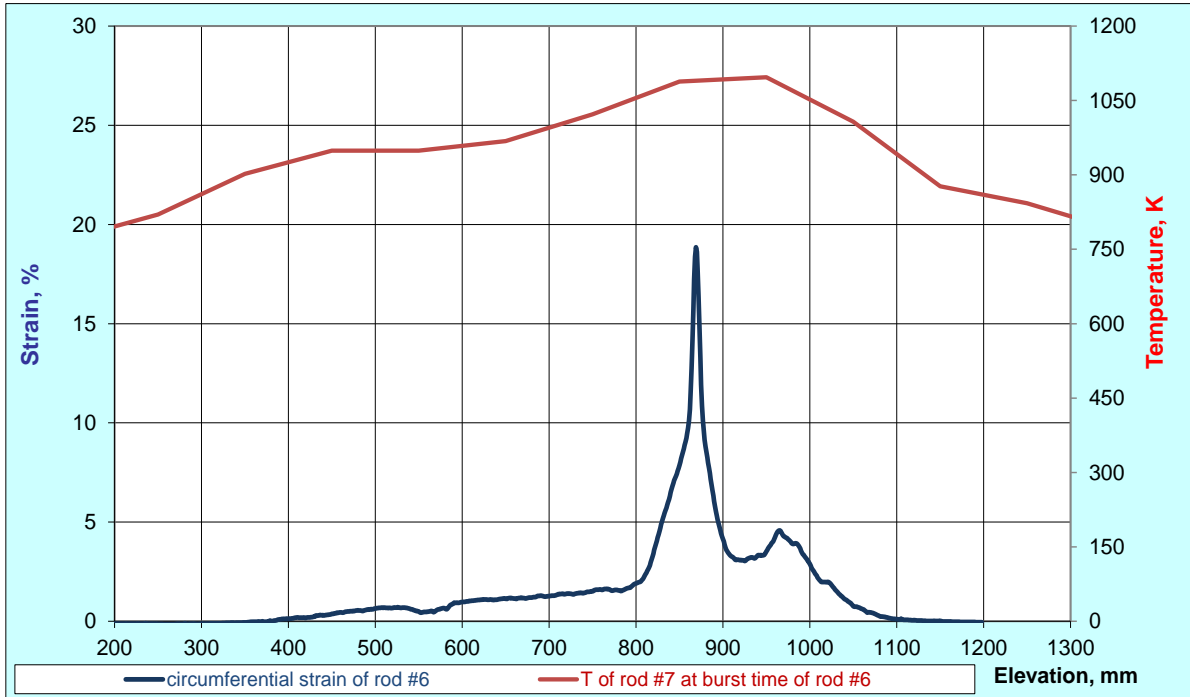
Figure 71   QUENCH-L2, Rod #6; longitudinal changing of circumferential strain (top); azimuthal diameter downwards from burst (bottom).
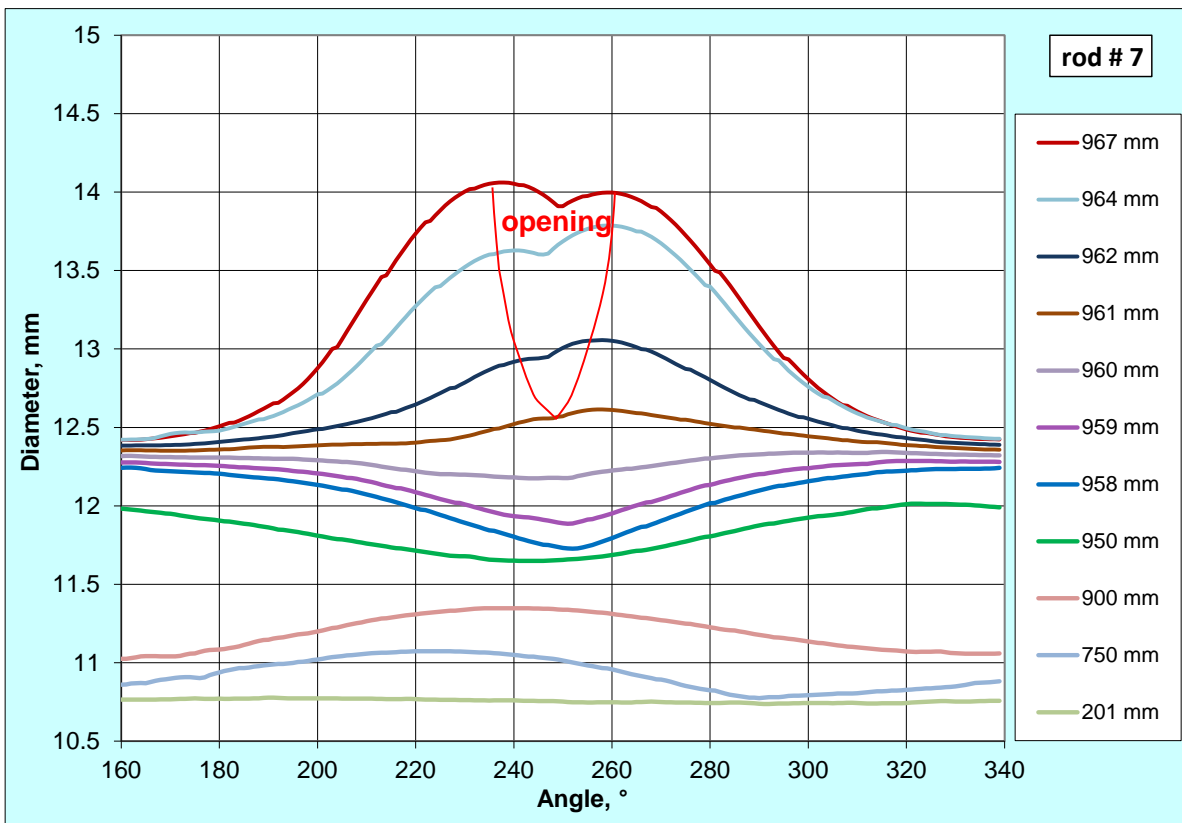
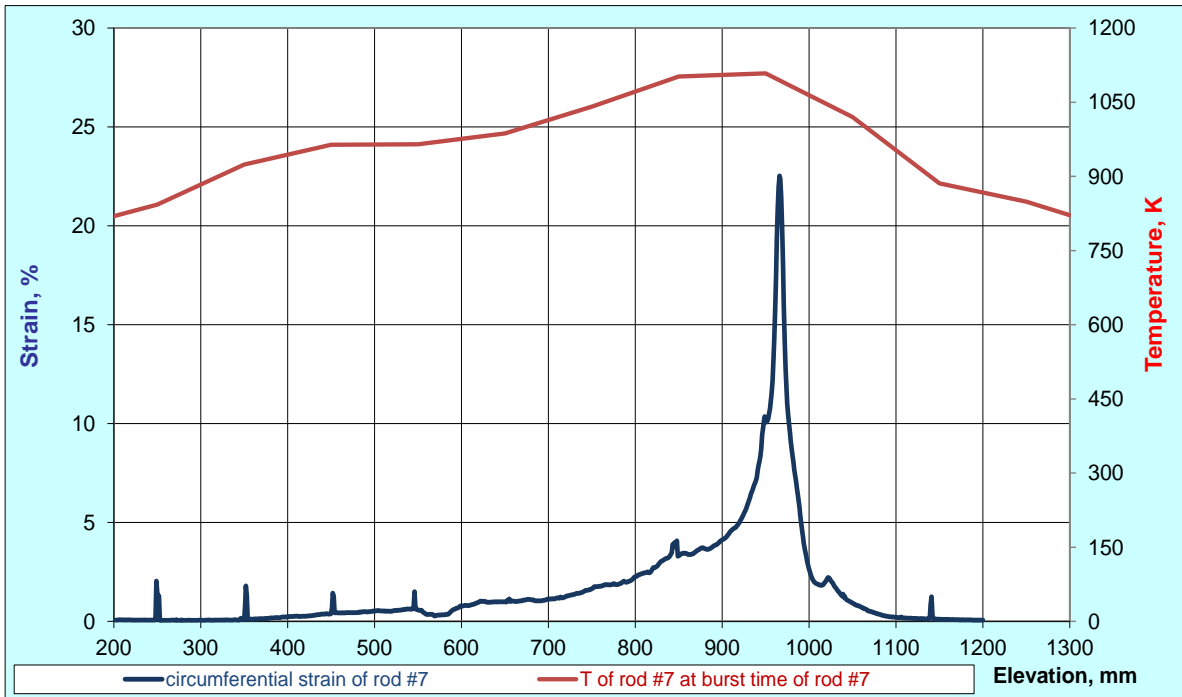Figure 72   QUENCH-L2, Rod #7; longitudinal changing of circumferential strain (top); azimuthal diameter downwards from burst (bottom).Spikes: thermocouples.

Figure 73   QUENCH-L2, Rod #8; longitudinal changing of circumferential strain (top); azimuthal diameter downwards from burst (bottom).

Figure 74   QUENCH-L2, Rod #9; longitudinal changing of circumferential strain (top); azimuthal diameter downwards from burst (bottom).

Figure 75   QUENCH-L2, Rod #10; longitudinal changing of circumferential strain (top); azimuthal diameter downwards from burst (bottom).

Figure 76   QUENCH-L2, Rod #11; longitudinal changing of circumferential strain (top); azimuthal diameter downwards from burst (bottom). Spikes: thermocouple.
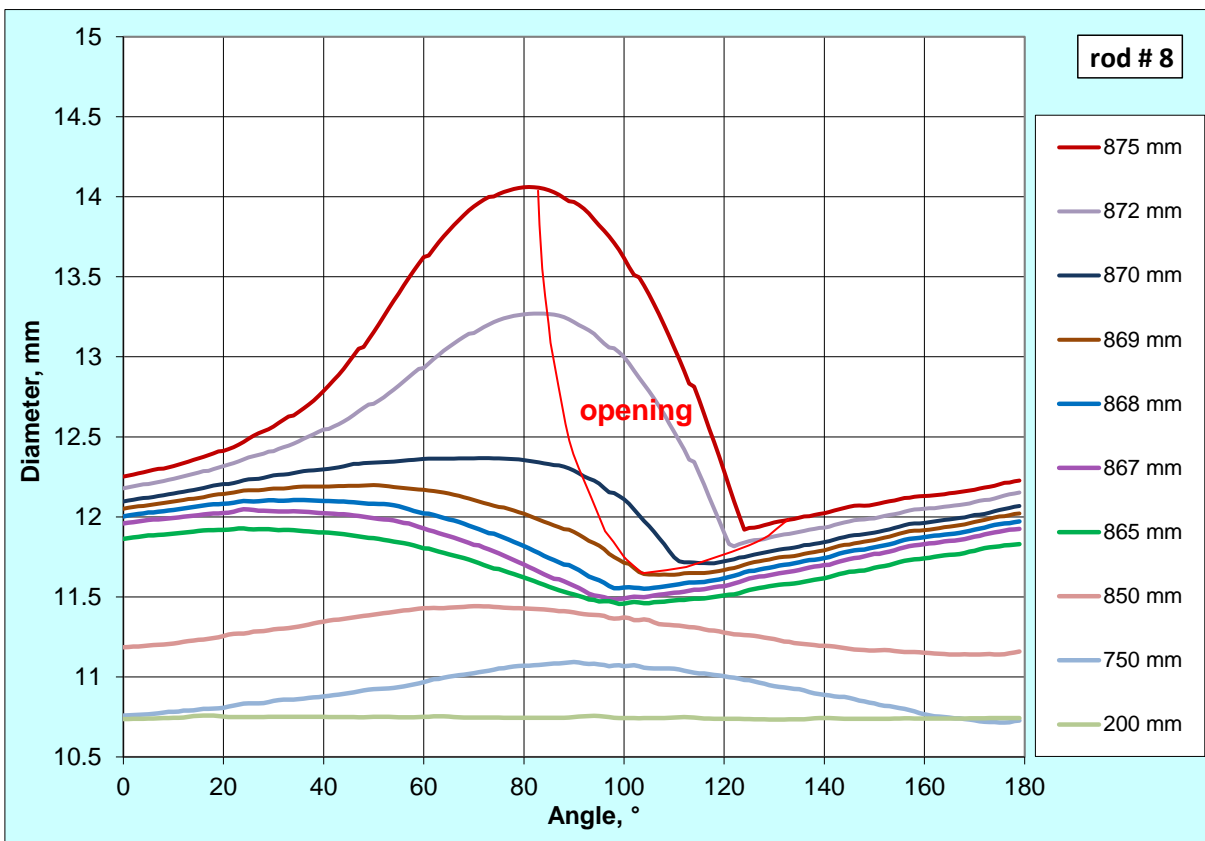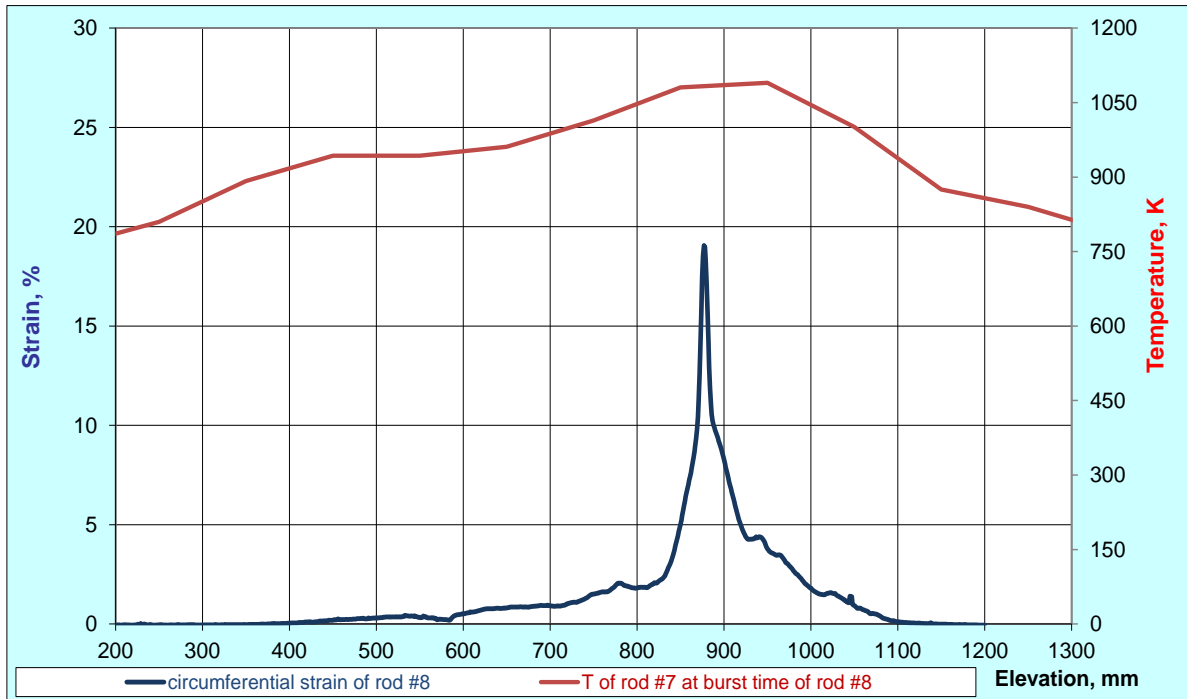
Figure 77   QUENCH-L2, Rod #12; longitudinal changing of circumferential strain (top); azimuthal diameter downwards from burst (bottom).
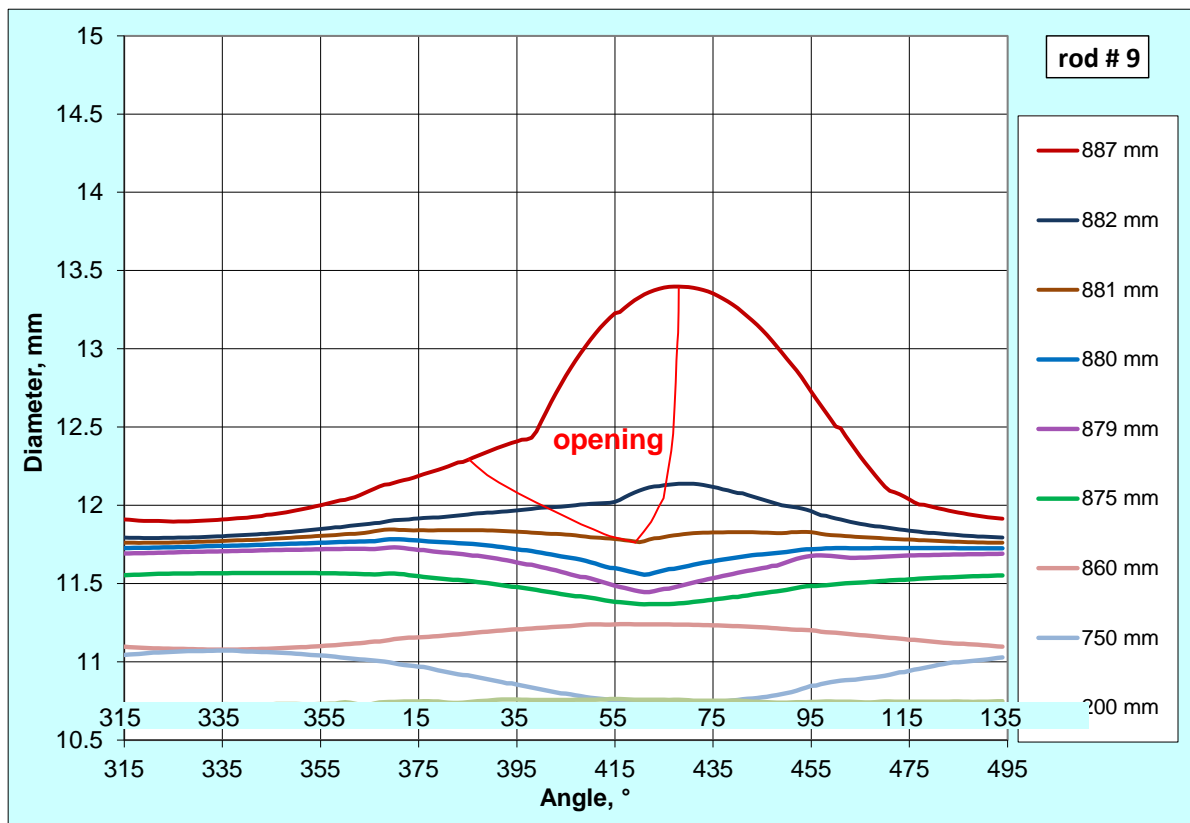
Figure 78   QUENCH-L2, Rod #13; longitudinal changing of circumferential strain (top); azimuthal diameter downwards from burst (bottom).
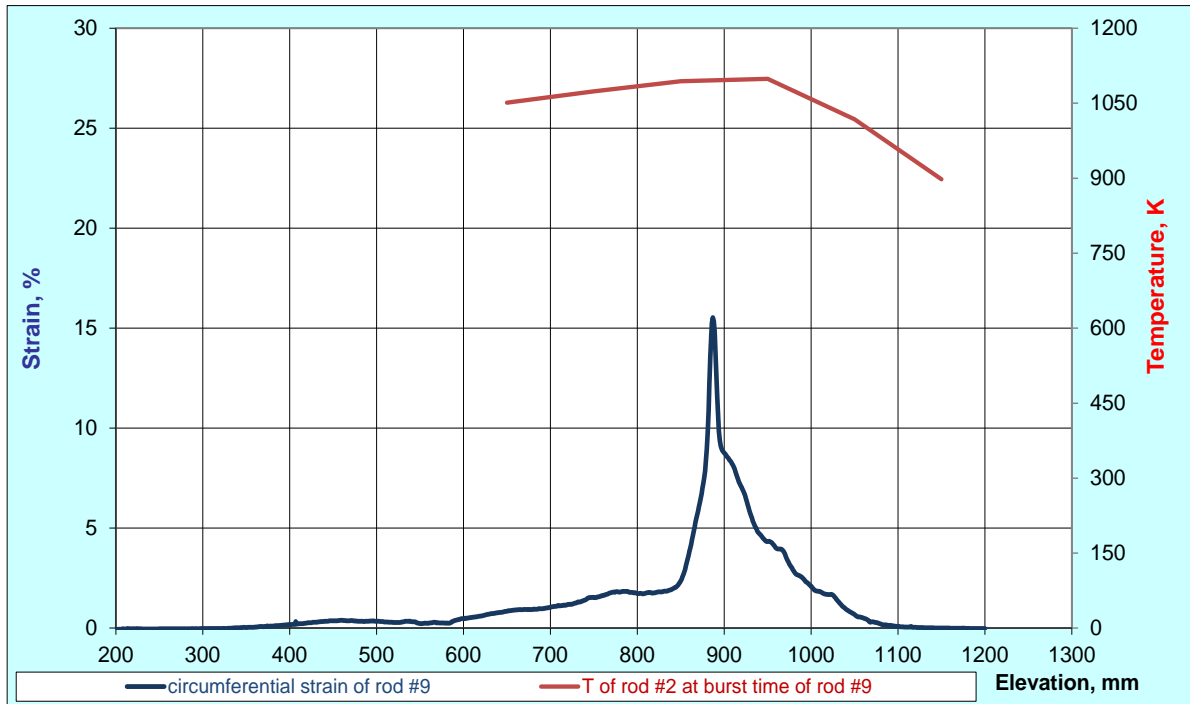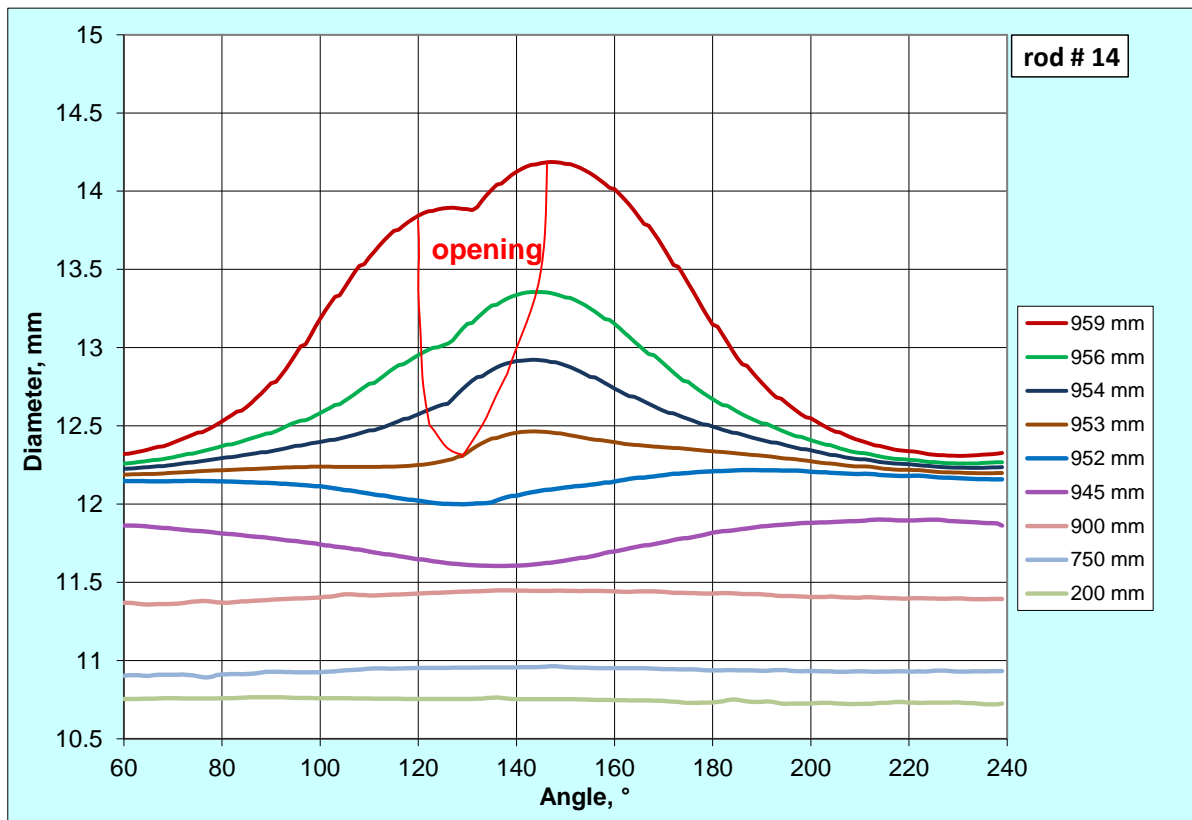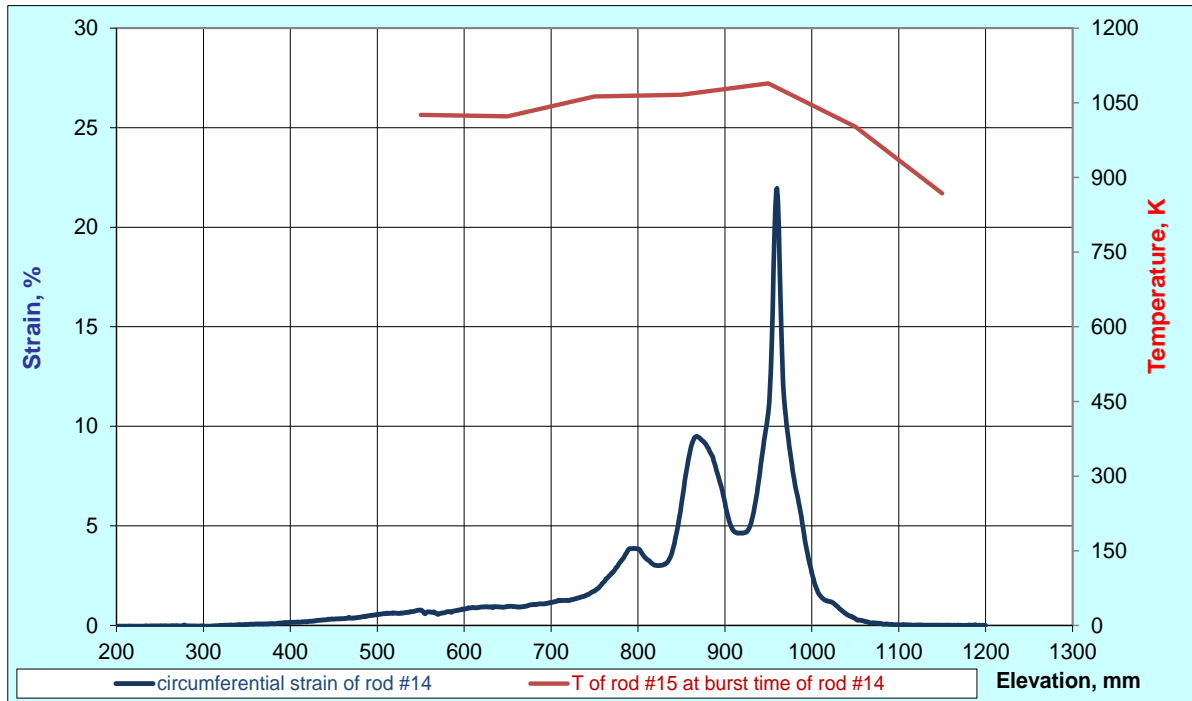
Figure 79   QUENCH-L2, Rod #14; longitudinal changing of circumferential strain (top); azimuthal diameter downwards from burst (bottom).
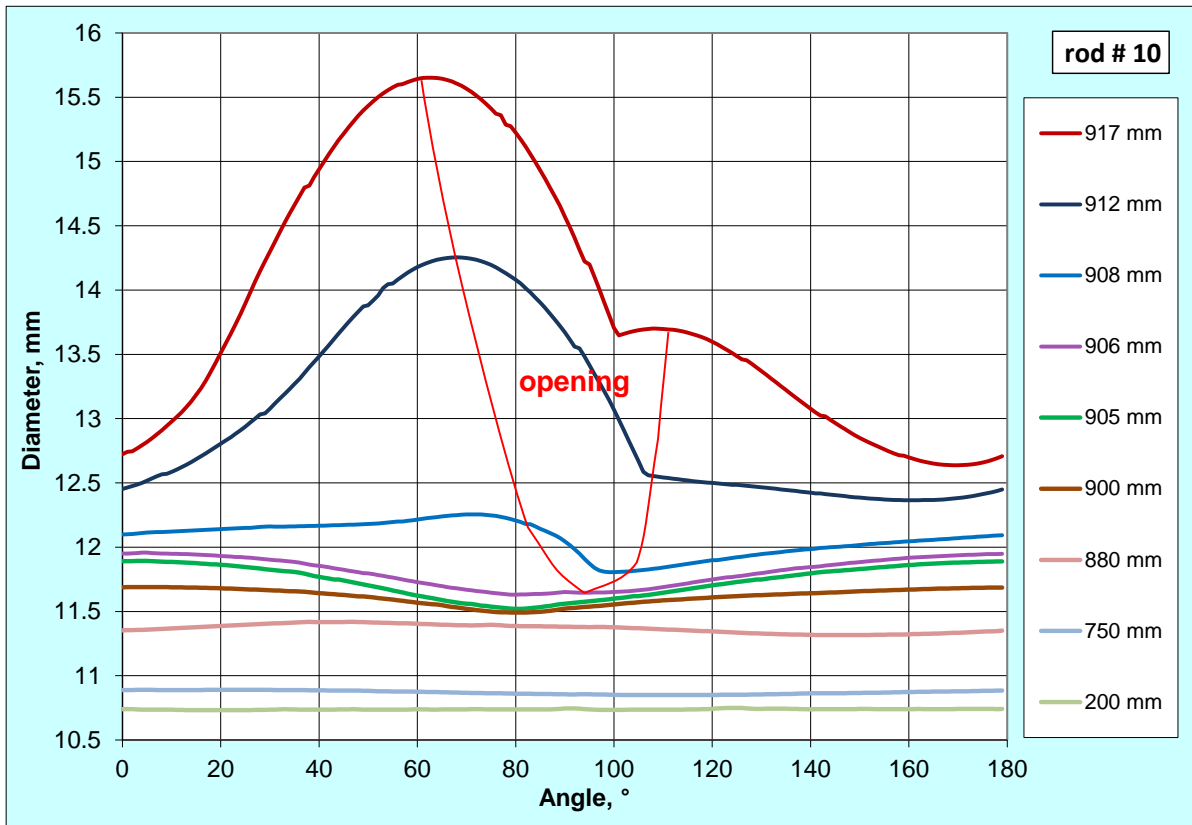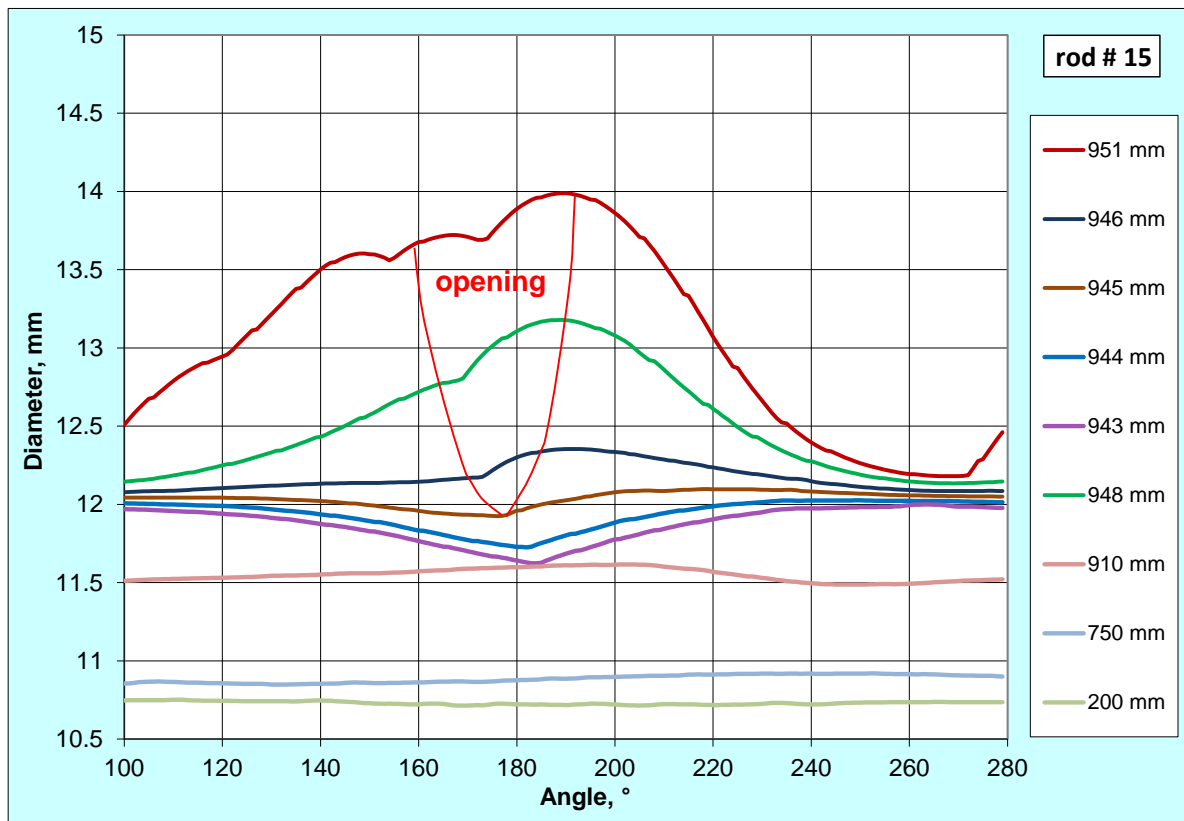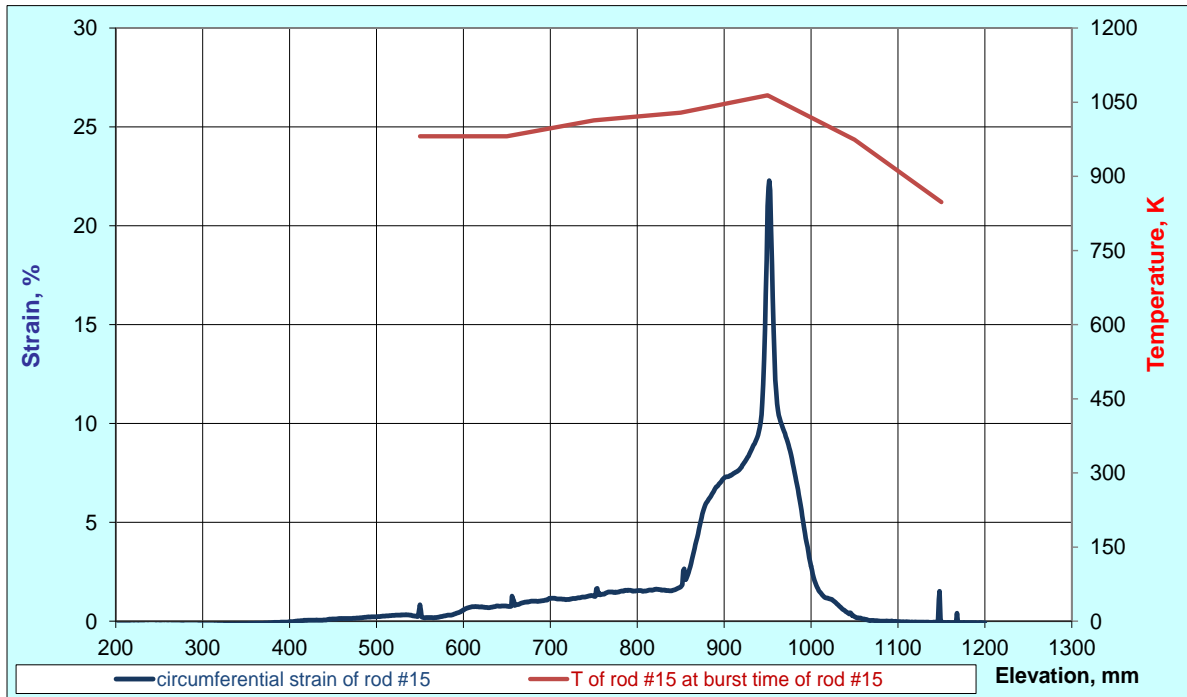
Figure 80   QUENCH-L2, Rod #15; longitudinal changing of circumferential strain (top); azimuthal diameter downwards from burst (bottom). Spikes: thermocouple.
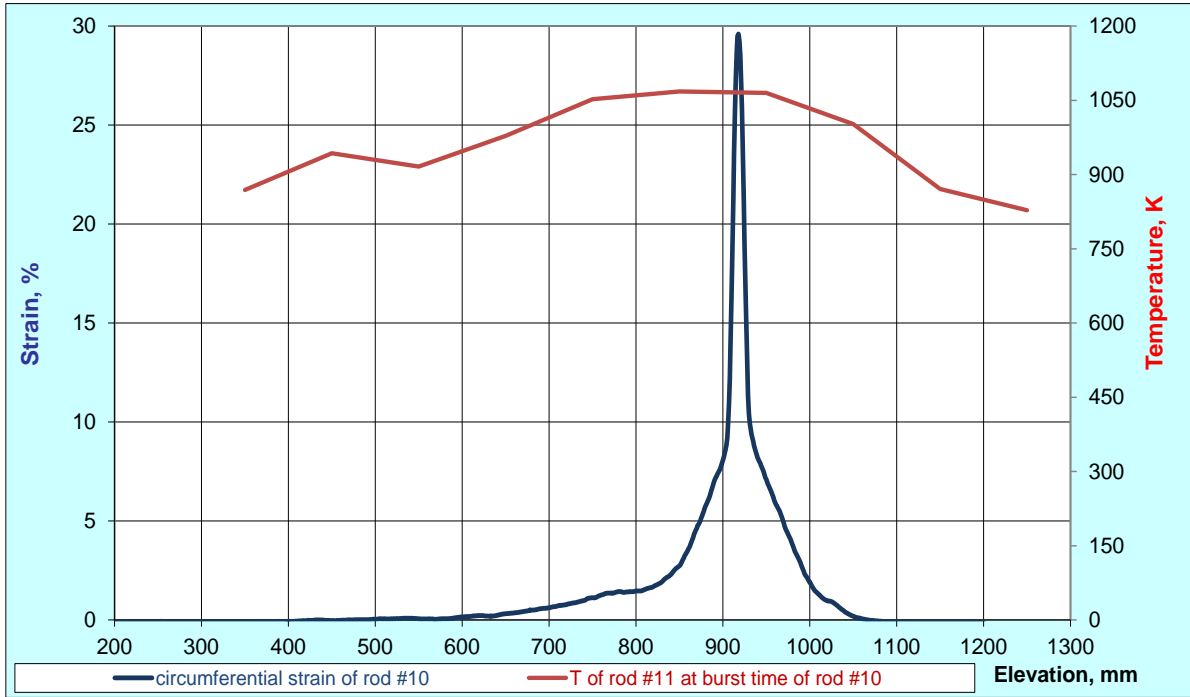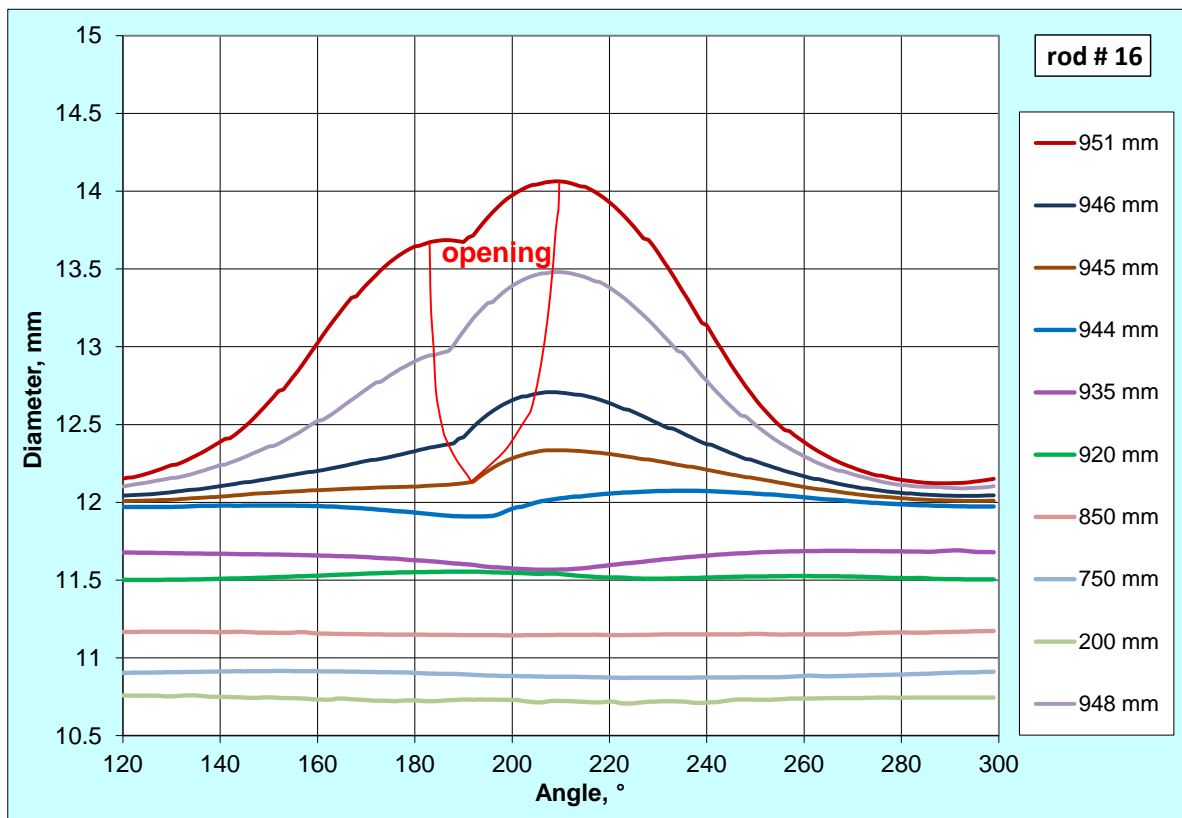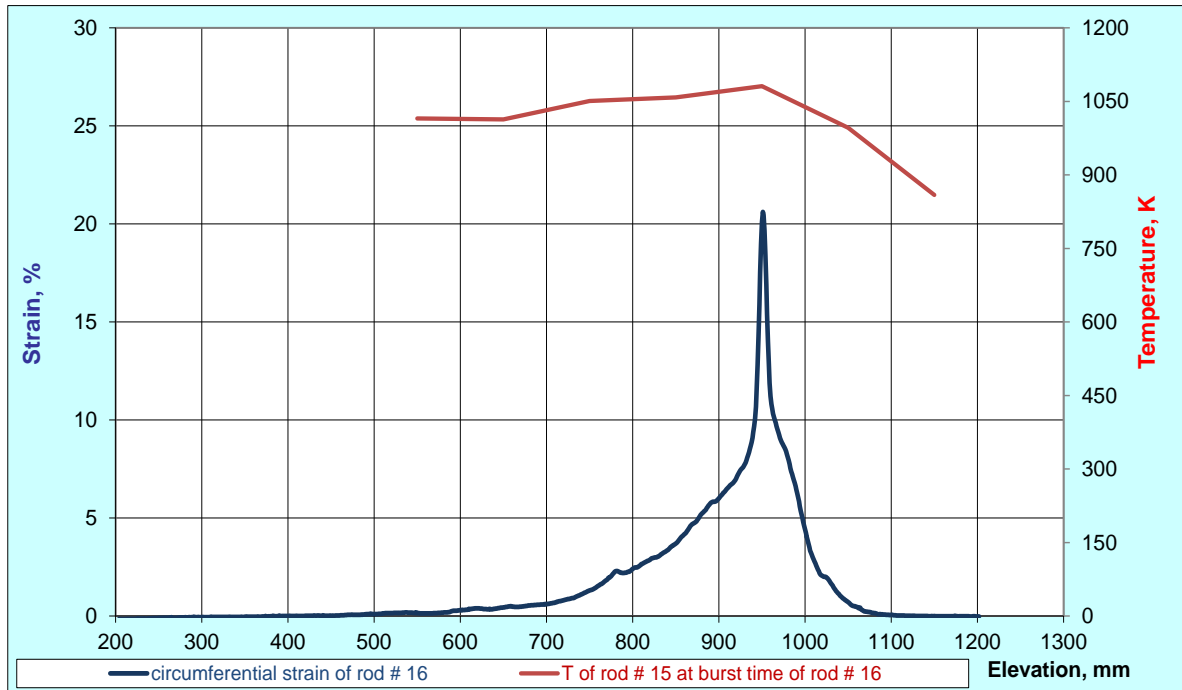
Figure 81   QUENCH-L2, Rod #16; longitudinal changing of circumferential strain (top); azimuthal diameter downwards from burst (bottom).
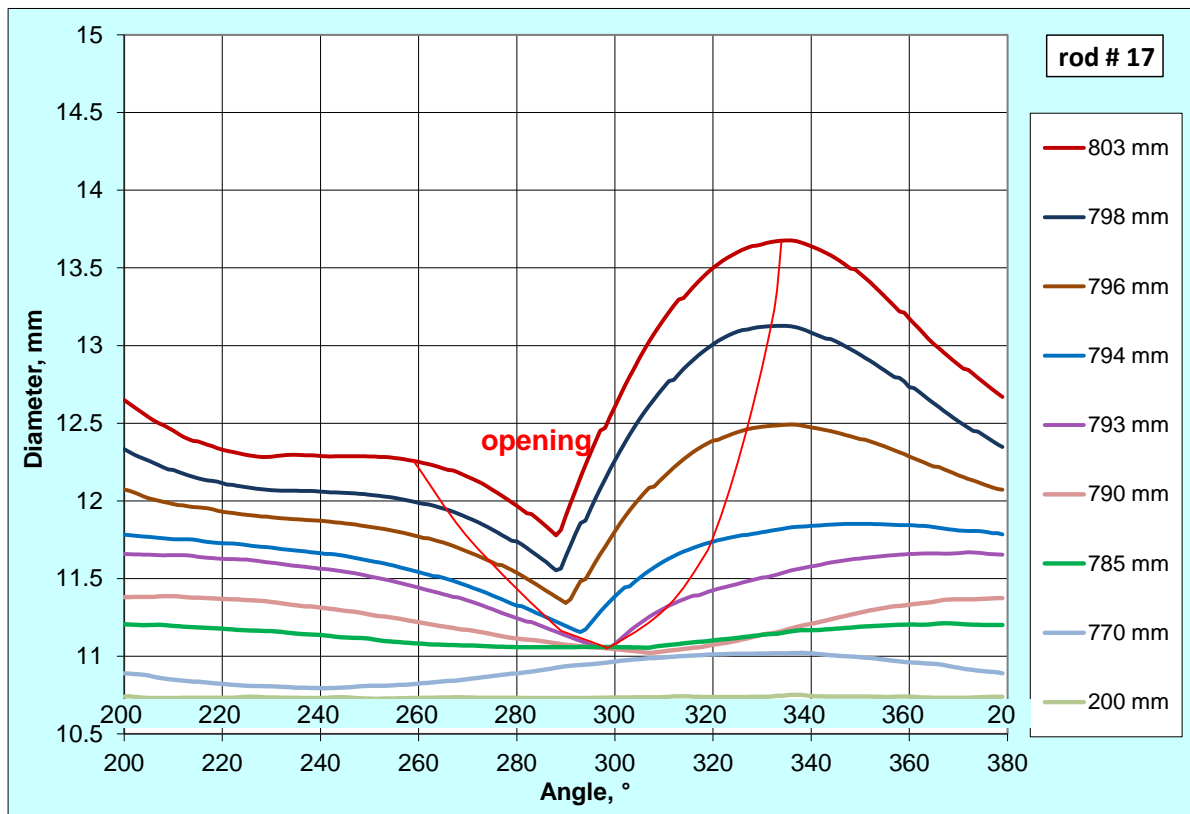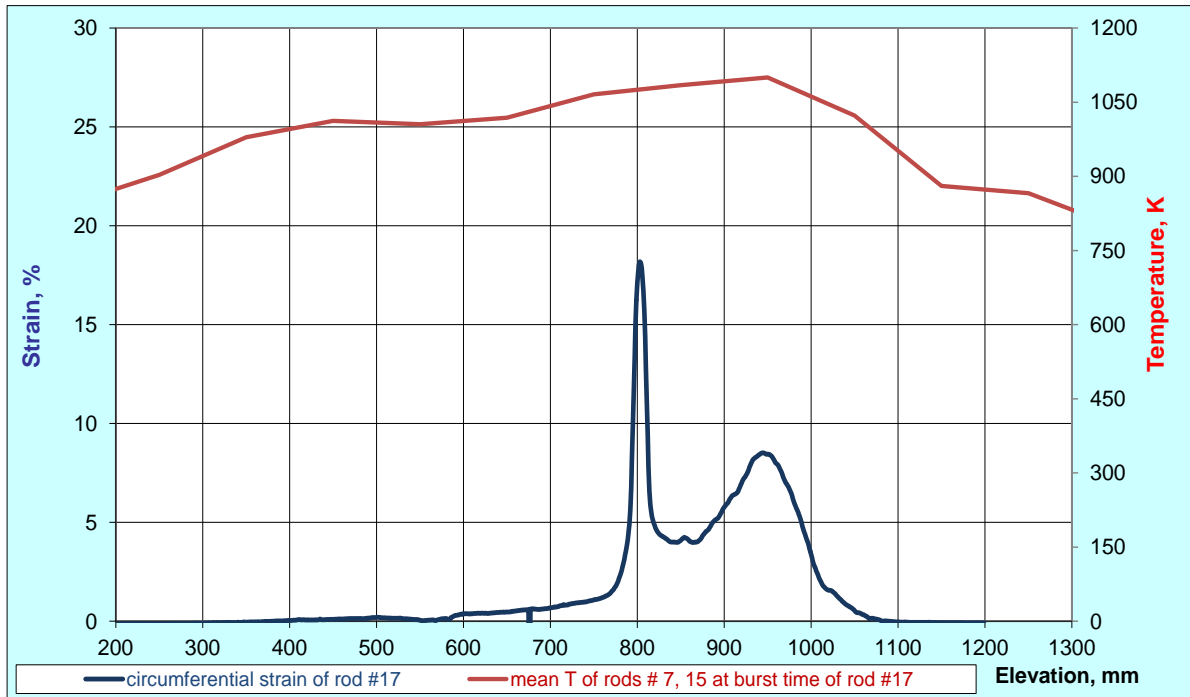
Figure 82   QUENCH-L2, Rod #17; longitudinal changing of circumferential strain (top); azimuthal diameter downwards from burst (bottom).
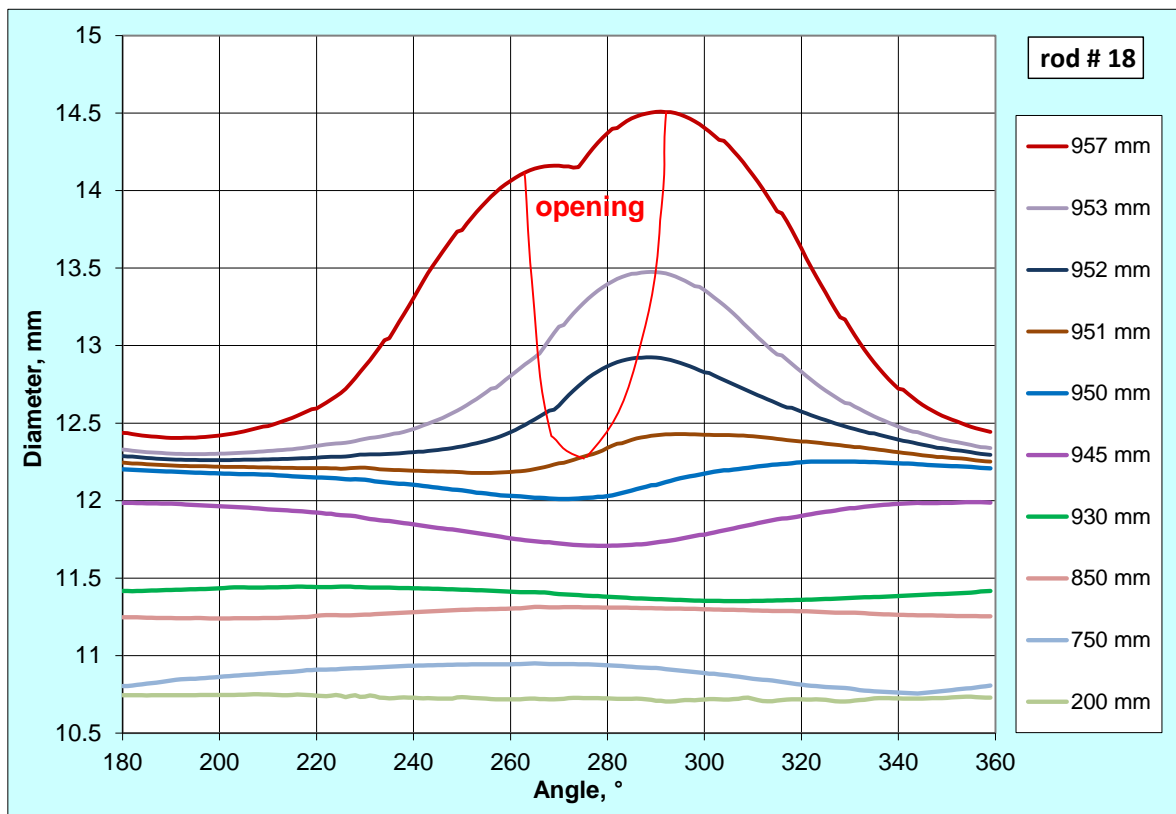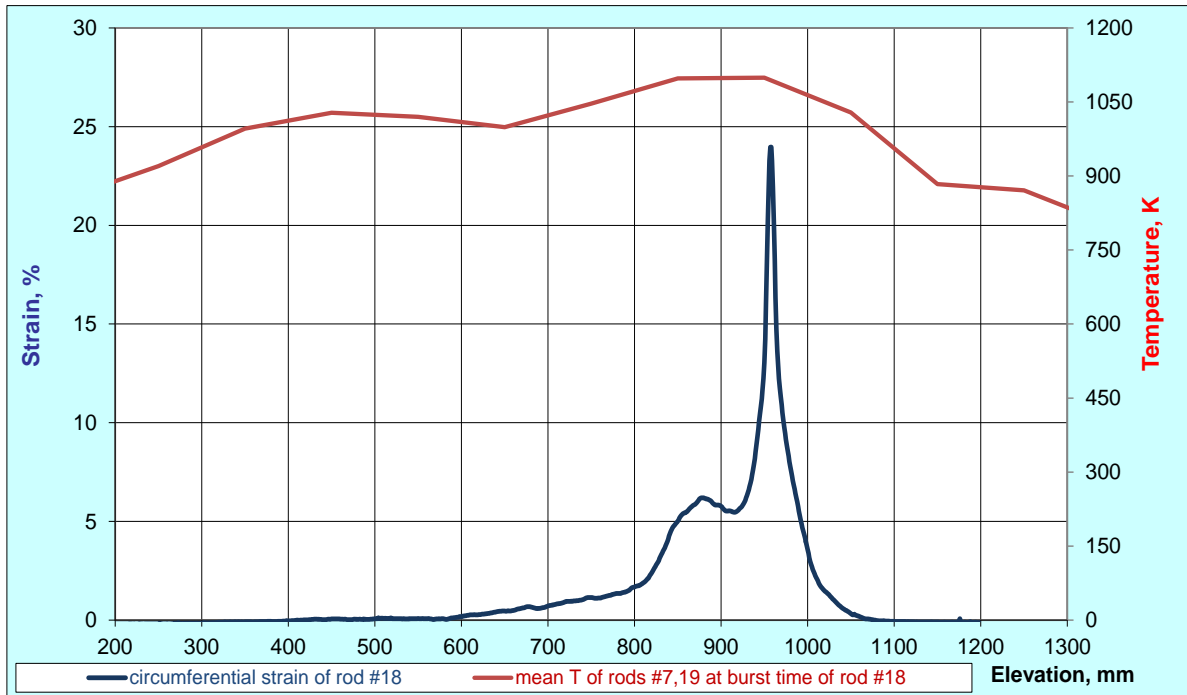
Figure 83   QUENCH-L2, Rod #18; longitudinal changing of circumferential strain (top); azimuthal diameter downwards from burst (bottom).
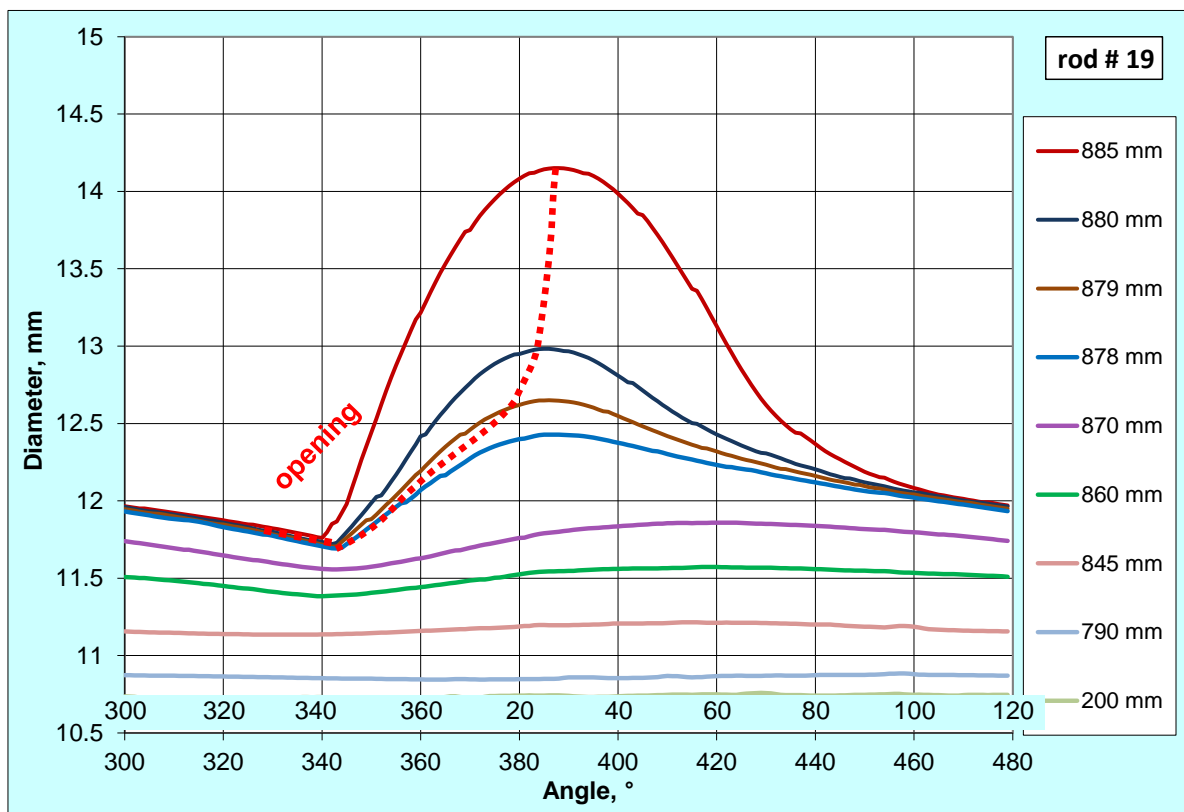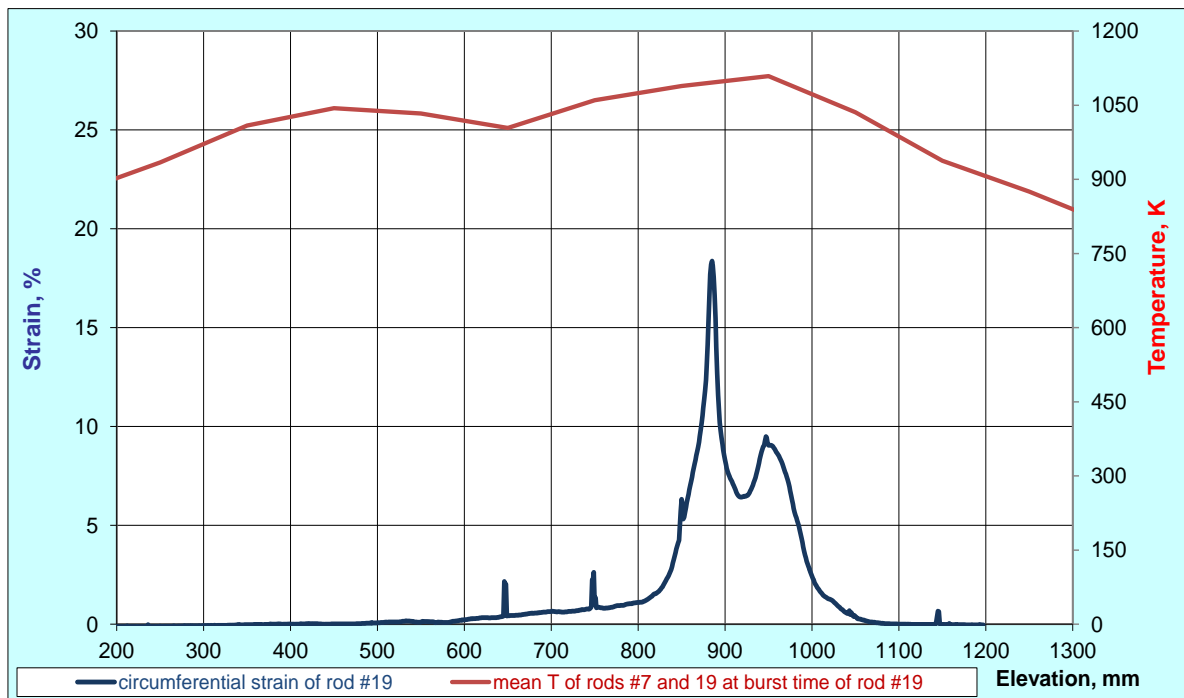
Figure 84   QUENCH-L2, Rod #19; longitudinal changing of circumferential strain (top); azimuthal diameter downwards from burst (bottom).Spikes: thermocouples.
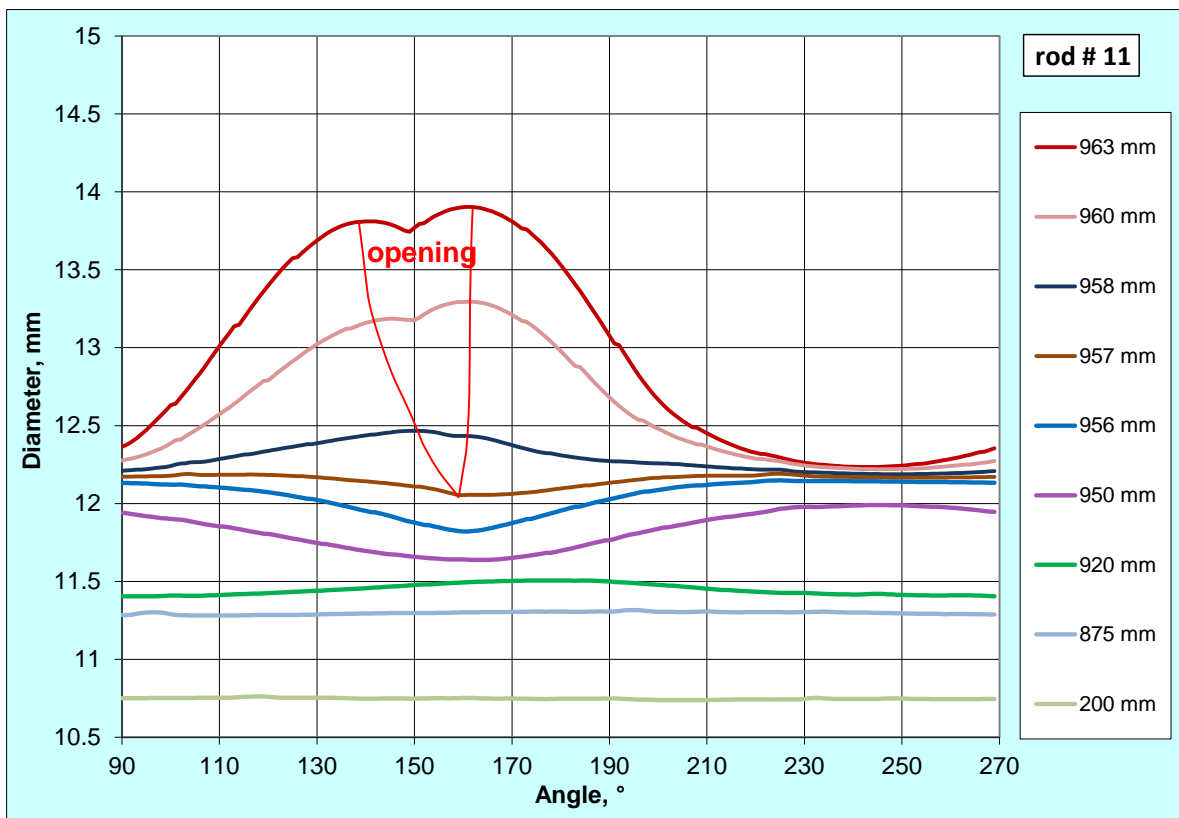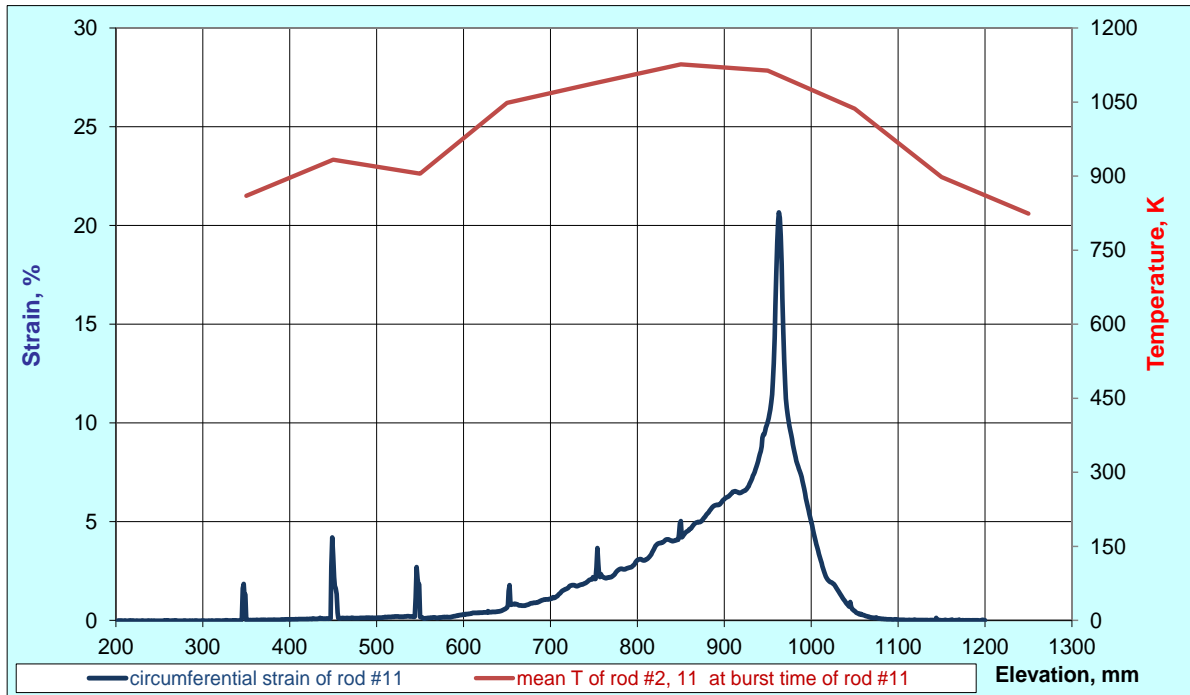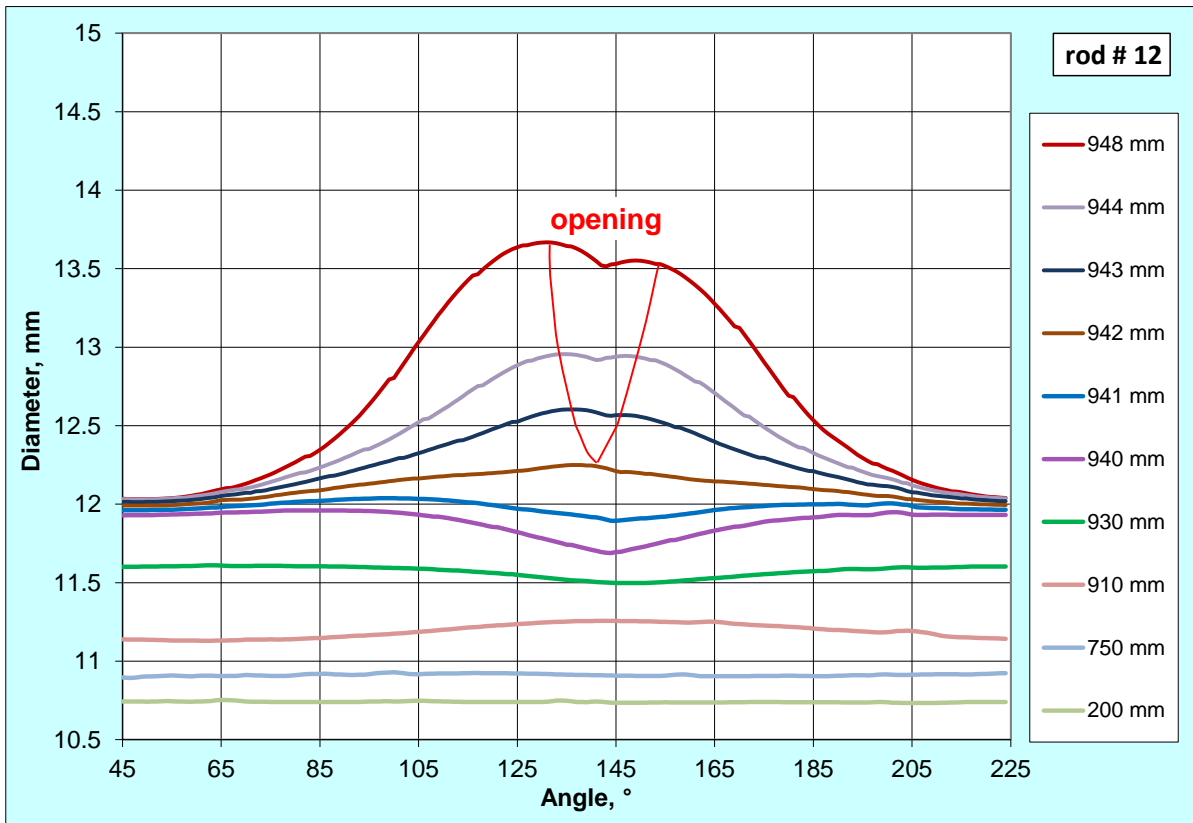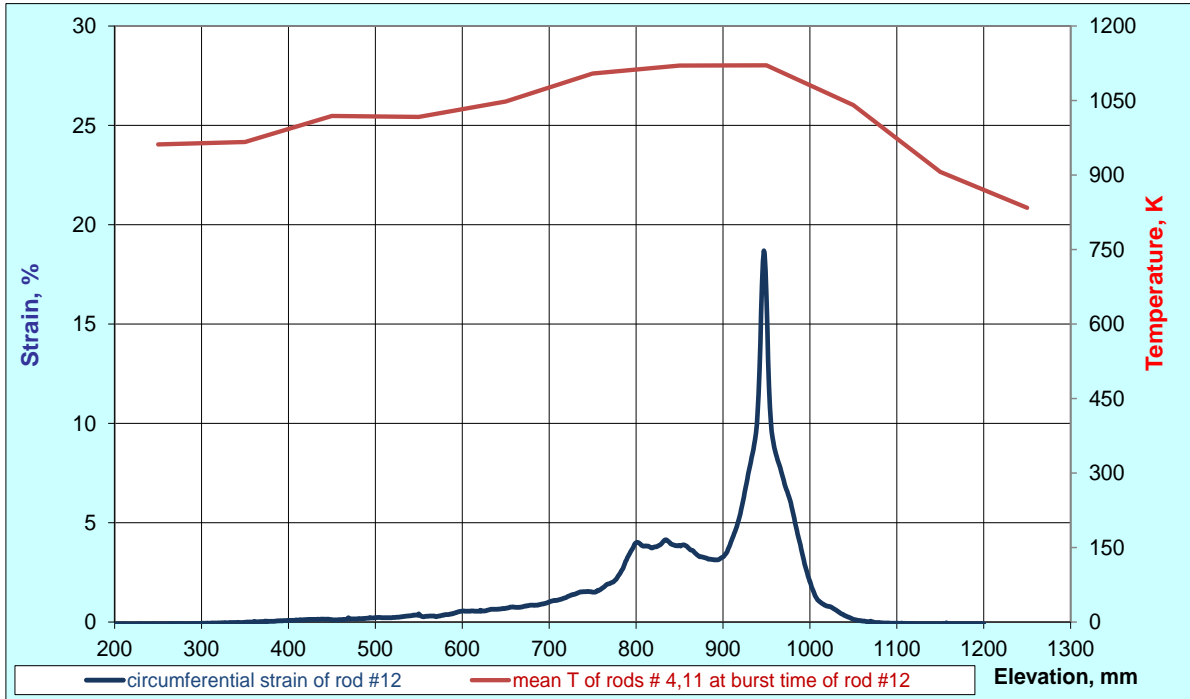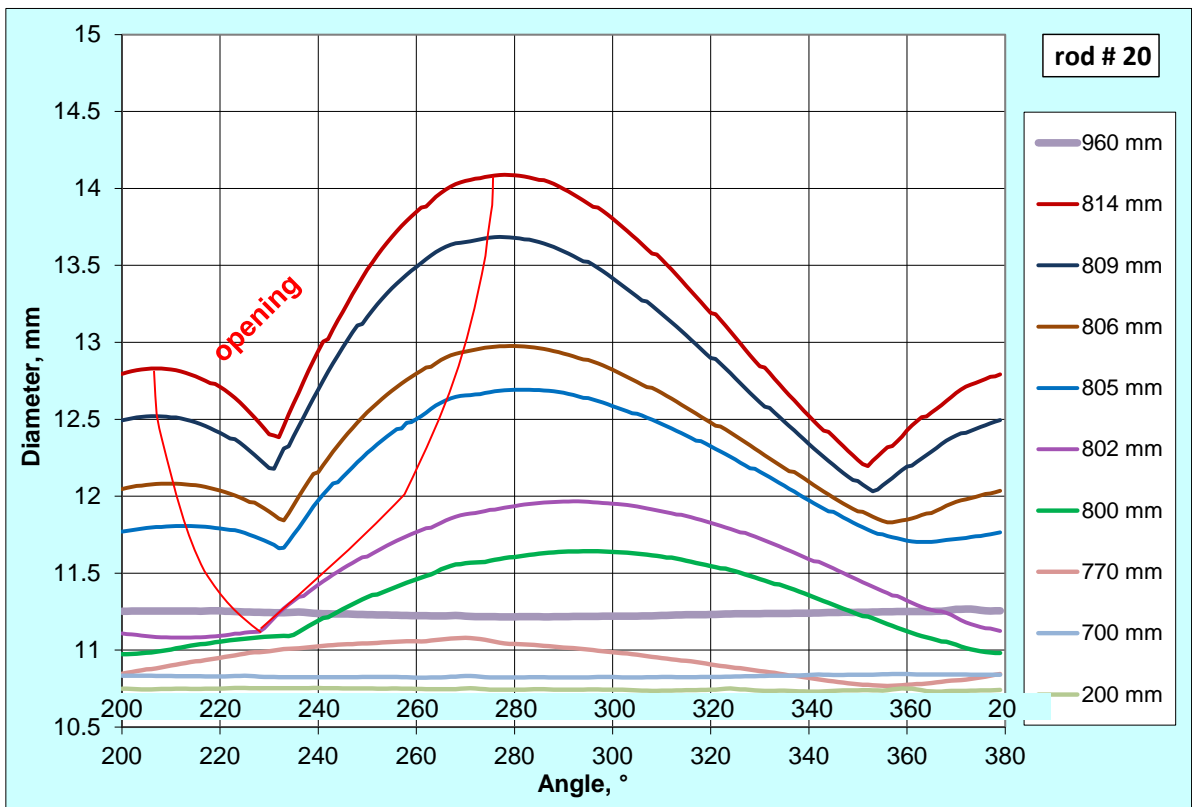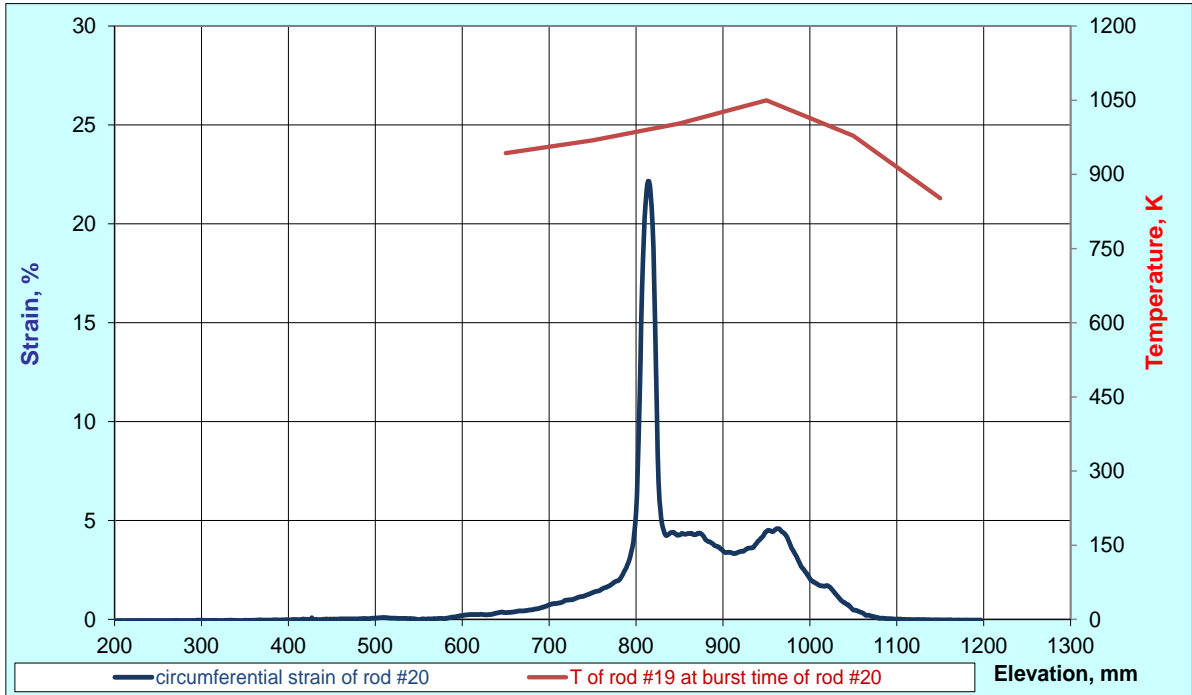
Figure 85   QUENCH-L2, Rod #20; longitudinal changing of circumferential strain (top); azimuthal diameter downwards from burst (bottom).
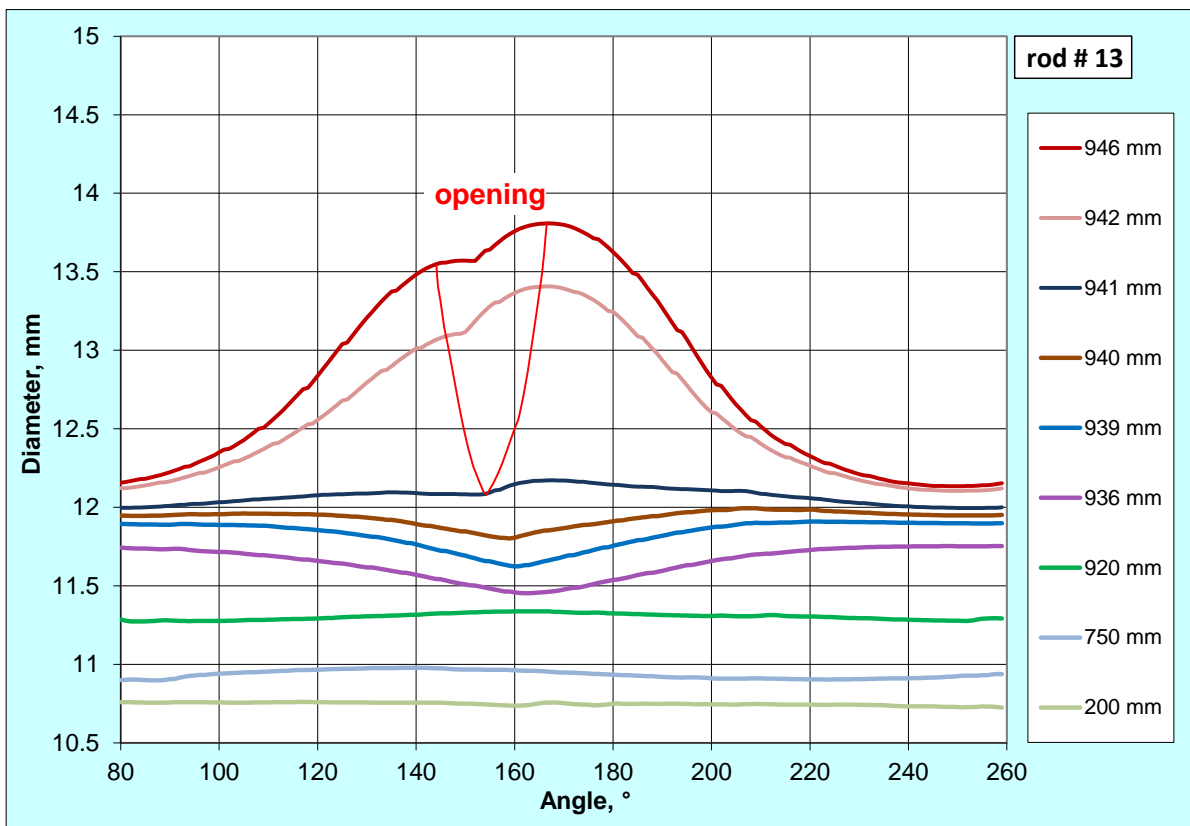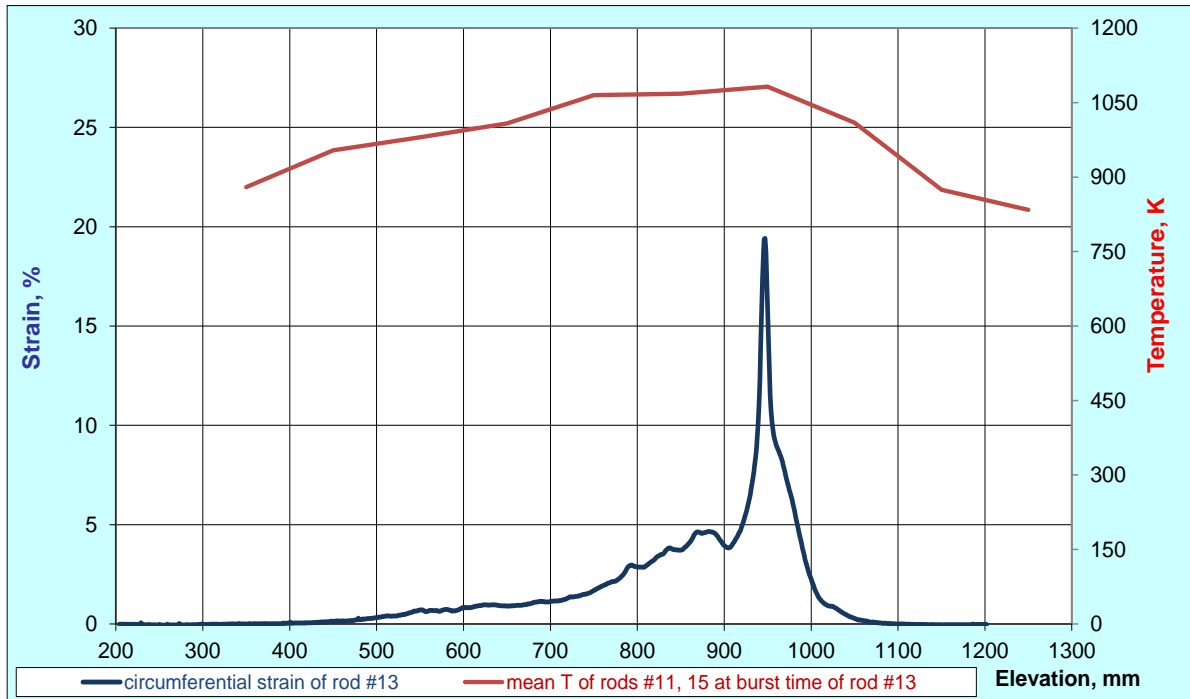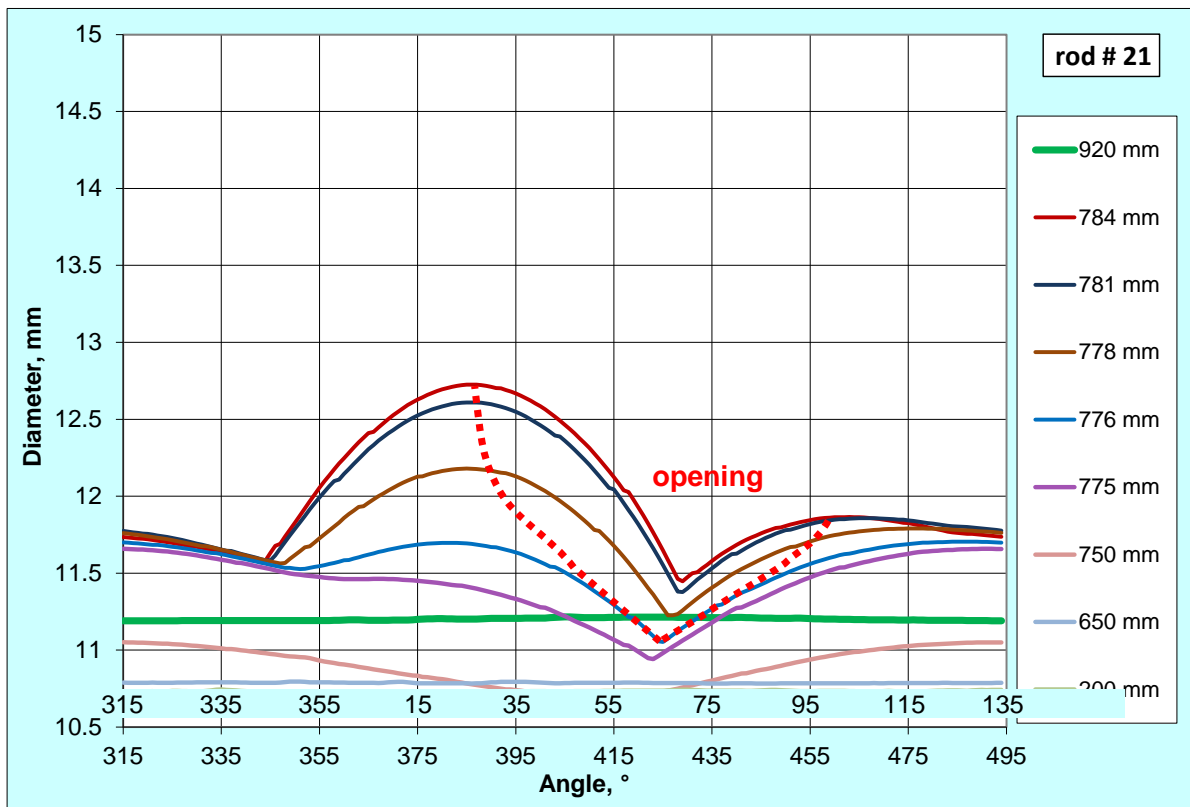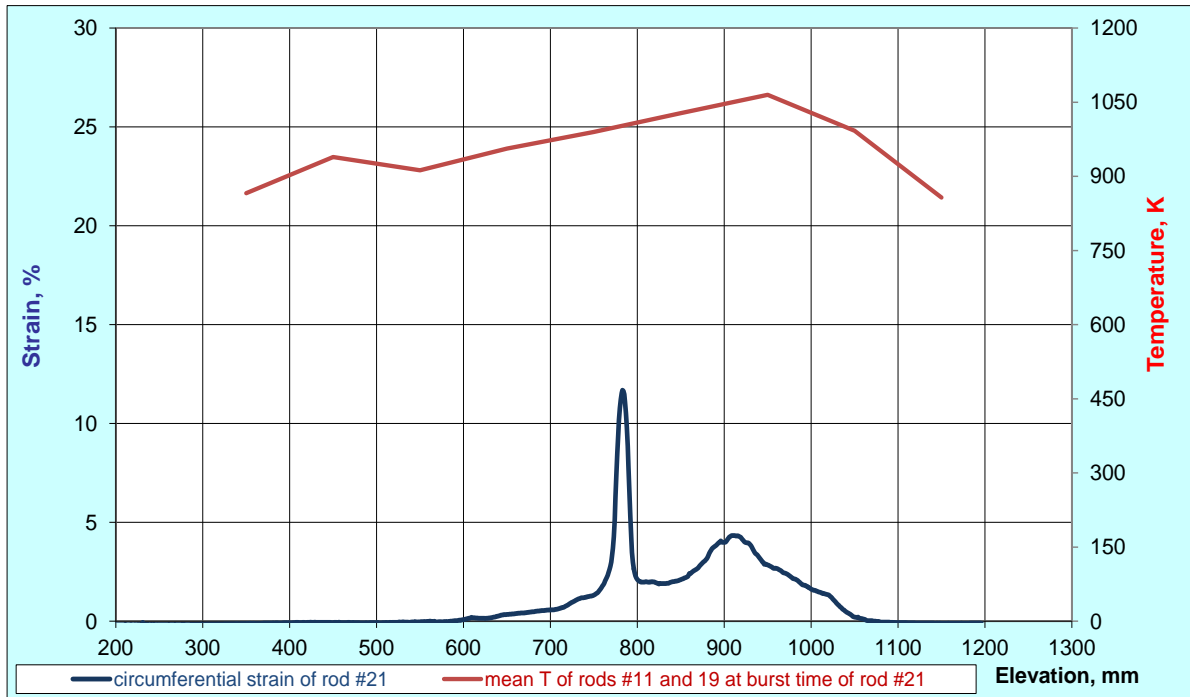
Figure 86   QUENCH-L2, Rod #21; longitudinal changing of circumferential strain (top); azimuthal diameter downwards from burst (bottom).
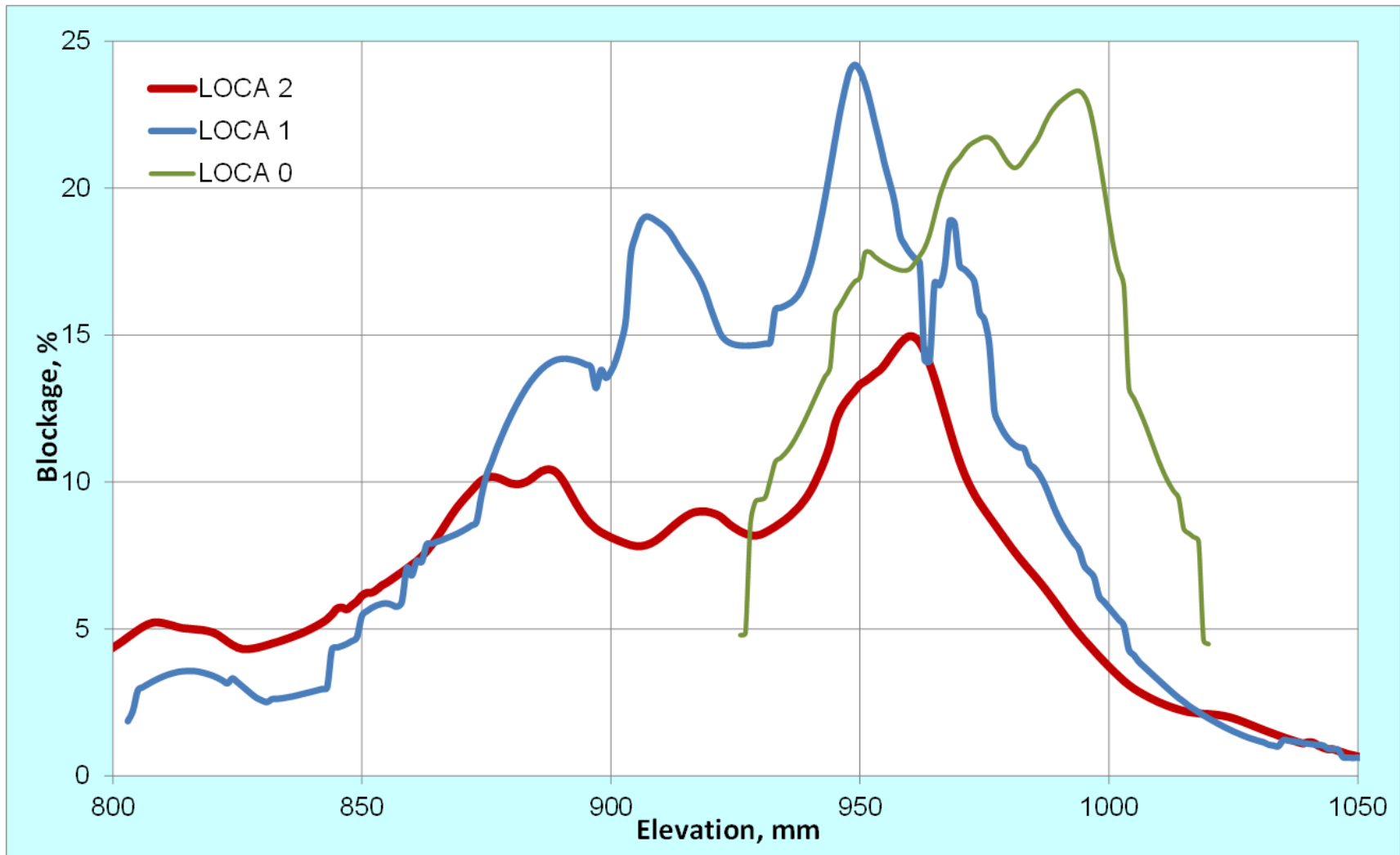
Figure 87   Blockage of coolant channel for QUENCH-L0, L1 and –L2 bundles.
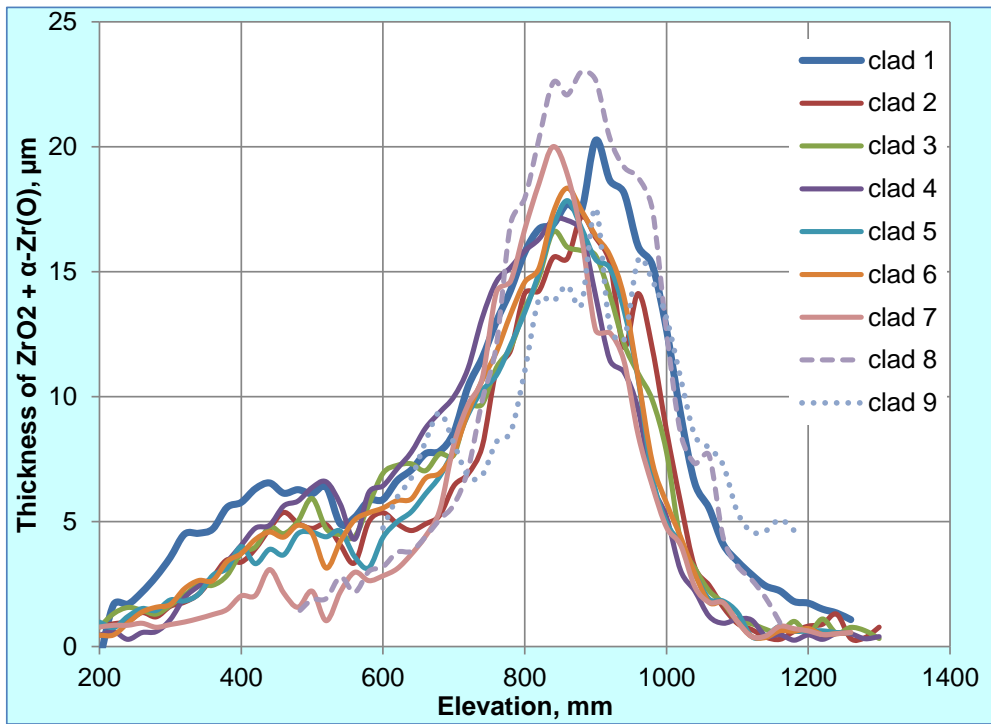
Figure 88   QUENCH-L2; Results of eddy-current measurements of axial layer thickness distribution for inner rods.
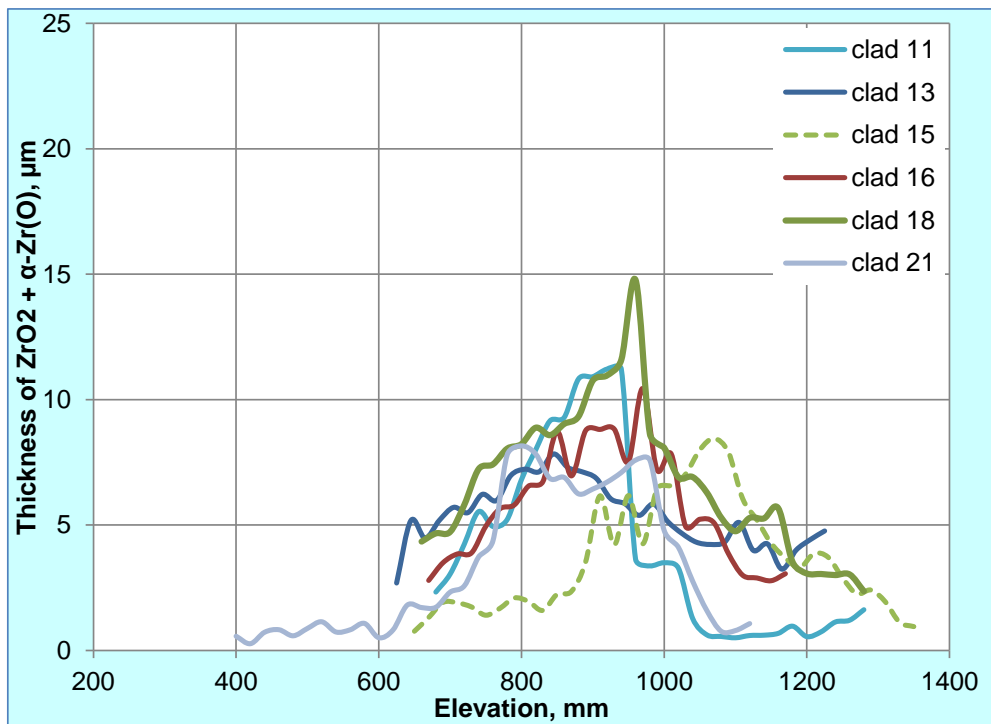
Figure 89   QUENCH-L2; Results of eddy-current measurements of axial layer thickness distribution for outer rods.
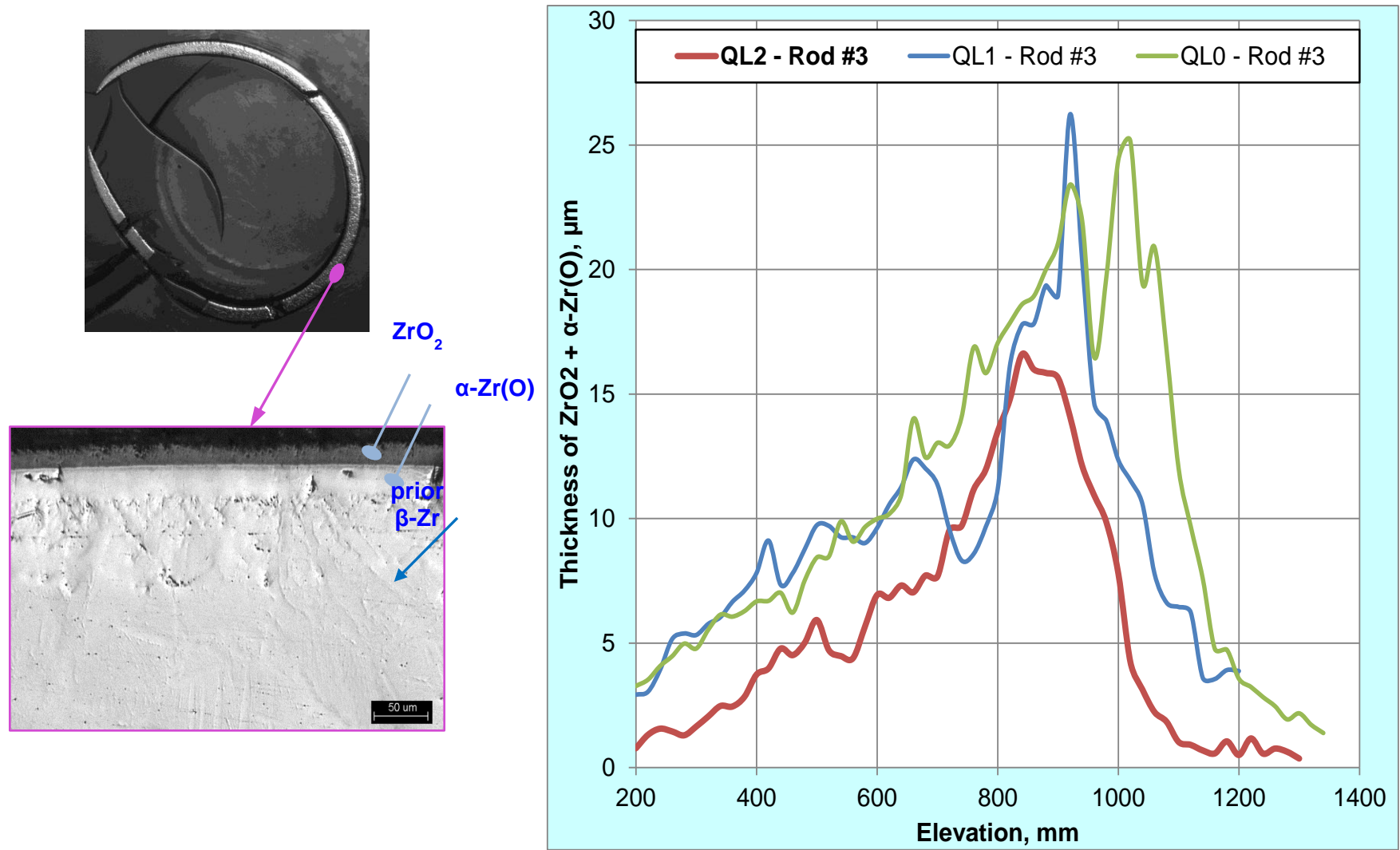
Figure 90   Comparison of cladding oxidation degree for tests QUENCH-L0, -L1 and -L2: total thickness of outer ZrO_2 and α-Zr(O) layers (tangential average of eddy-current measurements).
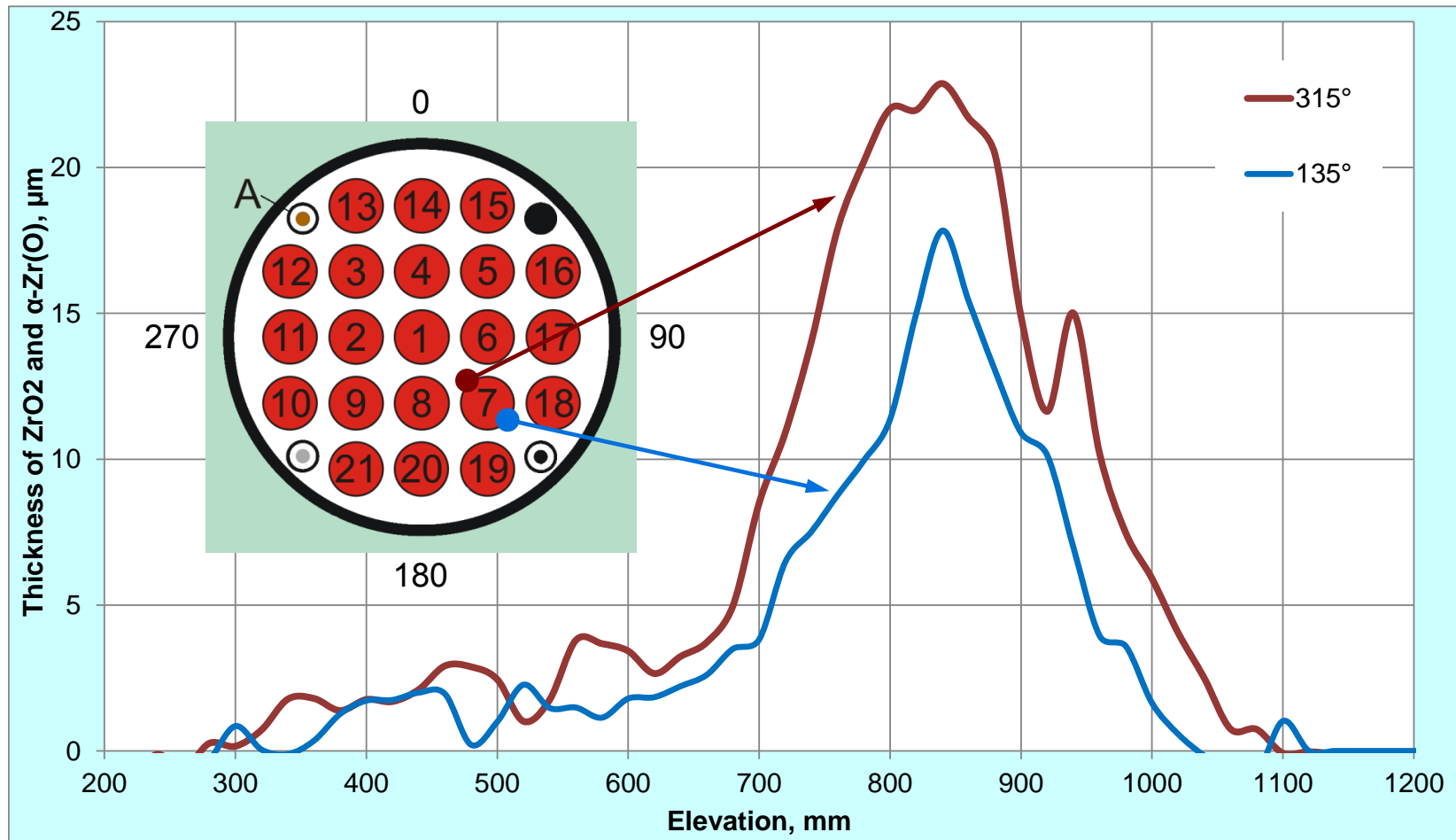
Figure 91   QUENCH-L2; layer thickness for two opposing circumferential positions of rod #7 (post-test eddy current measurements).
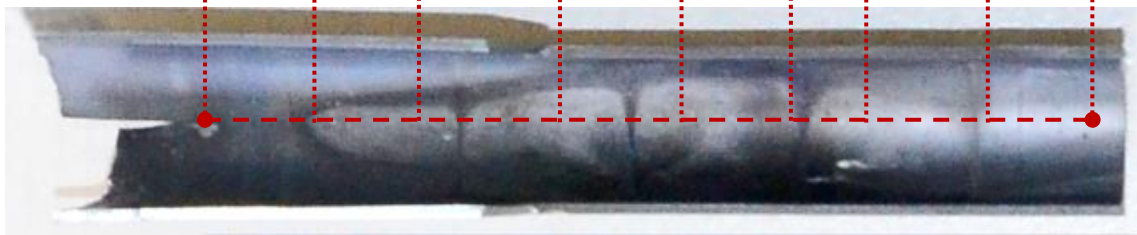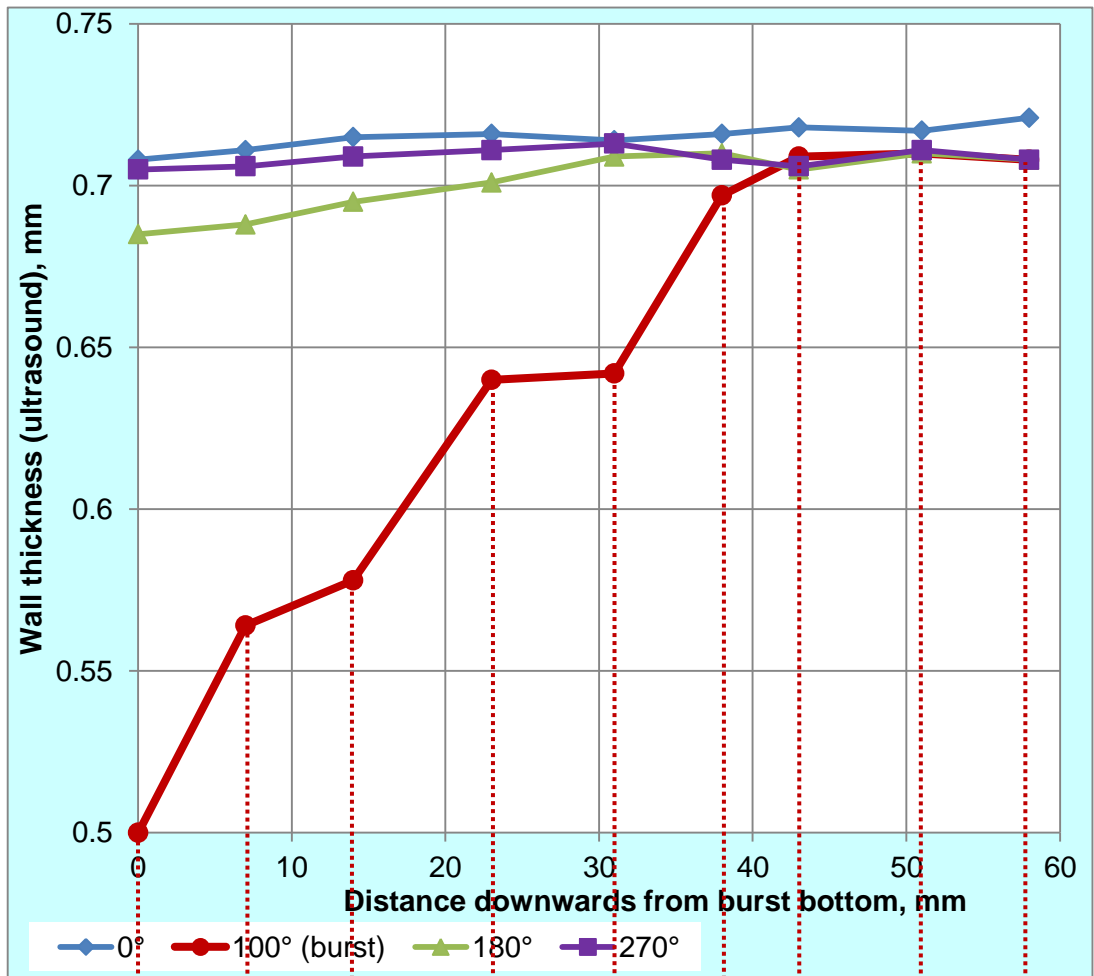
optical view of cladding inner surface downwards from burst opening

neutron radiography below burst opening: localization of hydrided region (dark)

Figure 92   QUENCH-L2; ultrasound measurement of wall thickness for rod #8.

ZrO₂: 11 µm

α-Zr(O): 20 µm

870 mm

838 mm

807 mm

ZrO₂: 10 µm

α-Zr(O): 16 µm

outer clad surface

inner clad surface

ZrO₂: 5 µm

α-Zr(O): 23 µm

ZrO₂: 10 µm

α-Zr(O): 16 µm
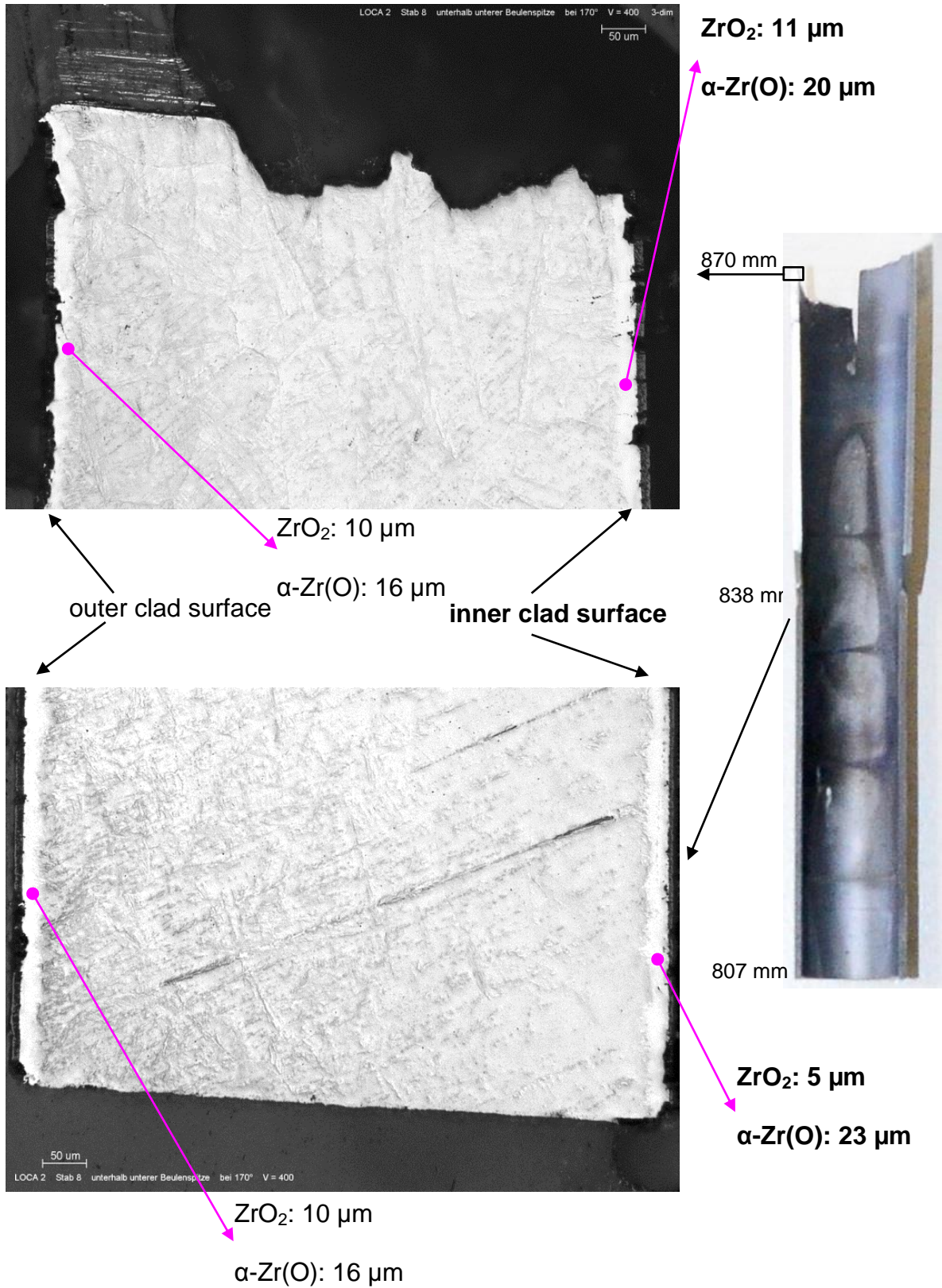
Figure 93   QUENCH-L2; metallographic results for oxidation of inner and outer surfaces of cladding #8.
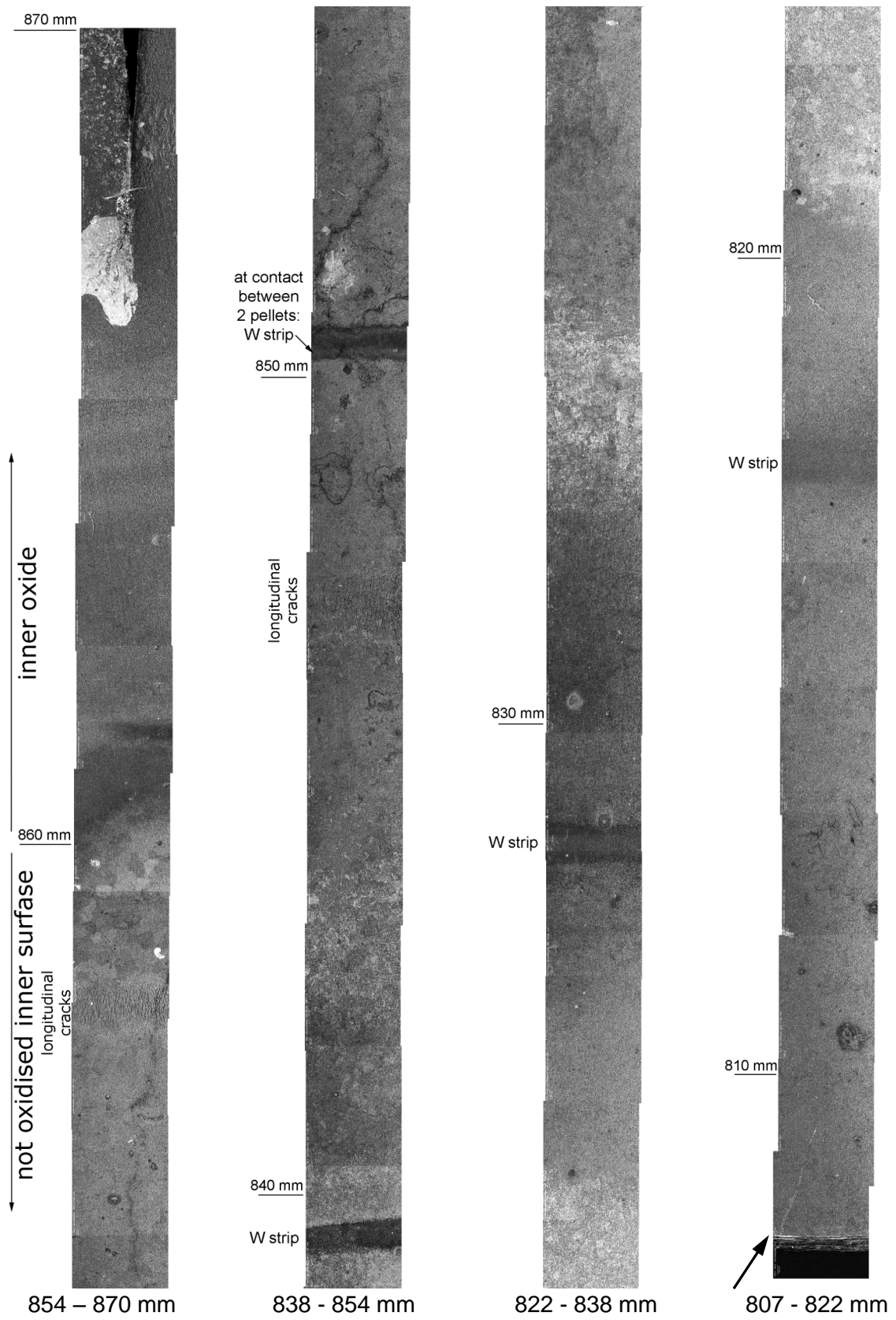
Figure 94   QUENCH-L2; optical mapping of inner surface of clad #8 below burst opening.

below burst opening: circumference cracks in oxide layer (left); EDX: oxygen in ZrO_2 (right)

oxide layer boundary: circumference cracks in oxide layer (left); EDX: oxygen in ZrO_2 (right)

pellet middle: metal surface (left); EDX: oxygen in α-Zr(O) (right)

tungsten ring between pellets: metal surface (left); EDX: tungsten indication (right)
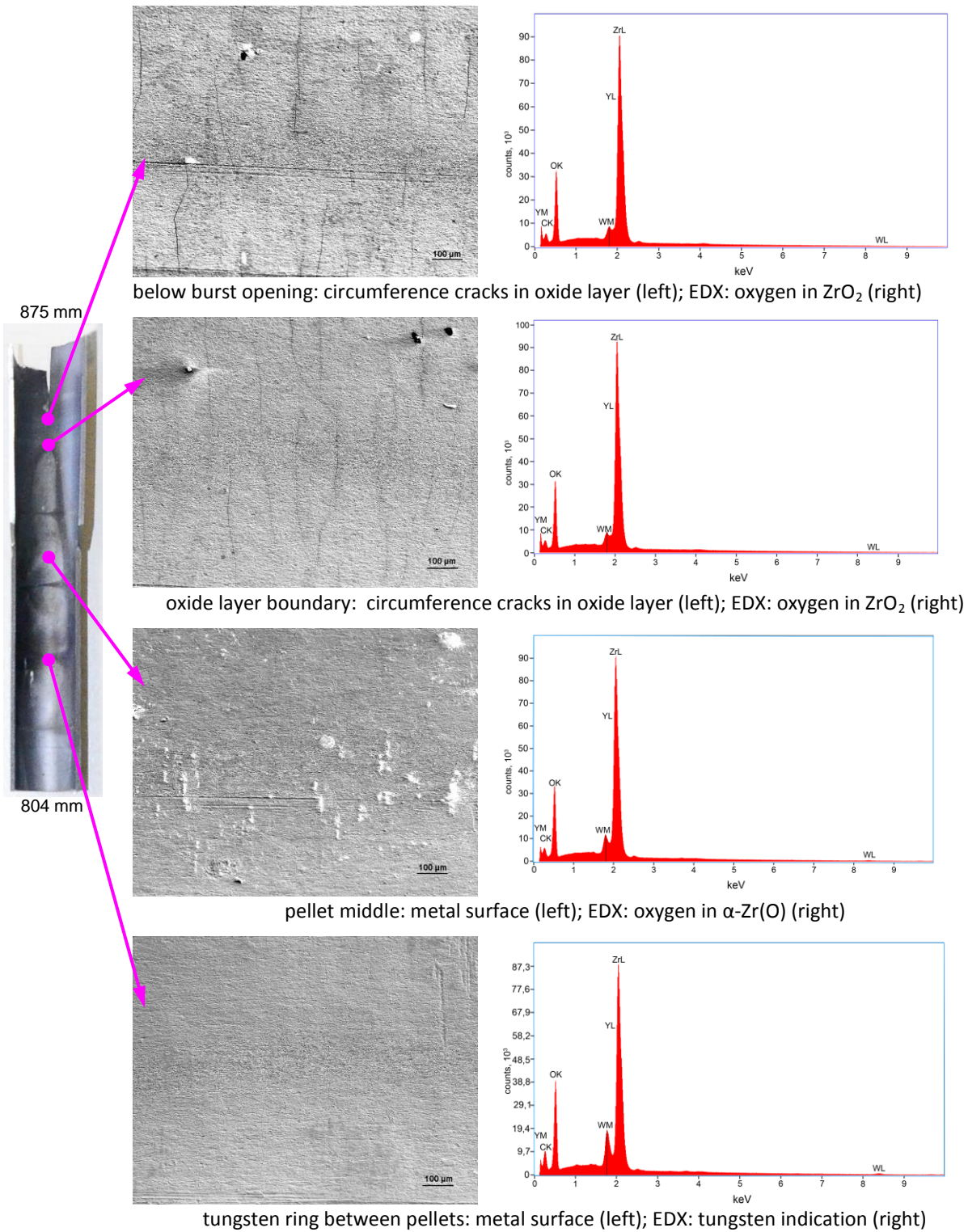
Figure 95   QUENCH-L2; cladding inner surface of rod #8 along a line of contact between pellets and cladding under the burst opening.

original ZrO$_2$ pellet

post-test ZrO$_2$ pellet
good contacted with
adjacent pellet:
negligible coating
of frontal surface

post-test ZrO$_2$ pellet
with large gap to
adjacent pellet:
significant coating of
frontal surface

(deposition
of W and Zr)

deposition of W
at inner surface
of cracked pellet
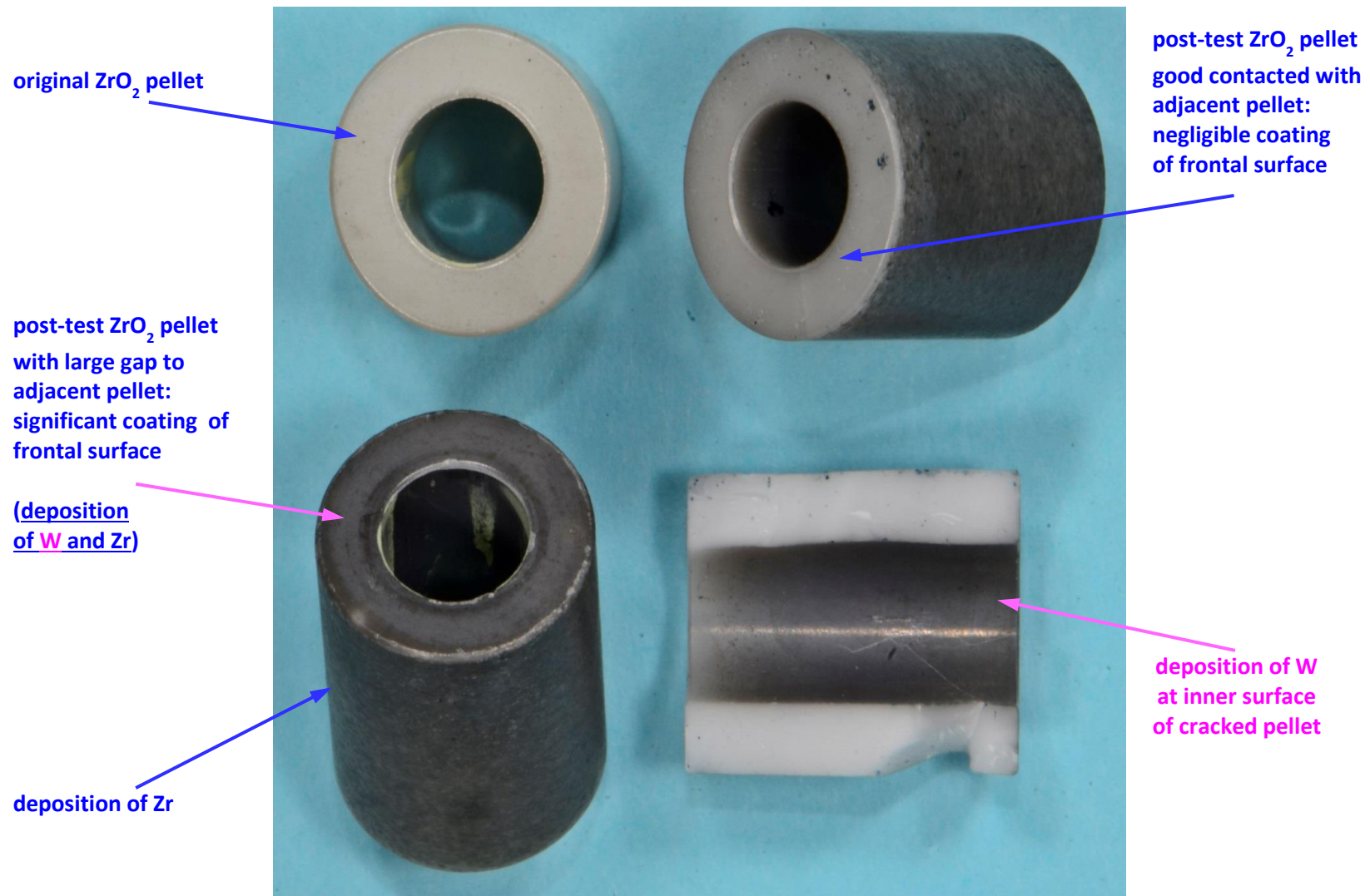
deposition of Zr

Figure 96   QUENCH-L2; Metal-vapour-phase deposition on the pellet surface.

band of hydrogen absorbed in Zr

Oxidation of inner cladding surface
$Zr+2H_2O=$
$ZrO_2+2H_2\uparrow$

steam
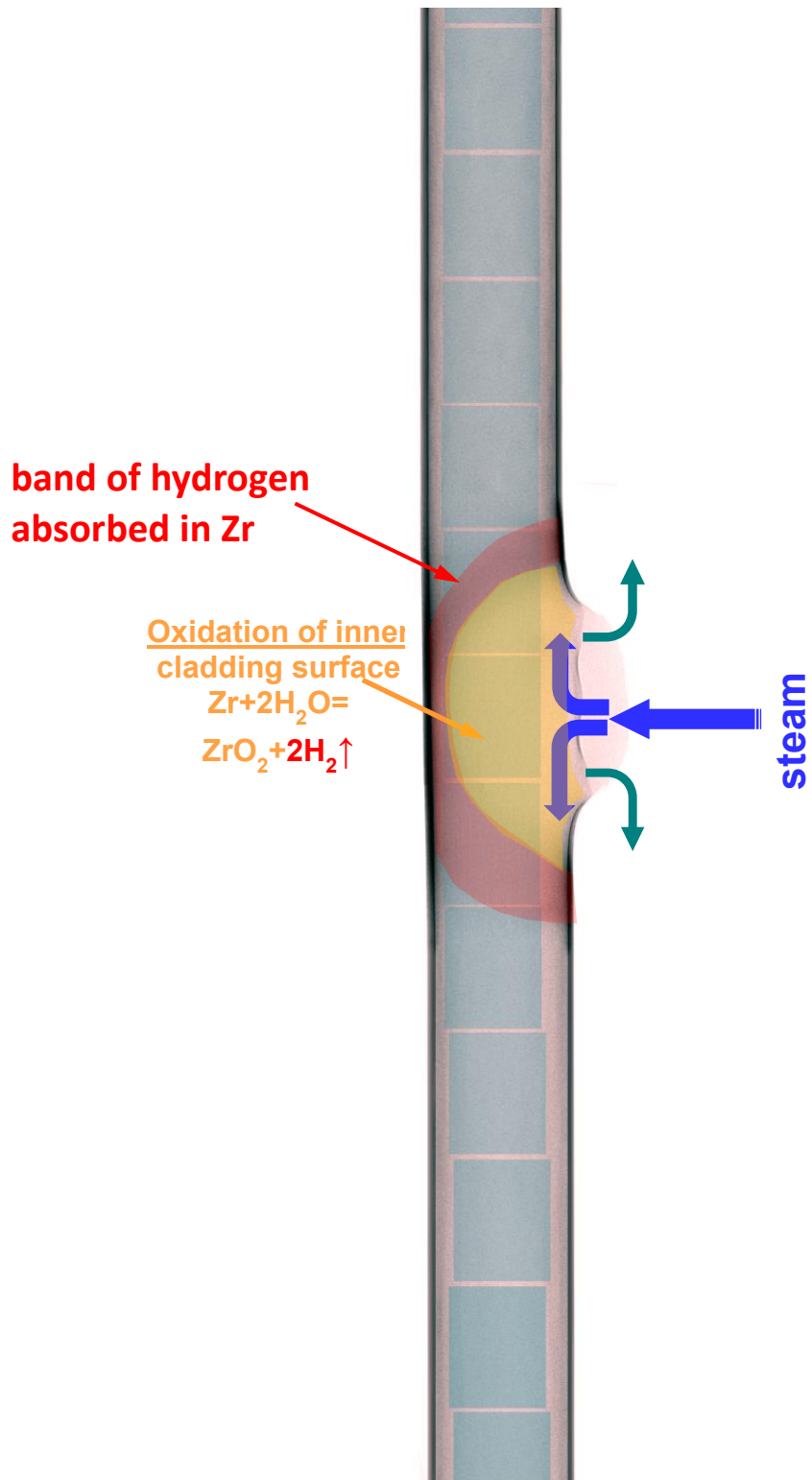
Figure 97   Mechanism of secondary hydrogenation.
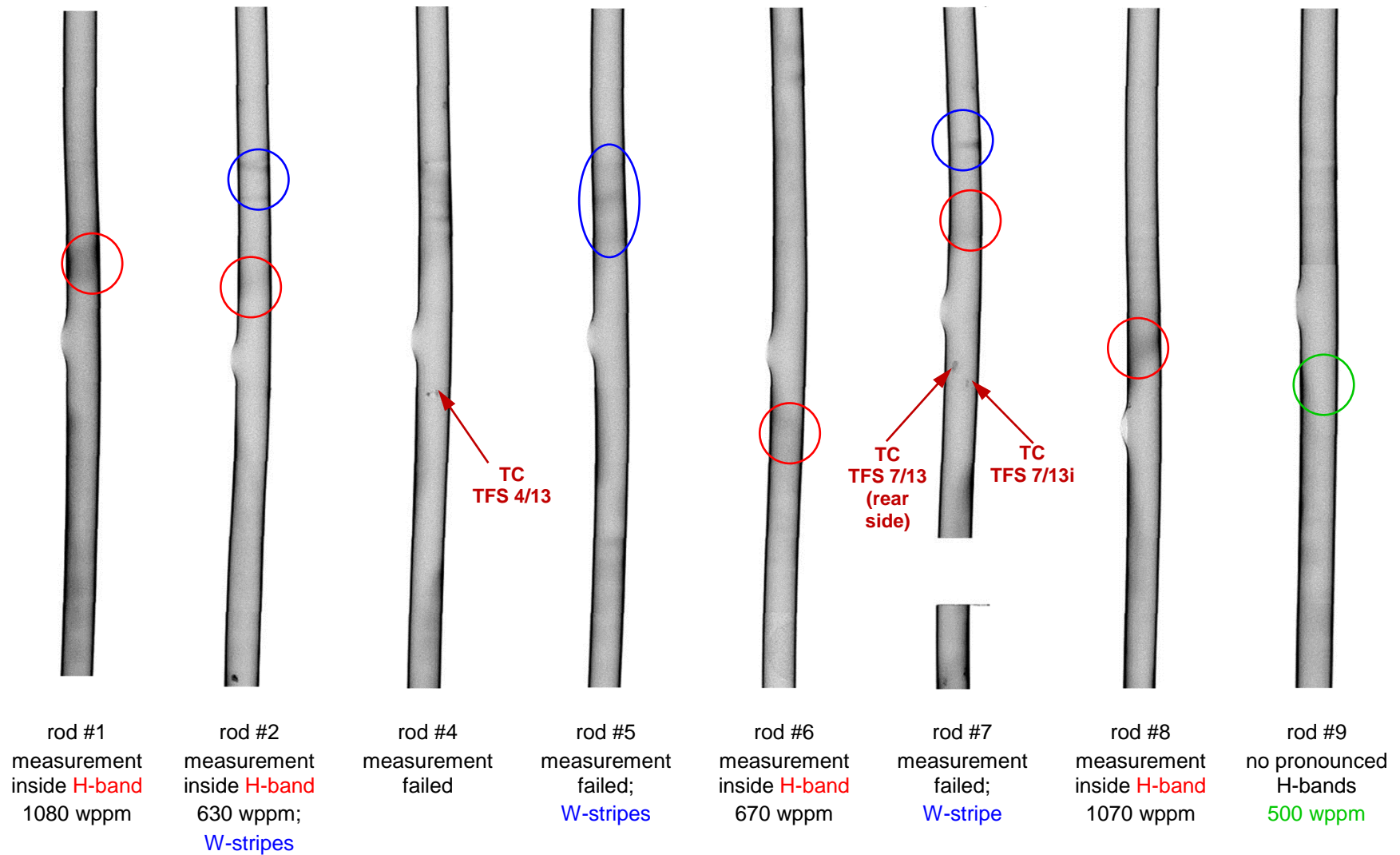
Figure 98   QUENCH-L2; Hydrogen bands on neutron radiographs of inner rods and maximum hydrogen content measured by neutron tomography.
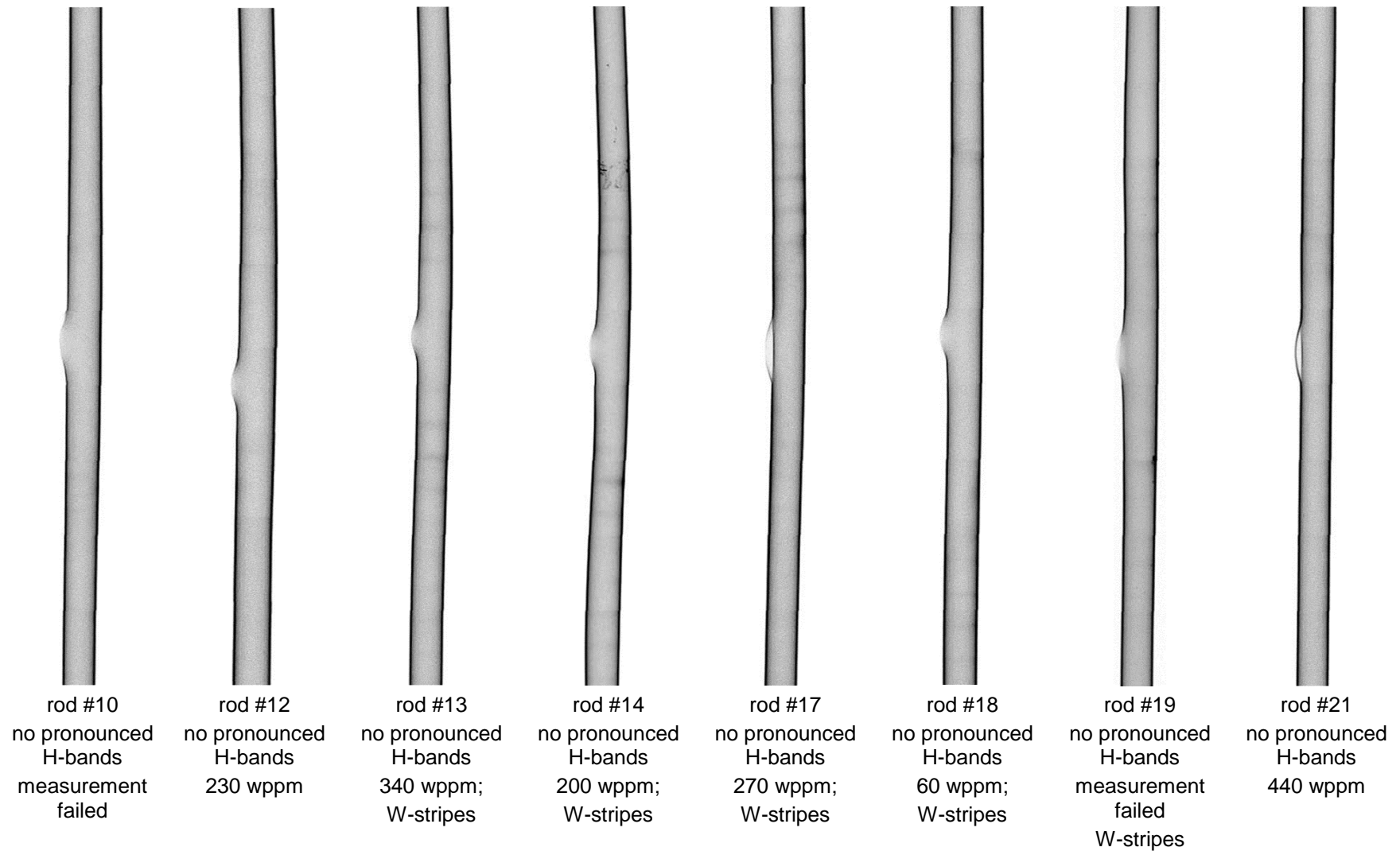
Figure 99   QUENCH-L2; Neutron radiographs of outer rods and maximum hydrogen content measured by neutron tomography.

rod #1   rod #2   rod #3   rod #4   rod #5   rod #6   rod #7   rod #8   rod #9
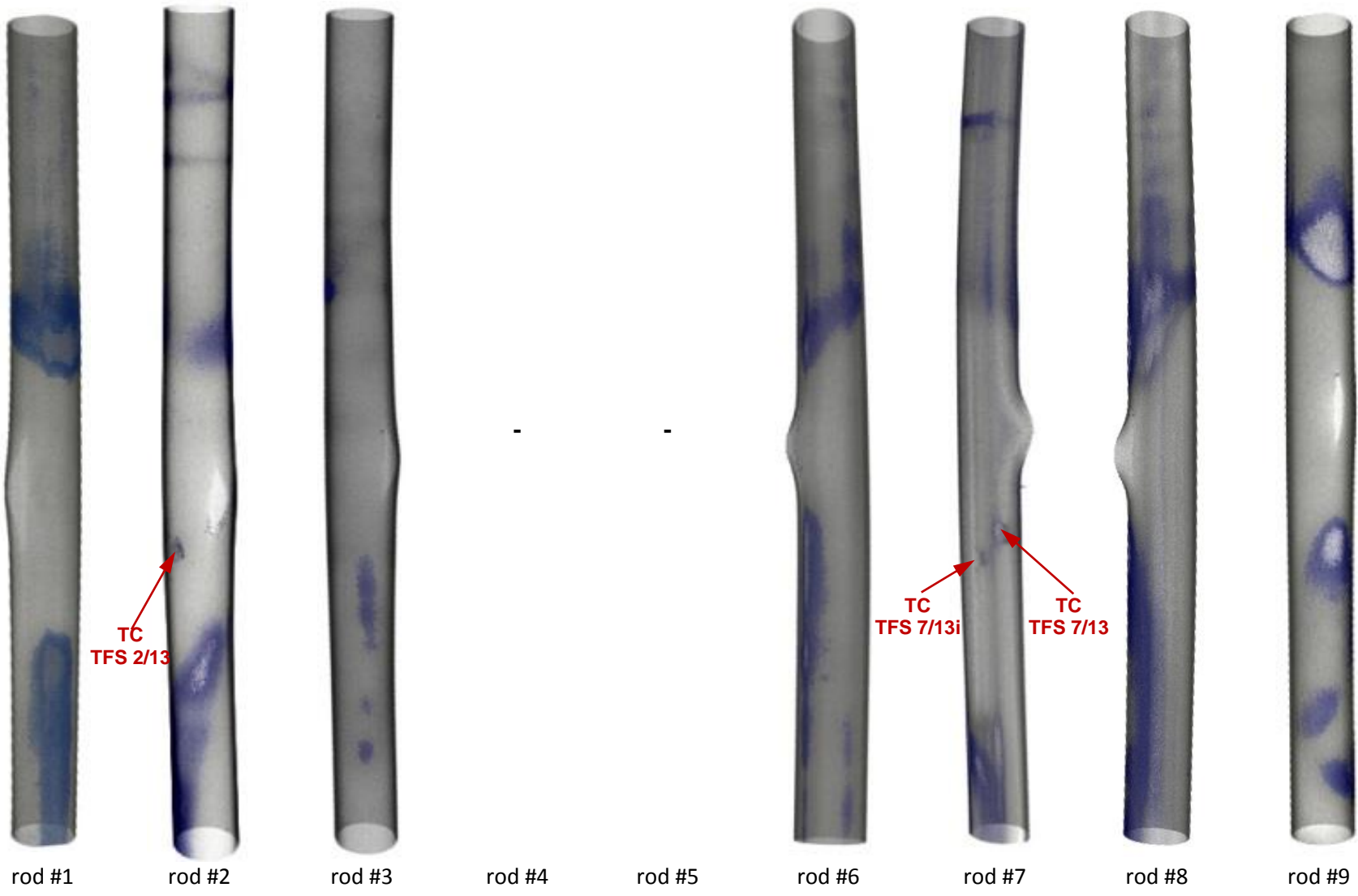
Figure 100   QUENCH-L2; tomography results for inner rods: hydrogen bands above burst opening and hydrogen spots below burst opening.

rod #12   rod #13   rod #14   rod #16   rod #17   rod #18   rod #20   rod #21
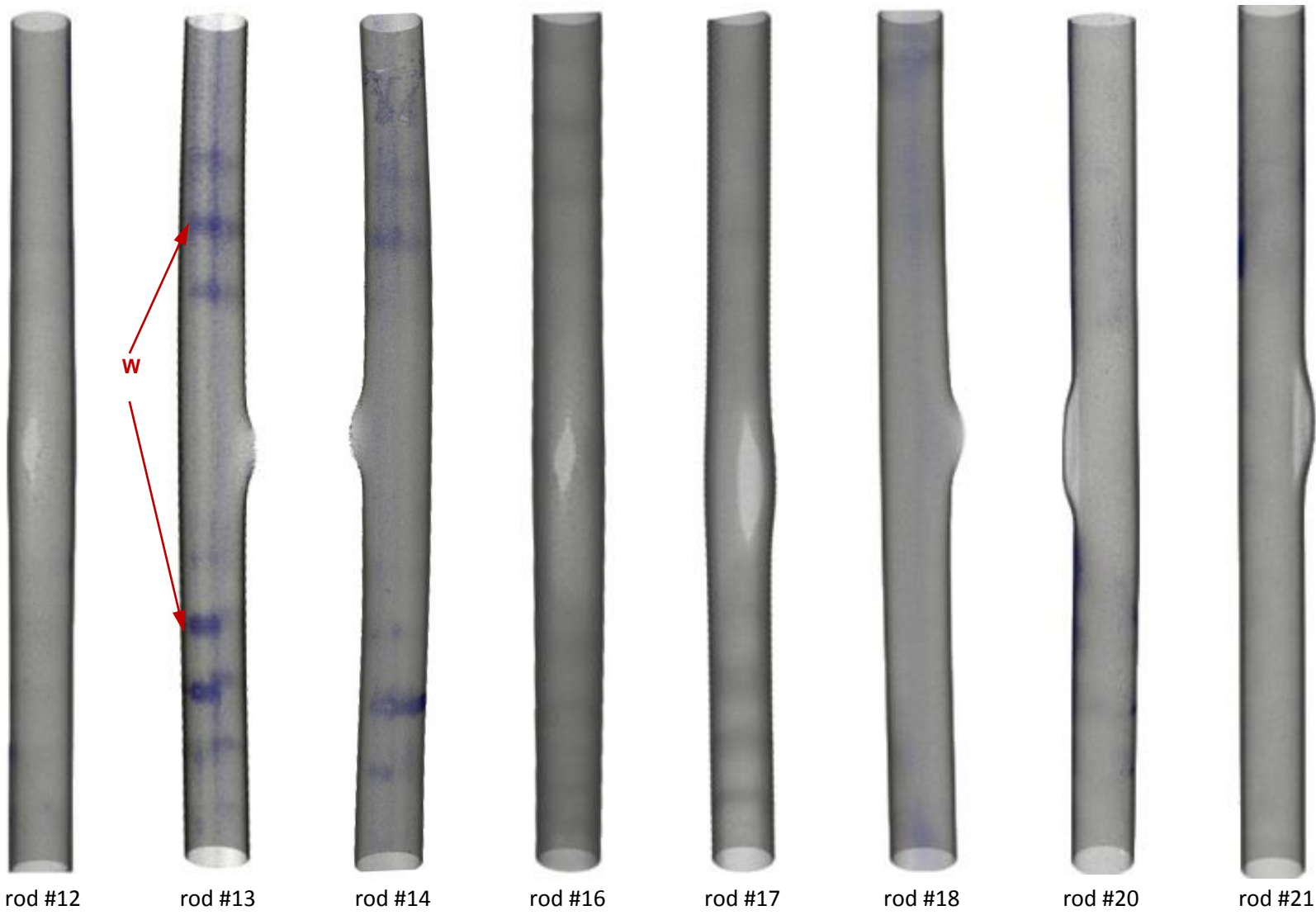
Figure 101   QUENCH-L2; tomography results for outer rods: no hydrogen bands and spots; formation of tungsten (evaporated from heaters) strips.
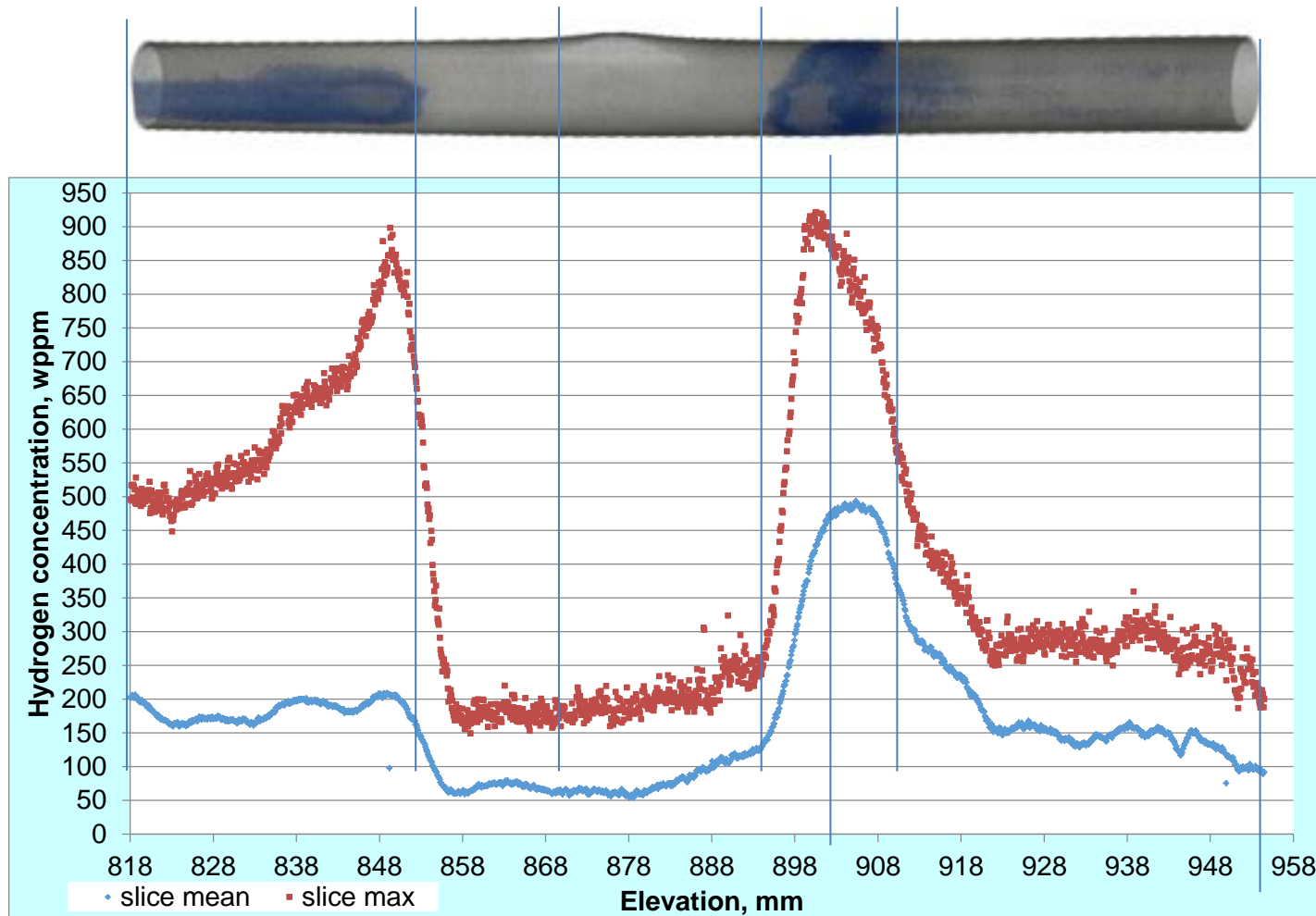
Figure 102   QUENCH-L2; correspondence between reconstruction of tomography image and plots of mean and maximal hydrogen concentrations (calculated for each cross section slice of 75 μm width) in rod #1: hydrogen band above and hydrogen spot below burst opening.
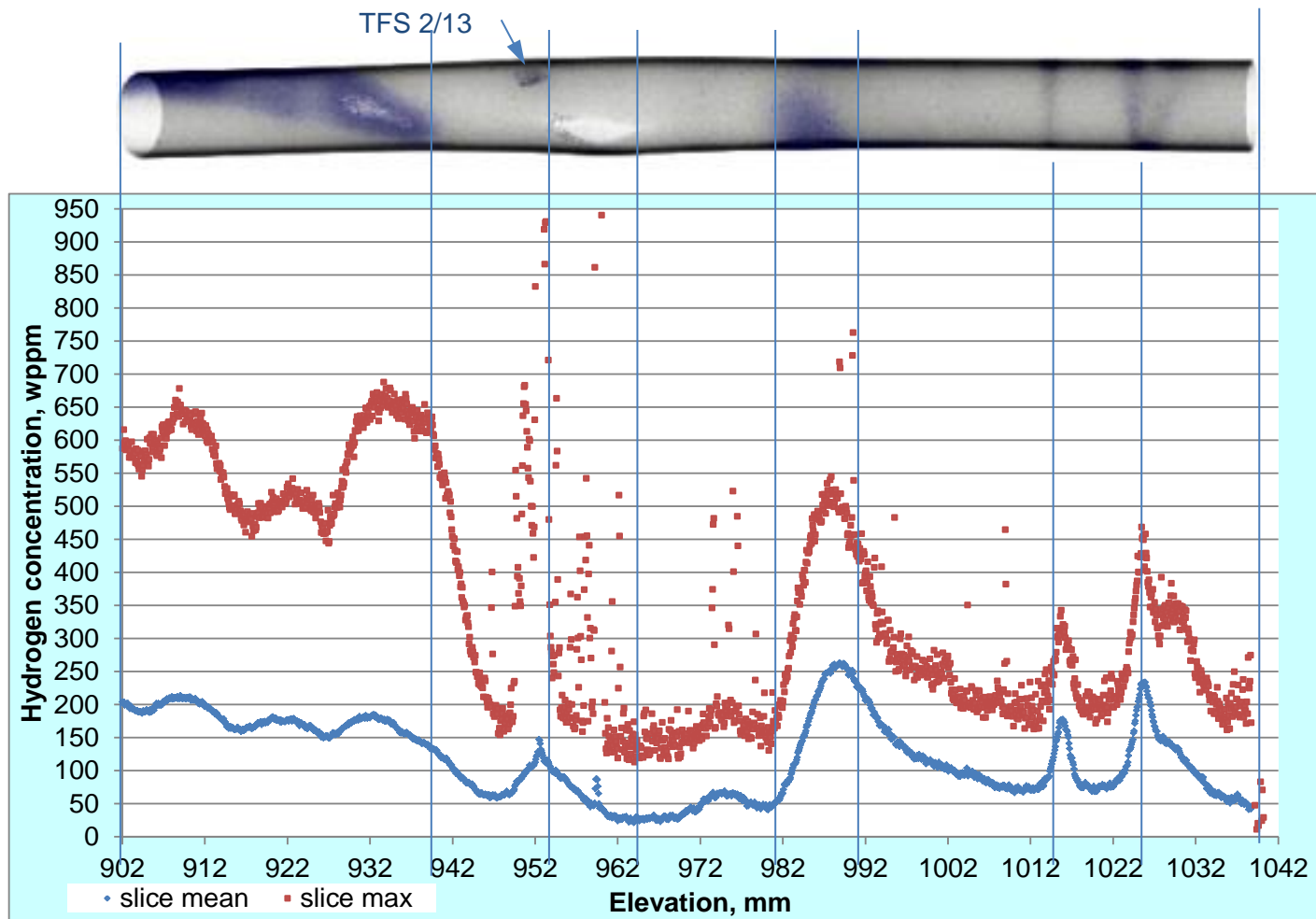
Figure 103 UENCH-L2; correspondence between reconstruction of tomography image and plots of mean and maximal hydrogen concentrations (calculated for each cross section slice of 75 μm width) in rod #2: hydrogen band above and hydrogen spot below burst opening, tungsten rings at the inner cladding surface between pellets.
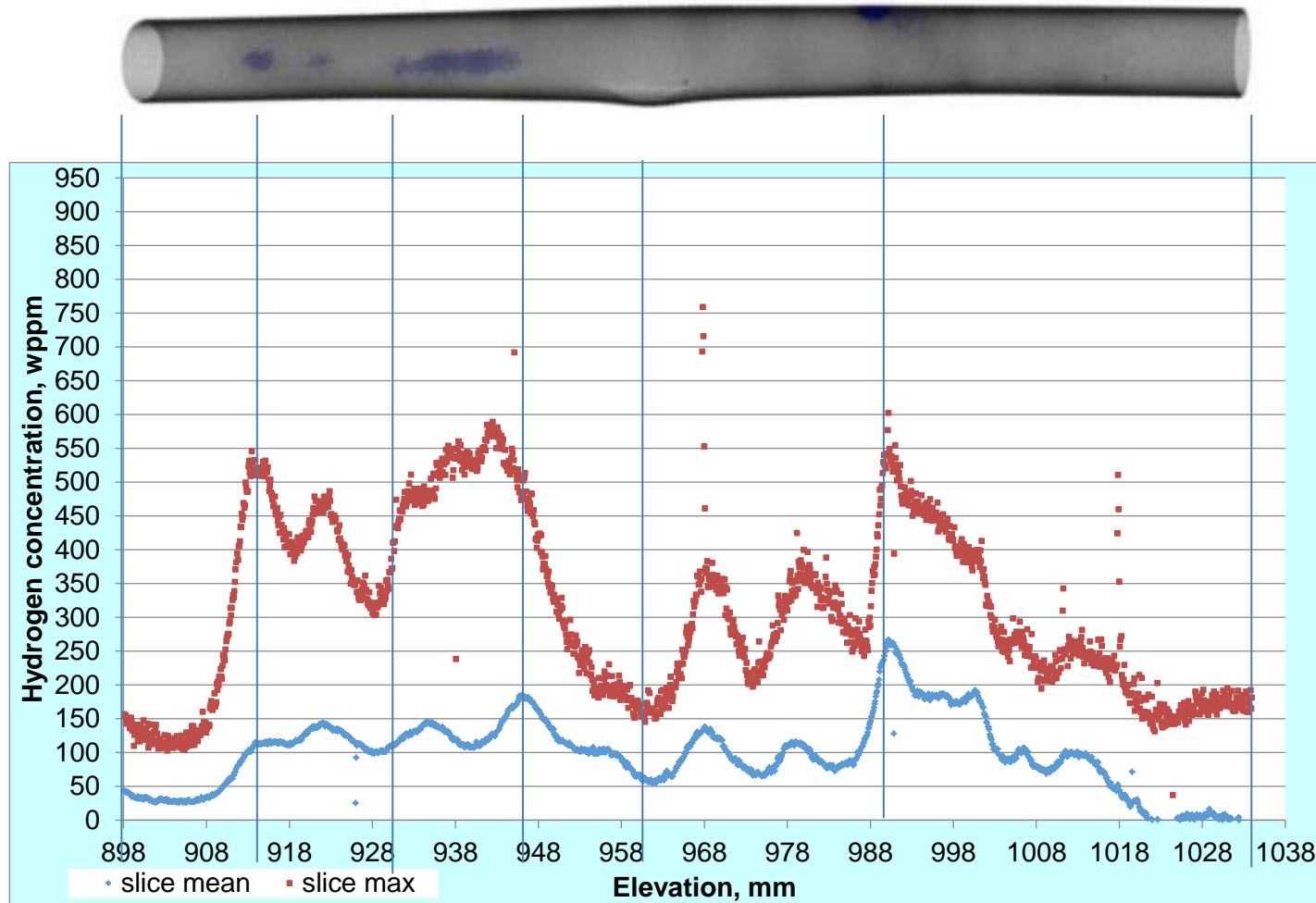
Figure 104   QUENCH-L2; correspondence between reconstruction of tomography image and plots of mean and maximal hydrogen concentrations (calculated for each cross section slice of 75 μm width) in rod #3: hydrogen spot below burst opening, tungsten rings between pellets.
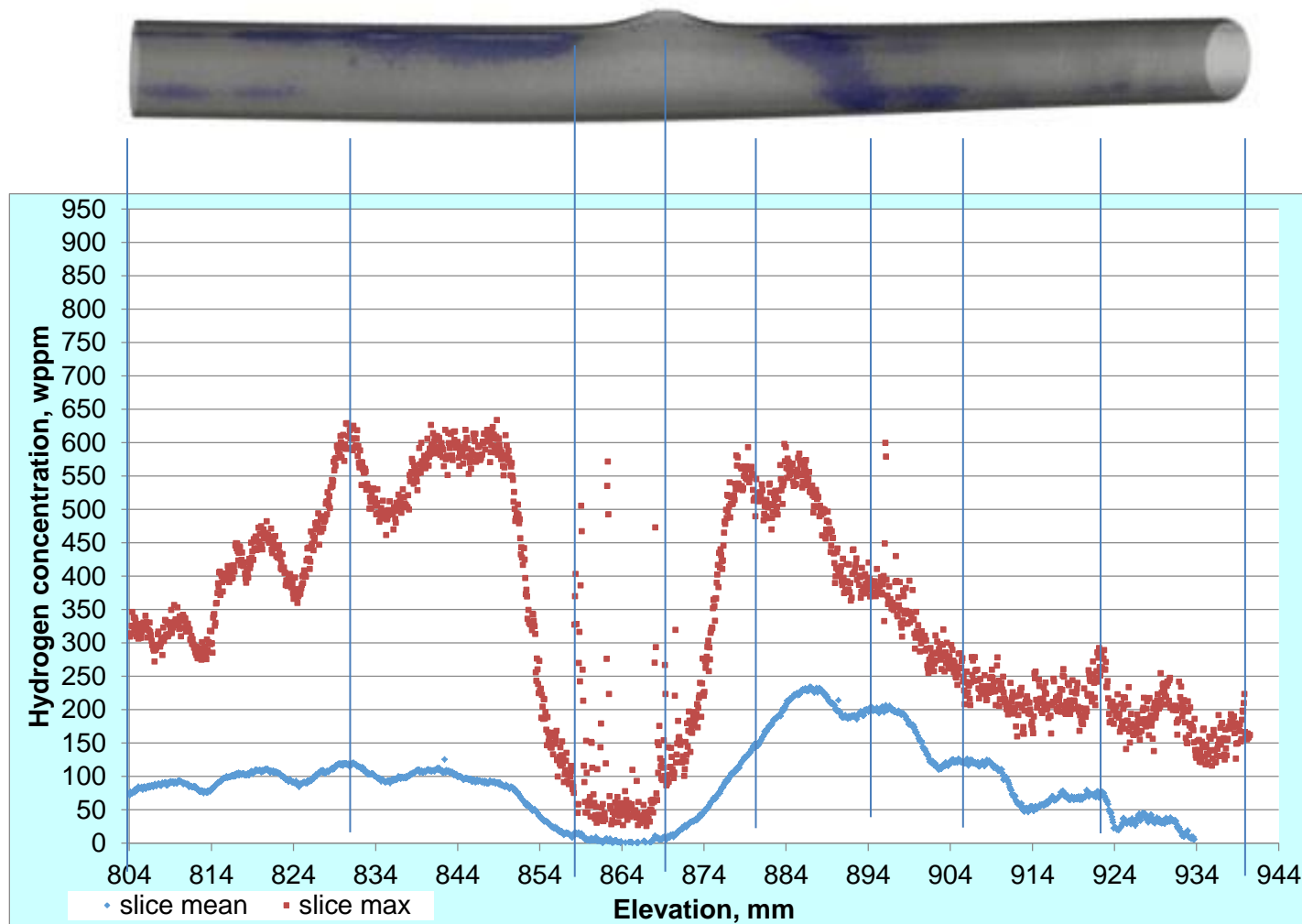
Figure 105   QUENCH-L2; correspondence between reconstruction of tomography image and plots of mean and maximal hydrogen concentrations (calculated for each cross section slice of 75 µm width) in rod #6: hydrogen band above and hydrogen spot below burst opening.
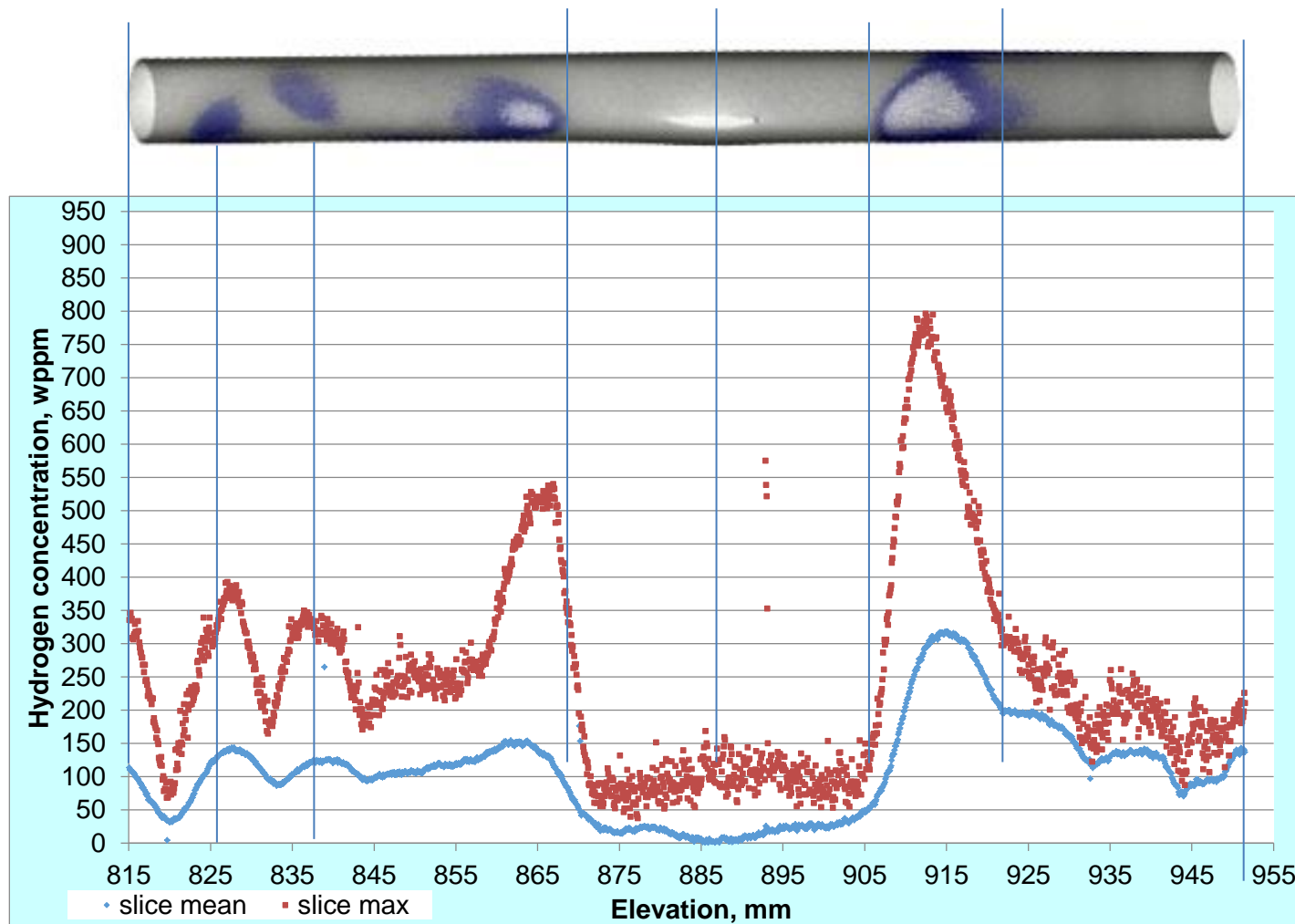
Figure 106 QUENCH-L2; correspondence between reconstruction of tomography image and plots of mean and maximal hydrogen concentrations (calculated for each cross section slice of 75 µm width) in rod #9: hydrogen band above and hydrogen spots below burst opening.
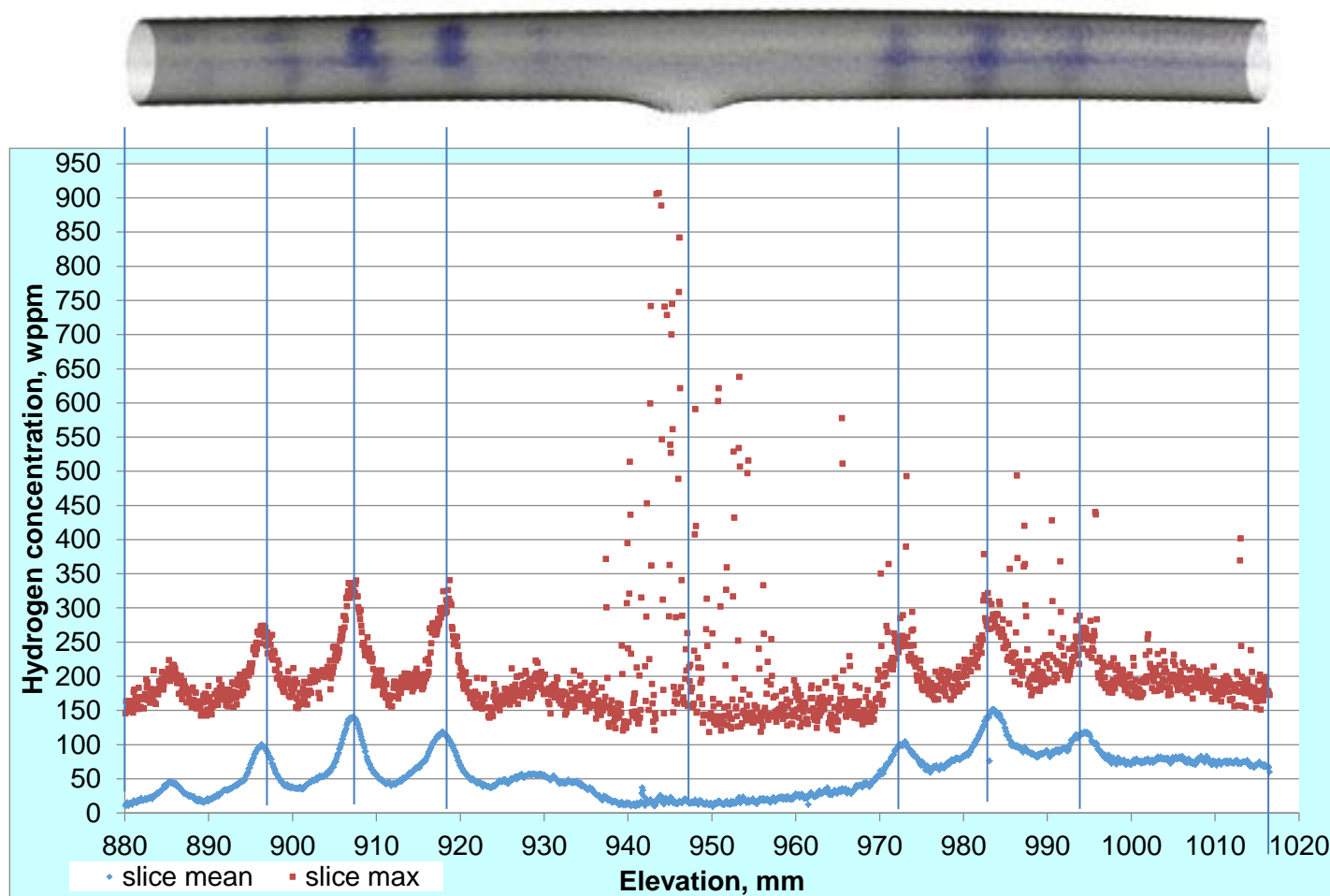
Figure 107   QUENCH-L2; correspondence between reconstruction of tomography image and plots of mean and maximal hydrogen concentrations (calculated for each cross section slice of 75 µm width) in rod #13: tungsten rings at the inner cladding surface between pellets.
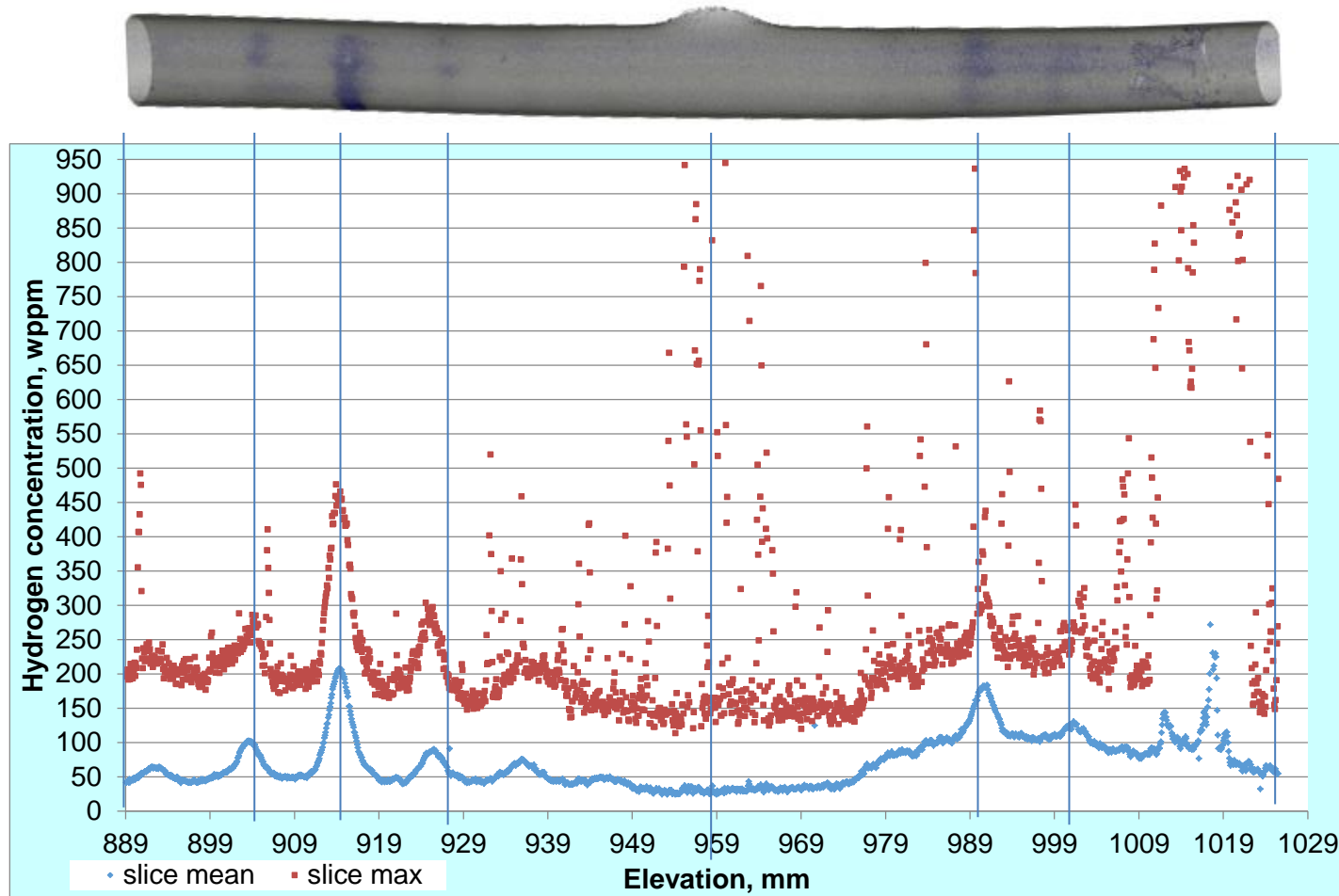
Figure 108 QUENCH-L2; correspondence between reconstruction of tomography image and plots of mean and maximal hydrogen concentrations (calculated for each cross section slice of 75 μm width) in rod #14: tungsten rings at the inner cladding surface between pellets.
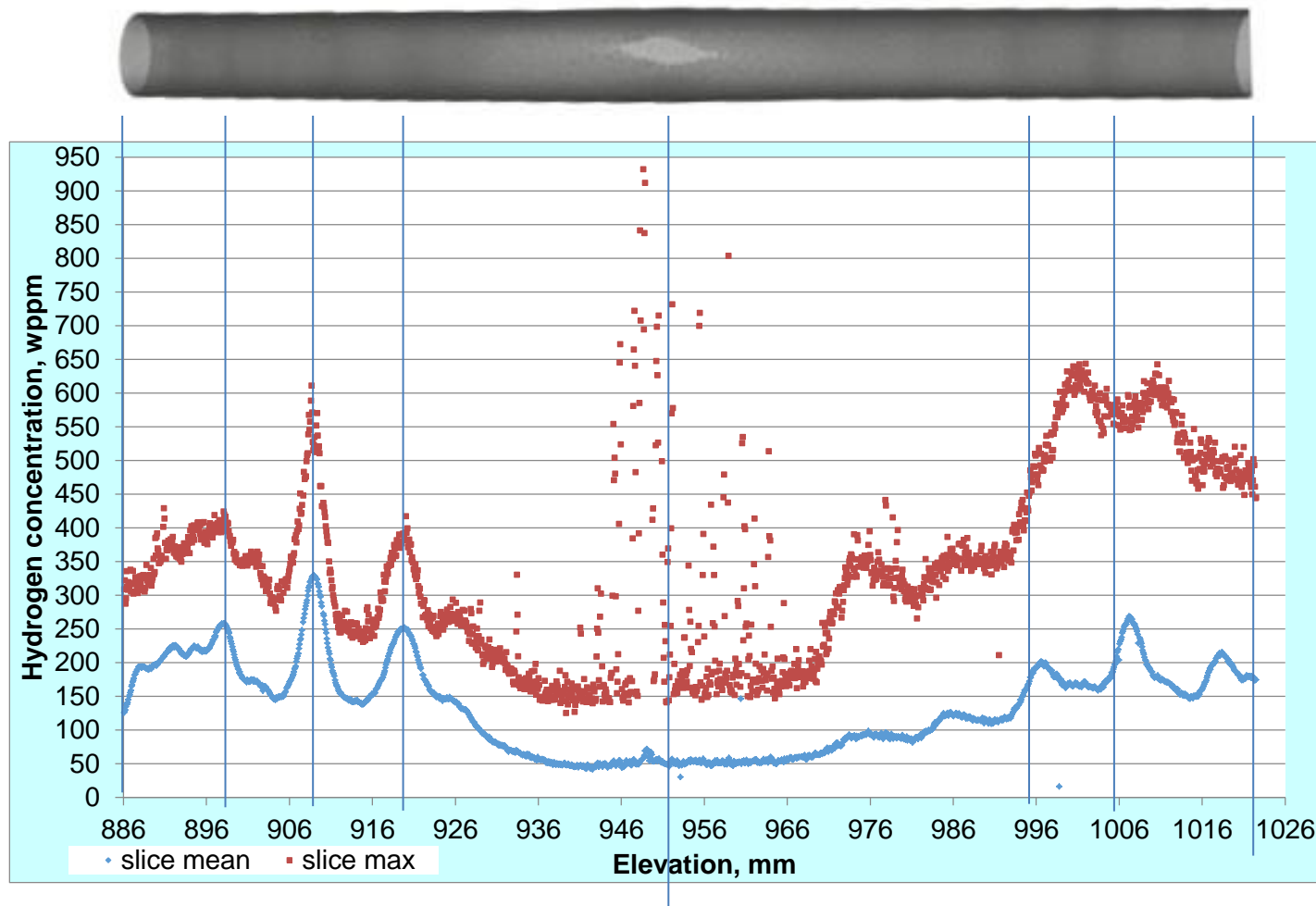
Figure 109   QUENCH-L2; correspondence between reconstruction of tomography image and plots of mean and maximal hydrogen concentrations (calculated for each cross section slice of 75 μm width) in rod #16: tungsten rings at the inner cladding surface between pellets.
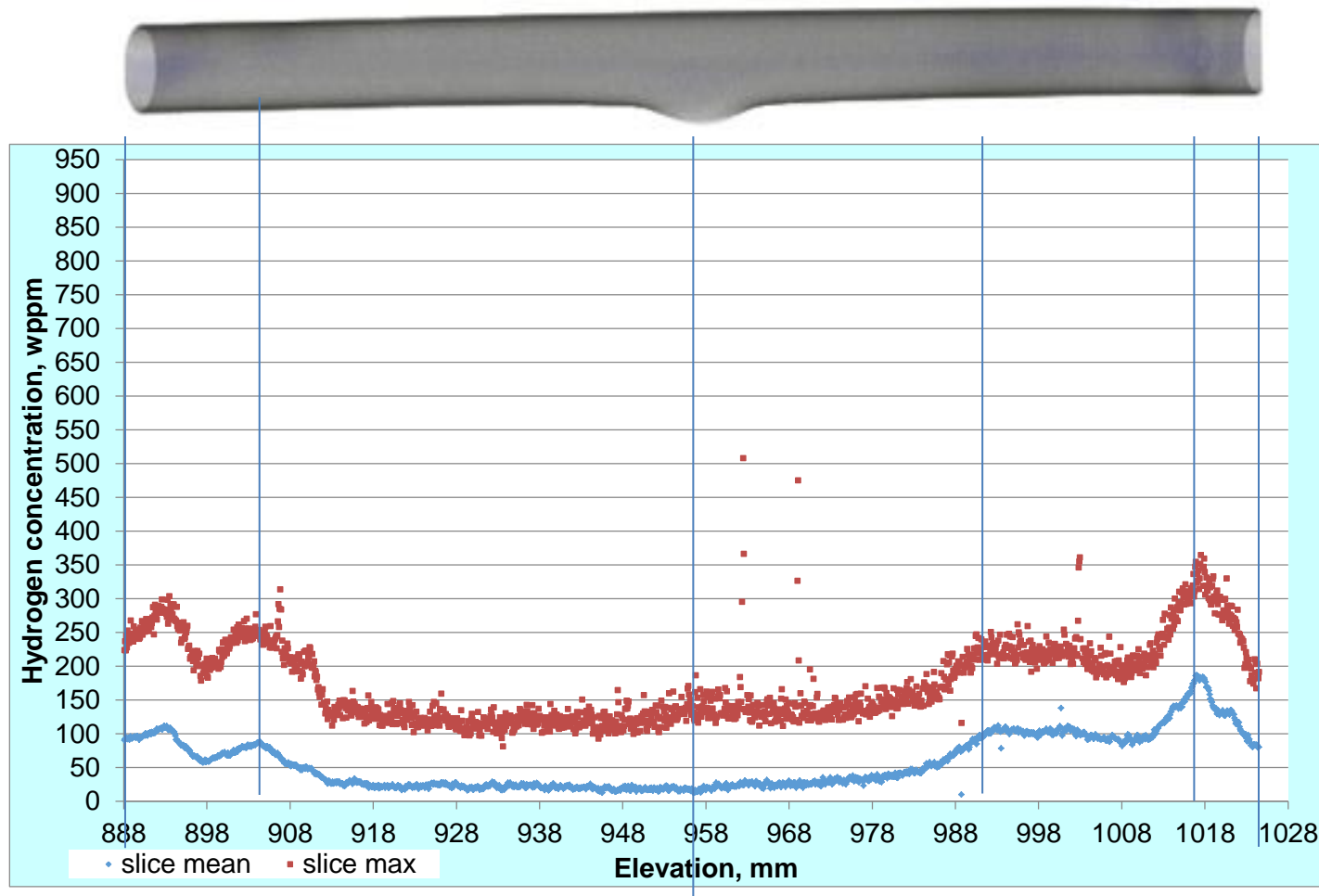
Figure 110   QUENCH-L2; correspondence between reconstruction of tomography image and plots of mean and maximal hydrogen concentrations (calculated for each cross section slice of 75 µm width) in rod #18: areas with low hydrogen content.
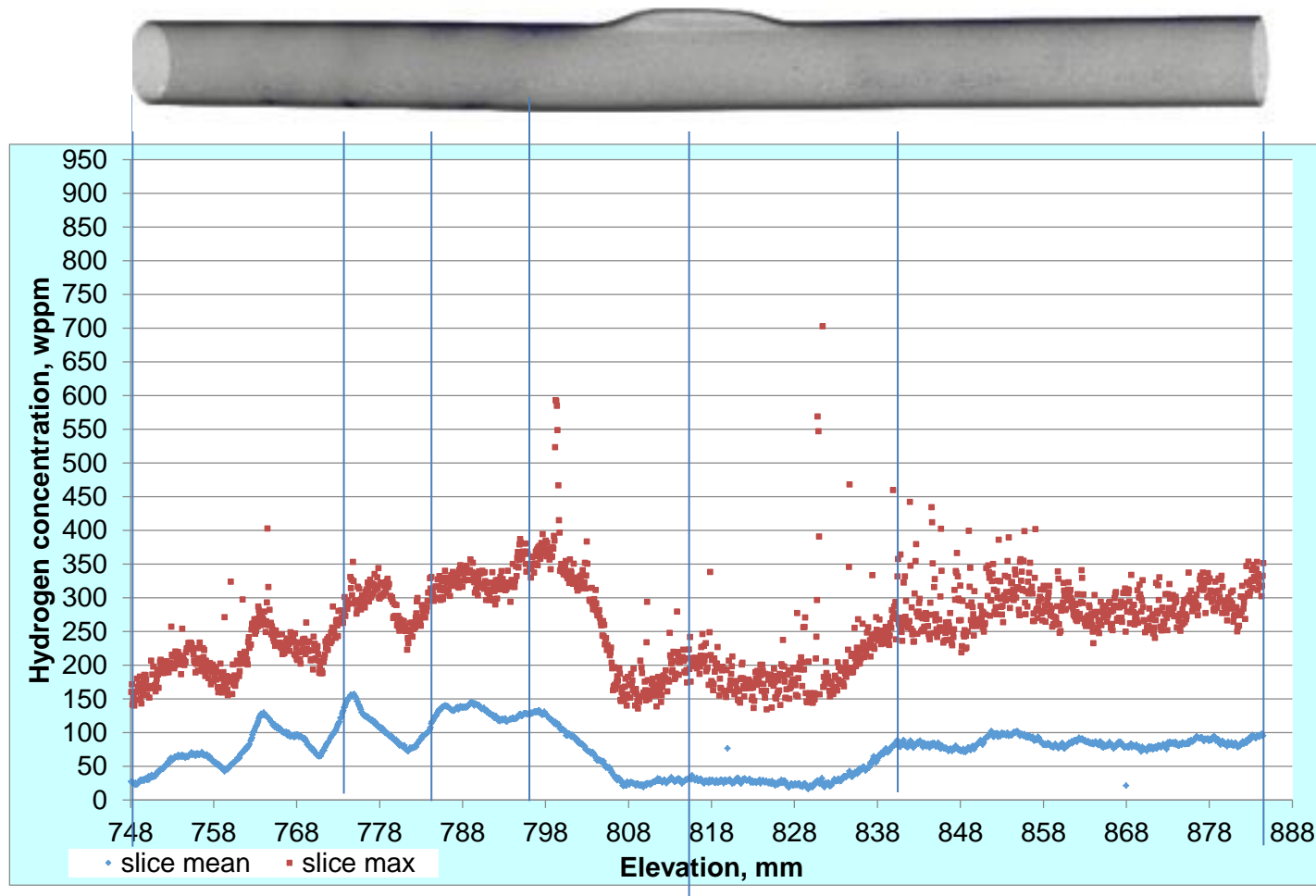
Figure 111   QUENCH-L2; correspondence between reconstruction of tomography image and plots of mean and maximal hydrogen concentrations (calculated for each cross section slice of 75 μm width) in rod #20: tungsten rings at the inner cladding surface between pellets.
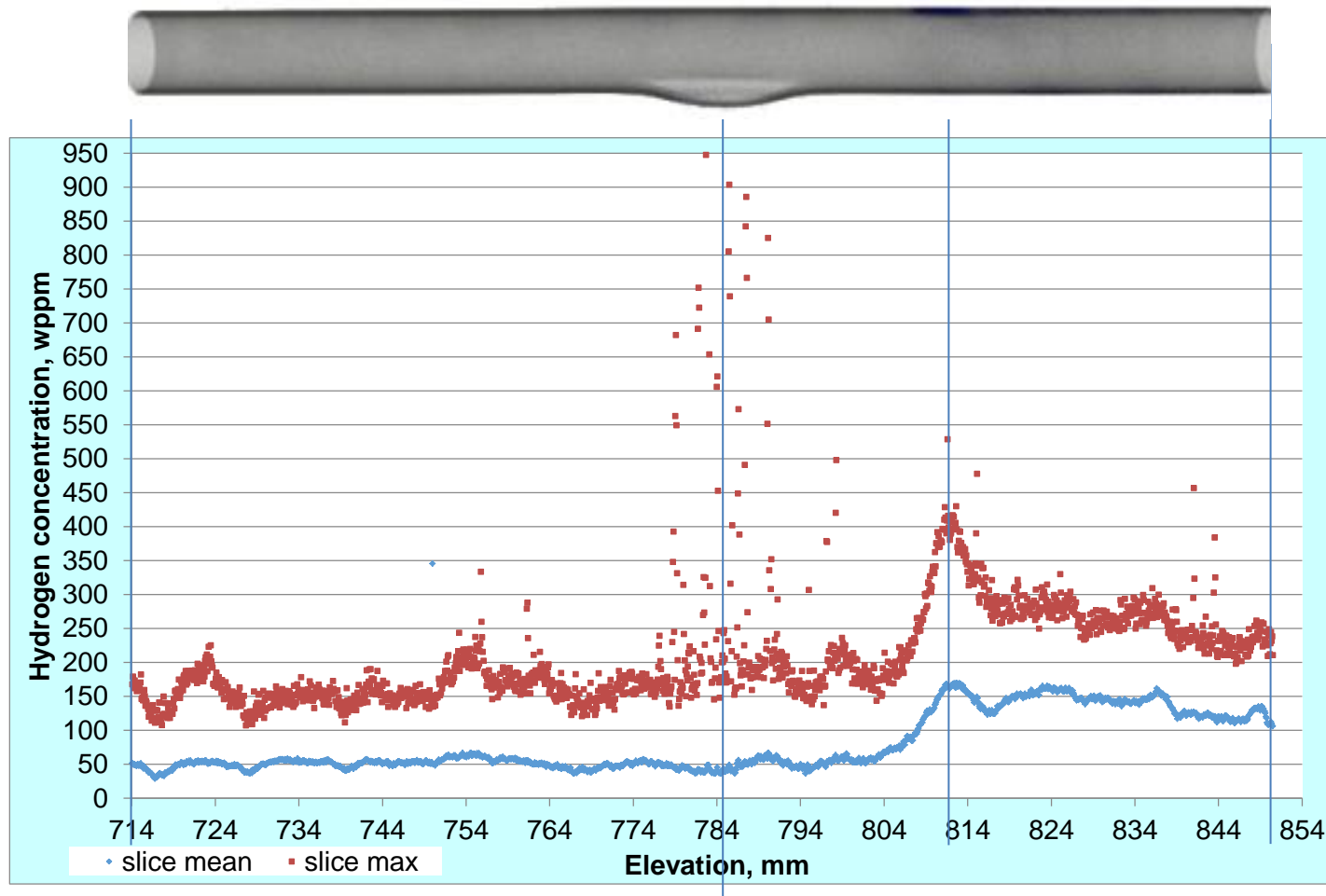
Figure 112   QUENCH-L2; correspondence between reconstruction of tomography image and plots of mean and maximal hydrogen concentrations (calculated for each cross section slice of 75 µm width) in rod #21: areas with low hydrogen content above burst opening.

rod #1: 875 mm

rod #2: 958 mm

rod #3: 961 mm

rod #6: 869 mm

rod #8: 875 mm

rod #9: 887 mm
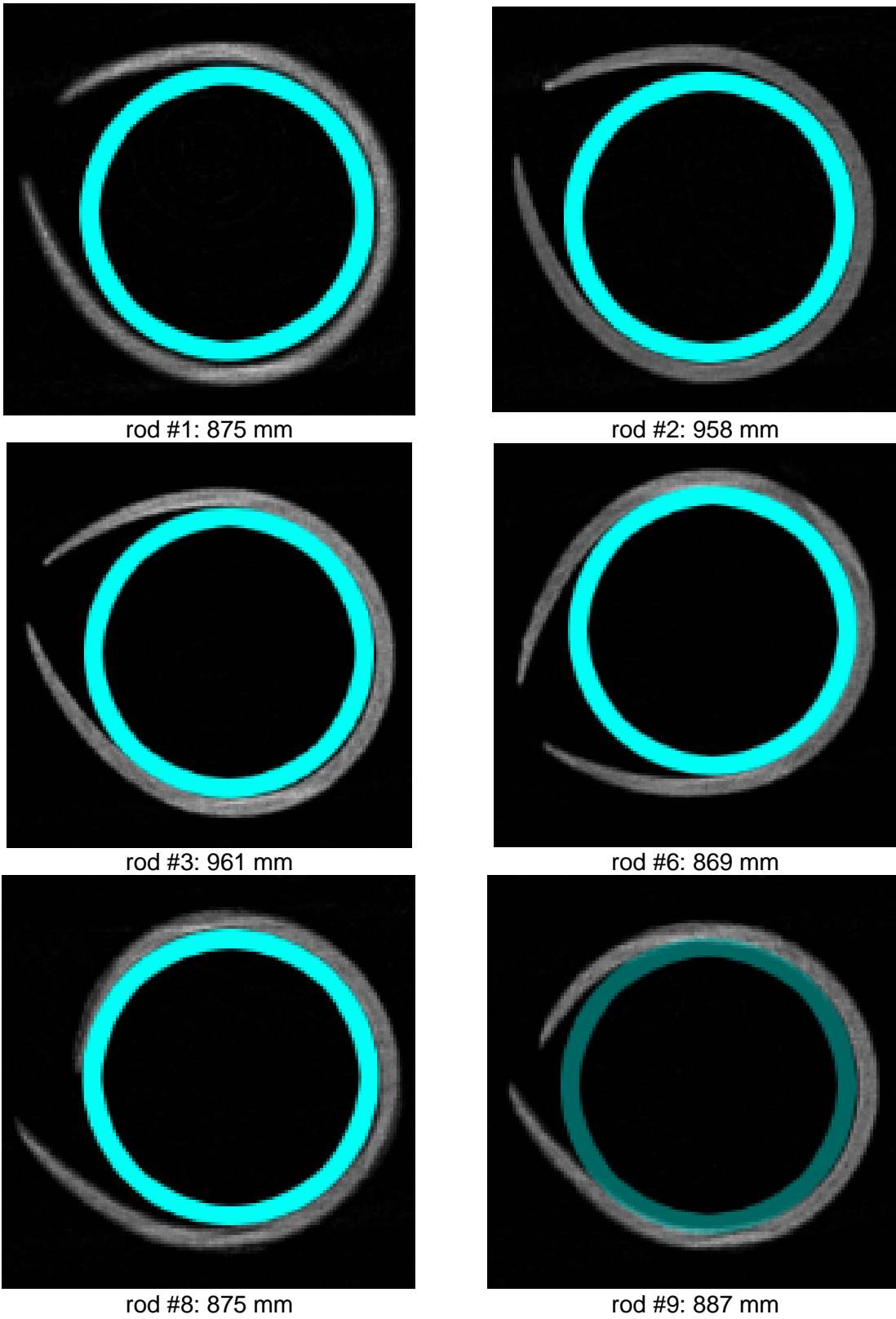
Figure 113   QUENCH-L2; comparison of tomography images at the axial middle of burst opening with initial (pre-test) cladding cross section (OD=10.75 mm; wall thickness 725 μm).

Figure 114   QUENCH-L2; claddings after tensile tests.

Figure 115   Failure modes of post tensile tested QUENCH-LOCA claddings; left: M5® (QUENCH-L2) and right: Zircaloy-4 (QUENCH-L0 and QUENCH-L1).
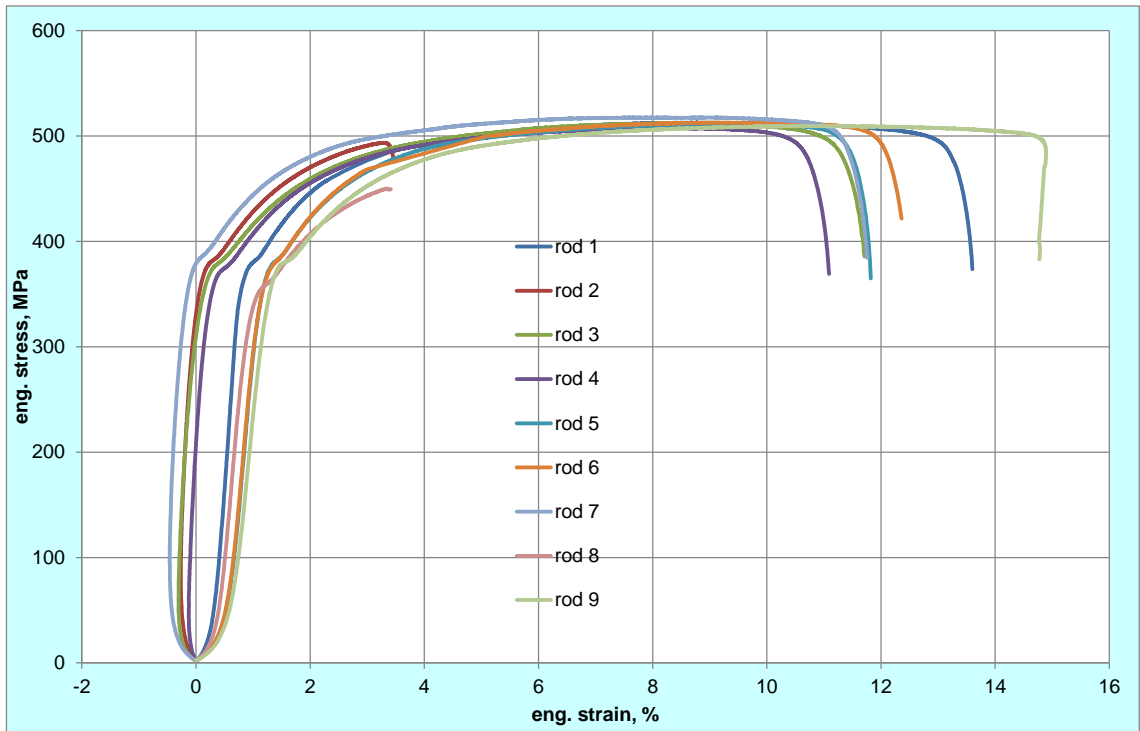
Figure 116   QUENCH-L2; results of tensile tests with claddings of the inner rodgroup.
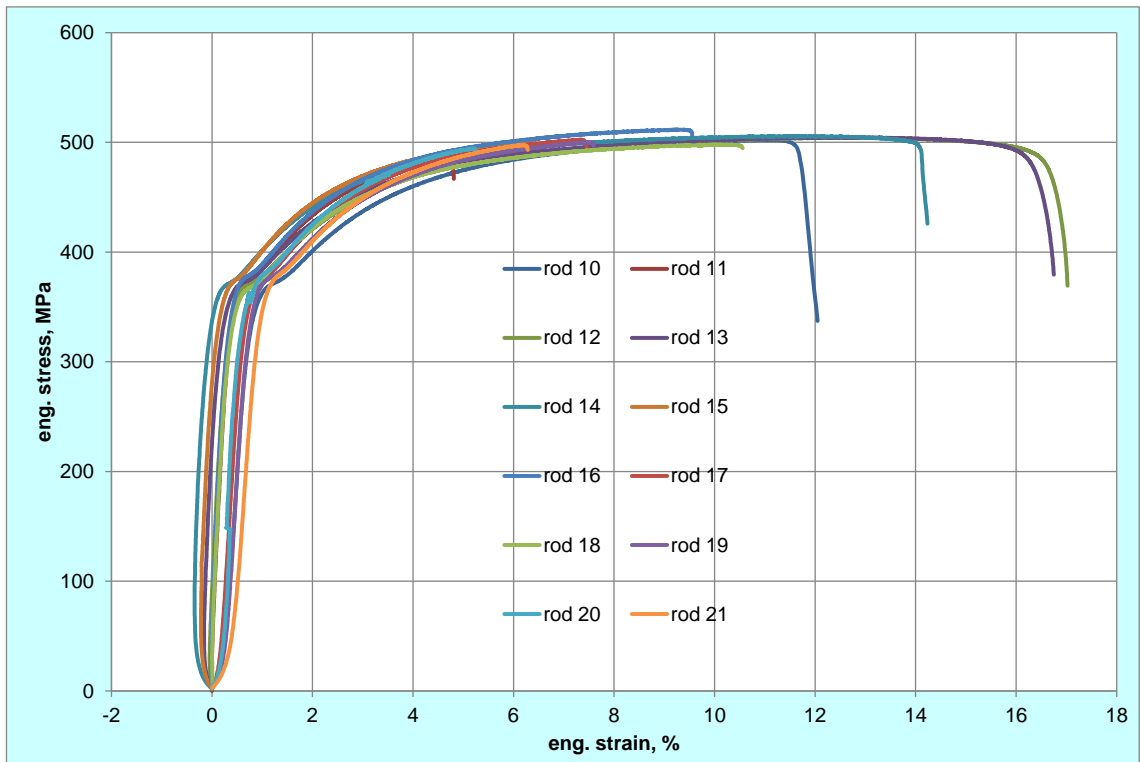
Figure 117   QUENCH-L2; results of tensile tests with claddings of outer rods.

Appendix A. Results of single effect tests

A. Pshenichnikov, J. Stuckert

Several investigations of specially hydrogenated cladding tubes were performed for detailed analysis of microstructure and its influence on mechanical properties of tubes.

1   Metallographic investigations

Change in the microstructure of M5[®] alloy was investigated by means of light microscopy with interference contrast.

At first several probes were annealed in argon to detect a degree of an annealing impact on the microstructure. Samples were heat treated in the LORA furnace at the temperatures of 600, 700, 800, 900 and 1000 °C during 8 minutes and then withdrawn to the air atmosphere. The mass gain of these probes (due to post-test oxidation in air) was used as the reference one to calculate the hydrogen content in further hydrogenated probes. If there were any mass gain due to gas mixture impurities, they were automatically included in the reference mass and thus not affect the result of the hydrogen content estimation.

The other probes were charged to different hydrogen contents in argon/hydrogen gas mixture under temperatures of 600-900 °C. Table 1 shows the experimental results for each probe. Hydrogen content was calculated on the basis of mass gain with a correction of gain during temperature treatment in pure argon without hydrogen.

The length of all tube samples was 150 mm.

Table A1.   Parameters of investigated samples.

Name	Temperature	H_2 duration	H_2 rate	H_2 (mass gain)
	°C	min	cm³/min	wppm
H22M5	600	2	530	**306**
H23M5	600	6	530	**1955**
H19M5	700	2	530	**1700**
H20M5	700	4	530	**1858**
H21M5	700	8	530	**3555**
H1RM5	800	4	530	**590**
H14M5b	800	8	530	**2643**
H15M5	800	16	530	**4523**
H12M5	900	4	2673	**4538**

Preparations for metallography were made in the following order: the samples were embedded into epoxy and then grinded with abrasive paper 500, 800, 1000, 2400, 4000 for approximately 45 seconds each. Then samples were polished with 3 µm diamond particles under load of 25N during 6 minutes and then etched in two stages:

1st stage. Etch polishing with cotton swab during 15-20 seconds in solution of 45 ml glycerin; 45 ml HNO$_3$; 10 ml HF.

2nd stage. Immerse etching during 10 seconds in solution of 60 ml glycerin; 10 ml HNO$_3$; 20 ml HF.

Then the specimens were rinsed in running water for 5 minutes.

After this treatment one can see microstructure without deformed layer which is always a problem during zirconium alloy sample preparation.

1.1 Metallographic investigations of M5 samples <u>annealed</u> in Ar

as received

600 °C

700 °C

800 °C

900 °C

1000 °C
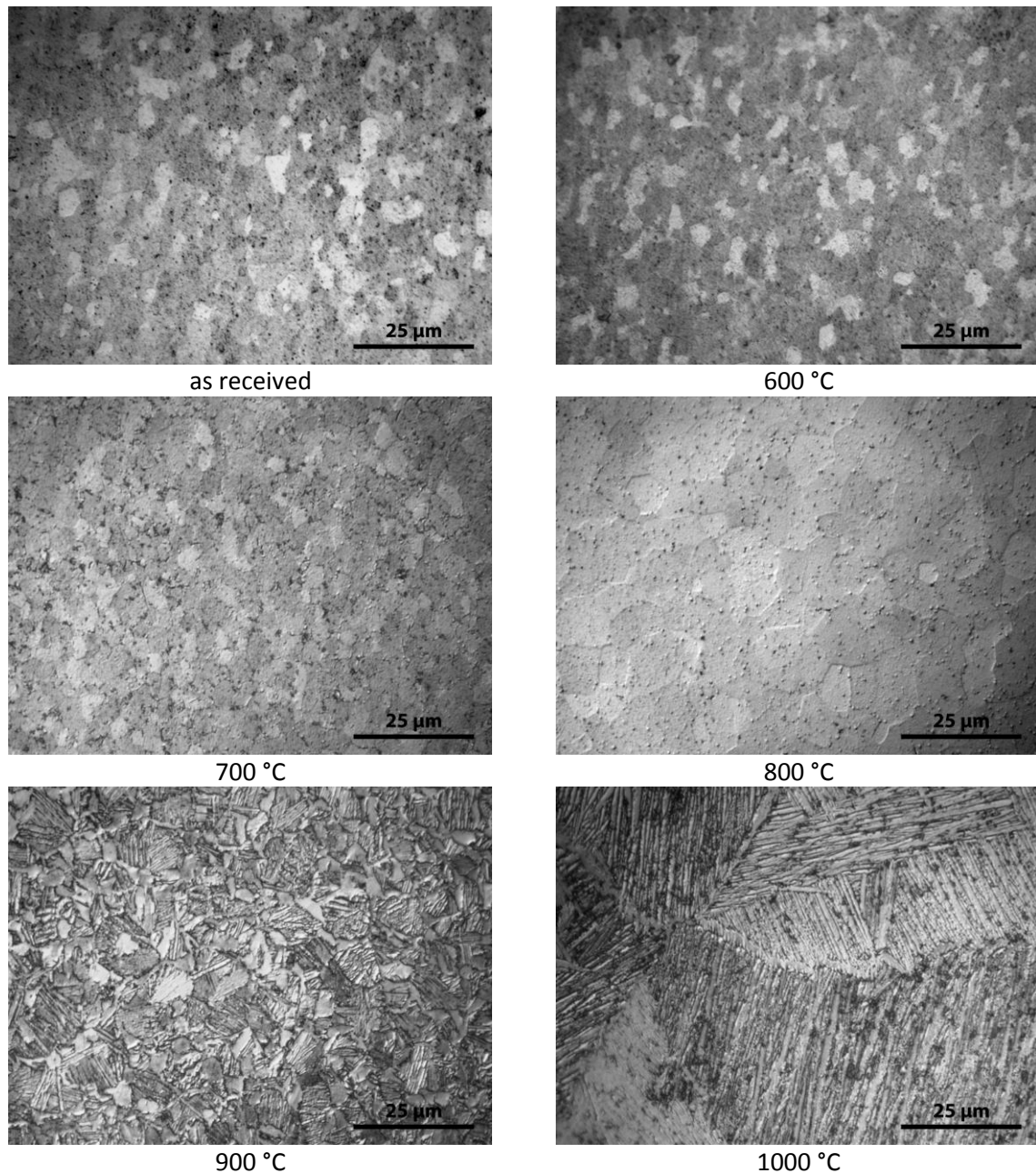
Figure A1   M5 samples annealed during 8 minutes in argon at different temperatures.

It is very important to understand the difference between hydrogen-induced and thermal-induced changes in microstructure. A series of annealing tests were performed in Ar atmosphere. The samples were threated

under temperatures of 600, 700, 800, 900 and 1000 °C during 8 minutes and then were quickly cooled in air. In the following images the structure evolution of these samples is presented (Fig. A1).

The structure of as-received sample is usual grain structure with average grain size of about 2.5 μm across. Due to anisotropic properties of zirconium and his alloys one can see that nearly the half of the grains were etched with different speed. Some grains are bright and the others are dark due to orientation to polarised light. This is exactly what can be expected from texturized zirconium tube wall material.

Treatment in pure Ar at 600 °C during 8 min changed the structure of as-received sample. The grain shape tends to become equiaxed with the size of 3 - 5 μm. The structure is typical for annealed specimen below the temperature of phase transformation. After treatment in Ar atmosphere at 700 °C during 8 minutes the microstructure is the similar as it was at 600 °C. Some grains become larger up to 8 μm due to started recrystallization. After treatment at 800 °C the grains become almost equiaxed and polygonal; one can see that the size is also increased up to 8 μm; some grains can be up to 15 μm.

After treatment at 900 °C the traces of the beginning of $\alpha \rightarrow \beta$ - transformation was observed; the structural parameters have been changed. Small 3 - 5 μm grains clean from inclusions, which were absent at the previous stage, are formed simultaneously with black and white stripy regions result from reverse $\beta \rightarrow \alpha$ martensitic type of transformation during cooling phase. After 8 minutes at 1000 °C microstructure was fully transformed. All the grains transformed into needles and combined to large recrystallized regions. These regions obviously consisted of the same-oriented sub-grains due to the same shade of grey on the image. The inclusion particles migrated towards the boundaries of various types thus arranging themselves into thin chains. The size of the big regions of same-oriented sub-grains was about 100 μm.

1.2 Results on metallographic observations of <u>hydrogenated</u> M5

In the presence of hydrogen completely different consequence of structure development was detected (<u>Fig. A2 and Fig. A3</u>).
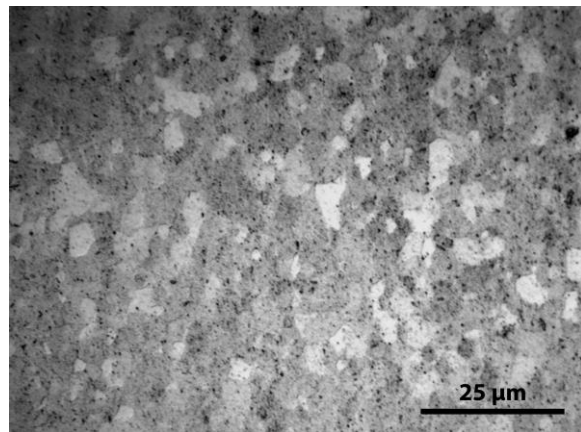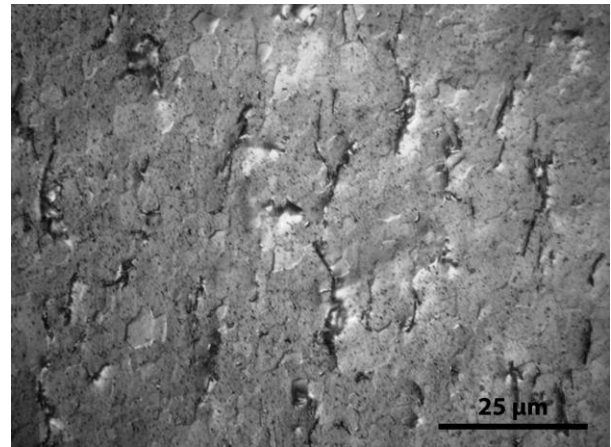
as - received   600 °C, 120 s
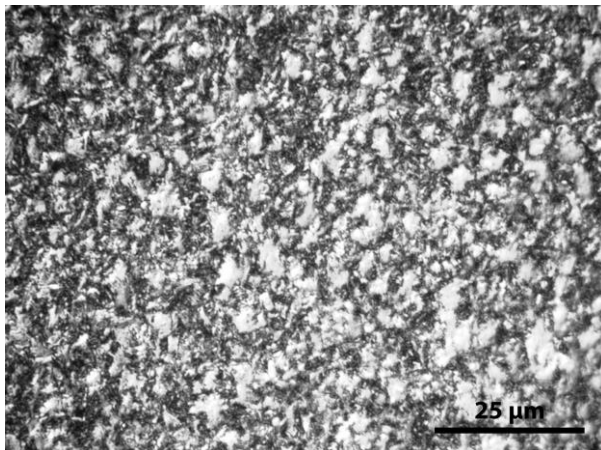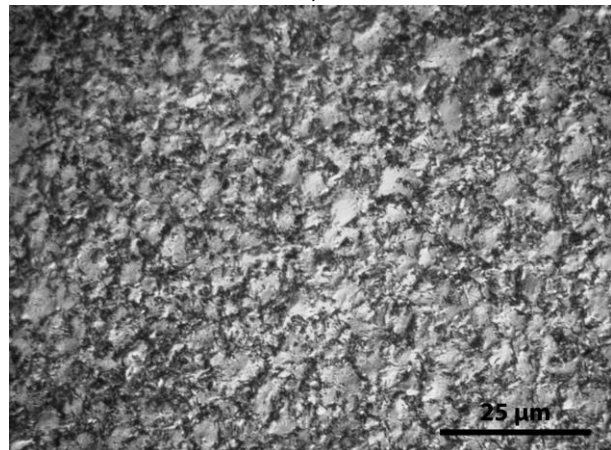
600 °C, 360 s   700 °C, 120 s
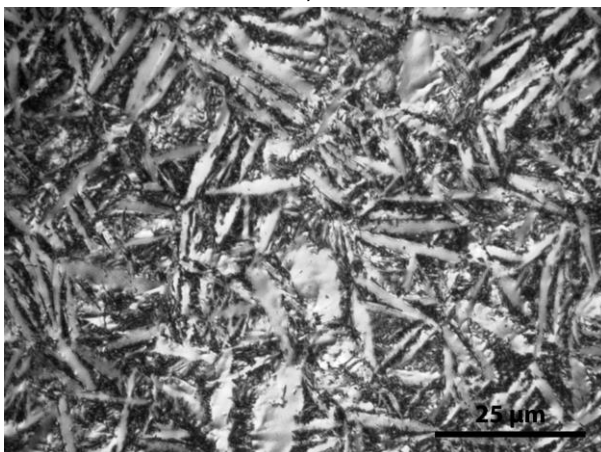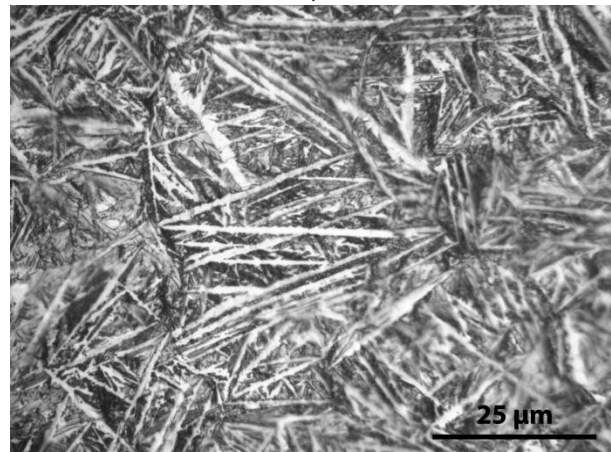
700 °C, 240 s   700 °C, 480 s

Figure A2   M5 samples hydrogenated at 600 and 700 °C during different durations.

<u>The grain structure of sample hydrogenated at 600 °C during 120 s in argon-hydrogen</u> atmosphere is not changed: average grain size was about 2.5 µm across. The black segmented stripes of 3.5 µm length and 0.2 µm width were observed. They are oriented in the tube longitudinal direction. Several stripe segments have declination of up to 45° to the longitudinal direction. These black stripes are supposed to be hydrides as there

were no such features in annealing experiments. This probe has the lowest level of absorbed hydrogen. Obviously no phase transformation was take place at all. And all hydrogen is probably precipitated as hydrides. In order to detect the presence and spatial distribution of the second phase it is necessary to perform the electron back scattered diffraction investigation, which enable phase map reconstruction and detailed analysis of the

The grain structure of sample hydrogenated at 600 °C during 360 s changed slightly. The grain boundaries have become non‑equilibrium. Grain size is of approximately 2.5 µm. Here the very beginning of the phase transformation can be observed.

Microstructure after Hydrogenation during 120 s at 700 °C has almost the same appearance as for 600 °C 360 s. The same features can be observed. The structure of grain boundary has changed. A process of recrystallization started to emerge, because the grain size raised a little and here it is about 3.2 µm. One can see a lot of beta phase nuclei.

The sample hydrogenated at 700 °C during 240 s shows significant phase transformation with acicular prior β‑ phase structure. Needles are approximately 12 µm length and 1.6 µm wide. But there are also the small islands of previous α‑phase.

800 °C, 240 s

800 °C, 480 s

800 °C, 960 s

900 °C, 240 s
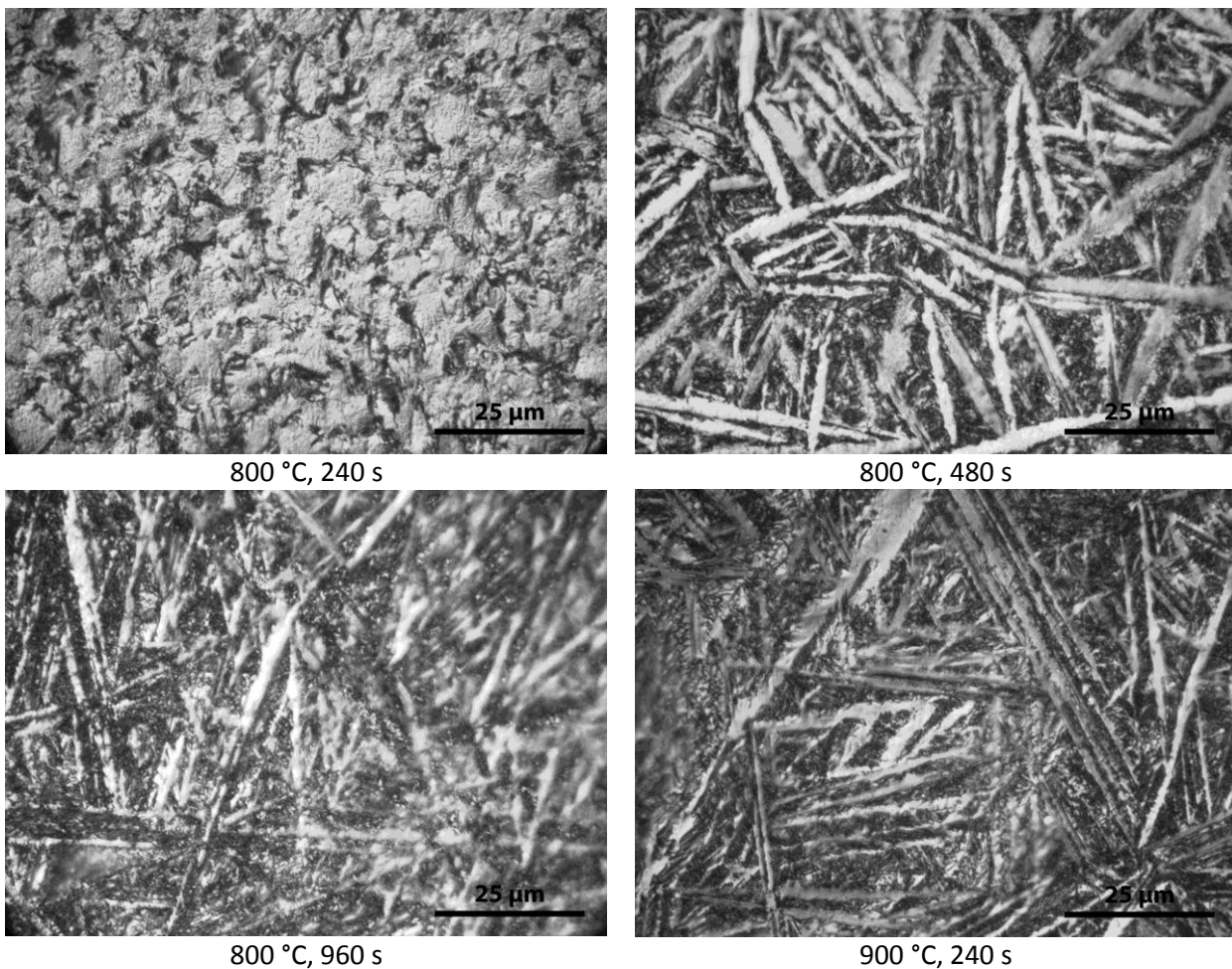
Figure A3   M5 samples hydrogenated at 800 and 900 °C during different durations.

The sample hydrogenated at 700 °C during 480 s minutes shows the structure completely transformed to the β‑phase. The needles became longer (30 µm) and thinner (1 µm). There are also α‑islands with characteristic size of about 15 x 8 µm. The only question is whether these needles are hydrides or these are zirconium needles result from β → α reverse martensitic transformation.

The structure of samples hydrogenated at 800 °C during 240 s and 480 s is very similar to corresponding samples hydrogenated at 700 °C. In the case of 480 s treatment full β - transformation occurred with formation of wide and relative long needles.

The sample hydrogenated at 800 °C during 960 s was completely β - transformed. The needles become longer with straighter edges. The average needle length was about 35 µm and 1.5 µm width. But several needles were as long as 70 µm. The islands of α - phase were filled with small black stripes, which were obviously emerged due to rearrangement of second phase particles. Between the needles there are also black regions full of the same shaped stripes. These stripes must be also additionally investigated by means of electron back scattered diffraction analysis.

The structure morphology and needle dimensions of sample hydrogenated at 900 °C during 240 s were all the same as for 800 °C and 960 s hydrogenation.

The metallography showed different details of microstructure, however, it was not possible to detect the hydrides. In a couple of specimens there were a lot of black stripes detected that looked very similar to hydrides described in literature and their morphological characteristics were measured. The next step should be the XRD analysis to verify the presence of hydrides and their crystal structure. This analysis will help to identify the phases, which are present. An additional method of electron back scattered diffraction analysis should be used to characterize the spatial distribution of the phases detected by XRD.

1.3   X - Ray diffraction analysis of hydrogenated M5.

X - ray diffractometry (XRD) analysis was applied to investigate the phases existing in the tested tubes including possibly precipitated hydrides. All samples were analysed at room temperature on conventional Seifert C3000 diffractometer equipped with a Meteor 1D linear detector and a MZ4 goniometer. As commonly applied in this technique, a monochromatic radiation corresponding to the copper CuKα emission line was used (E = 8047 eV, λ = 0.15406 nm). Measurements were made not on the surface of the tube but in the middle of the tube wall. At first the tube wall was grinded and polished to reach the half of its thickness in order to diminish the effect of the surface layer and to detect the presence of new phases in the bulk. Radial direction of the tube was parallel to the incident beam. Lattice parameters were calculated by DICVOL06 software after the whole profile fitting and background subtraction procedures by means of WinPLOTR program package.

XRD - profiles of as-received state showed that M5 diffraction peak positions were in very good agreement with the data for α-Zr obtained from International Centre for Diffraction Data database. No signs of any other phases were present.

X-ray pattern of hydrogen-free sample presented on all of the following figures (Fig. A4-A9) as a reference one. The main point of analysis was to find the peaks of γ, δ and ε zirconium hydride phases. For every phase reference peak data (angle and relative intensity) were taken out of the database and plotted on each figure for convenience. The numbers are 34-0690 for γ -, 34-0649 for δ - and 17-0314 for ε-hydride.

All kinds of treatments listed above in the Table 1 led to formation of hydrides. Simultaneously with hydrogen content the developing of a hydride pattern started with the two peaks of {111}$_\delta$ and {111}$_\gamma$. They emerged always together, providing the δ - hydride peak was in all cases higher than γ - hydride. After the development of the main peak {111}$_\delta$ further peaks with the lower intensity such as {200}$_\delta$ and {220}$_\delta$ started to develop. The peaks which used to have lower intensity can be visible only if the peak which normally has the highest intensity is enough developed. That is why for γ - phase the next visible peak {200}$_\gamma$ emerged only at the level of 8000 wppm H. Further increase of hydrogen content did not lead to formation of new peaks but to growth of the intensities of the already existing ones. In spite of a high content of β - stabiliser hydrogen at high hydrogen content there were no sign of β - Zr peaks observed. All β - Zr transforms into α - Zr + δ - and γ -

hydrides – in well accordance with the Zr – H equilibrium phase diagram. There was no evidence of ε - phase presence.

The peak position analysis gave the following result. All hydride peaks were shifted to the right from the table data values. It means that hydrides were elastically hydrostatically compressed in the zirconium matrix. In the case of zirconium peaks some of them were shifted from their values to the left, as for example $\{002\}_\alpha$ and $\{102\}_\alpha$. The rest of the peaks (for example $\{100\}_\alpha$ and $\{110\}_\alpha$) were exactly on their table values position. It means that the lattice of zirconium is inhomogeneously elastically or plastically distorted to accommodate the origination of hydrides without destruction.

The hydride pattern development described above is fulfilled for all investigated temperatures. No influence of temperature factor on the hydride peaks was detected..

There was a change in relative intensity of zirconium peaks after all the treatments. Main zirconium lines $\{100\}_\alpha$, $\{002\}_\alpha$, $\{101\}_\alpha$ were changed significantly. In particular after 360 s minutes of 700 °C treatment peaks $\{002\}_\alpha$ and $\{101\}_\alpha$ have exchanged their intensities. So the peak α $\{002\}_\alpha$ became 50% of its initial intensity and $\{101\}_\alpha$ raised up to 100%. In turn the intensity of $\{100\}_\alpha$ increased constantly during all the times and temperatures of treatment. As the peak intensity always tend to reach the intensity value of an annealed stress-free specimen it is obvious that temperature treatment and phase transformation have played the major role in the observed texture reorientation.

Figure A4   Sample H22M5: hydrogenation during 120 s at 600 °C, hydrogen content 306 wppm.

Figure A5   Sample H23M5: hydrogenation during 240 s at 600 °C, hydrogen content 1955 wppm.

Figure A6   Sample H19M5: hydrogenation during 120 s at 700 °C, hydrogen content 1700 wppm.

Figure A7   Sample H20M5: hydrogenation during 240 s at 700 °C, hydrogen content 1858 wppm.
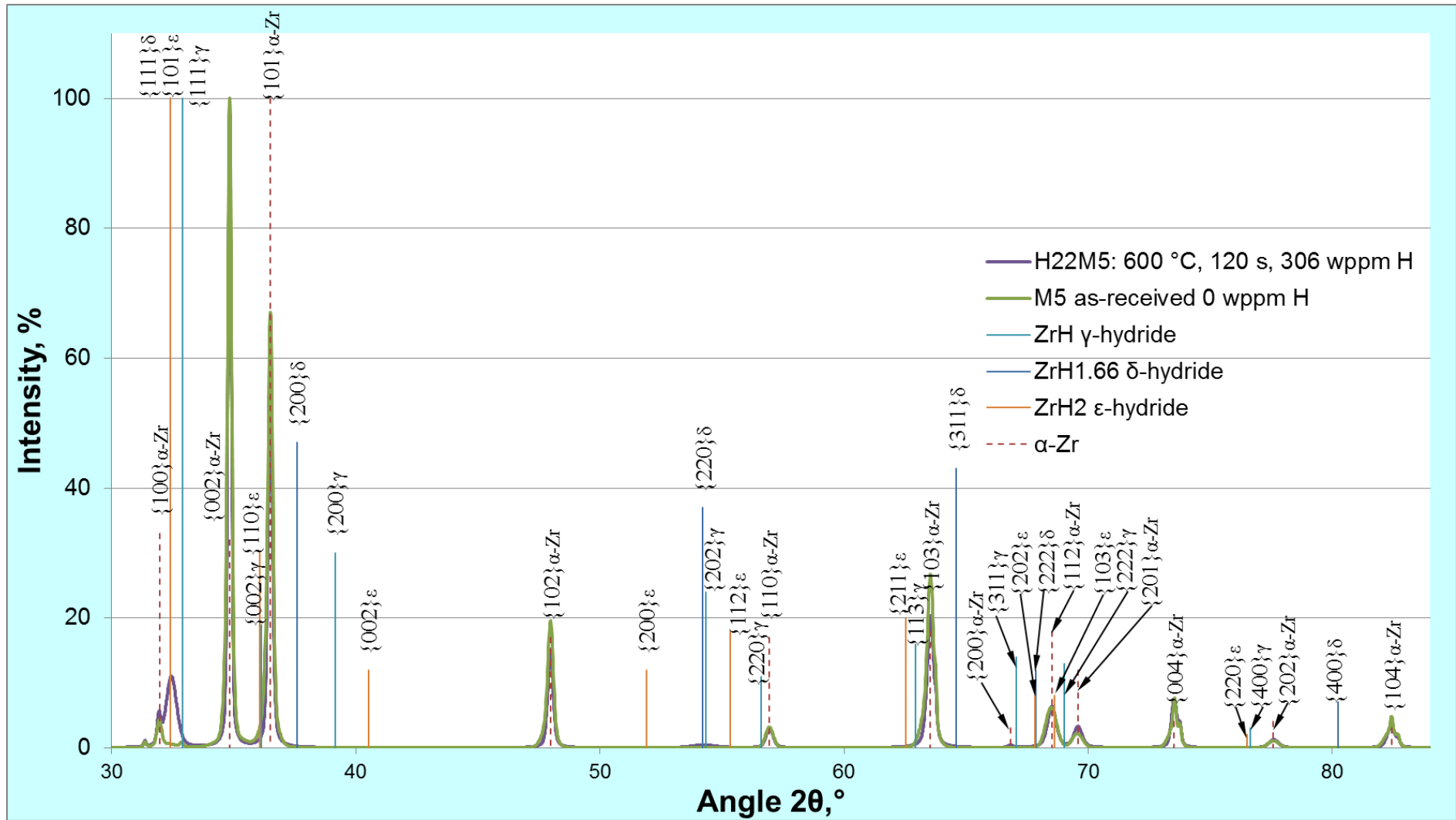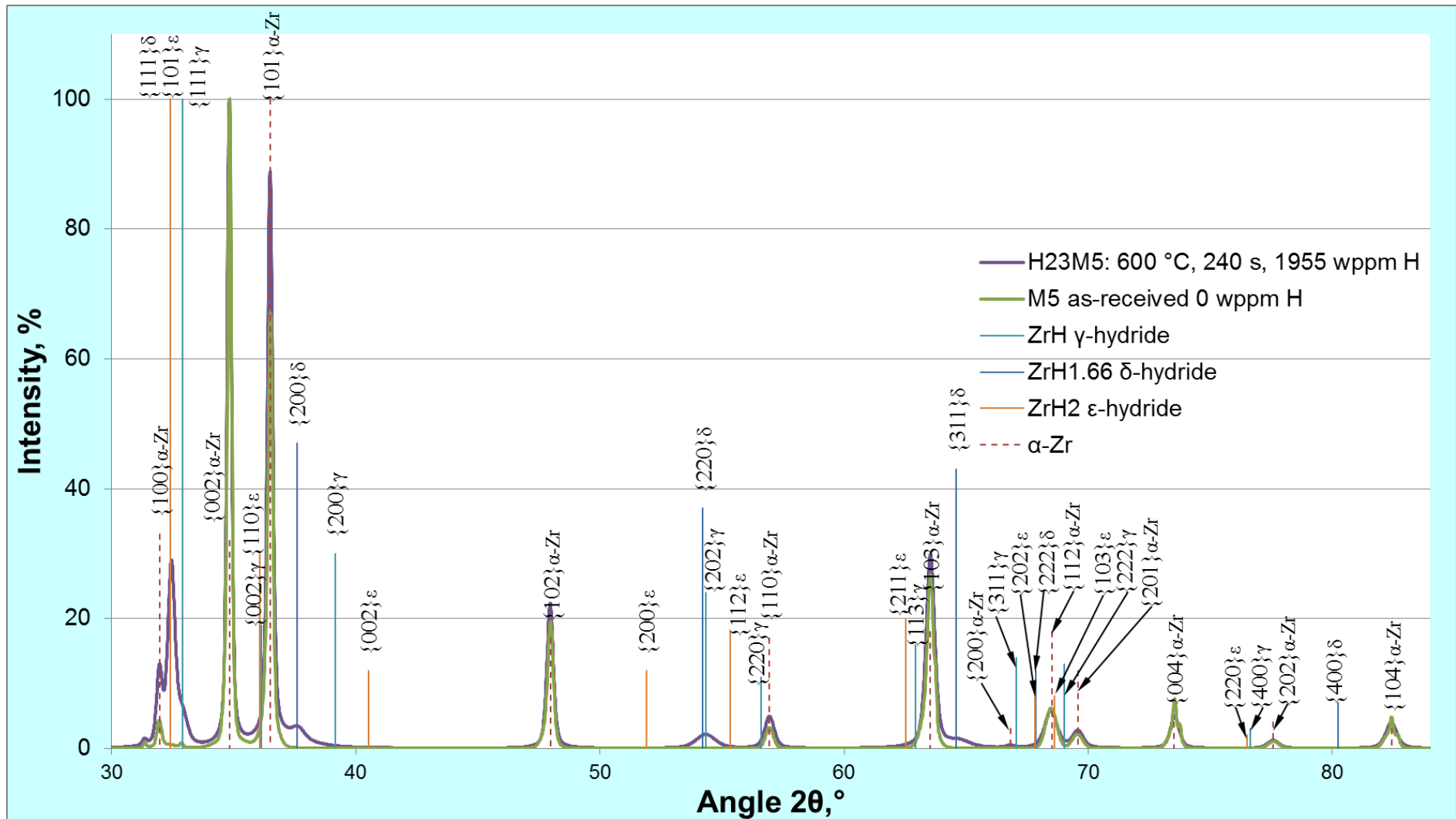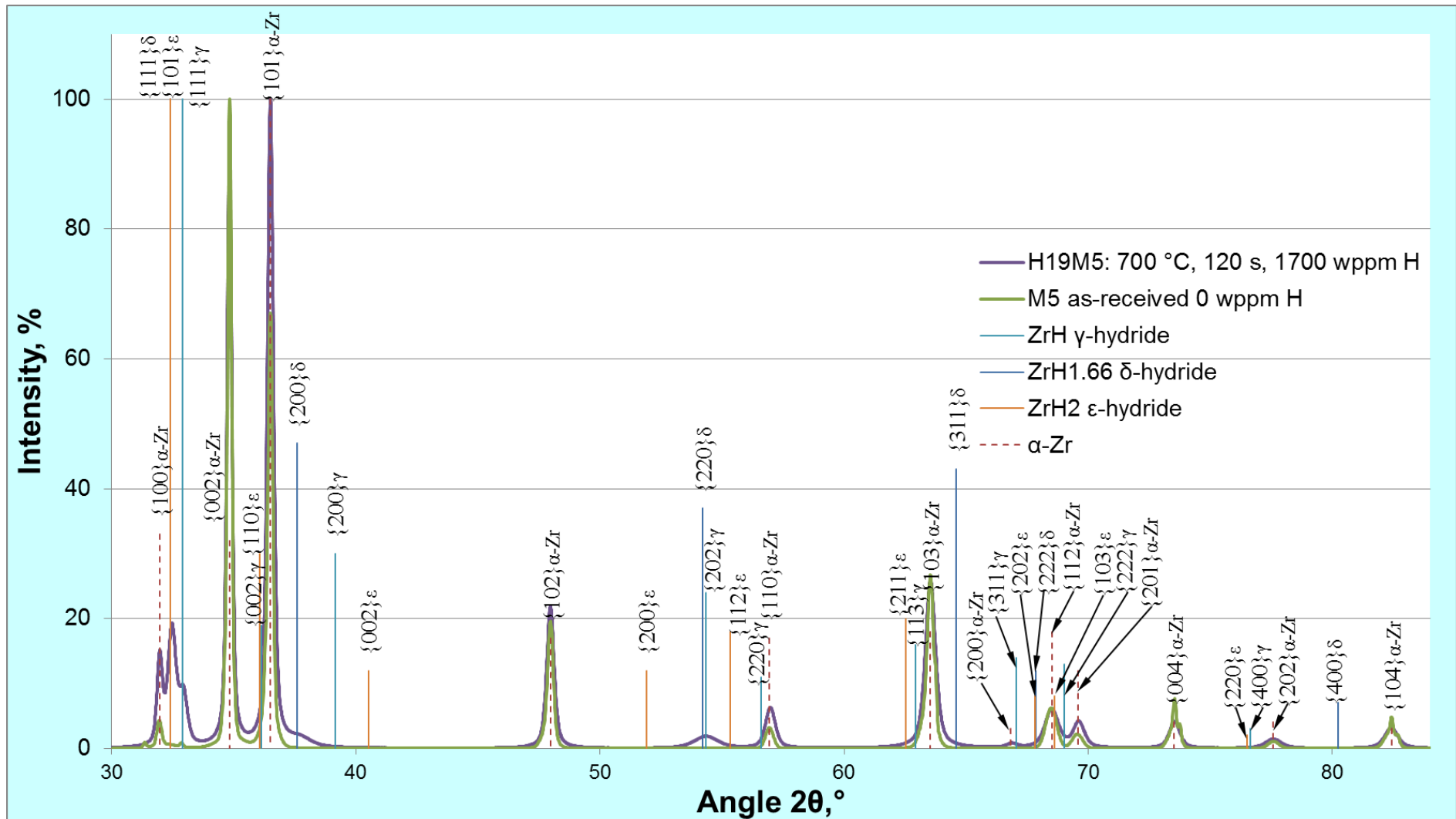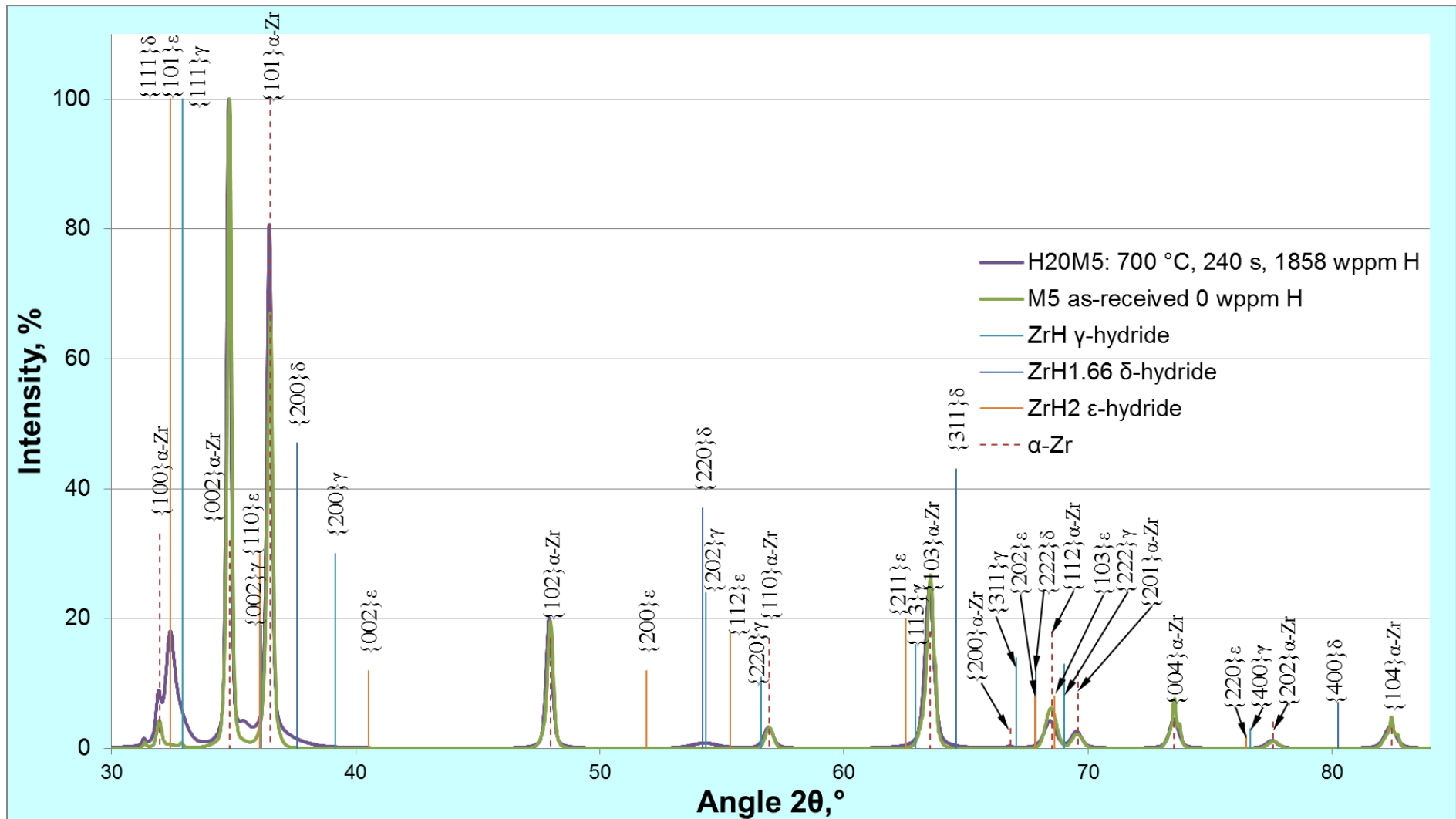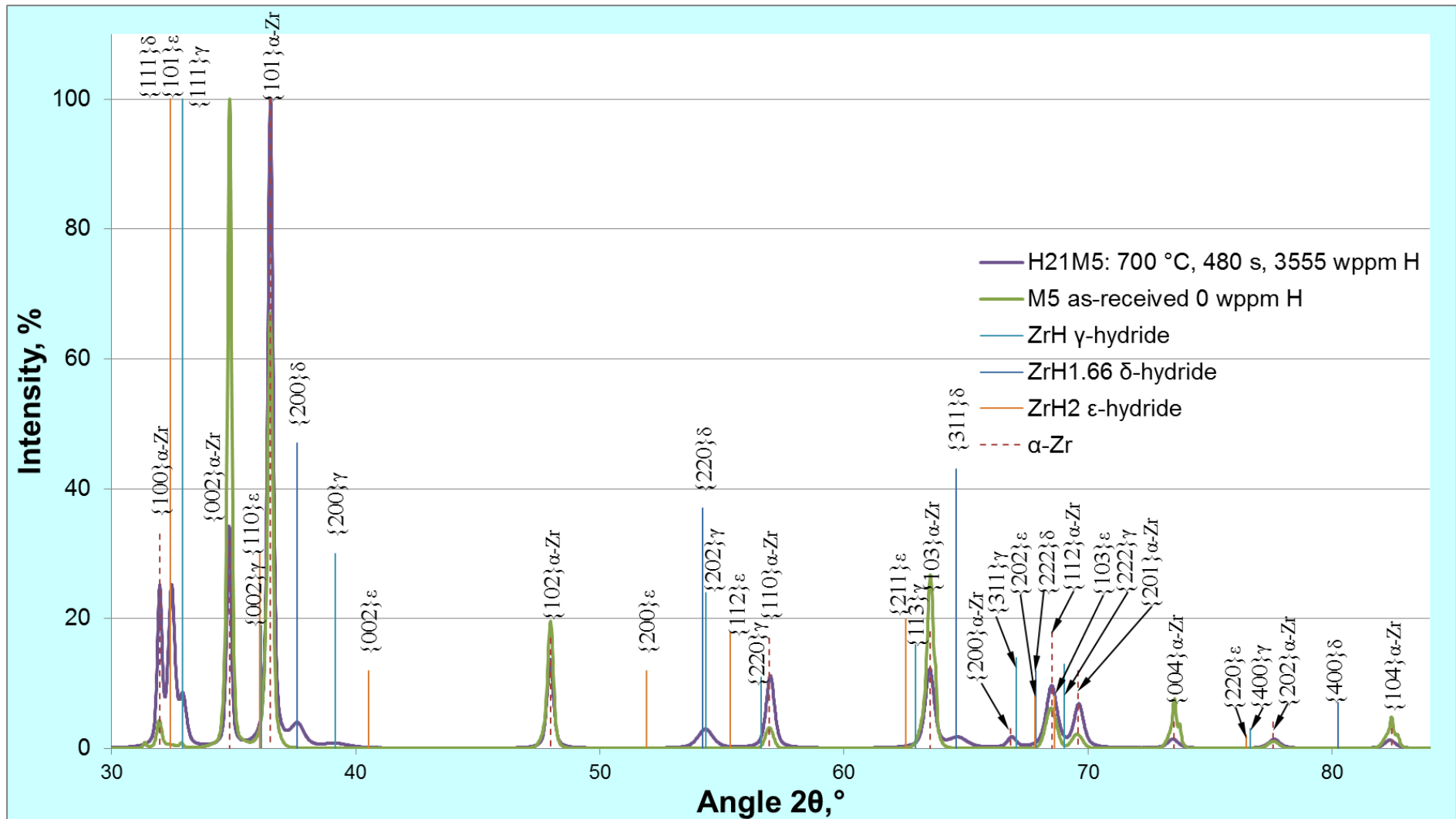
Figure A8   Sample H21M5: hydrogenation during 480 s at 700 °C, hydrogen content 3555 wppm.
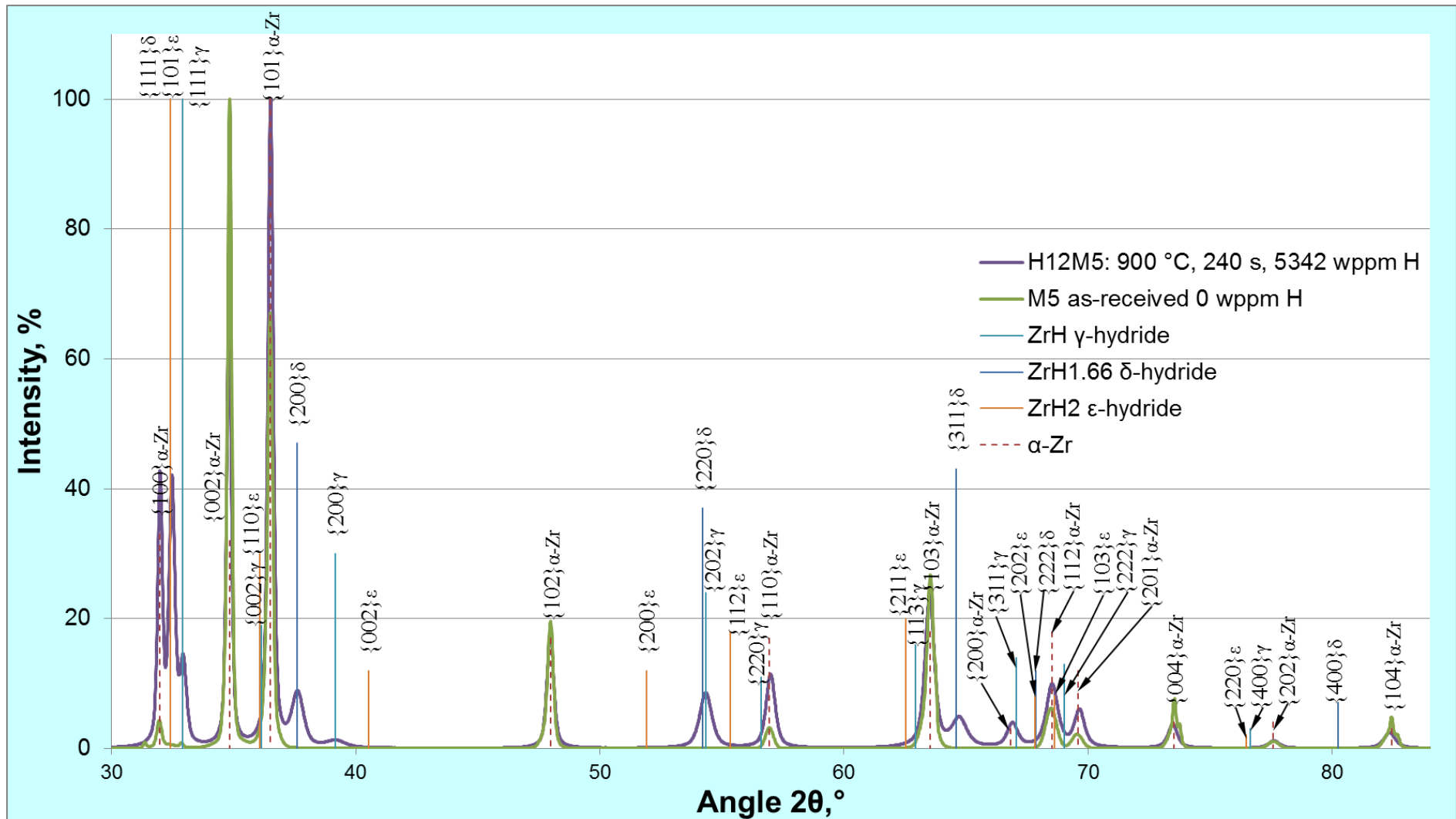
Figure A9   Sample H12M5: hydrogenation during 240 s at 900 °C, hydrogen content 4538 wppm.
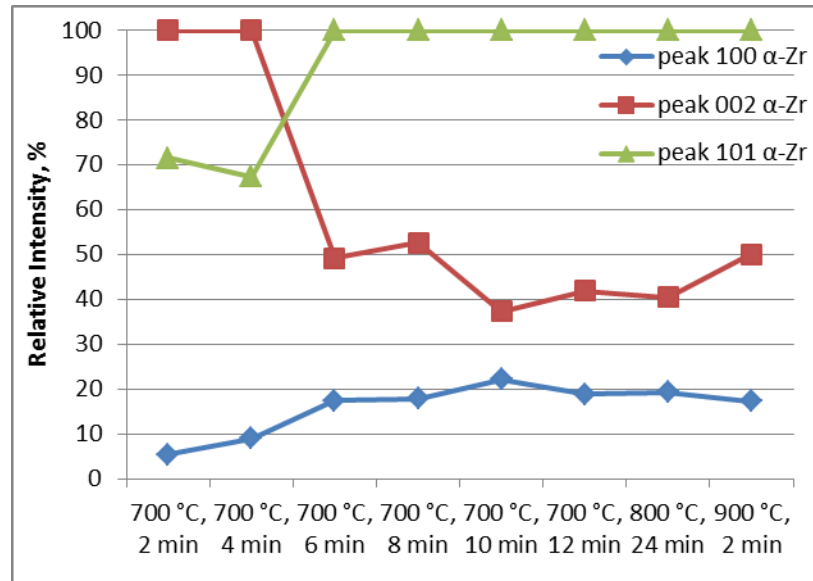
Figure. A10 Relative intensity evolution of α-Zr peaks.

The change in the texture observed by means of X-ray diffraction is in agreement with change in the microstructure of metal previously observed by optical metallography. It was already seen that from 120 to 240 s there were only α‑Zr grains of initial size with narrow boundaries to observe. But after 240 s of treatment at 700 °C microstructure evolution towards prior β‑phase becomes more pronounced and grain boundaries become unstable and the process of structure evolution is going further with the increasing treatment time and temperature (Fig. A10). According to the structures observed, change in the intensities was related to the course of α‑β transformation together with recrystallization (grain boundaries desintegration) and reorientation and regrouping of small grains into big regions of nearly the same orientation. Texture evolution processes went quicker in the presence of β‑stabilizer hydrogen because of his impact on the temperature boundary of phase transformation.

2 Microhardness test results

To evaluate the influence of synchronously developing processes of annealing and hydrogenation on the material properties the microhardness of hydrogenated and annealed specimens were measured. The tests were performed with Fischerscope Testing device. The values of microhardness, elastic modulus and elastic strain were obtained. It should be mentioned, that HV value is not pure Vickers hardness, but it was obtained by calculation of HV = 0.0945 H_{IT}, where H_{IT} is a maximal depth of the Vickers pyramid. It means that H_{IT} also includes elastic part of strain. Using this method one can obtain an estimation of HV according to DIN EN ISO 14577.

Microhardness tests have demonstrated a complex effect of hydrogen and temperature during the treatment (Fig. A11). All specimens annealed in argon atmosphere have almost the same level of about 195 HV Vickers hardness even after cooling from 900 °C. It is normal because there was no additional diluted element inside the structure to change its internal stress state.

In the presence of hydrogen the microhardness started to increase from the very beginning already at 600 °C. The one of the main possible reasons for microhardness increase is β‑quenching of oversaturated solid solution of hydrogen in zirconium matrix and martensitic type of structure transformation into prior β‑phase together with hydride phase formation which occur during cooling phase of the experiment. The

metallographic investigation of the samples hydrogenated at 600 and 700 °C to low hydrogen content detected the traces of β - transition in small local regions near to grain boundaries, where hydrides have probably formed. The volume fraction of prior β - structure will obviously define the overall microhardness level as it defines the place of preliminary hydride precipitation. The temperature and hydrogen together boosted the β - phase formation process. So at 800 and 900 °C there was more β - phase after short hydrogenation time period and in turn more prior β - phase after cooling with the fast increase of microhardness already at low hydrogen level due to homogeneous hydride redistribution. But there is an upper limit of about 320 HV for all curves in performed tests at high hydrogen content that is why it can be considered as the hydride microhardness level.
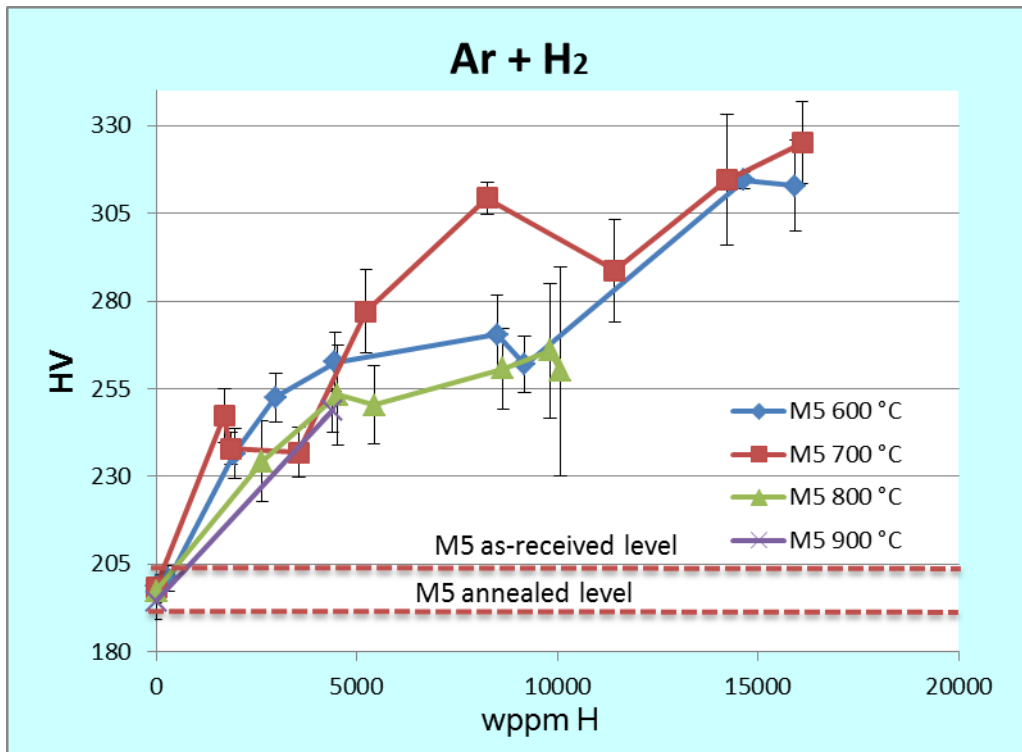
Figure A11   Microhardness of M5 hydrogenated to various hydrogen content under various temperature

.

3 Tension test results

M5 samples charged with hydrogen to different content were subjected to uniaxial tension under strain rate of $7*10^{-4}$ s^{-1} at room temperature. Details on the treatment of each sample are summarized in table 2.

Table A2.   Hydrogenated samples of Zircaloy-4 and M5 for tension test.

Name	Temperature	Duration in H$_2$	H$_2$ (mass gain)	Elongation at rupture	Ultimate tensile strength
	°C	min	wppm	%	MPa
Zircaloy-4 samples					
As-delivered	0	0	0	13.7	690
Annealed in Ar	700	30	0	33.7	500
M5 samples					
As-delivered	0	0	0	25.1	510
H1RM5	800	4	590	6.6	690
H14M5-a	800	8	2645	2.2	695
H14M5-b	800	8	2643	3.0	710
H14M5-c	800	8	3949	0.9	555
H15M5	800	16	4523	0.4	310

As-delivered Zircaloy-4 tube showed approximately 13% of strain and 700 MPa of ultimate stress as it is seen in the Fig. A12a. Annealing during 30 minutes in Ar atmosphere has led to the reduction of maximal engineering stress down to 500 MPa and strain to rupture has risen up to almost 35%, which is normal for annealed Zircaloy-4.

As one can see in the Fig. A12b all degrees of treatment in hydrogen mixed with argon atmosphere have led to a rapid reduce of plasticity. After 120 and 240 s high plasticity reduction but fracture of alloy is still looks plastic. At the time of 360 and 480 s the material is very brittle and overall strain is less than 3 and 1 % respectively. But in the case of 800 and 900 °C treatment after the same time periods the plasticity of alloy still remained not less than 4-5%.

The samples of M5 treated at 800 °C have shown nearly the same behavior. One can see the strong plasticity reduction and at the same time sufficient material hardening. The maximal stress is at the level of 700 MPa.
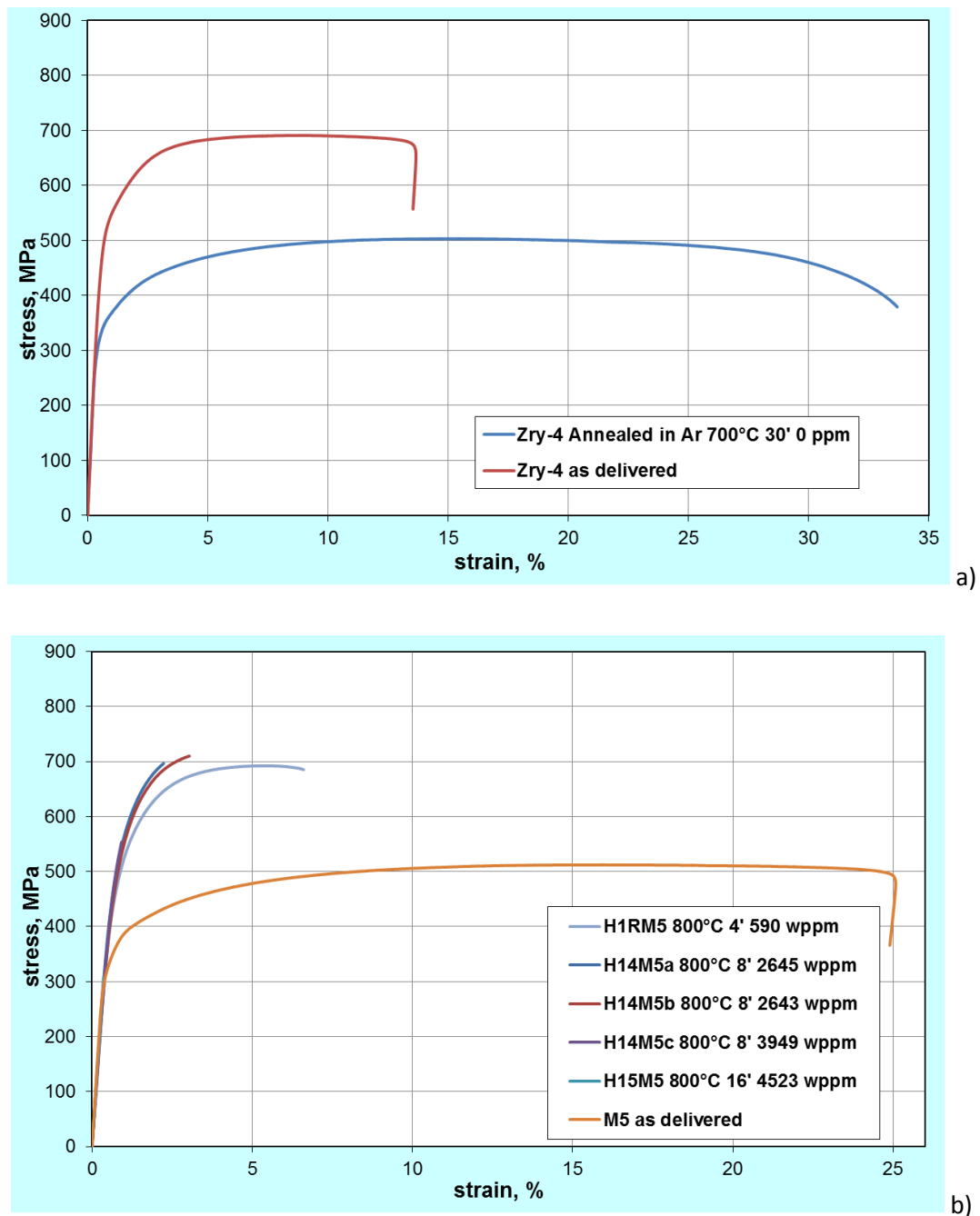
Figure A12   Stress-strain curves of zircaloy-4 samples charged with hydrogen at different temperatures: a) as-delivered and annealed in Ar; b) 800 °C M5 hydrogenated vs annealed in Ar, during different time intervals.

So it can be concluded that not the treatment time but the level of hydrogen content is responsible for plasticity reduction. It is shown in Fig. A13a that 500 wppm of hydrogen rapidly reduces plasticity by 2 times. Also we can observe small increase in maximal stress (Fig. A13b). So the approximate level of 1000 wppm leads to further reduction of plasticity and quasi-brittle fracture and 3000 wppm leads to high reduction of plasticity and to brittle fracture.

a)

b)
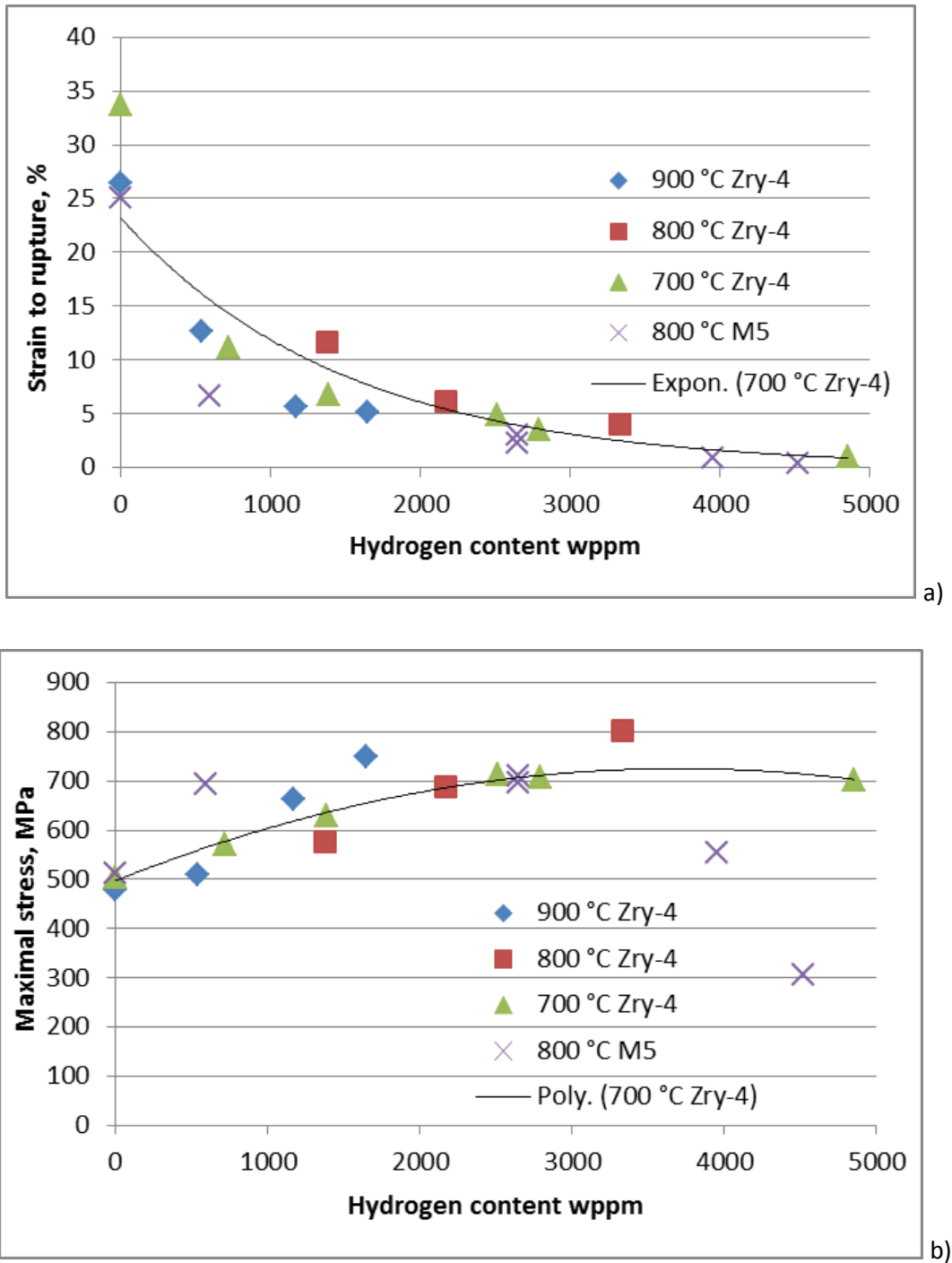
Figure A13   Dependences of maximal strain to rupture a) and maximal stress vs hydrogen content in wppm.

4 Observation of zirconium hydrides by Electron Back Scatter Diffraction (EBSD)

In spite of the results on hydrogenation of Zr and investigation of zirconium hydrides there was still no possibility to say the exact place of hydrides in the microstructure and their bulk distribution. The chance to detect hydrides after above-shown scenarios of structure transformation by means of optical methods is vanishing. Especially in the case of acicular structure which strongly prevents the analysis of hydride morphology and distribution. The analysis of literature has shown that no one has performed the investigation by means of electron back scattered diffraction (EBSD) of hydrogenated M5 particularly under the LOCA temperature modus.

The EBSD method is a relatively new technique which can be used to obtain the data on the type and orientation of local volume of tens of nanometre scale. It allows reconstructing a phase map and an orientation distribution map of a hundred micrometre scale region combining the resolution of TEM and a field of investigation of hundreds of material grains. On the basis of the neighbouring grain orientation the information on grain boundary type and its overall length can be obtained. This technique is very powerful in detecting the phases in two phase material.

It should only be mentioned, that this method differs only the crystal lattice, but not to what kind of phase it belongs to. One should consider some possible phases to look for. That is why EBSD was used only in conjunction with XRD. Only the coupled investigation allows full exclusion of errors in phase detection which could happen by means of EBSD. The material phase composition, the type of lattice and the distance between the characteristic planes were determined from XRD peak position. These type of phase and lattice parameter values were used during EBSD analysis to detect exactly this phases in the EBSD - map.

Data obtained by means of such tandem analysis helps 1) to detect hydrides, their morphology and distribution in different types of structure; 2) to establish crystallographic relation between Zr matrix and hydride; 3) detect the position and interrelation between γ - and δ - hydrides; 4) understand the mechanism of embrittlement. In the present report only the first point will be investigated.

The radial-axial section of the tube wall was cut from the middle part of the hydrogenated tube for investigation. The material preparation for EBSD - measurements was the same as used for metallography. The details of EBSD analysis were as follows.

After hydrogenation in α - region of the phase diagram at 600 °C to 306 wppm H the hydrides were already good detectable (<u>Fig. A14</u>). Only δ - hydrides were detected in the microstructure without any sign of γ – hydrides probably due to their low amount according to comparison of XRD peak intensities. Most of the hydrides at low hydrogen content looked like needles and grew along the grain boundaries (inter-granular). Image analysis gives 98% Zr, 2% δ - $ZrH_{1.66}$.
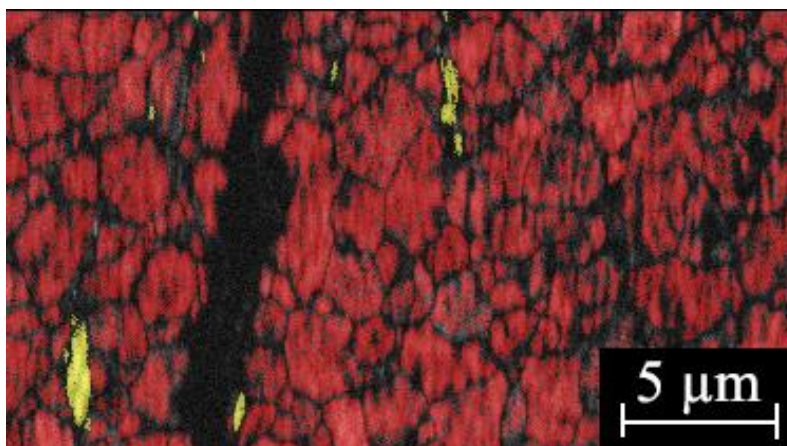
Figure A14   Phase map of the sample H22M5 (600 °C, 2') with 306 wppm H hydrogenated in α - Zr region of phase diagram (red – α - Zr, yellow – δ - ZrH1.66, black – undetectable zones).

Hydrogenation degree of 4523 wppm H is in the field of β at 800 °C in the phase diagram. At this hydrogenation degree there were large needles of α - Zr detected which could be easily taken for hydrides. Though the hydrides look like needles, but they fill rather the volume between two Zr needles. This type of structure is usually called Widmanstätten pattern. It can be seen in the Fig. A15 and Fig. A16 the hydride detection is very complicated without EBSD on this type of structure. The γ - hydride needles (Fig. A15 blue colour) were detected only when the peak intensity on the XRD - diagram was relatively high. A volume fraction of Zr metal in the form of needles which result from martensitic transformation during cooling is lower than one of hydride. Image analysis gives 48% Zr, 50% δ - ZrH$_{1.66}$, 2% γ - ZrH.
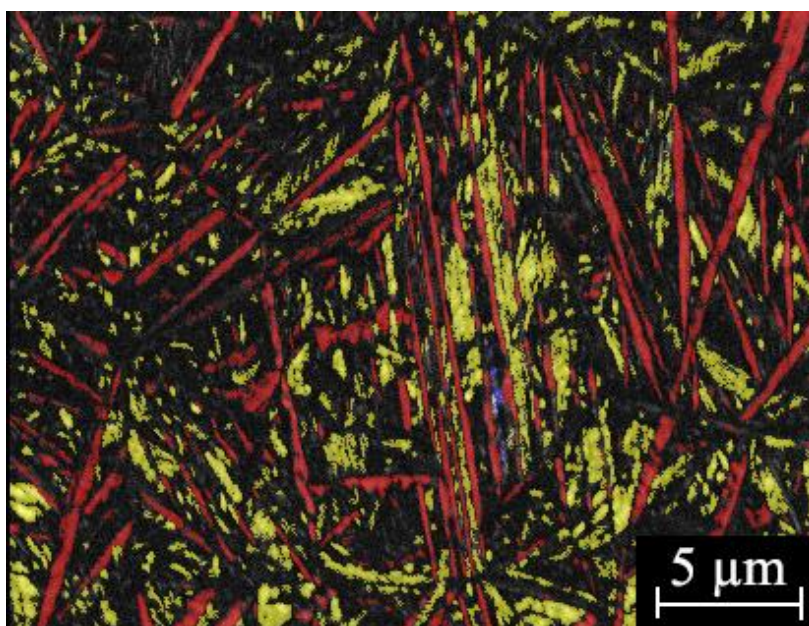
Figure A15   Phase map of the sample H15M5 (800 °C, 16') with 4523 wppm H hydrogenated in β - Zr region of phase diagram (red – α - Zr, yellow – δ - ZrH1.66, blue – γ - ZrH, black – undetectable zones).

On the example of these two samples one can see how different can be the structure of hydrogenated sample of M5 in spite of that in the phase diagram only α - Zr and δ - hydrides are presented. The further investigations in understanding the hydrogen embrittlement should include thorough analysis of grain orientation, grain boundary spectra. The crystallographic relation between Zr matrix and hydride as well as interrelation between γ - and δ - hydrides should be established. Also the role of alloy components should be investigated.

Figure A16   An example of hydride detection by means of EBSD and impossibility to do this by means of optical analysis. Phase map of the sample H15M5 with 4523 wppm H combined with SEM image.

Appendix B. Relation of experimental data to the ECR criterion modified by GRS

J. Stuckert

According to the definition, the ECR (Equivalent Cladding Reacted) shows the weight increase of 1 cm² cladding tube due to absorbed oxygen (ratio of mole fractions of oxygen and the metal in 1 cm² of the tube):
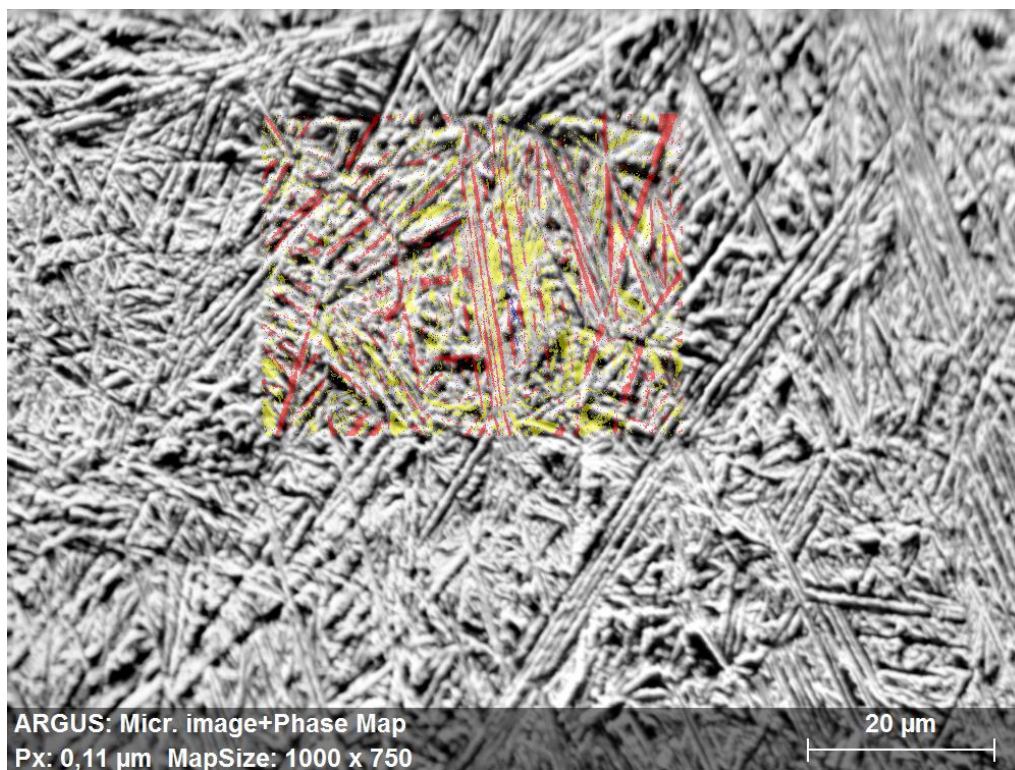
$$ECR = (m_O/M_{O2})/((\ \tau_{cl}*\rho_{Zr})/M_{Zr}),$$

with m_O – oxygen in 1 cm² of tube [g], τ_{cl} – initial thickness of tube [cm], ρ – density [g/cm³], M - molar mass.

The oxidation degree of claddings after the QUENCH-LOCA tests was measured by means of eddy-current method, which gives the summarized thickness of ZrO_2 and α-Zr(O) layers. Both Cathcart-Pawel correlations, for the mass gain as well as for the layer thicknesses, are known; therefore, there is direct correspondence between eddy-current data (in µm) and ECR (in wt%). This correspondences for the regions of hydrogen bands in claddings of the QUENCH-L0, -L1 and -L2 bundles are depicted in Tables B1, B2 and B3, correspondingly. The tables include also more conservative ECR values calculated by Baker-Just correlation. Hydrogen contents included in tables are results of the neutron tomography measurements.

Table B1 Results of the QUENCH-L0 test

rod #	Elevation of hydrogen band, mm	ZrO_2+α-Zr(O) eddy current, µm	ECR (Cathcart-Pawel), %	ECR (Baker-Just), %	Hydrogen (*point max), wppm
1	955	33	*2.10*	*2.35*	2560
3	937	22	*1.35*	*1.52*	2140
7	970	24	*1.48*	*1.66*	1940
14	960	9	*0.57*	*0.64*	1050

*point=x*y*z=3*3*1 pixels, pixel size: 14 µm

Table B2. Results of the QUENCH-L1 test

rod #	Elevation of hydrogen band, mm	ZrO_2+α-Zr(O) eddy current, µm	ECR (Cathcart-Pawel), %	ECR (Baker-Just), %	Hydrogen (*point max), wppm
2	907	22	*1.35*	*1.52*	1800
3	930	23	*1.42*	*1.59*	1115
4	990	12	*0.74*	*0.83*	730
5	930	19	*1.21*	*1.36*	755
6	925	17	*1.05*	*1.18*	795
7	940	16	*1.00*	*1.13*	695
8	908	15	*0.96*	*1.07*	1435
9	895	14	*0.86*	*0.96*	1270

* point=x*y*z=3*3*1 pixels, pixel size: 44 µm

Table B3. Results of the QUENCH-L2 test

rod #	Elevation of hydrogen band, mm	ZrO₂+α-Zr(O) eddy current, μm	ECR (Cathcart-Pawel), %	ECR (Baker-Just), %	Hydrogen (*point max), wppm
1	848	17	*1.09*	*1.12*	920
2	931	14	*0.87*	*0.89*	545
3	934	13	*0.82*	*0.84*	550
6	896	16	*1.02*	*1.05*	560
9	902	18	*1.14*	*1.16*	785

* point=x*y*z=3*3*1 pixels, pixel size: 75 μm

The relation between these data and GRS curve for the boundary between ductile and brittle claddings [B1] shows, that practically all hydrogenated claddings of three bundle tests correspond to ductile region of diagram (Fig. B1).
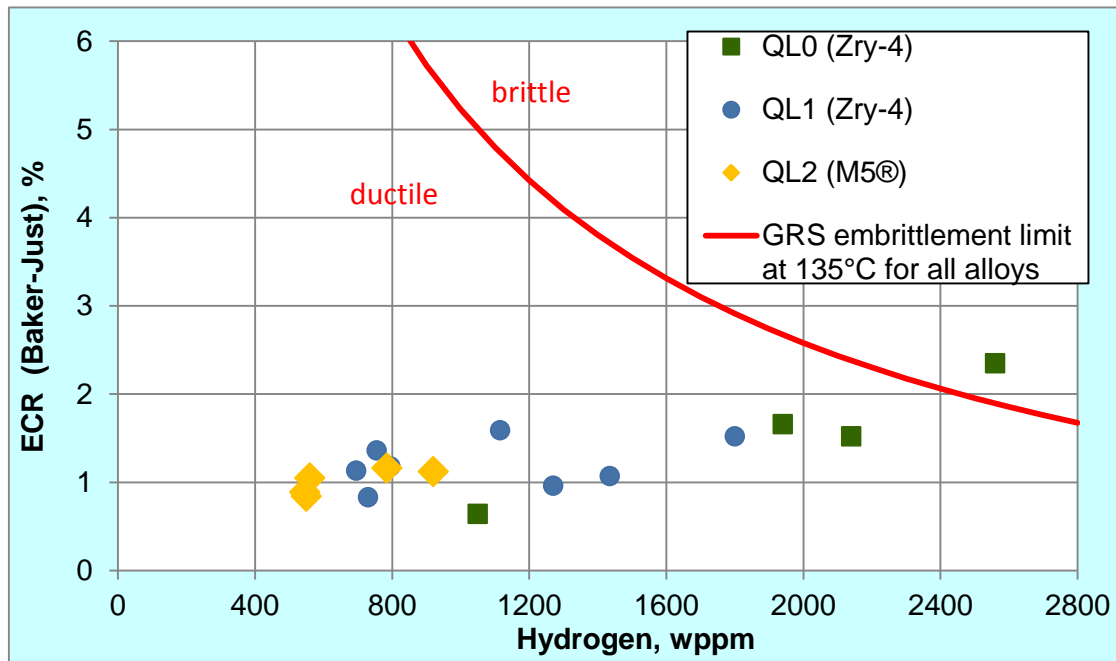

Figure B1.   Bundle data in relation to GRS "ductile – brittle" diagram.

Reference

[B1] J. Herb, J. Sievers, H.-G. Sonnenburg. Ermittlung der Festigkeit von Brennstab-Hüllrohren aus Zry-4, M5, ZIRLO und Zry-4-low-tin anhand von Ringdruckversuchen. GRS Report GRS-A-3698. April 2013.

The overall objective of the QUENCH-LOCA bundle test series is the investigation of ballooning, burst and secondary hydrogen uptake of the cladding under representative design basis accident conditions as well as detailed post-test investigation of cladding mechanical properties to analyze the material behavior with respect to embrittlement. The QUENCH-LOCA-2 bundle test with M5® claddings was performed according to a temperature/time-scenario typical for a LBLOCA in a German PWR with a maximal heat-up rate of 8 K/s, a cooling phase lasting 120 s and the terminated with 3.3 g/s/rod water flooding. The maximum temperature of 1400 K was reached at the end of the heat-up phase at elevation 850 mm. The tangential temperature difference across a rod was up to 70 K on the burst onset. Due to the low ballooning degree the maximum blockage ratio of the cooling channel (15% at 960 mm) was lower in comparison to the reference test QUENCH-LOCA-1 performed with Zircaloy-4 claddings (about 23%). The cladding burst occurred at temperatures between 1050 and 1195 K (similar to QUENCH-LOCA-1). During quenching, following the high-temperature phase, no cladding fragmentation was observed (residual ductility is sufficient).

The post-test neutron tomography of claddings showed that pronounced hydrogen bands inside QUENCH-LOCA-2 claddings (secondary hydriding) were observed only for five inner claddings and only in two cases the hydrogen concentration was higher than 1000 wppm (about 1100 wppm). Nine claddings (one from inner rods and eight from outer rods) failed during tensile tests due to stress concentration at the burst position – similar to rods of the QUENCH-LOCA-0 commissioning bundle with hydrogen concentration < 1500 wppm. All other claddings failed due to fracture after necking at elevations outside of the ballooning region.